Laboratoire Kastler Brossel - Université Pierre et Marie Curie
ACQAO - Physics Department - The Australian National University

Quantum imaging with a small number of transverse modes

Vincent Delaubert

A co-tutelle thesis submitted for the degree of
Doctor of Philosophy
of the Australian National University
and the Université Pierre et Marie Curie

January, 2007

Declaration

This thesis is an account of research undertaken between September 2003 and January 2007 in *the Department of Physics, Faculty of Science, Australian National University, Canberra, Australia*, and *the Laboratoire Kastler Brossel, Paris, France*.

Except where acknowledged in the customary manner, the material presented in this thesis is, to the best of my knowledge, original and has not been submitted in whole or part for a degree in any university.

Vincent Delaubert
January, 2007

Contents

Introduction

Optical images are very familiar to anyone : they correspond to any light distribution, that can be recorded onto our retinae or onto a detection device such as the film or the CCD detector of a camera. A photograph is hence an example of image intensity measurement.

In order to accurately describe the properties of optical images, the quantum nature of light must be taken into account, even when the image is formed of a great number of photons. Indeed, for most light sources, the time of arrival on the photons of the photons composing the image on the detector is random. This randomness is called *quantum fluctuations* and inevitably degrades the quality of the detected image, when all other sources of noise - electronic, mechanical, thermal - have been canceled. This ultimate detection limit is called the *standard quantum noise limit*. As a consequence, there exists a fundamental bound to the resolution of spatial details within an optical image arising from this phenomenon, and which can be estimated using quantum mechanics.

Nevertheless, recent progress have been obtained in quantum optics with the simultaneous development of stable and reliable laser sources, high quality optics and non-linear materials. These developments now allow the creation of strong quantum correlations or even entanglement between light beams. The quantum fluctuations discussed above can notably be reduced with the generation of the so called *squeezed states of light*. However, such results cannot be directly applied to spatial resolution improvement within an optical image, as these techniques only modify the fluctuations of the entire beam, considered as a *single mode field*, and do not selectively improve the detection of local spatial parameters.

In order to account for local detection improvement, additional spatial degrees of freedom have to be considered, in order to extend the previous results to the case of multi-mode quantum optics. This very recent field of research has notably introduced the notions of *local squeezing* [Kolobov 99] and *quantum imaging* [Lugiato02, Kolobov06].

Two regimes can be considered for the multi-mode description of an image. The first one is the photon-counting regime, for which photons can be detected individually and images are described in terms of photon number states, i.e. Fock states. Spatial aspects are usually not considered in this regime, but are still present and have been used to reconstruct an image using spatial correlations in a two-photon or "ghost imaging" setup [Gatti04]. In this thesis, we restrict our analysis to the second regime, termed *continuous variable* (CV) regime. It comprises experiments involving bright continuous wave (CW) and intense pulsed laser beams, for which the number of detected photons per detection time is large compared to the quantum fluctuations, and a continuous field description is adapted. The broad variety of multi-mode optical images allows to envision applications

such as high precision sensors and channels for quantum information. We hence distinguish two main fields developed in this manuscript where such a description is required in this regime : *image processing* - or *quantum imaging* - and *parallel quantum communication*.

Let us first introduce the field of *image processing* and its potential applications. To each optical measurement performed on an image corresponds a *standard quantum noise limit* for the extraction of information about a given spatial parameter. The performance of photo-detectors and array detectors allow a precise and efficient detection of the local field, and the Rayleigh criterion [Rayleigh1879], defined relative to the eye performance, is no longer the ultimate limit. The ultimate detail that can be distinguished is thus not necessarily the wavelength size anymore, and details below the diffraction limit are accessible. Moreover, it can be shown, and this is one of the main challenges of this thesis, that a specific multi-mode beam can be generated in order to reduce the fluctuations on any image measurement below the *standard quantum noise limit*. This is of great interest in ultra-sensitive image measurement for which quantum noise is a limiting factor, for example in pattern recognition for optical disc read-out [VanDeNes06,1], or nanometer scale laser beam displacement measurements in gravitational wave detectors [Willke02] or atomic force microscopes [Putman92].

Let us now present the field of *parallel quantum information communication*. Quantum information science is a new and rapidly expanding field of research which combines the techniques developed in quantum optics with those of information science[Europe05]. One of the challenges is to provide *quantum information channels* to convey the quantum information. Quantum protocols such as quantum entanglement, quantum cryptography, dense coding and quantum teleportation are for example related to this issue and have already been demonstrated in the single-mode regime [Ou92, Silberhorn01,2, Mattle96]. Moreover, it has been shown that parallel channels could coexist in a multi-mode laser beam, thus ensuring a parallel transfer of quantum information [Caves94]. This field has not yet been investigated experimentally in the continuous variable regime and its requirements are very similar to those of quantum imaging.

This thesis, which was a co-tutelle between the quantum optics groups of the Laboratoire Kastler Brossel and of the Australian National University, has been undertaken in the scientific context described above. The work presented in this manuscript has benefited from the expertise of Claude Fabre's group in image processing, and from the one of Hans Bachor's group in quantum communication. This PhD was a natural continuation of the very close collaboration that already existed between both laboratories and which led Nicolas Treps to spend some time in Canberra during his PhD and do a Post-Doctorate there. In particular, the work on the measurement of small beam displacement had already given high-quality results [Treps02, Treps03]. At this stage, the conjugate observable of the position of the beam was still to be found. This is what motivated the first part of my work, in collaboration with M. Hsu, and led first to propose a novel way of measuring beam displacement, and then to introduce the tilt of the beam as the conjugate variable of the beam displacement. My first experimental task has hence been to demonstrate similar results as the one obtained by Nicolas Treps, with a new detection system, and involving this time simultaneous displacement and tilt of a laser beam. The success of this experiment was made possible at the ANU thanks to the availability of a single-mode squeezed

light source developed by Ping Koy Lam and Ben Buchler. On the one hand, the seek to prove the optimality of our detection scheme has led us to investigate for the quantum limits in image processing in a very broad context and to collaborate with Philippe Réfrégier from the Institut Fresnel de Marseille. This theoretical work was complementing some results already obtained in image processing with multi-pixel detectors which had led us to the field of optical data storage. On the other hand, it was very natural to try to produce entanglement between the two spatial quantum variables that had been exhibited. I have thus taken part with Mikael Lassen and Jiri Janousek to the elaboration of a double squeezing source in order to produce entanglement between position and momentum of laser beams. A study of Optical Parametric Amplification and Second Harmonic Generation of higher order transverse modes had been necessary prior to the development of the entanglement setup. Note that most of the theoretical part of my work has been done in Paris whereas the experimental part has exclusively been performed in Canberra.

In the first chapter of this manuscript, we precisely define optical images and their quantum properties. We make a precise distinction between single-mode and multi-mode optical field and present how to selectively measure the information carried by one spatial mode of the field, either using a homodyne or an array detection. We also present how to perform measurement beyond the *standard quantum noise limit* with the use of squeezed light in an appropriate mode within the incident field.

The second chapter is dedicated to the application of array detection results to high-density optical data storage [VanDeNes06,1]. We show that more than one bit of information can be encoded and read-out per beam width on an optical disc, at a given wavelength and numerical aperture. We give a brief overview and include in the manuscript two topic-related articles published during the course of this PhD. The first article investigates the possibility of implementing an array detector in optical discs systems in order to differentiate complicated patterns diffracted by sub-wavelength details encoded onto the disc. In the second article, we additionally consider data encoding in the longitudinal phase by using pits of different heights.

In the third chapter, we introduce parameters that can be imprinted onto the transverse plane of a laser beam. We notably show that displacement, tilt, waist-size and waist-position mismatches of a gaussian TEM_{00} beam are simply related to specific Hermite Gauss modes. We then define the lowest bound, the *standard quantum noise limit*, under which the detection is seriously altered by quantum noise. Finally, we broaden our analysis to any spatial parameter and tackle the following question : what is the lowest limit imposed by a given distribution of quantum noise to the accuracy of a measurement of a transverse parameter, independently of the information processing protocol used for the information extraction?

The fourth chapter is experimentally oriented and presents how to manipulate single and multi-mode optical images. Key elements for the implementation of quantum imaging experiments are presented in the particular case of Hermite Gauss modes. We notably detail the selective generation, combination, and separation of modes. We then focus on parametric interaction between several modes in second harmonic generation (SHG) and optical parametric amplification (OPA) systems. This led to the first generation of squeezing in higher order Hermite Gauss modes.

The last chapter presents two entire setups making use of the concepts introduced

in the previous chapters. The first experiment deals with the optimal measurement of displacement and tilt of a TEM_{00} beam beyond the *standard quantum noise limit*. This quantum imaging experiment introduces the notion of position squeezed beam whose displacement measurement can be performed at a nanometer scale. The second one is more quantum information oriented, and aims at generating entanglement between position and momentum variables of two laser beams. Such an entanglement is obtained by combining two position squeezed beams on a 50/50 beam-splitter. This demonstration opens the way to parallel quantum information communication channels.

CHAPTER 1

Tools for Quantum Imaging

In most cases, the light used to carry an optical image comes from "classical sources", such as natural objects, lamps or usual lasers. For any type of detection of this image, the sensors provide signals in which the useful information contained in the optical beam is mixed with random noise. The major contribution to this noise generally arises from technical noise, i.e. mechanical vibrations or thermal noise, and is due to imperfections in the source, the optical system or the detector. Such sources of noise are termed "classical" as there is no fundamental limit to their reduction; seismic noise and acoustic noises can almost be canceled using complex dampening techniques and vacuum chambers [Robertson02, Bertolini06, Willke02], whereas thermal noise can be reduced using cryogenic apparatus[Kuroda99]. Another contribution to the noise originates from the quantum nature of light, monitored by the random arrival of individual photons on the detection sensor. Contrarily to technical noise this fundamental noise cannot be reduced by eliminating the defects in the measurement process. In our study, we will always consider that the main detection noise source is induced by the quantum nature of light, and that all other sources of noise have been canceled or reduced to a negligible amount of the quantum fluctuations.

During the detection of such an image, the latter fundamental fluctuations give rise to a measurement noise whose amplitude is proportional to the square root of the incident number of photons in the case of a coherent illumination, and which is referred to as *shot noise* [Grynberg97]. These fluctuations yield a "standard quantum noise limit" in the measurement of very small modifications in the optical image, namely when the noise becomes of the order of the signal to be extracted. Under these conditions, it is now well-known that "non-classical light", such as squeezed light or sub-Poissonian light, is likely to reduce quantum fluctuations on a given measurement [Bachor03]. However, if non-classical light in a single transverse mode is very effective to reduce the noise for a measurement performed on the total beam [Fabre00], it is of little use for a measurement performed on an image. One therefore needs "multi-transverse-mode non-classical light" for our purpose.

In this chapter, we will first determine the precise origin of the quantum noise for a non trivial detection of the optical field in the transverse plane. Then, we will devote the second section to a definition of the concept of "multi-transverse-mode non-classical light". And finally, we will focus on the detection devices that can be used from the extraction

of information from an optical image. We will analyze whether and how the quantum fluctuations can be reduced for each type of detection. With the analysis of the spatial distribution of this noise, we will single out the precise transverse modes whose fluctuations are at the origin of this quantum noise, and determine the parameters that have to be changed in order to reduce this noise.

A Generalities on optical images

The purpose of this section is to present the notations and approximations compatible with our quantum optics experiments. They will be used throughout the entire manuscript.

A.1 Image description in the transverse plane

A.1.1 Local electric field operator

Let us consider the general expression of the electric field operator in the Heisenberg representation $\hat{\vec{E}}(\vec{r},z,t)$ [Cohen87]. Its mean value depends on the time evolution t, on the position along the propagation axis z, and can vary according to the transverse plane position $\vec{r}$. A distribution of such a field in the transverse plane is referred to as an *optical image*.

In the work presented in this thesis, we only deal with stationary, linearly polarized, and quasi-monochromatic fields. These particular restrictions allow the manipulation of simpler expressions of the field operator which we propose to detail below.

The evolution of a linearly polarized electric field can be described in terms of its positive frequency part and hermitian conjugate as follows

$$\hat{\vec{E}}(\vec{r},z,t) = \vec{\epsilon}\left[\hat{E}^{(+)}(\vec{r},z,t) + \hat{E}^{(+)\dagger}(\vec{r},z,t)\right], \tag{1.1}$$

where $\vec{\epsilon}$ refers to the direction of polarization.

For a quasi-monochromatic field, whose linewidth $\delta\omega$ is such that $\delta\omega \ll \omega_0$, where ω_0 is the optical angular frequency, it can be expanded into

$$\hat{\vec{E}}(\vec{r},z,t) = \vec{\epsilon}\left[\hat{\mathcal{E}}^{(+)}(\vec{r},z,t)e^{-i\omega_0(t-\frac{z}{c})} + \hat{\mathcal{E}}^{(+)\dagger}(\vec{r},z,t)e^{i\omega_0(t-\frac{z}{c})}\right], \tag{1.2}$$

where $e^{-i\omega_0(t-\frac{z}{c})}$ is the carrier for a wave propagating in vacuum along the z axis at the speed of light c, and $\hat{\mathcal{E}}^{(+)}(\vec{r},t)$ is the envelope field operator, which can be rewritten [Grynberg97]

$$\hat{\mathcal{E}}^{(+)}(\vec{r},z,t) = i\sqrt{\frac{\hbar\omega_0}{2\epsilon_0 c}}\hat{a}(\vec{r},z,t), \tag{1.3}$$

where $\hat{a}(\vec{r},z,t)$ is the photon annihilation operator. The proportionality constant with the envelope field operator has been chosen so that $\hat{a}^\dagger(\vec{r},z,t)\hat{a}(\vec{r},z,t)$ is homogeneous to a photon flux, i.e. a number of photons per square meter per second incident at position $(\vec{r},z)$.

In this thesis, only stationary field evolutions, for which the field variations are slow compared to the integration time of the detector T, will be considered. Assuming that all quantities are integrated during the same time interval T by synchronized detectors, we will thus use the stationary envelope field operator given by

$$\hat{\mathcal{E}}^{(+)}(\vec{r},z) = \frac{1}{T}\int_{t_0}^{t_0+T}\hat{\mathcal{E}}^{(+)}(\vec{r},z,t)dt, \tag{1.4}$$

This quantity does not depend on the starting point of the time integration t_0 for a stationary evolution of the field, and does not explicitly depend on the time evolution. We

will also use the following integrated annihilation operators

$$\hat{a}(\vec{r},z)=\sqrt{\frac{1}{T}}\int_{t_0}^{t_0+T}\hat{a}(\vec{r},z,t)dt, \tag{1.5}$$

where the proportionality constant has this time been chosen so that $\hat{a}^\dagger(\vec{r},z)\hat{a}(\vec{r},z)$ is homogeneous to a number of photons per square meter incident at position ($\vec{r}$,z) during the time interval T.

With these definitions, the stationary envelope can be rewritten in terms of stationary operators as[1]

$$\hat{\mathcal{E}}^{(+)}(\vec{r},z)=i\sqrt{\frac{\hbar\omega_0}{2\epsilon_0 cT}}\hat{a}(\vec{r},z). \tag{1.6}$$

The stationary local photon annihilation operator satisfies the following commutation relation

$$\left[\hat{a}(\vec{r},z),\hat{a}^\dagger(\vec{r}',z)\right]=\delta(\vec{r}-\vec{r}'). \tag{1.7}$$

Although we consider a stationary evolution of all operators, their detection will give rise to *quantum fluctuations* around their mean value. We will thus write the annihilation operators as [Reynaud92]

$$\hat{a}(\vec{r},z)=\alpha(\vec{r},z)+\delta\hat{a}(\vec{r},z), \tag{1.8}$$

where $\alpha(\vec{r},z)=\langle\hat{a}(\vec{r},z)\rangle$ is a complex number corresponding to the mean value of the annihilation operator. With these definitions, $|\alpha(\vec{r},z)|^2$ corresponds to the local mean number of photons $N(\vec{r},z)$. $\delta\hat{a}(\vec{r},z)$ is the quantum fluctuations operator which satisfies the same commutation relation as the initial annihilation operator, and which has a zero mean value, i.e. $\langle\delta\hat{a}(\vec{r},z)\rangle=0$.

A.1.2 Local quadrature operators

The local creation and annihilation operators are non Hermitian, and therefore non measurable. Nevertheless, their real and imaginary parts are Hermitian. They are called the local amplitude $\hat{X}^+$ and phase $\hat{X}^-$ quadrature operators and are defined by[2]

$$\begin{aligned}\hat{X}^+(\vec{r},z) &= \hat{a}^\dagger(\vec{r},z)+\hat{a}(\vec{r},z)\\ &= -i\sqrt{\frac{2\epsilon_0 cT}{\hbar\omega_0}}\left[\hat{\mathcal{E}}^{(+)\dagger}(\vec{r},z)+\hat{\mathcal{E}}^{(+)}(\vec{r},z)\right] \qquad (1.9)\\ \hat{X}^-(\vec{r},z) &= i\left[\hat{a}^\dagger(\vec{r},z)-\hat{a}(\vec{r},z)\right]\\ &= \sqrt{\frac{2\epsilon_0 cT}{\hbar\omega_0}}\left[\hat{\mathcal{E}}^{(+)\dagger}(\vec{r},z)-\hat{\mathcal{E}}^{(+)}(\vec{r},z)\right] \qquad (1.10)\end{aligned}$$

[1] In the following, when there is no ambiguity on the transverse plane in which the field is considered (in the detector plane for example), we will omit the z dependence in the expression of all the operators.

[2] Amplitude and phase quadratures are normalized here to number of photons, but can be defined relative to field value, with the pre-factor $i\sqrt{\frac{\hbar\omega_0}{2\epsilon_0 cT}}$.

Positive frequency part of the electric field and local quadratures are thus related by

$$\hat{\mathcal{E}}^{(+)}(\vec{r},z) = i\sqrt{\frac{\hbar\omega_0}{2\epsilon_0 cT}}\left[\frac{\hat{X}^+(\vec{r},z)+i\hat{X}^-(\vec{r},z)}{2}\right] \tag{1.11}$$

An arbitrary quadrature operator $\hat{X}^\theta$ can also be defined as a linear combination of amplitude and phase quadratures by

$$\begin{aligned}\hat{X}^\theta(\vec{r},z) &= \hat{X}^+(\vec{r},z)\cos\theta + \hat{X}^-(\vec{r},z)\sin\theta \\ &= \hat{a}^\dagger(\vec{r},z)e^{i\theta} + \hat{a}(\vec{r},z)e^{-i\theta}\end{aligned} \tag{1.12}$$

$\hat{X}^\theta(\vec{r},z)$ is a Hermitian operator for all θ values.

The quantum fluctuations on the quadrature θ of the mode are described by the following operator

$$\delta\hat{X}^\theta(\vec{r},z) = \delta\hat{a}^\dagger(\vec{r},z)e^{i\theta} + \delta\hat{a}(\vec{r},z)e^{-i\theta} \tag{1.13}$$

which has a zero mean value $\langle\delta\hat{X}^\theta(\vec{r},z)\rangle = 0$. The variance of this operator is therefore given by

$$\begin{aligned}\triangle^2\,\hat{X}^\theta(\vec{r},z) &= \langle\,\delta\hat{X}^{\theta\,2}(\vec{r},z)\rangle - \langle\delta\hat{X}^\theta(\vec{r},z)\rangle^2 \\ &= \langle\,\delta\hat{X}^{\theta\,2}(\vec{r},z)\rangle\end{aligned} \tag{1.14}$$

and will be termed *local quantum noise on the quadrature* θ.

With these definitions, amplitude and phase quadrature operators are measurable, but do not commute as they are shown to satisfy the following commutation relation [TrepsPhD01]

$$\left[\hat{X}^+(\vec{r},z),\hat{X}^-(\vec{r}',z)\right] = 2i\delta(\vec{r}-\vec{r}') \tag{1.15}$$

A.1.3 Local number of photons and local intensity

The local number of photons incident at position ($\vec{r}$,z), detected during the time interval T, is described by the operator

$$\hat{\mathcal{N}}(\vec{r},z) = \hat{a}^\dagger(\vec{r},z)\hat{a}(\vec{r},z) \tag{1.16}$$

$$= \frac{2\epsilon_0 cT}{\hbar\omega_0}\left[\hat{\mathcal{E}}^{(+)\dagger}(\vec{r},z)\hat{\mathcal{E}}^{(+)}(\vec{r},z)\right] \tag{1.17}$$

The local intensity operator, which corresponds to the local energy density in the optical image, is given by

$$\hat{\mathcal{I}}(\vec{r},z) = \hbar\omega_0\hat{\mathcal{N}}(\vec{r},z). \tag{1.18}$$

Unless it is mentioned explicitly, we will always assume in the following that our detection devices are 100% efficient, i.e. that each photon impinging on the detector gives birth to an electron. We will thus often identify photocurrent and intensity.

A.1.4 Total number of photons and beam power

Total number of photons and beam power are not local quantities. They are related to the integration of the local number of photons and local intensity over the transverse plane, respectively

$$\hat{N}(z) = \int \hat{\mathcal{N}}(\vec{r}, z) d\vec{r}, \tag{1.19}$$

$$\hat{P}(z) = \frac{\hbar\omega_0}{T}\hat{N}(z) = \frac{1}{T}\int \hat{\mathcal{I}}(\vec{r}, z) d\vec{r}, \tag{1.20}$$

where we recall that T is the integration time of the detection.

A.2 Transverse modal decomposition of the electromagnetic field

In order to give a field description which is easier to manipulate, we propose to decompose the field in transverse modes. We will see that such a discretization of the transverse plane does not involve singularities, but also corresponds more closely to the experiments.

The evolution in free space of the mean value of the electric field is governed by the electromagnetic wave equation. The homogeneous form of the equation is given by [Siegman86]

$$\left(\Delta - \frac{1}{c^2}\frac{\partial^2}{\partial t^2}\right)\vec{E}(\vec{r}, z, t), \tag{1.21}$$

where Δ is the spatial Laplacian operator.

In the case of stationary fields, and in the paraxial approximation[3], this equation becomes

$$\Delta_\perp \mathcal{E}^{(+)}(\vec{r}, z) + 2ik\frac{\partial}{\partial z}\mathcal{E}^{(+)}(\vec{r}, z) = 0, \tag{1.22}$$

where $\mathcal{E}^{(+)}$ is the mean electric field envelope[4], $\Delta_\perp$ is the transverse Laplacian operator, and where λ is the optical wavelength. In this case, one can show that the electric field envelope can be decomposed in a transverse mode basis, where each mode is stable during its propagation.

Depending on the physical setup which is considered, it is often convenient to use a particular mode basis of the transverse plane in order to describe the field. The Hermite Gauss and Laguerre Gauss mode basis are for example particularly adapted to the description of an optical field in a cylindrical cavity [Siegman86]. Indeed, the mode spatial profiles thereby defined remain unchanged during propagation in such a cavity. They are called *eigen-modes of propagation*. For a cavity with "elliptical" symmetry[5], Ince Gauss mode basis would for instance be preferred [Bandres04]. As for the case of an array detection, a *pixel* description of the plane is often used [TrepsPhD01].

[3] This approximation assumes that the beam extension remains localized around the z axis during its propagation. We will wave temporarily this approximation in chapter 2.

[4] It corresponds to the mean value of the envelope field operator defined in Eq. 1.6.

[5] Such a cavity has two elliptical mirrors whose axes correspond to the same x and y axes.

A.2.1 Modal creation and annihilation operators

We consider any orthonormal basis of the transverse plane whose modes satisfy the paraxial wave equation, and are written $\{u_n(\vec{r},z)\}$. The mode profiles are complex in the general case and must satisfy the following orthonormal and completeness relations

$$\int_{-\infty}^{\infty} u_n^*(\vec{r},z)u_k(\vec{r},z)d^2r = \delta_{n,k} \tag{1.23}$$

$$\sum_i u_i^*(z,\vec{r})u_i(z,\vec{r'}) = \delta(\vec{r}-\vec{r'}) \tag{1.24}$$

The local annihilation operator defined in Eq.1.5 can be *univocally* expanded into [Fabre85]

$$\hat{a}(\vec{r},z) = \sum_n \hat{a}_n u_n(\vec{r},z) \tag{1.25}$$

The position dependence of the local annihilation operator is entirely transferred to the mode profiles $u_n(\vec{r},z)$. To each vector of the mode basis is associated a creation and an annihilation operators $\hat{a}_n$ and $\hat{a}_n^\dagger$, which we will refer to as *modal creation and annihilation operators*. Note that with this definition, when the basis chosen for the field description is stable during propagation, i.e. that the mode profiles satisfy the general field propagation equation, the number of photons in each mode remains unchanged during the propagation of the field.

The modal creation and annihilation operators satisfy the following commutation relation

$$\left[\hat{a}_n, \hat{a}_m^\dagger\right] = \delta_{nm} \tag{1.26}$$

where δ_{nm} is a Kronecker's delta function. As a consequence of the transverse plane discretization, the singularity in position previously shown in Eq. 1.7 has thus been replaced by a Kronecker delta. The singularity on the operators has been transferred to the completeness relation of the modes (see Eq. 1.24).

Using the definition of the field envelope given in Eq. 1.6, we obtain the general field decomposition in transverse modes that will be used as a starting point of nearly all theoretical sections in this thesis

$$\boxed{\hat{\mathcal{E}}^{(+)}(\vec{r},z) = i\sqrt{\frac{\hbar\omega_0}{2\epsilon_0 cT}}\sum_n \hat{a}_n u_n(\vec{r},z)} \tag{1.27}$$

A separation of the mean value and quantum fluctuations, similar to the one introduced in Eq.1.8 can be performed

$$\hat{a}_n = \alpha_n + \delta\hat{a}_n, \tag{1.28}$$

where $\langle\hat{a}_n\rangle = \alpha_n$ is the mean value of the annihilation operator of mode u_n, and $\delta\hat{a}_n$ is the corresponding quantum fluctuation operator. With these definitions, $|\alpha_n|^2$ corresponds to the total number of photons in the mode u_n, and will be denoted as N_n.

A.2.2 Modal quadratures

It is now natural to introduce quadrature operators for each transverse mode. They are defined similarly to the local quadratures (see Eq.1.9 and 1.10) by[6]

$$\hat{X}_n^+ = \hat{a}_n^\dagger + \hat{a}_n \tag{1.29}$$

$$\hat{X}_n^- = i\left(\hat{a}_n^\dagger - \hat{a}_n\right) \tag{1.30}$$

An arbitrary modal quadrature operator $\hat{X}_n^{\theta_n}$ can also be similarly defined, as in Eq.1.12 by

$$\begin{aligned}\hat{X}_n^{\theta_n} &= \hat{X}_n^+ \cos\theta_n + \hat{X}_n^- \sin\theta_n \\ &= \hat{a}_n^\dagger e^{i\theta_n} + \hat{a}_n e^{-i\theta_n}\end{aligned} \tag{1.31}$$

The quantum fluctuations on the quadrature θ_n of the mode u_n are described by

$$\delta\hat{X}_n^{\theta_n} = \delta\hat{a}_n^\dagger e^{i\theta_n} + \delta\hat{a}_n e^{-i\theta_n} \tag{1.32}$$

and $\langle \delta\hat{X}_n^{\theta^2} \rangle$ will be termed *quantum noise in the mode u_n on the quadrature θ_n*. $\hat{X}_n^{\theta_n}$ is an observable, and we will show in section 1 C how to measure its mean value and noise selectively. Moreover, the definition of the phase reference for each mode requires special attention, and will be developed in section 1 B.2.2.

The modal quadrature operators defined here are measurable, but do not commute, as shown similarly in Eq. 1.15, and are shown to satisfy the following commutation relation,

$$\left[\hat{X}_n^+, \hat{X}_m^-\right] = 2i\delta_{nm} \tag{1.33}$$

Again, the delta function in position has been replaced by a Kronecker's delta function.

As a direct consequence, using Cauchy-Schwarz inequality, modal quadrature operators satisfy the following inequality relation[7]

$$\triangle^2 \hat{X}_n^+ \, \triangle^2 \hat{X}_n^- \geq 1 \tag{1.35}$$

It shows that precise simultaneous determination of the modal amplitude and phase quadratures of a light beam is not possible. Electromagnetic fields that satisfy the equality in Eq. 1.35 are termed *minimum uncertainty states*. The parameter used to characterize how close a state is from a minimum uncertainty state is called the *purity* $\mathcal{P}$[8].

The manipulation of the balance of the Heisenberg inequality relation 1.35, i.e. enhancing the measurement precision of one quadrature at the cost of the other, is termed *squeezing*, and will be studied in section 1 A.3.3.

[6] Note that $\hat{X}_n^+$ and $\hat{X}_n^-$ are somehow abusively defined defined as "amplitude" and "phase" quadratures as they only correspond to the real and imaginary part of the annihilation operator when the mean field is real, as explained in section 1 B.2.2.

[7] Although the expression given in Eq. 1.35 is always valid, taking into account the possibility of correlations between the quadratures yields a more general expression of the Heisenberg inequality given by

$$\triangle^2 \hat{X}_n^+ \, \triangle^2 \hat{X}_n^- - \frac{1}{4}\langle \hat{X}_n^+ \hat{X}_n^- + \hat{X}_n^- \hat{X}_n^+ \rangle^2 \geq 1. \tag{1.34}$$

[8] For a pure state, i.e. a minimum uncertainty state, this value equals 1, and the state is termed *pure*, whereas for mixed states, $\mathcal{P} < 1$. We will come back on the expression of the purity in the case of Gaussian states in section 1 A.3.

A.2.3 Number of photons and intensity in a mode

The number of photons in mode n, detected during the interval T is described by the operator

$$\hat{N}_n = \hat{a}_n^\dagger \hat{a}_n \tag{1.36}$$

Its mean value, fluctuations and noise power are respectively described by

$$\langle \hat{N}_n \rangle = N_n \tag{1.37}$$

$$\delta\hat{N}_n = \alpha_n \left(\delta\hat{a}_n^\dagger + \delta\hat{a}_n \right) = \sqrt{N_n}\delta\hat{X}_n^+ \tag{1.38}$$

$$\langle \delta\hat{N}_n^2 \rangle = N_n \langle \delta\hat{X}_n^{+^2} \rangle \tag{1.39}$$

These definitions are directly transposable to the optical power present in each mode, defined by $\hat{P}_n = \frac{\hbar\omega_0}{T}\hat{N}_n$.

A.2.4 Description relative to the mean field

In order to manipulate expressions as simple as possible, we will often choose the transverse basis so that its first vector - denoted $u_0(\vec{r}, z)$ - identifies with the mean field profile, i.e.

$$u_0(\vec{r}, z) = \frac{\langle \hat{\mathcal{E}}^{(+)}(\vec{r}, z) \rangle}{|\langle \hat{\mathcal{E}}^{(+)}(\vec{r}, z) \rangle|} \tag{1.40}$$

In this case, the mean value of the local electric field operator can simply be described by[9]

$$\langle \hat{\mathcal{E}}^{(+)}(\vec{r}, z) \rangle = i\sqrt{\frac{\hbar\omega_0}{2\epsilon_0 cT}}\alpha_0 u_0(\vec{r}, z), \tag{1.41}$$

where α_0 and $u_0(\vec{r}, z)$ are complex numbers in the general case. α_0 is defined such as $|\alpha_0|^2 = N$, where N corresponds to the total number of photons detected in the mean field during the time interval T. α_0 can thus be written $\alpha_0 = \sqrt{N}e^{i\theta_{\alpha_0}}$. Without loss of generality, by defining all phases relative to the one of the mean field, we can write $\theta_{\alpha_0} = 0$, and α_0 simplifies into $\alpha_0 = \sqrt{N}$. Nevertheless, the mean field profile is still complex in the general case, and we write $u_0(\vec{r}, z) = |u_0(\vec{r}, z)|e^{i\theta_0(\vec{r},z)}$. We therefore allow non-planar wavefront, as the phase profile of the mean field depends on the transverse position $\vec{r}$. The mean values of amplitude and phase quadratures of the mean field simplify into

$$\langle \hat{X}_0^+(\vec{r}, z) \rangle = \sqrt{N}u_0(\vec{r}, z) \tag{1.42}$$

$$\langle \hat{X}_0^-(\vec{r}, z) \rangle = 0, \tag{1.43}$$

The profile of the transverse mode u_0 is thus exactly following the mean field amplitude quadrature along the propagation. This definition is of particular importance, as the quadratures of all the transverse modes are defined relative to the amplitude quadrature of the mean field, as will be explained in section 1 B.2.2.

[9] We will show a more complete description relative to the mean field by defining a *mean field basis* in section 1 B.2.2.

A.2.5 Changing the transverse basis

It is often useful to introduce at least two different transverse basis and change from one to another in order to describe as simply as possible the entire evolution of the field. For instance, it can be convenient to use one set of transverse modes to describe the propagation of the beam, and another one for the detection.

Let us consider two different basis of the transverse plane $\{u_n\}$, and $\{v_n\}$, and their corresponding annihilation operators $\hat{a}_n$ and $\hat{b}_n$. We want to deduce the field operator description in the basis $\{v_n\}$, i.e. the intensity and noise in each transverse mode, from the operators given in the basis $\{u_n\}$. As the field dependence on the position along the propagation axis is of no relevance here for this description, we will omit it.

The field is fully described in both transverse basis by

$$\hat{\mathcal{E}}^{(+)}(\vec{r}) = i\sqrt{\frac{\hbar\omega_0}{2\epsilon_0 cT}}\sum_n \hat{b}_n v_n(\vec{r}) = i\sqrt{\frac{\hbar\omega_0}{2\epsilon_0 cT}}\sum_n \hat{a}_n u_n(\vec{r}) \tag{1.44}$$

We define the complex coefficient $\Gamma_{k,n}$ as the overlap integral over the transverse plane between u_n and v_k^*

$$\Gamma_{k,n} = \int_{-\infty}^{\infty} u_n(\vec{r})v_k^*(\vec{r})d^2r \tag{1.45}$$

Multiplying Eq. 1.44 by $v_k^*(\vec{r})$ and integrating over the transverse plane yields

$$\sum_n \hat{b}_n \int v_n(\vec{r})v_k^*(\vec{r})d^2r = \sum_n \hat{a}_n \int u_n(\vec{r})v_k^*(\vec{r})d^2r \tag{1.46}$$

Using now the orthonormality relation defined in Eq. 1.23) and the previous definition of $\Gamma_{k,n}$, we can show that the final annihilation operators $\hat{b}_n$ are related to the initial ones $\hat{a}_n$ by the following relation

$$\hat{b}_k = \sum_n \hat{a}_n \Gamma_{k,n} \tag{1.47}$$

We can now relate $\delta\hat{X}^+_{v,k}$, the fluctuations in the amplitude quadrature of the mode v_k, to quadrature fluctuations in the other basis. Using Eq. 1.32, and by defining $\Psi_{k,n}$ such that $\Gamma_{k,n} = |\Gamma_{k,n}|e^{-i\Psi_{k,n}}$, we get

$$\delta\hat{X}^+_{v,k} = \sum_n |\Gamma_{k,n}|\delta\hat{X}^{\Psi_{k,n}}_{u,n} \tag{1.48}$$

The general expression of the noise in this mode is thus given by

$$\langle\delta\hat{X}^{+^2}_{v,k}\rangle = \sum_n |\Gamma_{k,n}|^2\langle\delta\hat{X}^{\Psi^2_{k,n}}_{u,n}\rangle + \sum_{n\neq m} |\Gamma_{k,n}||\Gamma_{k,m}|\langle\delta\hat{X}^{\Psi_{k,n}}_{u,n}\delta\hat{X}^{\Psi_{k,m}}_{u,m}\rangle \tag{1.49}$$

This general expression is difficult to use in practice and we will only be interested here in the particular case of a non correlated field in the basis $\{u_n\}$, when the expressions of u_n and v_n are real, for which $\Gamma_{k,n}$ is also real. In this case, the following correspondence between the quantum noise can be written

$$\langle\delta\hat{X}^+_{v,k}\rangle = \sum_n \langle\delta\hat{X}^{+^2}_{u,n}\rangle\Gamma^2_{k,n}. \tag{1.50}$$

This relation will notably be useful to deduce how the squeezing for a single mode is distributed when one uses a description of the field in another basis.

A.2.6 The Hermite-Gauss basis

We introduce here the mathematical formalism in order to describe the properties of the transverse basis that will be widely used throughout the thesis, namely the Hermite-Gauss basis [Siegman86].

The Hermite-Gauss basis is commonly used to describe the transverse distribution of optical fields propagating in a medium of cylindrical symmetry, typically an optical cavity. The cylindrical symmetry axis, which usually identifies with the beam propagation axis z, and two particular orthogonal transverse direction, often horizontal and vertical axis x and y, are usually chosen to give a complete description of the field.

Hermite-Gauss modes, denoted TEM_{nm}, are solutions of the paraxial field propagation equation, and are therefore limited to the description of beams whose propagation direction remains within a small angle with respect to the z axis. Their expression is composed of the Hermite polynomials H_n[10] multiplied by a Gaussian function.

Their general normalized expression is

$$\mathrm{TEM}_{nm}(x,y,z) = \frac{C_{nm}}{w(z)} H_n\left(\frac{\sqrt{2}x}{w(z)}\right) H_m\left(\frac{\sqrt{2}y}{w(z)}\right) e^{-\frac{(x^2+y^2)}{w(z)^2}} e^{ik\frac{(x^2+y^2)}{2R(z)}} e^{-i(n+m+1)\phi_G(z)} \quad (1.53)$$

where we have introduced

$$C_{nm} = \frac{1}{\sqrt{\pi 2^{n+m+1} n! m!}} \quad (1.54)$$

$$z_R = \frac{\pi w_0^2}{\lambda} \quad (1.55)$$

$$R(z) = z + \frac{z^2}{z_R} \quad (1.56)$$

$$w(z) = w_0 \sqrt{1 + \left(\frac{z}{z_R}\right)^2} \quad (1.57)$$

$$\phi_G(z) = arctan\left(\frac{z}{z_R}\right) \quad (1.58)$$

where λ is the wavelength, w_0 is the beam waist, z_R is the beam Rayleigh range, $R(z)$ is the radius of curvature, and $\phi_G(z)$ is the Gouy phase shift for the fundamental mode, which will play a particularly important role in the following. Note that a planar wave-front is obtained only in the waist plane ($z = 0$).

The quantity $w(z)$ is independent of n and m, but does not correspond to the beam radius. Indeed, the spatial extension of the modes increases with the order of the mode. A TEM_{nm} mode has n and m zeros on the x and y axis, and therefore $n+1$ and $m+1$ lobes along the same axis. The position of the furthest lobe away from the beam center is approximately at a distance $(x,y) = (\sqrt{n+\frac{1}{2}}w(z), \sqrt{m+\frac{1}{2}}w(z))$. As shown by Eq.1.53,

[10] We give below two interesting relations defining the Hermite polynomials. First, their definition relative to the error function:

$$\frac{d^{n+1}}{dz^{n+1}} Erf(z) = \frac{2}{\pi}(-1)^n H_n(z) e^{-z^2}, \quad (1.51)$$

and secondly their definition using a recurrence relation:

$$H_0(z) = 1, \quad H_1(z) = 2z, \quad and \quad H_{n+1}(z) = 2zH_n(z) - 2nH_{n-1}(z). \quad (1.52)$$

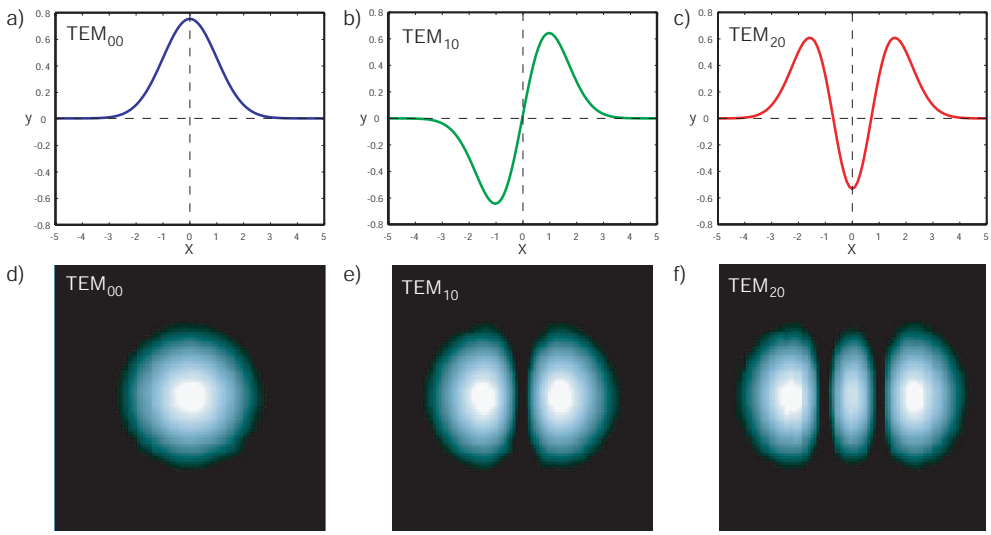

Figure 1.1: First three Hermite-Gauss modes. a) TEM_{00}, b) TEM_{10} and c) TEM_{20} normalized one dimensional representation in the transverse plane. Transverse axes are expressed in waist units. d)TEM_{00}, e) TEM_{10} and f) TEM_{20} two-dimensional representation in the transverse plane.

spatial modes of different order - n and m - can be present on each transverse direction. However, in our case of interest, we will consider the variations of the field along a single transverse axis, namely x. For the sake of simplicity, we will thus denote the one dimensional Hermite Gauss modes by $u_n(x,z)$, unless it is specified differently. Moreover, knowing that the dependence along the y axis will always be a simple Gaussian in our experiments, these modes will be related to the two dimensional ones by the relation

$$u_n(x,z) = \int_{-\infty}^{\infty} \mathrm{TEM}_{n0}(x,y,z)dy \tag{1.59}$$

We will be primarily concerned with the first three one-dimensional Hermite Gauss modes which are represented on Fig.1.1. We see that the spatial extension along the transverse axis increases with the order of the mode, as discussed above. Their expressions are

$$\begin{aligned}
u_0(x,z) &= \left(\frac{2}{\pi w^2(z)}\right)^{\frac{1}{4}} e^{-\frac{x^2}{w^2(z)}} e^{i\frac{kx^2}{2R(z)}} e^{-i\phi_G(z)} \\
u_1(x,z) &= \left(\frac{2}{\pi w^2(z)}\right)^{\frac{1}{4}} \frac{2x}{w(z)} e^{-\frac{x^2}{w^2(z)}} e^{i\frac{kx^2}{2R(z)}} e^{-2i\phi_G(z)} \\
u_2(x,z) &= \left(\frac{2}{\pi w^2(z)}\right)^{\frac{1}{4}} \frac{1}{\sqrt{2}} \left(\frac{4x^2}{w^2(z)} - 1\right) e^{-\frac{x^2}{w^2(z)}} e^{i\frac{kx^2}{2R(z)}} e^{-i3\phi_G(z)}
\end{aligned} \tag{1.60}$$

The complete expressions are heavy to manipulate, and we will therefore omit the phase factors when they are not relevant, for example for the description of single mode fields. The Gouy phase shift will however be of great importance in order to understand the properties of multi-mode beams.

Other relations satisfied by Hermite polynomials can be found in reference [Abramowitz72].

A.3 Gaussian quantum states of light

In this thesis, we limit ourselves to the analysis of the quantum states relevant to our quantum optics experiments in the continuous variable (CV) regime[11]: Gaussian quantum states[12]. They include coherent and squeezed states. We will also discuss the importance of entangled states which are obtained by the combination of two squeezed states in quadrature. Before presenting these optical states, we propose to introduce a way to describe their noise properties: the *covariance matrix*.

A.3.1 Covariance matrix

A Gaussian state is fully described by its first and second order momentum. The first order momentum simply corresponds to the complex mean value of the field, its amplitude and phase. We will therefore concentrate on the second order momentum, which notably determines the squeezing and entanglement properties of a state, and which can be described by a $2\mathcal{N}$x$2\mathcal{N}$ symmetric real matrix called the *covariance matrix*[13] Γ [Walls95, LauratPhD04].

Let us first consider the single mode case, $\mathcal{N} = 1$, for which the covariance matrix is written

$$\Gamma = \begin{pmatrix} \langle \delta\hat{X}^{+^2} \rangle & \langle \delta\hat{X}^{+}\delta\hat{X}^{-} \rangle_S \\ \langle \delta\hat{X}^{+}\delta\hat{X}^{-} \rangle_S & \langle \delta\hat{X}^{-^2} \rangle \end{pmatrix} \tag{1.61}$$

where we introduced the symmetrized notation

$$\langle \delta\hat{X}^{+}\delta\hat{X}^{-} \rangle_S = \frac{1}{2}\langle \delta\hat{X}^{+}\delta\hat{X}^{-} + \delta\hat{X}^{-}\delta\hat{X}^{+} \rangle \tag{1.62}$$

The covariance matrix describes all the noise properties of the single mode state: noise on amplitude and phase quadratures, $\langle \delta\hat{X}^{+^2} \rangle$ and $\langle \delta\hat{X}^{-^2} \rangle$, and noise correlations between both quadratures $\langle \delta\hat{X}^{+}\delta\hat{X}^{-} \rangle_S$. Its determinant is given by

$$det(\Gamma) = \langle \delta\hat{X}^{+^2} \rangle \langle \delta\hat{X}^{-^2} \rangle - \langle \delta\hat{X}^{+}\delta\hat{X}^{-} \rangle_S^2 \geq 1 \tag{1.63}$$

where we have recognized the general Heisenberg inequality given in Eq. 1.34.

Still in the case of Gaussian states, the purity, already introduced in section 1 A.1.2, can be shown to be related to the determinant of the covariance matrix by: $\mathcal{P} = 1/\sqrt{det(\Gamma)}$[14]. For a minimum uncertainty state for which the equality in Eq. 1.34 is fulfilled, the determinant of the covariance matrix equals 1, and $\mathcal{P} = 1$, i.e. the state is pure. For other states, Eq. 1.63 shows that $\mathcal{P} < 1$.

Considering now a gaussian continuous bi-partite state, the covariance matrix is a 4x4 matrix whose general expression is given by

$$\Gamma = \begin{pmatrix} \langle \delta\hat{X}_x^{+^2} \rangle & \langle \delta\hat{X}_x^{+}\delta\hat{X}_x^{-} \rangle_S & \langle \delta\hat{X}_x^{+}\delta\hat{X}_y^{+} \rangle_S & \langle \delta\hat{X}_x^{+}\delta\hat{X}_y^{-} \rangle_S \\ \langle \delta\hat{X}_x^{+}\delta\hat{X}_x^{-} \rangle_S & \langle \delta\hat{X}_x^{-^2} \rangle & \langle \delta\hat{X}_x^{+}\delta\hat{X}_y^{-} \rangle_S & \langle \delta\hat{X}_x^{-}\delta\hat{X}_y^{-} \rangle_S \\ \langle \delta\hat{X}_x^{+}\delta\hat{X}_y^{+} \rangle_S & \langle \delta\hat{X}_x^{+}\delta\hat{X}_y^{-} \rangle_S & \langle \delta\hat{X}_y^{+^2} \rangle & \langle \delta\hat{X}_y^{+}\delta\hat{X}_y^{-} \rangle_S \\ \langle \delta\hat{X}_x^{+}\delta\hat{X}_y^{-} \rangle_S & \langle \delta\hat{X}_x^{-}\delta\hat{X}_y^{-} \rangle_S & \langle \delta\hat{X}_y^{+}\delta\hat{X}_y^{-} \rangle_S & \langle \delta\hat{X}_y^{-^2} \rangle \end{pmatrix}, \tag{1.64}$$

[11] This regime corresponds to large photon flux, and is to be opposed to the photon counting regime.

[12] Quantum optics is however not limited to the study of Gaussian states. The production of non-Gaussian states is now a hot field of research. One achievement is for example the generation of optical states with negative Wigner function, aiming at producing optical Schrödinger cat states [Ourjoumtsev06, Neergaard-Nielsen06].

[13] This matrix is sometimes also called *correlation matrix*.

[14] Note that this expression can be proved using the most general definition of the purity with the trace of the square of the density matrix ρ : $\mathcal{P} = 1/Tr\rho^2$.

where x and y respectively refer to the first and second mode, and where each coefficient corresponds to the correlation between two variables among $\delta\hat{X}_x^+$, $\delta\hat{X}_x^-$, $\delta\hat{X}_y^+$ and $\delta\hat{X}_y^-$. We used symmetrized notations similarly to the one presented in Eq. 1.62. Note that in Eq. 1.64, the two 2x2 diagonal blocks correspond to the covariance matrix of individual modes as in Eq. 1.61, and that the anti-diagonal 2x2 blocks correspond to the correlations between the two modes.

A.3.2 Coherent states

Let us first comment on a very specific quantum state : the *vacuum* state. This state must satisfy the Heisenberg inequality, and therefore present quantum fluctuations although its mean photon number is zero. Every mode component of a vacuum state has identical fluctuations along all quadratures, i.e.

$$\langle \delta\hat{X}_n^{\theta_n^2} \rangle = 1, \quad \forall n, \quad \forall \theta_n. \tag{1.65}$$

These noise properties set a reference for fluctuations and are called the *standard quantum noise limit*. We will often abusively term it the quantum noise limit (QNL) in the following.

A *coherent state* is then defined as a classical field on which are added vacuum fluctuations. Such states have been introduced by R. Glauber in 1965 [Glauber65], and describe very well the properties of a stable laser output beam[15].

Adopting a corpuscular description of the beam, made of photons - here thought as grains of light - the QNL is often called the *shot noise* limit, in reference to the noise that would arise for example from sand grains impinging on a metal board.

R. Glauber showed that the photons were randomly ordered in time in a coherent beam, and that their temporal distribution was Poissonian [Glauber65]. We can also add here that photons are additionally randomly ordered in the transverse plane of the beam, and that their spatial distribution is defined by the amplitude of transverse mode of interest[16].

Let us briefly present the consequences of these quantum fluctuations on the intensity measurement of a coherent beam[17]. Considering the detection of N photons in the beam, and assuming a perfect detection of the entire field, the *intensity signal* corresponds to the mean beam power $\langle \hat{N} \rangle$, whereas the noise in the mean field corresponds to the *shot noise* $\sqrt{\langle \delta\hat{N}^2 \rangle}$, the signal-to-noise ratio (SNR) thus equals

$$\mathrm{SNR} = \frac{\langle \hat{N} \rangle}{\sqrt{\langle \delta\hat{N}^2 \rangle}} = \sqrt{N} \tag{1.66}$$

where we have used the expression of the noise on the number of photons given in Eq. 1.39 transposed here to the coherent mean field mode : $\langle \delta\hat{N}^2 \rangle = N\langle \hat{X}^{+^2} \rangle = N$. The noise power is thus equal to the signal. The $\sqrt{N}$ factor shown in Eq. 1.66 is characteristic of the shot noise. In our continuous variable quantum experiments, this factor is typically of the order of $10^7 - 10^8$[18].

A convenient representation of the quantum noise is given by the superposition of an fluctuations area to a classical field[19]. The classical field is represented in the Fresnel

[15] This statement assumes that the phase diffusion of the laser output is negligible.
[16] This distribution can have any profile, as we will see nearly everywhere in this thesis.
[17] Note that we dedicate a full section(see section 1C) to the detection of optical images.
[18] This value is obtained for a beam power of 1 mW, and an integration time of 1 μs.
[19] This representation is often called "the ball on stick picture".

plane by a vector whose norm defines the amplitude and whose angle to the horizontal axis defines its phase. The quantum fluctuations generate a displacement of the extremity of this vector within a zone of the Fresnel plane. The distance from the mean value to the contour of this zone represents the variance of the noise for a given quadrature.

In the case of a coherent field, this contour is a circle, as represented in Fig. 1.2a).

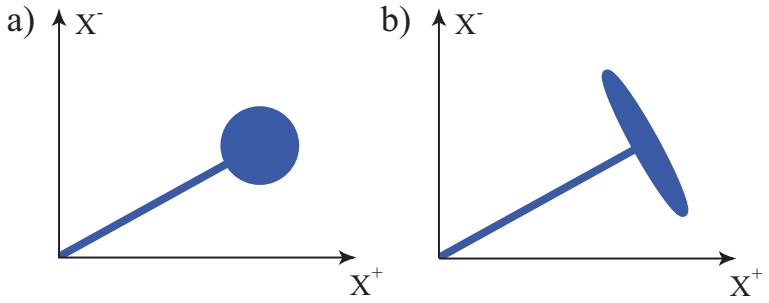

Figure 1.2: Gaussian quantum states of light. Single mode states: a) a coherent state, and b) an amplitude squeezed state.

A.3.3 Squeezed states

Even if the Heisenberg inequality introduced in Eq. 1.35 defines a minimum value to the product of the variance of two conjugated quadratures, it does not impose any restriction to the value of individual variances. It is therefore possible to produce states for which the variance of one quadrature is reduced below the standard quantum noise limit, at the cost of increasing the variance of the conjugate quadrature. It is not restricted to minimal uncertainty states. Such a state is termed *squeezed*[20], and have already been produced using many non-linear physical systems [SQZ87], such as four-wave mixing, optical parametric amplifier, optical fiber, cold atomic vapors. The first demonstration has been done by Slusher *et al.* in 1985, using four wave mixing in a sodium vapor [Slusher85] .

As for the need of this thesis, we will focus on the production of squeezed light by parametric down-conversion, which was first achieved by Wu et al. in 1986 [Wu86]. More recently, squeezed noise power variances of -7 dB [Lam99, Suzuki06], and even -9.5 dB [Furusawa07], at sideband frequencies down to sub-kHz frequencies [McKenzie04] and up to the GHz regime [Senior07] have been demonstrated. Note that the squeezed optical mode was limited until recently to the TEM_{00} mode, and that we will present in section 4C the first generation of squeezed light in higher order Hermite Gauss modes.

The fluctuations of squeezed states are represented by an ellipse in the diagram described in the previous section, as shown in Fig. 1.2b). We have chosen the example of an *amplitude squeezed state*, for which a corpuscular image can be given : it corresponds to a beam whose photons are ordered more regularly in time than in the coherent case. The photon distribution is in this case sub-Poissonian. The influence of loss as a decoherence process on such a beam appears clearly . Loss corresponds to randomly taking photons

[20] The term *squeezed state*, strictly speaking, is reserved to free propagating quantum states. It has been shown that the use of a feedback loop could reduce the fluctuations in one quadrature of the in-loop field without increasing the fluctuations in the other. Such a state is called *squashed* [Buchler99, Wiseman99].

out of the beam, and rapidly shapes the initial distribution to a Poissonian one. More formally, the effect of any losses can be modeled by a partially reflecting beam-splitter, of transmission η, which couples vacuum fluctuations in the input field, as shown in Fig. 1.3. The fluctuations $\delta\hat{X}^{\theta}_{n,out}$ on any quadrature θ of mode n within the output field is related

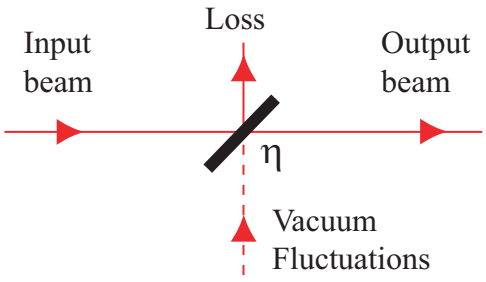

Figure 1.3: Modelisation of loss on a quantum state using a partially reflecting beam-splitter of transmission η. The noise properties of the output state are modified by the vacuum fluctuations entering via the empty port of the beam-splitter.

to the one of the input field $\delta\hat{X}^{\theta}_{n,in}$ by

$$\delta\hat{X}^{\theta}_{n,out} = \sqrt{\eta}\delta\hat{X}^{\theta}_{n,in} + \sqrt{1-\eta}\delta\hat{X}^{\theta}_{n,vac} \tag{1.67}$$

where $\delta\hat{X}^{\theta}_{n,vac}$ corresponds to vacuum fluctuations[21]. Using Eq. 1.65, the noise power of the output quadrature thus becomes

$$\langle\delta\hat{X}^{\theta^2}_{n,out}\rangle = \eta\langle\delta\hat{X}^{\theta^2}_{n,in}\rangle + 1 - \eta \tag{1.68}$$

This relation, as well as Eq. 1.50 giving the distribution of the noise when the basis of description is changed, will be most useful to analyze the detection of squeezed states in our experiments. The detection of such states will be detailed in section 1C.

Let us now briefly comment on the relevance of squeezed states. First, in order to give a clear idea of the order of the noise reduction experimentally achievable, let us give two examples. -3dB and -10dB of noise reduction on the amplitude quadrature corresponds to $\langle\delta\hat{X}^{+^2}\rangle$=1/2 and 1/10. It means that the amplitude of the fluctuations are respectively reduced by a factor of $\sqrt{2} = 1.4$ and $\sqrt{10} = 3.2$ relative to the coherent case. Nevertheless, such a factor can be of great importance in order to distinguish a very faint signal from the quantum noise. Although the typical beam power used in our experiments is 1 mW, the SNR of the measurement only equals $10^7 - 10^8$ for a total measurement of the beam, i.e. for intensity measurement, and do not correspond to other detections. For instance, the signal obtained with a split-detection, when the position of an incident laser beam is modulated around the center of the detector, only involves a few photons. When the displacement is very small, the SNR can thus go below 1[22].

[21] Note that vacuum fluctuations can also be squeezed similarly to the fluctuations of a bright state. A squeezed vacuum state has the particularity to have a zero mean field value, but a non-zero squared field mean value. In terms of photons, it means that a squeezed vacuum field has photons, unlike the vacuum state.

[22] This is effectively observed in the experiment presented in section 5 A.

Moreover, the use of squeezed light is only appropriate when the available optical power is limited, for example because of the existence of a damage threshold in the experiment, or because of safety restrictions. Indeed, as shown in Eq. 1.66, similar signal-to-noise ratios can be achieved with a resource demanding beam with -3dB of noise reduction below the QNL and with a coherent beam twice as powerful.

Finally, the squeezing spectrum has to be compatible with the frequency of analysis and the bandwidth required for the experiment. We have chosen not to develop the frequency aspect of the light fluctuations in this thesis, as one can directly transpose all the theoretical results presented before[23] to any *sideband frequency*[24]. Details on side-band representation can be found in references [BowenPhD03, Bachor03]. Although no calculation presented in this thesis will explicitly specify the frequency dependence of the quantum operators, it is important to keep in mind that we will always consider an analysis at RF side-band frequency - typically at frequencies above 1 MHz, as squeezed sources of light present excess noise at lower frequencies, mainly because of the contributions of electronic, acoustic, thermal noise and relaxation oscillation [Bachor03]. It means that the use of squeezed light for measurement noise reduction is restricted to physical systems oscillating at RF frequencies.

The use of squeezed states is thus restricted to RF measurements, for which quantum noise is a limiting factor, i.e. when all other sources of noise are negligible or have been previously canceled, and for which the optical power is limited. Pertinent examples of applications of single mode squeezed light are hence the detection of gravitational waves using large interferometers [McKenzie02, Vahlbruch05], or sub-shot-noise high-sensitivity spectroscopy [SoutoRibeiro97]. Moreover, the production of squeezed states of light is also required for CV quantum communication protocols and quantum calculations, such as teleportation, dense coding, etc[25], as the combination of squeezed states allows the production of CV entanglement, as shown in the next section. Moreover, we will show in this thesis how the use of *multi-mode squeezed beams*, i.e. squeezing not limited to the TEM_{00} component, can broaden these possibilities of applications to imaging beyond the quantum limit, or even beyond the diffraction limit, and to parallel quantum information processing.

A.3.4 Entangled states

Entanglement is certainly the most intriguing feature of quantum mechanics. Its theoretical as well as experimental implications are at the core of all quantum information protocols. The concept of entanglement was first introduced by Einstein, Podolsky, and Rosen in 1935 [Einstein35]. They demonstrated that an apparent violation of the Heisenberg inequality could be achieved between the position and momentum observables of a pair of particles.

[23] We recall that we have restricted our analysis in section 1A.1.1 to stationary evolutions of the field without specifying the frequency of analysis in the following, as our calculations were transposable to any frequency.

[24] Optical measurements are limited by the bandwidth of the photo-detectors, typically around 20 MHz in our experiments, and are performed at a frequency Ω such as $\Omega \ll \nu_L$, where ν_L is the laser frequency. A detection of the fluctuations at *sideband frequency* Ω - with a spectrum analyzer on zero span for example - hence correspond to detection of the optical beam fluctuations at frequency $\nu_L \pm \Omega$.

[25] It would be impossible to list all the different protocols. One could therefore first refer to [BowenPhD03] for an excellent introduction to this domain.

This apparent violation has since been termed the EPR paradox. Demonstration of the EPR paradox relies on quantum correlations between a pair of non-commuting observables, so that measurement of either observable in sub-system x allows the inference of that variable in sub-system y to better than the quantum noise limit.

In this thesis, we will focus on the entanglement of optical fields in the continuous variable regime[26], which has recently been extensively investigated since the first experiment by Ou. *et al.* in 1992, which involved a non-degenerate optical parametric amplifier [Ou92]. More recently, we can reference the generation of sideband entanglement [Pirandola03], and quadrature entanglement using phase-locked OPOs [Jing06]. For an excellent review on optical quadrature entanglement, see reference [BowenPhD03].

The generation of optical quadrature entanglement can be obtained directly out of a nonlinear device such as an OPO [Laurat05, Laurat06], or by a combination of two quadrature squeezed beams with orthogonal squeezing[27] on a 50/50 beam-splitter [Ou92, Zhang00, Silberhorn01,1, Bowen03, Laurat04], as shown in Fig. 1.4. Two input fields[28] denoted with the indexes 1 and 2 are incident on the beam-splitter. Their amplitude and phase quadratures are respectively described by $\hat{X}_1^{\pm}$ and $\hat{X}_2^{\pm}$. The quadratures of the output beams x and y after the beam-splitter are given by

$$\hat{X}_x^{\pm} = \frac{1}{2}\left(\pm\hat{X}_1^{+} + \hat{X}_2^{+} + \hat{X}_1^{-} \mp \hat{X}_2^{-}\right) \tag{1.69}$$

$$\hat{X}_y^{\pm} = \frac{1}{2}\left(\hat{X}_1^{+} \pm \hat{X}_2^{+} \mp \hat{X}_1^{-} + \hat{X}_2^{-}\right) \tag{1.70}$$

Sum of amplitude fluctuations, and difference of phase fluctuations between both beams can be written

$$\delta\hat{X}_x^{+} + \delta\hat{X}_y^{+} = \delta\hat{X}_1^{+} + \delta\hat{X}_2^{+} \tag{1.71}$$

$$\delta\hat{X}_x^{-} - \delta\hat{X}_y^{-} = \delta\hat{X}_2^{+} - \delta\hat{X}_2^{+} \tag{1.72}$$

$$\tag{1.73}$$

We see for example that when the amplitude quadrature of the two input beams are perfectly squeezed, i.e. when $\{\Delta\hat{X}_1^{+}, \Delta\hat{X}_2^{+}\} \to 0$, we get

$$\langle\left(\delta\hat{X}_x^{+} + \delta\hat{X}_y^{+}\right)^2\rangle \to 0 \tag{1.74}$$

$$\langle\left(\delta\hat{X}_x^{-} - \delta\hat{X}_y^{-}\right)^2\rangle \to 0 \tag{1.75}$$

In this limit, an amplitude quadrature measurement on beam x would therefore provide an exact prediction of the amplitude quadrature of beam y. Similarly a phase quadrature

[26] Attempts are now being made to entangle light beams with atoms [Blinov04, Haine05], atoms with atoms [Duan00,2], and light with nano-mechanical devices [Eisert04]. In the condensed matter field, schemes are proposed to couple nano-mechanical resonators and a super-conducting electrical resonator, using SQUID technology [Tian06].

[27] This can first be achieved with two amplitude - or phase - squeezed beams in quadrature in the beam-splitter plane. Another option is to combine an amplitude squeezed and a phase squeezed beam, in phase in the beam-splitter plane. Note that the generation of entanglement with two squeezed beams incident on a beam-splitter does not allow to produce all the possible entangled states accessible with an OPA, as shown in reference [Laurat05, Laurat06].

[28] We have chosen in Fig. 1.4 to emphasize the fact that the entanglement considered here is involving only one spatial transverse mode, generally the TEM_{00} mode, as represented in the figure.

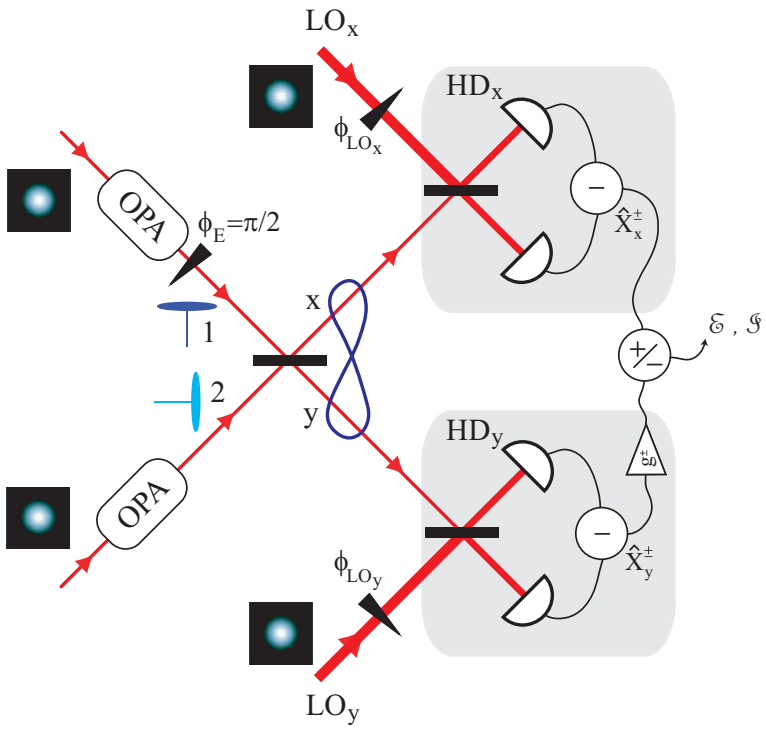

Figure 1.4: TEM_{00} quadrature entanglement. Two TEM_{00} amplitude squeezed beams in quadrature, i.e. such as $\phi_E = \pi/2$, are incident on a 50/50 beam-splitter. Two homodyne detections (HD) with TEM_{00} local oscillators (LO) are used to analyze the properties of each output beam. The appropriate combination of both detected signal yields either the degree of EPR paradox $\mathcal{E}$ or the degree of inseparability $\mathcal{I}$ of the two latter beams.

measurement on beam x would provide an exact prediction of the phase quadrature of beam y. However, note that both variables cannot be simultaneously measured. Fluctuations on the amplitude quadratures of both beams are said to be *anti-correlated*, whereas the fluctuations on their phase quadratures are said to be *correlated*. These properties are summarized in Fig. 1.5 [LauratPhD04]. Although each part of the entangled state represented in Fig. 1.5a) is noisy on all its quadratures, some particular quadratures are correlated with the other part of the entangled state, as represented in Fig. 1.5b) and c).

The short calculation presented above is a demonstration of entanglement, similar to the one thought of in the seminal paper of Einstein *et al.* [Einstein35]. Analysis of the entanglement in the physically realistic regime where $\{\Delta\hat{X}_1^+, \Delta\hat{X}_2^+\} \neq 0$ is more complex, and is what we concentrate on in the end of the section.

Although the specification of the coefficients of the covariance matrix offers a complete description of the entanglement, it does not immediately provide a measure of whether beams x and y are entangled, or how strongly they are entangled. We use two criteria, both of which can be inferred from the correlation matrix, to measure those properties. We first discuss the inseparability criterion proposed by Duan *et al.* [Duan00,1], which provides a necessary and sufficient condition for Gaussian entanglement. We then introduce the EPR paradox criterion proposed by Reid and Drummond [Reid88] which has been used to characterise entanglement in past experiments. It should be noted that a good measure of

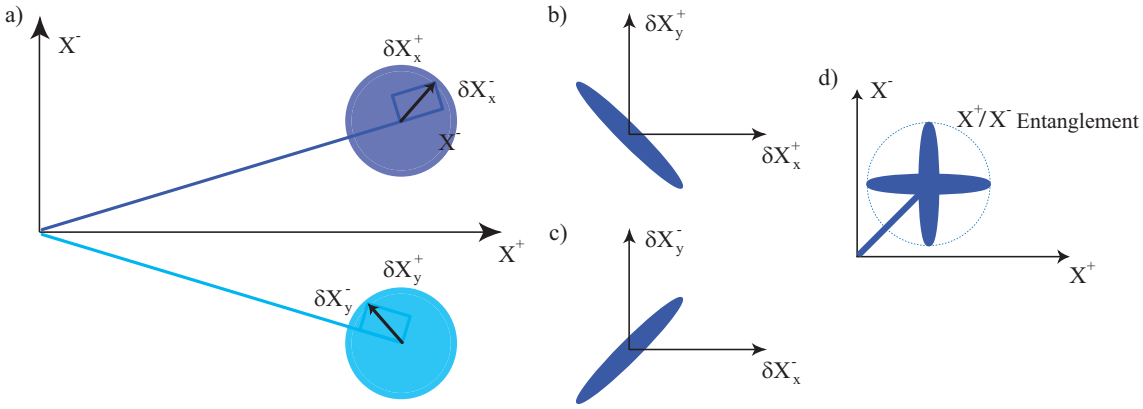

Figure 1.5: a) Representation in the Fresnel plane of ideal EPR states, for which b) amplitude fluctuations are anti-correlated ($\delta\hat{X}_x^+ = -\delta\hat{X}_y^+$), and c) phase fluctuations are correlated ($\delta\hat{X}_x^- = \delta\hat{X}_y^-$). d) Common representation of an amplitude-phase entangled state. It shows the axis along which correlations are hidden in the apparently noisy states represented in a).

entanglement should satisfy four conditions detailed in reference [Vedral97, Plenio00], and that neither the inseparability nor the EPR criteria have been shown to satisfy these conditions. Indeed, to our knowledge no such measure exists to date for continuous variable entanglement [Peres96, Horodecki97, Simon00, Laurat05]. However, both criteria considered here have strong physical significance, as they have a straightforward dependence on the strength of the quantum resources used to generate the entanglement, and are commonly used to gauge the strength of entanglement in experiments. We therefore refer to both criteria as measures of the strength of entanglement.

- Inseparability criterion and *degree of inseparability* $\mathcal{I}$

This criterion quantifies the entanglement or *inseparability* of a quantum state. Note that the term inseparability, refers to the definition of entanglement with respect to a property of its density matrix operator : "a state is said entangled if and only if its density matrix operator is non-separable".

For entanglement produced on a 50/50 beam splitter, the quadratures of beams x and y given in Fig.1.4 are symmetric. In such a case, the estimation of the *degree of inseparability* $\mathcal{I}$ proposed by Duan *et al.* in reference [Duan00,1][29] is equivalent to the one proposed by Giovannetti *et al.* in reference [Giovannetti03] and provides a direct measure of the strength of the entanglement between the two input beams. It is given by the rather simple expression [Bowen03], expressed here in the case of two amplitude squeezed beams[30]

$$\mathcal{I} = \sqrt{\Delta^2\hat{X}_{x+y}^+ \Delta^2\hat{X}_{x-y}^-} \tag{1.76}$$

[29]Note that the criterion given in reference [Duan00,1] corresponds to $\mathcal{I} = \frac{1}{2}\left[\Delta^2\hat{X}_{x+y}^+ + \Delta^2\hat{X}_{x-y}^-\right] < 1$, and is often referred to as the 'sum form', in opposition with the 'product form' presented in Eq. 1.76.

[30]In the general case, $\mathcal{I} = \sqrt{\Delta^2\hat{X}_{x\pm y}^+ \Delta^2\hat{X}_{x\pm y}^-}$, where $\Delta^2\hat{X}_{x\pm y}^+$ is the minimum of the variance of the sum or difference of the operators $\hat{X}_x^+$ and $\hat{X}_y^+$ between beams x and y normalized to the quantum noise limit, $\Delta^2\hat{X}_{x\pm y}^+ = \min\langle\ \delta\hat{X}_x^+ \pm \delta\hat{X}_y^{+\ 2}\rangle/2$. A similar definition applies for $\Delta^2\hat{X}_{x\pm y}^-$.

where $\Delta^2\hat{X}^+_{x+y}$ is the variance of the sum of the amplitude operators $\hat{X}^+_x$ and $\hat{X}^+_y$ of beams x and y, normalized to the quantum noise limit, i.e. $\Delta^2\hat{X}^+_{x+y} = \langle\left(\delta\hat{X}^+_x + \delta\hat{X}^+_y\right)^2\rangle/2$. A similar definition applies for $\Delta^2\hat{X}^-_{x-y}$. The boundary $\mathcal{I} = 1$ of the quantum regime corresponds to two incident coherent beams. If $\mathcal{I} < 1$, two incident beams are said *inseparable*. In the symmetric case for which both incident beams have identical gaussian noise, it can be shown that this criterion is a necessary and sufficient condition for entanglement. Note that the best possible entanglement is obtained for two perfectly squeezed beams, which corresponds to the case detailed at the beginning of the section. Eq. 1.74 and 1.75 directly show that $\mathcal{I} = 0$ in this limit case.

It is interesting to focus on the effect of de-coherence in the form of optical loss on the inseparability criteria. It can be shown [BowenPhD03] that for entanglement generated from a pair of uncorrelated squeezed beams, with equal optical loss for beams x and y, $\mathcal{I}$ can be expressed as a function of the overall detection efficiency η as

$$\mathcal{I} = \eta\Delta^2\hat{X}^+ + (1-\eta) \tag{1.77}$$

where $\Delta^2\hat{X}^+$ refers to the common noise variance on the amplitude quadrature of both input beams 1 and 2, i.e. $\Delta^2\hat{X}^+ = \Delta^2\hat{X}^+_1 = \Delta^2\hat{X}^+_2$. Eq. 1.77 shows that as long as the two beams used to generate the entanglement are squeezed, whatever this level, and even when η approaches zero, $\mathcal{I}$ remains below unity, i.e. that the output beams are always entangled according to this criterion[31]. We see that the entanglement is robust against losses at least in the sense that loss alone cannot transform an inseparable state into a separable one. These results are compared with the ones obtained for the second criterion in Fig. 1.6.

- Reid or EPR paradox criterion and *degree of EPR paradox* $\mathcal{E}$

This criterion quantifies the *degree of EPR paradox* of a state, which is slightly more restrictive than the general concept of entanglement or inseparability. Its is derived from the ability of a state to produce an apparent violation of Heisenberg inequalities between two conjugate variables, similarly to what Einstein, Podolsky, and Rosen have shown in 1935 between the position and momentum observables of a pair of particles.[Einstein35]. This apparent violation has since been termed the EPR paradox. It relies on the fact that measurement of either observable in sub-system x allows the inference of that variable in sub-system y to better than the quantum noise limit, even if the two beams are far apart from each other. Between the amplitude and phase quadratures of a pair of optical beams this is quantified by the product of conditional variances [Reid88], the degree of EPR paradox $\mathcal{E}$ can therefore be defined as

$$\mathcal{E} = \Delta^2\hat{X}^+_{x|y}\Delta^2\hat{X}^-_{x|y}, \tag{1.78}$$

where the EPR paradox is demonstrated for E < 1 and the quadrature conditional variances $\Delta^2\hat{X}^\pm_{x|y}$ are given by

$$\begin{aligned}\Delta^2\hat{X}^\pm_{x|y} &= \Delta^2\hat{X}^\pm_x - \frac{|\langle\delta\hat{X}^\pm_x\delta\hat{X}^\pm_y\rangle|^2}{\Delta^2\hat{X}^\pm_y} \\ &= min_{g^\pm}\langle\left(\delta\hat{X}^\pm_x - g^\pm\delta\hat{X}^\pm_y\right)^2\rangle,\end{aligned} \tag{1.79}$$

[31] We will see that it is not the case for the EPR criterion.

where $g^{\pm}$ are experimentally adjustable variables. Experimentally, such adjustable gains can be achieved electronically as shown in Fig.1.4.

In order to see the sensitivity to optical loss, assuming identical noise properties for the two beams incident on the beam-splitter in Fig.1.4, i.e. $\Delta^2\hat{X}_1^+ = \Delta^2\hat{X}_2^+ = \Delta^2\hat{X}^+$ and $\Delta^2\hat{X}_1^- = \Delta^2\hat{X}_2^- = \Delta^2\hat{X}^-$, and assuming an identical detection efficiency η for each beam, the degree of EPR paradox becomes

$$\mathcal{E} = 4\left(1-\eta+\frac{2\eta-1+\eta^2(\Delta^2\hat{X}^+.\Delta^2\hat{X}^- - 1)}{\eta\left(\Delta^2\hat{X}^+ + \Delta^2\hat{X}^- - 2\right)+2}\right)^2 \tag{1.80}$$

The degree of EPR paradox is thus directly related to optical losses, to the amount of squeezing, and also to the purity of the state, as we will emphasize later on.

A comparison between both characterization of entanglement is presented in Fig.1.6 as a function of the detection efficiency η[32]. In Fig. 1.6a), we have compared the degree

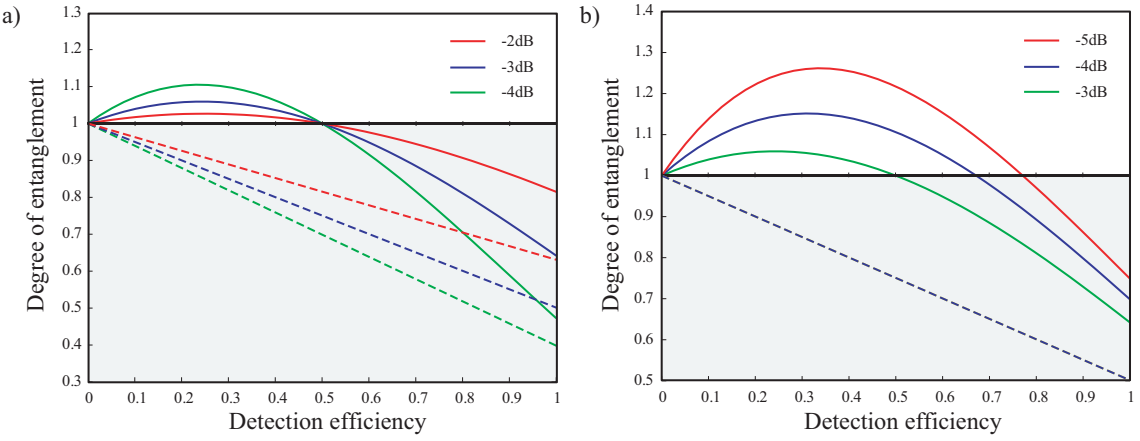

Figure 1.6: Comparison of EPR paradox criterion (continuous lines) and Duan's inseparability criterion (dotted lines). a) influence of the squeezing level of the input beams, for pure states. b) influence of the purity of the input states, with a fixed value of the squeezing level of the input beams of -3dB, with 3dB, 4dB and 5dB of anti-squeezing. The corresponding values of the purity are respectively 1, 0.89, and 0.79.

of EPR paradox $\mathcal{E}$ (continuous lines) and degree of inseparability $\mathcal{I}$ (dotted lines) for pure states, for different squeezing values. Note that in this case of pure input states for which $\Delta^2\hat{X}_1^+.\Delta^2\hat{X}_1^- = \Delta^2\hat{X}_2^+.\Delta^2\hat{X}_2^- = \Delta^2\hat{X}^+.\Delta^2\hat{X}^- = 1$, $\mathcal{E} = 1$ when $\eta = 0.5$, independently of the level of squeezing. This defines a boundary such as if $\eta > 0.5$, the EPR paradox criterion is satisfied for any level of squeezing, and if $\eta < 0.5$, it can never be satisfied. This is a striking contrast to the inseparability criterion which, as we showed earlier in Eq. 1.77, is satisfied for any level of squeezing and any detection efficiency. Satisfaction of the EPR paradox criterion between two beams is thus a sufficient but not necessary condition for their entanglement. However, we have chosen to present this

[32]Losses which can occur before and after the beam combination are assumed to be symmetrical and are taken into account in the detection efficiency.

criterion as it is used to characterize the strength of entanglement in several experiments [Ou92, Zhang00, Silberhorn01,1], and still often referred to[33].

Fig .1.6b) presents the influence of the purity of the input states that are mixed on the beam-splitter for a fixed squeezing value of -3dB. Again, continuous lines represents the degree of EPR paradox $\mathcal{E}$, whereas the dotted line[34] refers to the degree of inseparability $\mathcal{I}$. We see that the inseparability criterion is independent of the purity of the entanglement, a property to which the EPR paradox criterion is very sensitive. The boundary below which the EPR paradox is satisfied is highly dependent on the purity. The observation of EPR paradox therefore requires very low losses for increasingly non-purity of the input states. Optical loss changes the purity of the entanglement and therefore affects the EPR paradox and inseparability criteria differently. However, if $\eta = 1$, the measured entangled state is pure, and both criteria are monotonically increasing functions of the amount of squeezing. In the limit of pure measured entanglement, the inseparability and EPR paradox criteria become equivalent.

Note that quadrature entanglement has already been extended to polarization entanglement in the continuous variable regime. Indeed, any pair of conjugate observables can be used to generate entangled beams. In this precise case, Stokes parameters accounting for the polarization states do not commute and can lead to polarization entanglement [Bowen02, Korolkova02]. We will also extend this notion in section 5 B to the entanglement of position and momentum of two TEM_{00} mode beams.

[33] It can be shown that the production of EPR beams compared to the one a simple entangled state is as different as performing a QND and a squeezing measurement [Treps04,2].

[34] Note here the absence of dependence of the inseparability criterion with the purity of the input states.

B Single/Multi-mode criterium

In this section, we introduce the theoretical basis required to develop a quantum study of optical image measurements. A part of the work presented here has been published in reference [Treps05].

We have already termed the quantum states described in the transverse plane by Eq. 1.27 as *multi-mode transverse fields*. We propose here to give an accurate definition of this term.

First, we will show that a pure classical state[35]. Then, we will give a precise definition of a transverse multi-mode quantum state, and finally, we give experimental tools to differentiate a single mode field from a multi-mode quantum field.

B.1 Classical approach

We consider the propagation of a coherent light beam in vacuum. We can describe such a field with the same formalism as the one used in Eq.1.27 by

$$\mathcal{E}^{(+)}(\vec{r},z) = i\sqrt{\frac{\hbar\omega_0}{2\epsilon_0 cT}}\sum_n \alpha_n u_n(\vec{r},z) \tag{1.81}$$

where quantum operators are replaced by numbers, and especially $\hat{a}_n$ is replaced by its mean value α_n,i.e. the square root of the number of photons in mode n.

When more than one α_n is non zero, it seems at first sight natural to state that this field is *multi-mode*. However, if the α_n coefficients are fixed (i.e. we deal with a coherent superposition of modes and not a statistical one), one can always define a new mode v_0 such as

$$v_0(\vec{r},z) = \frac{1}{\sqrt{\sum_n |\alpha_n|^2}}\sum_n \alpha_n u_n(\vec{r},z) \tag{1.82}$$

and build a basis $\{v_n\}$ in which v_0 is the first element. In this basis, the field is proportional to v_0. It means that we deal with a *single mode field*.

We can conclude that for a coherent superposition of modes, there is no intrinsic definition of a multi-mode beam (i.e. a definition independent of the basis choice). Of course if the field is a stochastic superposition of modes, the mode v_0 cannot be defined as in Eq. 1.82, and the multi-mode character has a clear meaning. We will exclude this case in the following and only consider spatial "mode-locked" field patterns. We will restrict our analysis to spatial variables, but it can be applied to any physical dimension. For instance, in the time domain, a mode locked laser is single mode, as it is a coherent superposition of many temporal modes. However, a usual laser is often multi-mode because its output is a statistical superposition of polarization, temporal and spatial modes. Note that an approach with the density operator formalism could extend our considerations to mixed states.

[35] Such a state has all its classical parameters fixed, and has thus a perfect degree of spatial and temporal coherence. In other words, it does not result of a statistical superposition of states.

B.2 Quantum approach

B.2.1 Single Mode quantum light

In order to give a proper definition of a single mode state, let us write the most general state of the field in the Fock state basis $|N_1, \dots, N_n, \dots\rangle$[Grynberg97], where N_n stands for the number of photons in the transverse mode n, whose transverse distribution is described by $u_n(\vec{r})$

$$|\psi\rangle = \sum_{N_1,\dots,N_n,\dots} C_{N_1,\dots,N_n,\dots} |N_1, \dots, N_n, \dots\rangle \tag{1.83}$$

where $\{C_{N_1,\dots,N_n,\dots}\}$ are complex coefficients of the decomposition in the Fock state basis[36]. In order to link this description with the previous notations, for which the most general envelope field operator was written [37]

$$\hat{\mathcal{E}}^{(+)}(\vec{r}) = i\sqrt{\frac{\hbar\omega_0}{2\epsilon_0 cT}} \sum_n \hat{a}_n u_n(\vec{r}), \tag{1.84}$$

we write the mean value of the electric field positive envelope as

$$\langle\psi|\hat{\mathcal{E}}^{(+)}(\vec{r})|\psi\rangle = i\sqrt{\frac{\hbar\omega_0}{2\epsilon_0 cT}} \sum_n \left(\sum_{N_1,\dots,N_n>1,\dots} C^*_{N_1,\dots,N_n-1,\dots} C_{N_1,\dots,N_n,\dots} \right) \sqrt{N_n} u_n(\vec{r})$$

Using these notations, we can now give a definition of a single mode beam :

Definition 1 *A state is single mode if there exists a mode basis $\{v_0, v_1, \dots\}$ in which it can be written :*

$$|\psi\rangle = |\phi\rangle \otimes |0, \dots, 0, \dots\rangle \tag{1.85}$$

where $|\phi\rangle$ is the field state in the first transverse mode.

The question is now whether, in contrast with classical states, there exists quantum states that cannot be written as in Eq. 1.85. To answer this question, we will demonstrate the following proposition :

Proposition 1 *A quantum state of the field is single mode if and only if the action on it of all the annihilation operators of a given basis gives proportional vectors.*

One can note that if this property stands for a given basis, it then stands for the action of any annihilation operator.

In order to prove the first implication, we initially assume that $|\psi\rangle$ is a single mode field with respect to the basis $\{u_n, \hat{a}_n\}$, then

$$\hat{a}_0|\psi\rangle = |\psi_0\rangle \quad \text{and} \quad \hat{a}_n|\psi\rangle = 0 \quad \forall n \neq 0 \tag{1.86}$$

Consider now any linear combination of the operators

$$\hat{b} = \sum_n c_n \hat{a}_n \tag{1.87}$$

[36] Note that such a description allows any photon distribution in the transverse modes, but also allows correlations between the different modes.

[37] It corresponds to Eq.1.27, where we have not specified here the field propagation through the z dependence, as our study will always remain in the detector plane.

where $\sum_n |c_n|^2 = 1$. The action of this operator on the state $|\psi\rangle$ is given by

$$\hat{b}|\psi\rangle = \sum_n c_n \hat{a}_n |\psi\rangle = c_0 |\psi_0\rangle \tag{1.88}$$

This demonstrates the first implication of our proposition : all the projections of the field are proportional.

In order to prove the other implication, we consider now a field $|\psi\rangle$ on which the action of any annihilation operator $\hat{a}_n$ is proportional to $|\psi_0\rangle$. This is in particular true for the basis $\{u_n, \hat{a}_n\}$:

$$\hat{a}_n|\psi\rangle = \alpha_n |\psi_0\rangle \tag{1.89}$$

If we assume that $\sum_n |\alpha_n|^2 = 1$ (which is always possible by changing the normalization of $|\psi_0\rangle$), we can define a new basis $\{v_n, \hat{b}_n\}$ such as

$$\hat{b}_0 = \sum_k \alpha_k^* \hat{a}_k, \quad \text{and } v_0(\vec{r}) = \sum_k \alpha_k^* u_k(\vec{r}) \tag{1.90}$$

and complete the basis by choosing the other vectors and defining a unitary matrix $[c_{nk}]$ such as

$$\hat{b}_n = \sum_k c_{nk} \hat{a}_k \quad \text{with } c_{0k} = \alpha_k^* \quad \text{and } \sum_k c_{nk} c_{jk}^* = \delta_{nj}. \tag{1.91}$$

It is then straightforward to show that

$$\hat{b}_n|\psi\rangle = \delta_{0n}|\psi_0\rangle \tag{1.92}$$

which concludes the demonstration.

In addition to the proposition, Eq. 1.90 gives the expression of the mode on which lies the field, knowing its projection on a particular basis. We can also note that, in order to show that a field is single mode, it is sufficient to show that all its projection on the annihilation operators of one particular basis are proportional.

To illustrate the proposition, if one considers the superposition of coherent states

$$|\psi\rangle = |\alpha_1\rangle \otimes \ldots \otimes |\alpha_n\rangle \otimes \ldots \tag{1.93}$$

it is straightforward to see that all the projections of this state are proportional to the state itself. Hence, it corresponds to a single mode beam. The basis in which it is single mode is the same as the one already introduced for the classical case, i.e. the one whose first vector is set to $v_0(\vec{r})$ as given by Eq. 1.82.

Using this proposition, we can also look for the different states that qualify to our definition of single mode quantum beam. As a state that cannot be written as follows in any mode basis :

$$|\psi\rangle = |\phi_1\rangle \otimes \ldots \otimes |\phi_n\rangle \otimes \ldots \tag{1.94}$$

is obviously not a single mode beam, we will consider now such a factorized state of the field, on which the action of the annihilation operators gives :

$$\hat{a}_n|\psi\rangle = |\phi_1\rangle \otimes \ldots \otimes (\hat{a}_n|\phi_n\rangle) \otimes \ldots \tag{1.95}$$

Consequently, there are only two possibilities to have all these states proportional :

- either only one of the projection is different from zero, which means we are already in the basis in which the state is single mode.
- or all the states are coherent states.

We have described here all the possible single mode states, which agree with the intuitive description one can have. For instance, if one considers the superposition of several transverse modes, if at least one of them is a non-coherent state, one gets a multi-mode quantum state.

B.2.2 Multi-mode quantum light

A beam of light is said multi-mode, from a quantum point of view, when ... it is *not* single mode according to definition 1! We can characterize such a beam by its degree n (this degree equals one for a single mode beam):

Definition 2 *For a beam $|\psi\rangle$, the minimum number of modes necessary to describe it (or the minimum number of non-vacuum modes in its modal decomposition), reached by choosing the appropriate basis, is called the degree n of a multi-mode beam. Any corresponding basis is called a minimum basis for the field $|\psi\rangle$.*

The degree of a multi-mode beam can also be related to the generalization of proposition 1 to a n-mode beam. Using the same technique, one can show that a quantum field is a n-mode beam if and only if the action on it of all the annihilation operators belongs to the same n dimensioned sub-space.

Whereas the previous paragraph gives a good definition of the degree of a multi-mode beam, it is not very convenient as one has no information on the basis in which the beam is exactly described by n modes. We can however define a particular basis[38], useful for calculations :

Proposition 2 *For a beam $|\psi\rangle$ of degree n, it is always possible to find a basis $\{u_i, \hat{a}_i\}$ such as*

- *The mean value of the electric field is non zero only in the first mode.*
- *It is a minimum basis for the field $|\psi\rangle$, as defined in definition 2.*

We will call this basis an eigenbasis or a mean-field basis.

In order to demonstrate this proposition, we consider a minimum basis $\{u_i, \hat{a}_i\}$ for the field $|\psi\rangle$. This basis is supposed to be ordered such as the n first modes are the relevant ones. We can then define a new basis $\{v_i, \hat{b}_i\}$ such as :

$$\begin{aligned} v_0 &= \frac{1}{\sqrt{\sum_{i=0}^{n-1}\langle\hat{a}_i\rangle^2}}\sum_{i=0}^{n-1}\langle\hat{a}_i\rangle u_i \\ v_{i,0<i<n} &= \sum_{j=0}^{n-1} c_{ij}u_j \\ v_{i,i\geq n} &= u_i \end{aligned} \tag{1.96}$$

[38] It is straightforward to see that such a basis is not unique.

mode, operator	single mode quantum light	multi-mode quantum light
v_0, $\hat{b}_0$	any state such as $< \psi\|\hat{b}_0\|\psi >= \langle\psi\|\hat{E}\|\psi\rangle$	any state such as $< \psi\|\hat{b}_0\|\psi >= \langle\psi\|\hat{E}\|\psi\rangle$
v_1, $\hat{b}_1$	vacuum	non-classical state such as $< \psi\|\hat{b}_1\|\psi >= 0$
$\vdots$	$\vdots$	$\vdots$
v_n, $\hat{b}_n$	vacuum	non-classical state such as $< \psi\|\hat{b}_n\|\psi >= 0$
v_{n+1}, $\hat{b}_{n+1}$	vacuum	vacuum
$\vdots$	$\vdots$	$\vdots$

Table 1.1: Comparison between single and multi-mode light beam written in the mean field basis. In this example, the multi-mode beam is of order n, as n modes are filled with non vacuum states in the eigenbasis.

where the coefficient $\{c_{ij}\}$ are chosen in order to get an orthonormal basis. Definitions similar to the one of Eq.1.96 apply for the creation operators with the conjugated basis. The first vector of this basis is the same as the one defined for a classical beam in Eq.1.82. This description completes the definition of the mean field given in section 1 A.2.4. In that basis, the field is single mode in a classical sense. However the energy lying in all the modes indexed from 1 to n is not necessarily zero. These states are indeed not necessarily traditional vacuum states. Although their electric field mean value is zero, then can still correspond to squeezed vacuum states or correlated vacuum states. As the modes for $i \geq n$ are not changed, this new basis is still a minimum one for the field $|\psi\rangle$. This demonstrates the proposition and illustrates the construction of a basis as defined in proposition 2 from a minimum basis[39]. A representation of a multi-mode quantum field in such a basis, compared with the one of a single quantum mode field, is given in table B.2.2.

The existence of this basis is also a confirmation of the intuitive idea of the difference between single mode and multi-mode quantum light. Indeed, for a single mode beam, the spatial variation of the noise is the same as the one of the mean field. For a multi-mode beam, the previous description shows that some of the modes orthogonal to the mean field are sources of noise but do not contribute to the mean field. This implies that the spatial variation of the noise is independent of the one of the mean field. This property can be used to experimentally characterize the multi-mode character of light. One of the difficulties of such experiments is the knowledge of the mode structure of the field, as it is not possible to test all the transverse modes. Nevertheless, there exists some simple experimental tests which can provide signatures of a multi-mode quantum field. This is what we propose to present in the next section.

[39]Because of the absence of restrictions for the choice of the $\{c_{ij}\}$ coefficients, their exists an infinite number of possible eigenbasis.

Before that, let us now come back on the modal quadrature definition given in section A.2.2. The phase reference relative to which the modal quadratures θ_n are defined has to be clearly introduced at this point. For a single mode field, there is no ambiguity as amplitude and phase quadratures correspond to the real and imaginary part of the annihilation operator, respectively. However, for a multi-mode field, in order to have a single phase reference for the description of the field, we define all quadratures relative to the ones of the mean field. For this reason, $\hat{X}_n^+$ and $\hat{X}_n^-$ defined in Eq. 1.29 and 1.30 with real and imaginary part of $\hat{a}_n$ only when the mean field is real.

This definition is of particular importance for the definition of the quadratures of a state orthogonal to the mean field. Such a state is necessarily a vacuum state, as a direct consequence of the definition of the mean field, and the importance of a clear definition of a phase reference is easy to understand as no orientation in the Fresnel plane is given by the amplitude of the field.

Moreover, it means that real and imaginary parts of the annihilation operator of a mode component different from the mean field do not necessarily identify with amplitude and phase quadratures in thus mode, as we will see in Fig. 3.4.

B.3 Towards an experimental criterium

It has been shown recently that the quantum multi-mode character of light could be tested experimentally by cutting the beam with a razor blade [Poizat98, Hermier99], or by using an iris whose aperture size is continuously varied [Martinelli03]. The proposed criterium in the last reference can be summarized as follows : *When the normalized noise variance is plotted as a function of the iris transmission, the beam is multi-mode if the noise variation is not linear.*

We propose here to use our formalism to explain this result, through the study of the differences that can be observed between two very basic examples : *single* and *bi-mode* fields.

The idea is here to predict the evolution of the noise variance measured on a photo-detector, when a knife edge - which will play the role of the iris here - is slowly moved into the detected beam, cutting it in its transverse plane, as schematized in Fig.1.7.

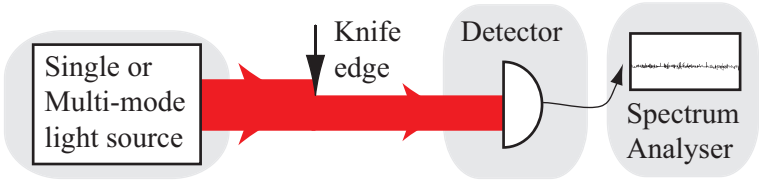

Figure 1.7: An experiment to investigate for the multi-mode transverse character of a light beam. The variation of the detected noise when a "knife-edge" is slowly translated into the beam can yield a multi-mode signature.

The quantum operator describing the total number of photons detected during the time interval T, when the knife edge is positioned at $x = d$, is denoted $\hat{N}(d)$ and its expression is

$$\hat{N}(d) = \frac{2\epsilon_0 cT}{\hbar\omega_0} \int_{-\infty}^{d} \hat{\mathcal{E}}^{(+)\dagger}(x)\hat{\mathcal{E}}^{(+)}(x)dx \tag{1.97}$$

where the incident field operator is described by Eq.1.27[40].

Let us first consider a single mode quantum field. We will call u_0 the mode of its mean field, which is potentially squeezed. As explained in proposition 2, all other modes are filled with vacuum, and the field can be described by

$$\alpha_0 = \sqrt{N} \tag{1.98}$$

$$\alpha_n = 0 \quad , \quad \forall n \neq 0 \tag{1.99}$$

where N is the total number of photons in the mean field[41].

Using the definitions presented in section 1 A.2.3, the mean value of the total number of photons detected when the knife-edge is at the position $x = d$ is given by

$$\langle \hat{N}(d) \rangle = N\Gamma_{00}(d) \tag{1.100}$$

where we have introduced the overlap integral $\Gamma_{nm}(d)$ between the modes u_n and u_m, whose expression is

$$\Gamma_{nk}(d) = \int_{-\infty}^{d} u_n^*(x) u_k(x) dx \tag{1.101}$$

Note that $\Gamma_{00}(d)$ introduced in Eq.1.100 identifies with the transmission of the knife edge. In order to simplify the expressions, we will consider from now on in this section that the mode profiles are all real.

A simple calculation yields the general expression of the detection noise variance :

$$\langle \delta\hat{N}^2(d) \rangle = N \left[\langle \delta \hat{X}_0^{+\,2} \rangle \Gamma_{00}^2(d) + \sum_{n=2}^{\infty} \Gamma_{0n}^2(d) \right] \tag{1.102}$$

where the first term corresponds to the noise contribution of the mode u_0, and the sum represents the noise contribution of all the other modes. All these latter modes are vacuum fields as we deal with a single mode field, and are such as $\langle \delta \hat{X}_n^{+\,2} \rangle = 1$.

Eq.1.102, normalized to the shot noise, can be simplified as follows

$$\frac{\langle \delta\hat{N}^2(d) \rangle}{\langle \hat{N}(d) \rangle} = 1 + \Gamma_{00}(d) \left[\langle \delta \hat{X}_0^{+\,2} \rangle - 1 \right], \tag{1.103}$$

by using the following relation[42]

$$\Gamma_{00}(d) = \sum_{n=0}^{\infty} \Gamma_{0n}^2(d). \tag{1.104}$$

The normalized noise varies linearly as a function of the transmission factor $\Gamma_{00}(d)$, as shown by trace (i) in Fig.1.8a), in the case of a -3dB amplitude squeezed single mode beam. This will be the case *whatever* the profile of the mean field mode. Measuring only

[40] We recall that using transverse modes limited to a single dimension in the detection plane Eq.1.27 can be written as $\hat{\mathcal{E}}^{(+)}(x) = i\sqrt{\frac{\hbar\omega_0}{2\epsilon_0 cT}} \sum_{n=0}^{\infty} \hat{a}_n u_n(x)$.

[41] Note that does N not strictly correspond to the number of photons in the entire beam, but in the mean field only. Indeed, squeezed vacuum modes do not belong to the mean field but still have photons [Grynberg97]. However, in the regime of bright optical beams, i.e. of large photon flux, to which this thesis is restricted, the number of photons contributing to the squeezed vacuum modes is negligible relative to the one in the mean field.

[42] This relation between the overlap integrals can be proven using the particular case of a coherent illumination, for which $\langle \delta \hat{X}_0^{+\,2} \rangle = 1$. In this case, the noise level corresponds to the shot noise, i.e. $\langle \hat{N}(d) \rangle = \langle \delta\hat{N}^2(d) \rangle$, as shown by Eq. 1.66. Rewriting the previous expression with Eq. 1.100 and 1.102 directly yields Eq. 1.103.

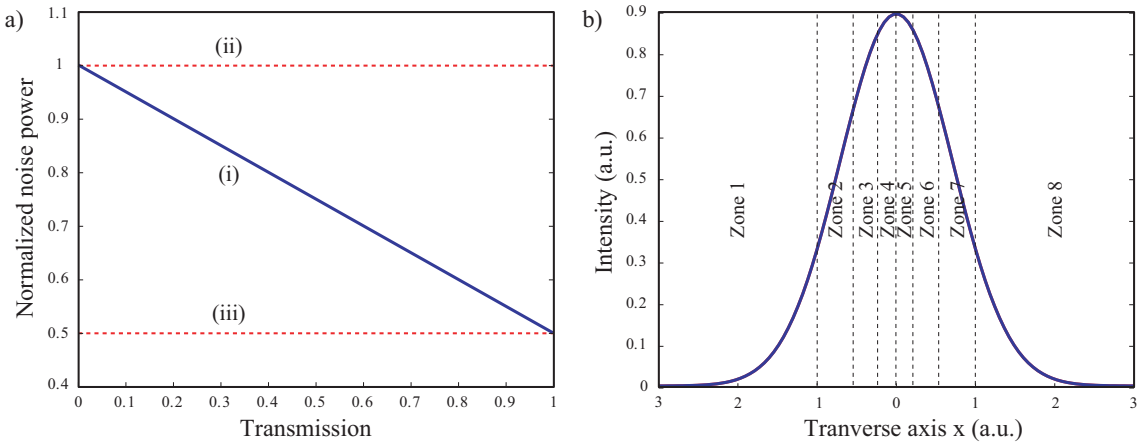

Figure 1.8: Single squeezed mode case. a) (i) Normalized noise as a function of the transmission with -3dB of squeezing.(ii) Shot noise level. (iii) Squeezing level for a total detection of the mode u_0. b) Spatial repartition of the noise reduction on the transverse plane for the particular case of a single mode squeezed TEM_{00} field. The detection of each zone independently would lead to identical noise reduction relative to the shot noise.

half of a single mode field will for instance always result in a 50% losses effect on the noise reduction.

Let us now briefly comment on the measured noise for extreme positions of the knife edge. On the one hand, when the beam is completely blocked, i.e. for $d \to \infty$, the transmission goes down to zero, and $\Gamma_{00}(\infty) = 0$. Hence, the noise tends towards a value of 1, corresponding to the shot noise limit (trace (ii) on Fig.1.8a)). On the other hand, when the knife edge is completely removed, i.e. for $d \to 0$, the transmission reaches unity, and $\Gamma_{00}(0) = 1$. Therefore, the noise tends towards the noise of the mode u_0 only, i.e. towards $\langle \delta \hat{X}_0^{(+)^2} \rangle$ (trace (iii) on Fig.1.8a)).

The linear variation of the noise with the transmission for a single mode state is sometimes at the origin of the unappropriate term of "homogeneous squeezing" in a single mode squeezed state[43]. A more accurate statement is that the local noise reduction relative to the shot noise is directly proportional to the local intensity. Indeed, if we were to partially detect a squeezed beam with a detector small compared to the beam size, the noise reduction would be measured mostly in the intense regions of the beam. As expected, it implies that the detection of a squeezed field with finite detectors is possible as long as the most intense areas of the beam are localized on the detector. Moreover, it justifies why the presence of, for instance, a dust particle in the most intense part of the beam can have dramatic consequences on the squeezing level. In order to help visualizing these properties, we have schematized in Fig.1.8b) the spatial extension of detectors that would measure identical noise reduction relative to the shot noise[44], in the particular case of a squeezed TEM_{00} mode.

[43] The term of "homogeneous squeezing" would be more adapted to a totally multi-mode beam, which detection yields the same noise reduction with *any* detection device. This property is also termed *local squeezing*.

[44] The spatial extension of such detectors has to be inversely proportional to the detected power.

Assuming now that the field is bimodal, we use the eigenmode basis described in proposition 2, in which the first mode u_0 carries the mean field, and u_1 is a vacuum mode that can be squeezed or correlated with the mode u_0. All the other modes are vacuum modes.

Similarly to the single mode case, a simple calculation yields the following noise variance in the general bi-modal case, normalized to the shot noise

$$\frac{\langle \delta\hat{N}^2(d)\rangle}{\langle \hat{N}(d)\rangle} = 1+\Gamma_{00}(d)\left[\langle \delta\hat{X}_0^{+\,2}\rangle - 1\right] + \frac{\Gamma_{01}^2(d)}{\Gamma_{00}(d)}\left[\langle \delta\hat{X}_1^{+\,2}\rangle - 1\right] + 2\Gamma_{01}(d)\langle \delta\hat{X}_0^{+}\delta\hat{X}_1^{+}\rangle$$

where the second and third terms correspond to the noise modification relative to the shot noise, arising from the properties of the modes u_0 and u_1, and the fourth one to the modification due to the presence of correlations between the same modes. Note that none of the other modes contribute to the final expression.

Let us now illustrate this result with two very simple examples. We have first represented on Fig.1.9a) the normalized noise as a function of the transmission, in a bimodal case, where the mean field is a TEM_{00} mode with -3dB of amplitude squeezing, and where the TEM_{10} - trace (iv) - or TEM_{20} - trace (v) - vacuum modes are filled with -3dB of amplitude squeezing, respectively. We see that the noise goes below the line defined for a

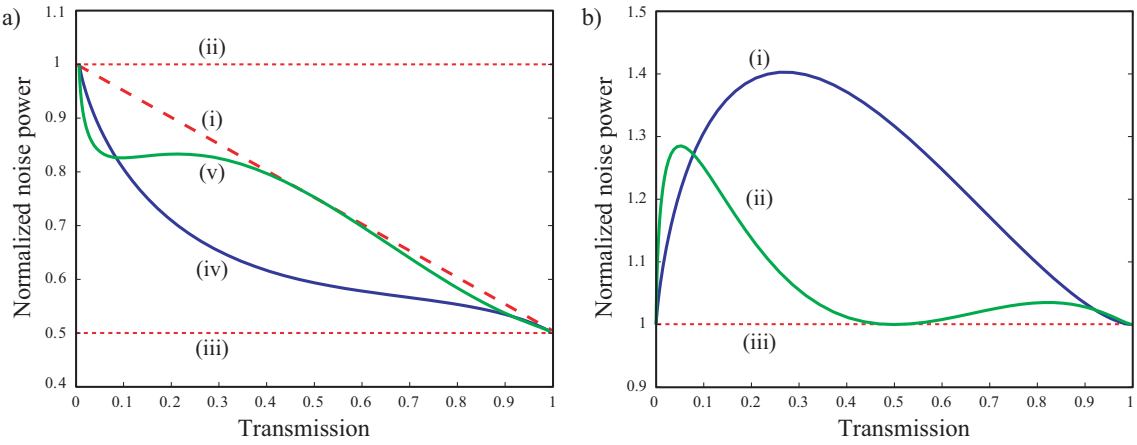

Figure 1.9: Bimodal case. a) Normalized noise as a function of the transmission, when the mean field is a TEM_{00} mode with -3dB of squeezing, and where the TEM_{10} - trace (iv) - or TEM_{20} - trace (v) - vacuum modes are filled with -3dB of squeezing, respectively. Traces (i), (ii) and (iii) respectively correspond to the single mode case with -3dB of squeezing, the shot noise level, and the squeezing level, as in Fig.1.8. b) Normalized noise as a function of the transmission, when the mean field is a coherent TEM_{00} mode, and where the TEM_{10} - trace (i) - or TEM_{20} - trace (ii) - vacuum modes are filled with 3dB of anti-squeezing, respectively. Trace (iii) corresponds here to the shot noise level.

single mode beam - trace (i) - for intermediate positions of the knife edge in both cases. This is the proof of the multi-mode character of this beam. Note that for zero transmission, the noise always tends to the shot noise level - trace (ii) -, as no squeezing can obviously be detected. Moreover, the noise goes back to the noise level defined by the mean field - trace (iii) - when the knife edge is entirely removed from the beam. A complete detection

of the transverse plane corresponds to the detection of the mean field, i.e. to the TEM_{00} mode. It corresponds to a simple "bucket" detector intensity measurement. Since complete TEM_{10} and TEM_{20} modes are orthogonal to the mean field, i.e. $\Gamma_{01} = 0$ and $\Gamma_{02} = 0$, they do not contribute to the measurement noise. The variations of the noise in between these two extreme values are mode dependent as they are related to the overlap integral between the mean field and the other modes.

Secondly, we consider the bimodal case where the TEM_{00} mode is a coherent mean field and the TEM_{10} - trace (i) -, or the TEM_{20} - trace (ii) - mode is a squeezed vacuum field with 3dB of amplitude anti-squeezing. The results are presented in Fig.1.9b). As in the previous example, the noise goes from the shot noise - trace (iii) - when the beam is blocked, and back to the shot noise when the entire field is detected, as mean field and squeezed mode are orthogonal[45], i.e. $\Gamma_{01} = 0$ and $\Gamma_{02} = 0$. Again, for intermediate knife edge positions, the noise diverges from the shot noise. Even if the noise goes above the line this time, it is still a proof of the multi-mode aspect of the field.

The observation of a non linear variation of the noise as a function of the transmission - above or below the single mode line - is thus the signature of a multi-mode field. This is the key element of the statement presented in reference [Martinelli03].

It is very important to note that observing a non linear variation of the noise with the transmission is only a *sufficient* condition to state that the measured field is multi-mode. Indeed, particular multi-mode fields that yield a linear variation of the measurement noise with the transmission can be found[46]

As a conclusion, it is possible to deduce from experimental results that a field is multi-mode, but no definite experimental proof can ensure that we are in presence of a single mode state, unless one tries an infinite set of experiments! In order to give an idea of the complexity of the results that can be obtained, we present in appendix C knife edge experiments with several detection schemes : complete detection, split-detection, homodyne detection with different local oscillator profiles. We show that several experiment can provide a complementary analysis of a multi-mode beam.

[45] This result can be generalized easily to a multi-mode beam of any order : *the modes orthogonal to the mean field do not contribute to the measurement noise for a complete detection of the field.* We will come back in section 1 C on the very important consequences of this remark.

[46] For instance, a knife edge experiment with an incident bimodal field, again composed of a bright squeezed TEM_{00} mode and a TEM_{10} or TEM_{20} squeezed vacuum mode, results in a linear variation of the noise if the beam is cut along the y axis instead of the x axis. Indeed, even when the knife edge is moved into the beam, the partially blocked TEM_{00}, TEM_{10} and TEM_{20} modes always remain orthogonal relative to the x axis. As a consequence, no squeezing in these modes is detected, whatever the position of the knife edge. This provides an example of a multi-mode beam yielding a linear noise variation with a knife edge experiment. Several simple examples are presented in appendix C with different types of detection.

C Image detection in the transverse plane

We present here the optical detection devices that are used throughout the experimental demonstrations of this thesis. The first one is the common photo-detector - also termed "bucket detector" - measuring the total beam power. Secondly, we will briefly introduce a measurement relying on the interference with another beam whose properties are well known, hence providing information on the mode quality of the incident beam. The third one is the homodyne detection, well adapted to the study of a particular spatial mode within an optical image, and which allows field quadrature measurement. The fourth one is the array detector, adapted to a pixel description of the transverse plane. Finally, we will investigate briefly for the possibility of combining the two latter detections devices. All detection devices are presented in Fig. 1.10.

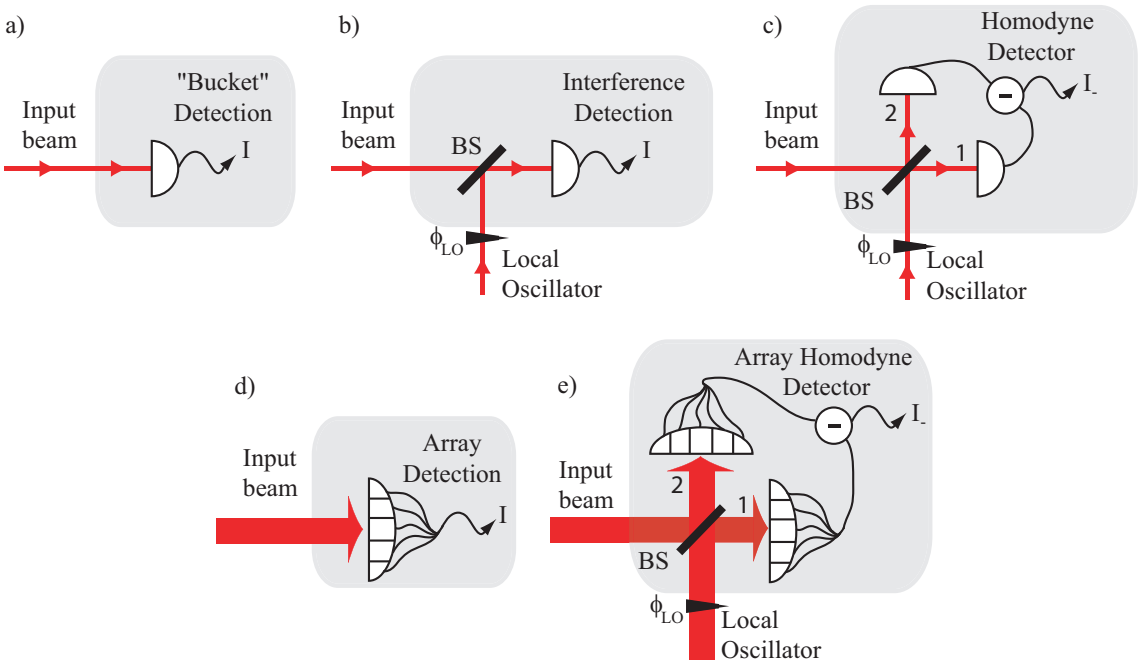

Figure 1.10: Optical detection devices. a) "Bucket" detection. b) Interference detection. c) Homodyne detection. d) Array detection. e) Homodyne array detection. (BS) 50/50 beamsplitter.

In this section, we will always assume a prefect detection efficiency, i.e. that we consider that each photon impinging on the detector creates an electron. The photo-current is reproducing exactly the number of created electrons, and hence the intensity of the incident beam.

Before detailing each detection device, let us introduce the notion of *noise mode of detection*.

C.1 Noise-modes of detection

When a measurement is performed on an optical image, a single parameter within the image is interrogated. The measurement of this parameter, which can be for instance the

beam intensity, position, or rotation, is characterized by a single number. It seems thus reasonable to expect the detection to extract an optical information and its corresponding noise from a single mode within the optical image. This mode does depend on the detection device, and we therefore term it *noise-mode of detection*. This concept was first introduced in reference [Delaubert06,1].

The concept introduced here is very general. For any type of detection, a single spatial mode contributes to the detected signal and noise. The information encoded in any other mode orthogonal to the *noise-mode of detection* is thus undetected.

This apparently very simple result is of most importance for the detection of spatial parameters within an optical image. The identification of the only transverse mode which is contributing to the measurement noise notably allows to match the detection system to the spatial information that we want to extract from the light beam. It also allows to modify the fluctuation properties of specific modes within the input beam in order to improve the signal-to-noise ratio of the detection. Indeed, filling the *noise-mode of detection* with squeezed light within the incident beam is a necessary and sufficient condition to reduce the noise related to the measurement[47].

C.2 "Bucket" detection

The "bucket" detector measures the intensity of the incident beam integrated over the entire transverse plane as shown on Fig.1.10a), and thus gives access to the beam power $\hat{P}$, and the total number of photons $\hat{N}$.

Although it corresponds to the simplest possible optical detection, it is still interesting to briefly study the properties of its measured noise. We will especially focus on the spatial modes within the optical beam that are contributing to it.

For any optical image incident on the photo-detector, the field can be described by Eq.1.27. It yields in the detector plane

$$\hat{\mathcal{E}}^{(+)}(\vec{r}) = i\sqrt{\frac{\hbar\omega_0}{2\epsilon_0 cT}}\sum_{n=0}^{\infty}\hat{a}_n u_n(\vec{r}). \tag{1.105}$$

Using the field expansion in the eigenmode basis defined in proposition 2, for which the mean field lies in mode u_0, the operator describing the total number of photons detected over the entire transverse plane during the time interval T is

$$\hat{N} = \frac{2\epsilon_0 cT}{\hbar\omega_0}\int_{-\infty}^{\infty}\hat{\mathcal{E}}^{(+)^\dagger}(\vec{r})\hat{\mathcal{E}}^{(+)}(\vec{r})dr^2 = \sum_{n,k}\hat{a}_n^\dagger\hat{a}_k\Gamma_{nk} = \sum_n\hat{a}_n^\dagger\hat{a}_n, \tag{1.106}$$

where we have used the spatial modal overlap integral Γ_{nk} defined by

$$\Gamma_{nk} = \int_{-\infty}^{\infty}u_n^*(\vec{r})u_k(\vec{r})dr^2 = \delta_{n,k}, \tag{1.107}$$

and the orthonormality relation satisfied by the spatial modes, as presented in Eq. 1.23.

The mean number of photons is thus

$$\langle\hat{N}\rangle \quad = \quad \sum_{n=0}^{\infty}\langle\hat{a}_n^\dagger\hat{a}_n\rangle = N \tag{1.108}$$

[47] The proof of this statement directly arises from the definition of the *noise-mode of detection*.

where we have used that $\langle \hat{a}_n^\dagger \hat{a}_n \rangle = |\alpha_n|^2 \delta_{n,0} = N$, where N is the total number of photons detected in the mean field (see section 1A.2).

Let us now introduce the linearization approximation, for which the modal annihilation operators and their fluctuations introduced in Eq. 1.28 are such that $\langle \hat{a}_n \rangle \ll \delta \hat{a}_n$. [48]

The fluctuation operator of the number of photons is given at first order in the linearization approximation by

$$\delta \hat{N} = \sum_{n=0}^{\infty} \alpha_n (\delta \hat{a}_n^\dagger + \delta \hat{a}_n) = \sqrt{N} \delta \hat{X}_0^+ \tag{1.109}$$

The detection noise is finally given by

$$\langle \delta \hat{N}^2 \rangle = N \langle \delta \hat{X}_0^{+^2} \rangle \tag{1.110}$$

It shows that mean number of photons - which we can call the signal - and the measurement noise both arise *solely* from the mean field mode[49].

For a "bucket" detection of the field, the *noise-mode of detection*, defined in section 1 C.1, thus corresponds to the mean field mode.

C.3 Interference detection

The previous detector only allows global intensity measurements. A first idea in order to access some information on the image profile would be to combine the image - the incident beam on Fig.1.10b) - with a reference beam on a 50/50 beam-splitter. We will call this reference beam, whose profile is well defined, the *local oscillator*.

Let us analyze the classical detection of the interferences between an input field and a local oscillator whose mean fields are respectively described by

$$\langle \hat{\mathcal{E}}^{(+)}(\vec{r}) \rangle = i \sqrt{\frac{\hbar \omega_0}{2 \epsilon_0 c T}} \alpha_0 u_0(\vec{r}) \tag{1.111}$$

$$\langle \hat{\mathcal{E}}_{LO}^{(+)}(\vec{r}) \rangle = i \sqrt{\frac{\hbar \omega_0}{2 \epsilon_0 c T}} \alpha_{LO} u_{LO}(\vec{r}) \tag{1.112}$$

where u_0 and u_{LO} respectively correspond to the input and local oscillator mean field profile. Denoting N_0 and N_{LO} the number of photons in each beam and taking the input beam as a phase reference[50], we can write $\alpha_0 = \sqrt{N_0}$ and $\alpha_{LO} = \sqrt{N_{LO}} e^{i\theta_{LO}}$, where θ_{LO} is the phase of the local oscillator beam, as shown on Fig.1.10b). The mean value of the detected intensity I is therefore given by

$$I = \frac{\hbar \omega_0}{4 \epsilon_0 c T} \left[N_0 + N_{LO} + 2\Gamma \sqrt{N_0 N_{LO}} \cos \theta_{LO} \right] \tag{1.113}$$

[48] This approximation is generally fulfilled in most continuous variables (CV) quantum optics experiments. Nevertheless, it is sometimes necessary to go beyond this approximation for example when vacuum states are considered, or other particular cases as the optical parametric oscillation near threshold [Dechoum04].

[49] This result explains why the common description of the field in quantum optics, where the positive frequency part is given by $\hat{\mathcal{E}}^{(+)} = i\sqrt{\frac{\hbar\omega_0}{2\epsilon_0 cT}}\hat{a}$ is perfectly valid as long as one detects the total beam power. Any noises present in other modes than the mean field are not detected, and hence does not necessarily need to be described. However, they will be of most importance in the experiment presented in this thesis, as we will notably consider partial detection of the field, hence also interrogating other spatial modes.

[50] Note that a calibration of the local oscillator phase could potentially lead to phase measurements of the incident beam using Eq 1.113.

where Γ is the spatial overlap between the input mean field and the local oscillator mean field, and is defined by

$$\Gamma = \int_{-\infty}^{\infty} u_0^*(\vec{r}) u_{LO}(\vec{r}) d^2r \tag{1.114}$$

Some interesting information on the mode quality can be extracted from this measurement. First, in the case of two incident beams of equal optical power, i.e. $N_0 = N_{LO}$, the optimal fringe visibility yields the "spatial purity" of the input beam relative to the local oscillator profile. Indeed, the fringe visibility identifies with the spatial overlap coefficient Γ, as shown by[51]

$$V = \frac{I_{max} - I_{min}}{I_{max} + I_{min}} = \Gamma \tag{1.115}$$

This can notably be useful in order to see the spatial modification of a given transverse mode after propagation or after amplification with a non linear device as will be discussed in chapters 4 and 5.

C.4 Homodyne Detection

The homodyne detection is widely used in quantum optics as it allows quadrature measurements, as a result of interferences between an incident beam and a bright beam called *local oscillator* on a 50/50 beam-splitter, similar to the one defined in the previous section. The difference between the intensity detected on both output ports of the beam-splitter yields the quadrature information. The detection scheme is presented in Fig.1.10c).

We detail here how a homodyne detection can measure any quadrature of any transverse mode of the incoming beam, according to the phase and profile of the local oscillator beam (LO).

The electric field operator to be detected, denoted as "input beam" in Fig.1.10c) can be described as in Eq.1.27, by[52]

$$\hat{\mathcal{E}}^{(+)}(\vec{r}) = i\sqrt{\frac{\hbar\omega_0}{2\epsilon_0 cT}} \sum_{n=0}^{\infty} \hat{a}_n u_n(\vec{r}). \tag{1.116}$$

We introduce the local oscillator field operator in the same basis[53]

$$\hat{\mathcal{E}}_{LO}^{(+)}(\vec{r}) = i\sqrt{\frac{\hbar\omega_0}{2\epsilon_0 cT}} \sum_{n=0}^{\infty} \hat{a}_{LO,n} u_n(\vec{r}). \tag{1.117}$$

[51] We can generalize the definition of the fringe visibility in the case of the interference of two beams of different optical power by $V' = \frac{I_{max} - I_{min}}{2\sqrt{N_0 N_{LO}}}$. Using the expression of the intensity given in Eq.1.113 with the previous definition gives $V' = \Gamma$. The fringe visibility is thus still measurable when one of the beams is much brighter than the other one. This is especially interesting to characterize the mode purity of the very dim squeezed beam coming out of an optical parametric amplifier (OPA), as will be detailed in chapter 4.

[52] Note that there is here no restriction on the choice of the transverse basis. In particular, the mean field is not necessarily filling only the first mode as presented in proposition 2.

[53] Strictly speaking, the basis used to describe the LO cannot be identical to the previous one, as input field and LO beam are contained in orthogonal planes before the beam-splitter, as represented in Fig. 1.10. However, after the beam-splitter, the propagation axis is identical for both beams and they can be described in the same basis. Not to complicate our equations uselessly, we will therefore not distinguish the two basis as long as the spatial variation of the modes are identical in a given plane.

The two uncorrelated field operators described by Eq.1.116 and 1.117 are combined on a 50/50 beam-splitter. The two output field operators, indexed 1 and 2 as in Fig. 1.10c), are given by

$$\begin{aligned}\hat{\mathcal{E}}_1^{(+)}(\vec{r}) &= \frac{\hat{\mathcal{E}}^{(+)}(\vec{r}) + \hat{\mathcal{E}}_{LO}^{(+)}(\vec{r})}{\sqrt{2}} \\ &= i\sqrt{\frac{\hbar\omega_0}{2\epsilon_0 cT}}\sum_{n=0}^{\infty}\left[\frac{\hat{a}_n + \hat{a}_{LO,n}}{\sqrt{2}}u_n(\vec{r})\right], \qquad (1.118)\\ \hat{\mathcal{E}}_2^{(+)}(\vec{r}) &= \frac{\hat{\mathcal{E}}^{(+)}(\vec{r}) - \hat{\mathcal{E}}_{LO}^{(+)}(\vec{r})}{\sqrt{2}} \\ &= i\sqrt{\frac{\hbar\omega_0}{2\epsilon_0 cT}}\sum_{n=0}^{\infty}\left[\frac{\hat{a}_n - \hat{a}_{LO,n}}{\sqrt{2}}u_n(\vec{r})\right], \qquad (1.119)\end{aligned}$$

where we have used a particular convention for the beam-splitter output field, which will always be used throughout this thesis. Note that other conventions can be adopted [Bachor03].

Both fields are then detected by "bucket" detectors. We assume that the phase curvature of the beams in the detector planes is small, i.e. that the detection is done close to the waist position. Focusing now on the intensity operator of beam 1, we get

$$\begin{aligned}\hat{I}_1 &= \int_{-\infty}^{\infty}\hat{\mathcal{E}}_1^{(+)\dagger}(\vec{r})\hat{\mathcal{E}}_1^{(+)}(\vec{r})d^2r \\ &= \frac{\hbar\omega_0}{4\epsilon_0 cT}\sum_{n,k}\left[(\hat{a}_n^\dagger + \hat{a}_{LO,n}^\dagger)(\hat{a}_k + \hat{a}_{LO,k})\int_{-\infty}^{\infty}u_n^*(\vec{r})u_k(\vec{r})d^2r\right], \qquad (1.120)\end{aligned}$$

where we recognize the overlap integral Γ_{nk} given in Eq.1.107. It yields for both beams

$$\hat{I}_1 = \frac{\hbar\omega_0}{4\epsilon_0 cT}\sum_{n=0}^{\infty}\left[\hat{a}_n^\dagger\hat{a}_n + \hat{a}_n^\dagger\hat{a}_{LO,n} + \hat{a}_{LO,n}^\dagger\hat{a}_n + \hat{a}_{LO,n}^\dagger\hat{a}_{LO,n}\right], \qquad (1.121)$$

$$\hat{I}_2 = \frac{\hbar\omega_0}{4\epsilon_0 cT}\sum_{n=0}^{\infty}\left[\hat{a}_n^\dagger\hat{a}_n - \hat{a}_n^\dagger\hat{a}_{LO,n} - \hat{a}_{LO,n}^\dagger\hat{a}_n + \hat{a}_{LO,n}^\dagger\hat{a}_{LO,n}\right]. \qquad (1.122)$$

The difference between these two operators, denoted $\hat{I}_-$, which is the quantity measured experimentally, can be written

$$\hat{I}_- = \frac{\hbar\omega_0}{2\epsilon_0 cT}\sum_{n=0}^{\infty}\left[\hat{a}_n^\dagger\hat{a}_{LO,n} + \hat{a}_{LO,n}^\dagger\hat{a}_n\right] \qquad (1.123)$$

Using the fluctuations operators defined in section 1 A.1.1, it becomes

$$\hat{I}_- = \frac{\hbar\omega_0}{2\epsilon_0 cT}\sum_{n=0}^{\infty}\left[(\alpha_n^* + \delta\hat{a}_n^\dagger)(\alpha_{LO,n} + \delta\hat{a}_{LO,n}) + (\alpha_{LO,n}^* + \delta\hat{a}_{LO,n}^\dagger)(\alpha_n + \delta\hat{a}_n)\right]$$

Let us now consider the case of a local oscillator beam whose mean field profile is described by the transverse mode u_k, i.e. $\alpha_{LO,n} = \delta_{n,k}\sqrt{N_{LO}}e^{i\theta_{LO}}$[54], where N_{LO} is the

[54] θ_{LO} does not depend on the transverse position $\vec{r}$ as we have assumed that the wave front was plane in the detector plane.

number of photons detected during T in the LO beam, and where θ_{LO} is the local oscillator longitudinal phase, which is typically experimentally controlled with a piezoelectric device (PZT). The mean value of the intensity difference is in this case

$$\langle \hat{I}_- \rangle = \frac{\hbar\omega_0}{2\epsilon_0 cT} 2\sqrt{N_{LO} N_k}\cos(\theta_{LO}), \tag{1.124}$$

where N_k is the number of photons present in mode u_k of the input beam[55]. It is important to note here that the only component of the input beam contributing to $\langle \hat{I}_- \rangle$ is the one defined by the profile of the local oscillator[56].

In order to provide a noise reference[57], the LO beam is chosen experimentally much brighter than the input beam, i.e. such as $N_{LO} \gg N$. The quantum fluctuations at first order on the intensity difference, in the linearization approximation defined in section C.2 are given by

$$\delta\hat{I}_- = \frac{\hbar\omega_0}{2\epsilon_0 cT}\sqrt{N_{LO}}(\hat{a}_k^\dagger e^{i\theta_{LO}} + \hat{a}_k e^{-i\theta_{LO}}) = \frac{\hbar\omega_0}{2\epsilon_0 cT}\sqrt{N_{LO}}\delta\hat{X}_k^{\theta_{LO}}, \tag{1.125}$$

where we have used the definition of the quadrature of angle θ_{LO} introduced in Eq.1.31.

The noise on the intensity difference is finally given by approximation presented in Eq.1.28,

$$\langle \delta\hat{I}_-^2 \rangle = \left(\frac{\hbar\omega_0}{2\epsilon_0 cT}\right)^2 N_{LO}\langle \delta\hat{X}_k^{\theta_{LO}\,2}\rangle. \tag{1.126}$$

Again, only the mode selected by the local oscillator profile is contributing to the noise. Moreover, it is interesting to note here that the shot noise level, defined for $\langle \delta\hat{X}_k^{\theta_{LO}\,2}\rangle = 1$, is independent of the power of the input beam[58].

The previous results show the importance of homodyne detection for the study of quantum optical images. Signal - i.e. mean detected value - and noise contributions arise only from *one single mode* within the input beam, which can be selected at will by the local oscillator profile. Moreover, for each mode, the analyzed noise quadrature can easily be varied by tuning the LO phase. Homodyne detection therefore acts as a *projection of the input beam on a particular quadrature of a particular mode determined by the local oscillator phase and mode, respectively.*

Using the concept introduced in section 1 C.2, we can state that when a measurement is performed with a homodyne detector, the *noise-mode of detection* is the mode defined by the local oscillator.

C.5 Array Detection

We now consider intensity measurements of an optical beam with an array detector, where the electronic gain of each pixel is individually tunable, as represented in Fig. 1.10d). Such

[55] We recall that the quadratures, and thus the phases of each components, are defined relative to the mean field, i.e. $\alpha_k = \sqrt{N_k}e^{i\theta_k}$. Each component can thus have a different phase.

[56] In particular, it is not necessarily the mean field.

[57] This can be clearly understood by looking at Eq.1.126 obtained later on, where the shot noise is defined solely relative to the local oscillator beam.

[58] This results from the approximation $N_{LO} \gg N$, and is not the case for comparable LO and input beam powers.

detection device allows to explore the complexity of optical images, thanks to the many degrees of freedom offered by the gain distribution on all the pixels. Depending on the need, there exist many ways to extract an information coded into an image intensity distribution in the transverse plane [Jain89, Katsaggelos91, Bertero98]. The extraction of the pertinent information generally arises from the numerical computation of a function $F\left(I(D_1), I(D_2), ..., I(D_n)\right)$ of the intensities $I(D_i)$ $(i = 1, ..., n)$ measured on each pixel D_i. To simplify the following discussion, we will restrict ourselves to the *linear* case. It is often encountered in real situations, for example when one wants to determine the spatial Fourier components of an image, or when the variations of the parameter to measure are small enough so that the function F can be linearized.

The most simple configurations - split-detector and quadrant-detector - are well known, and widely used. We will often refer to these cases, which have been extensively studied in our group in order to measure very small displacements of a laser beam. We propose here a generalization of the results obtained in the following references [Treps02, Treps03, Treps04,1], not limited to split and quadrant detections.

We first briefly define here the processed signal, and then present in the next sections the interesting properties and applications of what is referred to as *difference measurements*. Finally we will give some more general results on linear measurement using an array detector. Most of the work presented here has been published in reference [Treps05].

C.5.1 Measured signal

An array detector will be described in its most general configuration by a set of pixels, each of whom occupying a transverse area D_i, and measuring the optical power on this area. The detectors will be assumed to cover the entire transverse plane, with no overlap between each of them. Each photo-detector delivers a power given by

$$\hat{I}(D_i) = 2\epsilon_0 cT \int_{D_i} \hat{\mathcal{E}}^{(+)\dagger}(\vec{r})\hat{\mathcal{E}}^{(+)}(\vec{r})d^2r \tag{1.127}$$

where T is the integration time, assumed to be identical for all detectors. The quantum field operator Eq. 1.127 can also be written in photons per second as

$$\hat{N}(D_i) = \frac{2\epsilon_0 cT}{\hbar\omega_0} \int_{D_i} \hat{\mathcal{E}}^{(+)\dagger}(\vec{r})\hat{\mathcal{E}}^{(+)}(\vec{r})d^2r. \tag{1.128}$$

In the following, we will use the expansion of the positive frequency part of the field $\hat{\mathcal{E}}^{(+)}(\vec{r})$ in any transverse basis[59], written in the detection plane (see Eq. 1.27)

$$\hat{\mathcal{E}}^{(+)}(\vec{r}) = i\sqrt{\frac{\hbar\omega_0}{2\epsilon_0 cT}} \sum_n \hat{a}_n u_n(\vec{r}). \tag{1.129}$$

The quantum operator describing the number of photons incident on pixel i, previously introduced in Eq. 1.128 can thus be rewritten

$$\hat{N}(D_i) = \sum_{i,j} \hat{a}_i^\dagger \hat{a}_j \int_{D_i} u_i^*(\vec{r})u_j(\vec{r})d^2r \tag{1.130}$$

[59] The field does not need to be written in its eigenbasis at this stage.

A given information will be extracted from an image through the computation of a definite function of the intensities measured by each pixel. We assume this function to be linear and we define a measurement by :

$$\hat{M}(\{g_i\}) = \sum_i g_i \hat{I}(D_i) \quad \text{such as } g_i \in \mathbb{R} \tag{1.131}$$

or again in terms of number of photons per second :

$$\hat{N}(\{g_i\}) = \sum_i g_i \hat{N}(D_i) \tag{1.132}$$

where g_i corresponds to the electronic gain of detector i.

C.5.2 Difference measurements

- Description

The first type of measurement we consider consists in recording the difference between the intensities on transverse areas of the field[60], which are such as

$$\langle \hat{N}(\{g_i\}) \rangle = 0, \tag{1.133}$$

where we have used the notations introduced in the previous section. We call such a measurement, whose mean value is zero, a *difference measurement*. It has high experimental relevance. We have proven in appendix A.1 that difference measurements was the an optimal gain configuration in the two-zone detection case.

A direct consequence arising from the definition is that any difference measurement yields a cancelation of what is termed the "common mode noises", i.e. the noises which have the same distribution as the mean field. Such noises are directly proportional to the detected intensity and will therefore cancel for a difference measurement. They for example arise from classical intensity fluctuations of the light source.

This simple technique of noise cancelation is used to measure for example very small absorptions [SoutoRibeiro97] by inserting the absorbing medium in the path of one of the detection areas. It is also extensively used in multi-pixel measurements, either with split-detectors or quadrant detectors, to measure sub-micrometer displacements, for example of nano-scale fluorophores in biological samples [Tisher01], for Atomic Force Microscopy [Senden01], and for ultra-small absorptions by the mirage effect [Boccara80].

However, the detailed analysis of the origin of quantum noise in multi-pixel detectors has been investigated only for the most simple configurations, i.e. for split-detectors and quadrant detectors, for which it has been investigated theoretically [Fabre00] and experimentally [Treps02, Treps03, Treps04,1]. This work, done previously in our group, led to the identification of a particular transverse mode called the *flipped mode* which was identified as the only spatial mode contributing to the noise altering a gaussian beam position measurement. Squeezing this component within the incident field has allowed a reduction of the measurement noise, and hence an improvement of the detection sensitivity for displacement measurement.

[60] Note that even if the detection areas are not paving the entire plane, we can still consider its full description by virtually adding detectors with null gain to complete it. Moreover, the different detection areas can even be physically separated, for example using a 50/50 beam-splitter.

What we propose here is to extend this quantum study to an array of arbitrary shaped detectors, still for *difference measurements* first. Of course, this kind of measurement is strongly field dependent, as the detector is adapted to the field used in the measurement. For instance, in the case of small displacement measurement of a gaussian beam with a split-detector, the beam must be centered on the detector, in order to qualify as a *difference measurement*. The quantum limits then also depend on the position and shape of the incident field. It is necessary first to consider which image we want to characterize, and then consider the limitations in its characterization.

- Single difference measurement with two "detectors"

Let us begin with the description of simplest difference measurement : a difference between the intensities on two areas[61] of the transverse plane, which means that $g_i = \pm 1$. This configuration corresponds for instance to split-detection or quadrant-detection. If one consider such a difference measurement performed with a coherent state, which has spatially uncorrelated quantum fluctuations, the noise arising from the measurement will not depend on the choice of $\{g_i\}$ if $g_i = \pm 1$, and will be equal to the square root of the total number of photons [TrepsPhD01]. This corresponds to the shot noise, as detailed in section 1 A.3.2. In the general case, in order to compute the noise, an analysis equivalent to the one performed in the case of a small displacement measurement, as done in reference [Fabre00], is necessary. We recall it here and extend it to the general case of transverse modes of any shape, in order to show the following proposition :

Proposition 3 *The noise on a difference measurement performed on an optical beam originates from a single mode, orthogonal to the mean field : the "flipped mode". In order to reduce the noise in that measurement, it is necessary and sufficient that the flipped mode component is a squeezed state.*

In order to perform the general noise calculation, let us define the two "detectors" :

$$\begin{aligned} D_+ &= \bigcup_{i,g_i=+1} D_i \\ D_- &= \bigcup_{i,g_i=-1} D_i \end{aligned} \tag{1.134}$$

which gives, using Eq. 1.130

$$\begin{aligned} \hat{N}_- &= \hat{N}(D_+) - \hat{N}(D_-) \\ &= \sum_{i,j} \hat{a}_i^\dagger \hat{a}_j \left[\int_{D_+} u_i^*(\vec{r}) u_j(\vec{r}) d^2r - \int_{D_-} u_i^*(\vec{r}) u_j(\vec{r}) d^2r \right] \end{aligned} \tag{1.135}$$

Considering the quantum fluctuations operators $\delta\hat{a}_i = \hat{a}_i - \langle \hat{a}_i \rangle$, the fluctuations of $\hat{N}_-$ are, at first order in the linearization approximation

$$\begin{aligned} \delta\hat{N}_- &= \hat{N}_- - \langle \hat{N}_- \rangle \\ &= \sum_i \left[\delta\hat{a}_i^\dagger C_-^i + \delta\hat{a}_i C_-^{i*} \right] \end{aligned} \tag{1.136}$$

[61] Both areas can consist of several non-joined parts, as in the case of the quadrant detector.

with C_-^i defined as

$$\begin{aligned} C_-^i &= \sum_j \langle \hat{a}_j \rangle \Big[\int_{D_+} u_i^*(\vec{r}) u_j(\vec{r}) d^2r - \int_{D_-} u_i^*(\vec{r}) u_j(\vec{r}) d^2r \Big] \\ &= -i\sqrt{\frac{2\epsilon_0 cT}{\hbar\omega_0}} \left[\int_{D_+} u_i^*(\vec{r}) \langle \hat{\mathcal{E}}^{(+)}(\vec{r}) \rangle d^2r - \int_{D_-} u_i^*(\vec{r}) \langle \hat{\mathcal{E}}^{(+)}(\vec{r}) \rangle d^2r \right] \end{aligned} \quad (1.137)$$

and where $\langle \hat{\mathcal{E}}^{(+)}(\vec{r}) \rangle = i\sqrt{\frac{\hbar\omega_0}{2\epsilon_0 cT}} \sum_j \langle \hat{a}_j \rangle u_j(\vec{r})$ is the mean value of the positive frequency part of the electric field operator. Hence, the C_-^i coefficients are the partial overlap integrals between the modes u_i and the mean field.

We can now compute the noise related to this measurement :

$$\langle \delta \hat{N}_-^2 \rangle = \sum_i |C_-^i|^2 \quad + \quad \left[\sum_{i,j} \langle \delta\hat{a}_i^\dagger \delta\hat{a}_j^\dagger \rangle C_-^i C_-^j + \langle \delta\hat{a}_i^\dagger \delta\hat{a}_j \rangle C_-^i C_-^{j*} + c.c. \right] \quad (1.138)$$

This shows that the noise related to this measurement arises a priori from all the modes.

We will now demonstrate that the noise comes in fact from a single mode when we write $\langle \delta \hat{N}_-^2 \rangle$ in the appropriate basis.

We call v_0 the amplitude[62] of the mode carrying the mean field as defined in section 1 A.2.4, such as

$$\langle \hat{\mathcal{E}}^{(+)}(\vec{r}) \rangle = i\sqrt{\frac{\hbar\omega_0}{2\epsilon_0 cT}} \sqrt{N} v_0(\vec{r}) \quad (1.139)$$

where the mean number of photons in the entire field will be denoted N. Let us define an eigen-basis[63] of the field, using v_0 as the first mode of the basis. The mean value of the electric field in all the other modes will therefore be zero. We define the real mode v_1, which we will refer to as the "flipped mode" of v_0, such as :

$$\begin{aligned} v_1(\vec{r}) &= v_0(\vec{r}) \quad \text{if } r \in D_+ \\ v_1(\vec{r}) &= -v_0(\vec{r}) \quad \text{if } r \in D_- \end{aligned} \quad (1.140)$$

A one-dimensional example of a *flipped mode* is presented in Fig. 1.11 for a gaussian TEM_{00} mean field illumination, and where D_- and D_+ respectively correspond to the left and right half of the transverse plane, i.e. to a split-detection[64]. The profile is in this case a TEM_{00} with a π phase flip in its center [Delaubert02].

A very important property of the mode defined in Eq.1.140 is its orthogonality to the mean field. Using Eq. 1.135, the mean value of the total measurement is

$$\begin{aligned} \langle \hat{N}_- \rangle &= N \Big[\int_{D_+} v_0(\vec{r}) v_0(\vec{r}) d^2r - \int_{D_-} v_0(\vec{r}) v_0(\vec{r}) d^2r \Big] \\ &= N \int_D v_0(\vec{r}) v_1(\vec{r}) d^2r = 0, \end{aligned} \quad (1.141)$$

[62] As the array detector is only sensitive to the mean intensity of the field and not to the phase of the mean field, we choose to take into account only the amplitude of the light field. v_0 is thus a real mode profile.

[63] See proposition 2.

[64] Note that this particular case has been extensively studied in reference [TrepsPhD01]. We will also detail the experimental relevance of this flipped mode in the following.

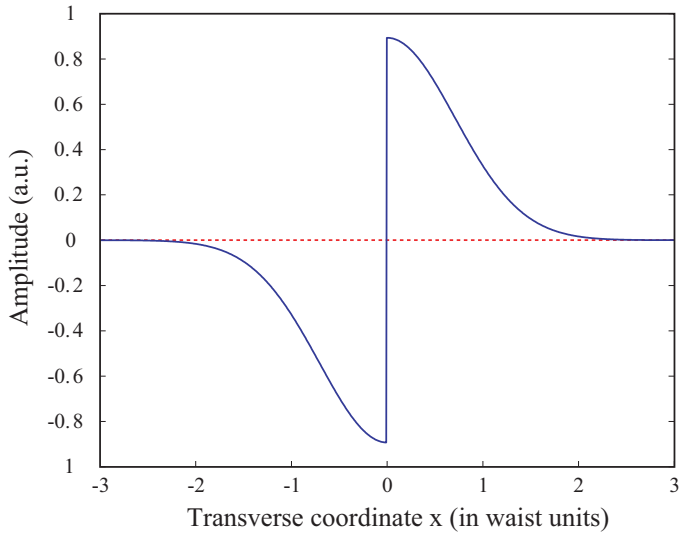

Figure 1.11: Flipped mode in the case of a TEM_{00} illumination on a split-detector.

where we have used the expression flipped mode defined in Eq. 1.140, and where we have added that $\langle \hat{N}_- \rangle = 0$, as we deal with a *difference measurement*. Hence, we get $\int_D v_0(\vec{r}) v_1(\vec{r}) d^2r = 0$, where the integration spans here over the entire transverse plane. This proves that v_1 is orthogonal to v_0. It is thus possible to find a real basis $\{v_i, \hat{b}_i\}$ where v_0 and v_1 are the two first modes. In that basis, the overlap integrals defined in Eq. 1.137 become :

$$\begin{aligned} C_-^i &= \sqrt{N}\Big[\int_{D_+} v_i(\vec{r}) v_0(\vec{r}) d^2r - \int_{D_-} v_i(\vec{r}) v_0(\vec{r}) d^2r\Big] \\ &= \sqrt{N}\int_D v_i(\vec{r}) v_1(\vec{r}) d^2r \\ &= \sqrt{N}\delta_{i,1}. \end{aligned} \tag{1.142}$$

These integrals are different from zero only for the flipped mode. The noise defined in Eq. 1.138 thus becomes

$$\langle \delta\hat{N}_-^2 \rangle = N\left[1 + \langle \delta\hat{b}_1^{\dagger 2} \rangle + \langle \delta\hat{b}_1^2 \rangle + \langle \delta\hat{b}_1^\dagger \delta\hat{b}_1 \rangle + \langle \delta\hat{b}_1 \delta\hat{b}_1^\dagger \rangle\right], \tag{1.143}$$

and ordering terms in the natural order yields

$$\begin{aligned} \langle \delta\hat{N}_-^2 \rangle &= N\langle : (\delta\hat{b}_1^\dagger + \delta\hat{b}_1)^2 : \rangle \\ &= N\langle \delta\hat{X}_1^{+2} \rangle \end{aligned} \tag{1.144}$$

where N represents the shot noise, i.e. the noise level obtained for a coherent illumination, for which $\langle \delta\hat{X}_1^{+2} \rangle = 1$. This calculation shows that, for a difference measurement with two "detectors", the noise in the measurement is exactly the one of the flipped mode of v_0 which is in phase with the mean field mode, and does not arise from any other mode. It is therefore here the *noise-mode of detection*, as defined in section 1 C.2. Changing the noise properties of the flipped mode is then the only way to change the noise in the measurement. Filling this mode with squeezed light is thus a necessary and sufficient condition to

improve the measurement relative to the quantum noise limit. This demonstrates proposition 3. Note that the result given in Eq. 1.144 involves the noise of only one quadrature of the flipped mode. Therefore, the conjugate quadrature of the flipped mode can be filled with large anti-squeezing noise without increasing the measurement noise. Moreover, all the other modes do not contribute either, and can be in any state. Note that there is not only one practical solution to the improve the measurement below the quantum noise limit[65].

In order to summarize our results, we present below a definition of a perfect difference measurement, which can be shown to be valid not only in the two-zone case, but for any difference measurement[66].

Proposition 4 *In order to improve the sensitivity of a difference measurement, it is necessary to use a non-classical multi-mode beam of degree superior or equal to 2. A two mode beam is a perfect solution of the problem if and only if it can be described in a transverse mode basis* $\{\hat{a}_i, v_i\}$ *such as :*

- v_0 *is proportional to the electric field profile of the beam, it is then the only non-vacuum mode.*
- v_1 *is the flipped mode of the measurement defined by Eq. 1.140.*
- *all the modes, apart from* v_0 *and* v_1*, are vacuum states (i.e. it is an eigen-basis of the field).*
- *the noise of the flipped mode, in the quadrature homodyned by the main mode, is perfectly squeezed.*

We have demonstrated which mode one needs to fill with squeezed light in order to perform a single difference measurement on a beam. We can now extend this analysis to the case of several difference measurements.

- Multiple difference measurement with two "detectors"

Let us consider n difference measurements of the type of equation (1.133). We will assume that these measurements are independent, which means that none of them is a linear combination of the other ones. One can show that the corresponding flipped modes are then also linearly independent. We have shown that in order to improve simultaneously the sensitivity of all these measurements, it is necessary and sufficient to fill all these flipped modes with squeezed light. Practically these modes are in general not orthogonal, but one can find an orthogonal basis of the subspace generated by these modes. Injecting squeezed vacuum states in each of these modes will result in squeezed states in each of the flipped modes.

[65] A *locally squeezed* state would yield the same result. However, the cost in resources is enormous compared to the requirement of a single squeezed state.

[66] We have chosen here to limit our analysis to 2 detection zones in order to highlight the properties of difference measurements more clearly. All the results presented here are still valid for any number of pixels, with gains different from $g_i = \pm 1$. The general case of the difference measurement is in fact a particular case of *linear measurement* presented in section C.5.3, from which results it can be proven that any difference measurement satifies proposition 4.

Regarding the degree of the beam necessary to improve simultaneously all the measurements, it is clear that in order to perfectly squeeze all the flipped modes, a beam of degree $n+1$ is necessary (and sufficient). We can summarize all the considerations of section 1 C.5.2 into a proposition :

Proposition 5 *In order to reduce the noise simultaneously in n independent difference measurements it is necessary and sufficient to use a beam of degree at least n+1 that can be described in a transverse mode basis $\{\hat{a}_i, u_i\}$ such as : u_0 is proportional to the electric field profile of the beam; $\{u_i\}_{0<i\leq n}$ is the basis of the space-vector generated by the flipped modes of the measurements and all these modes are perfectly squeezed.*

It is interesting to note that this proposition involves only the noise of a single quadrature of each flipped mode. All the other parameters (noise of the other quadrature, of the remaining modes,...) are not relevant for these specific measurements[67].

C.5.3 General linear measurement

Difference measurements are obviously not the only ones performed in image processing [Jain89, Katsaggelos91, Bertero98].

We consider now a general linear measurement of the optical field. In the formalism of Eq. 1.131 and 1.132, it means that the electronic gains g_i can now take any real value and are not restricted to ± 1 anymore. A measurement is now defined by

$$\begin{aligned} \hat{M}(\{g_j\}) &= \sum_j g_j \hat{I}(D_j) \\ \hat{N}_g &= \sum_j g_j \hat{N}(D_j) \end{aligned} \tag{1.145}$$

We emphasize that, unlike in the previous section, the mean value of the measurement is not necessarily zero. In that case, we will show the following proposition :

Proposition 6 *Considering a field described in an eigenbasis $\{\hat{b}_i, v_i\}$, and considering a linear measurement performed with and array of detectors D_i, each detector having a gain g_i, the noise on the measurement $\hat{N}_g = \sum_j g_j \hat{N}(D_j)$ arises only from the generalized flipped mode w defined by :*

$$\forall \vec{r},\ \vec{r} \in D_i \ \Rightarrow\ w_1(\vec{r}) = \frac{1}{f} g_i v_0(\vec{r}) \tag{1.146}$$

where f is a normalization factor, and $v_0(\vec{r})$ is the mode carrying the mean field.

Here, there is not much sense in defining the positive and negative gain domains. We can however extend the notion of overlap integral between a basis vector and the mean field, as defined in Eq. 1.137 :

$$C_g^i = -i\sqrt{\frac{2\epsilon_0 cT}{\hbar\omega_0}} \sum_j g_j \int_{D_j} u_i^*(\vec{r}) \langle \hat{\mathcal{E}}^{(+)}(\vec{r}) \rangle d^2 r \tag{1.147}$$

[67] Our proposition corresponds to the minimal resources necessary to have a perfect measurement. However, more complex states can be used, with the same performances, such as *locally squeezed* beams.

which leads to the following expression, equivalent to Eq. 1.138

$$\langle \delta \hat{N}_g^2 \rangle = \sum_i |C_g^i|^2 \quad + \quad \left[\sum_{i,j} \langle \delta \hat{a}_i^\dagger \delta \hat{a}_j^\dagger \rangle C_g^i C_g^j + \langle \delta \hat{a}_i^\dagger \delta \hat{a}_j \rangle C_g^i C_g^{j*} + c.c. \right] \tag{1.148}$$

Recalling that $\langle \hat{\mathcal{E}}^{(+)}(\vec{r}) \rangle = i\sqrt{\frac{\hbar\omega_0}{2\epsilon_0 cT}}\sqrt{N} v_0(\vec{r})$, we can also extend the notion of *flipped mode* introduced in Eq.1.140 and define a *generalized flipped mode*, or a *noise-mode of detection* by

$$\forall \vec{r},\ \vec{r} \in D_i \ \Rightarrow\ w_1(\vec{r}) = \frac{1}{f} g_i v_0(\vec{r}) \tag{1.149}$$

where f ensures the normalization of w_1 :

$$f^2 = \sum_j g_j^2 \int_{D_j} v_0^*(\vec{r}) v_0(\vec{r}) d^2 r. \tag{1.150}$$

In order to calculate the noise in the measurement, it is necessary to construct a basis that contains the detection mode w_1. However, as the mean value of the electric field in this mode is different from zero, w_1 in not necessarily orthogonal to v_0, and it is not always possible to obtain an eigenbasis with w_1. Nevertheless, we can still choose w_0 such as the mean field mode v_0 is a linear combination of w_0 and w_1. Choosing all the other modes w_i (with $i \geq 2$) in order to obtain an orthonormal basis, we get a basis such as the mean field is distributed in the two first modes w_0 and w_1, where w_1 is the detection mode. The other modes are chosen in order to complete the basis, and are such as their mean electric field value is zero. We can then perform a calculation similar to the one presented in the previous section, yielding:

$$C_g^i = \sqrt{N} f \int_D w_i(\vec{r})^* w_1(\vec{r}) d^2 r = \sqrt{N} f \delta_{i,1} \tag{1.151}$$

Once again the detection mode is the only relevant one for the calculation of the measurement noise. Taking into account that the normalization giving rise to the shot noise has changed because the gains do not all necessarily have a gain of modulus 1,

$$\sum_i |C_g^i|^2 = |C_g^1|^2 = N f^2, \tag{1.152}$$

and the noise formula given in Eq. 1.148 becomes

$$\langle \delta \hat{N}_g^2 \rangle = f^2 N \langle \delta \hat{X}_1^{+^2} \rangle \tag{1.153}$$

where $\langle \delta \hat{X}_1^{+^2} \rangle$ is the amplitude quadrature noise corresponding to the mode $w_1(\vec{r})$ of the incoming field.

The f^2 factor is a global effect of the gain, and modifies both the measured signal and the shot noise level. In any case, if the flipped mode is perfectly squeezed, we can still perform a perfect measurement. However, the experimental configuration is more complicated as, in general, the mean value of the electric field in mode w_1 is different from 0, which means that, as is shown in appendix A.2, generating the good mode is difficult. An appropriate approach would be to describe the field back into an eigen-basis, and check how to set the noise of the different modes in that basis. We will see in appendix A how this can be done in a simple case. The important result of this part is that whatever the

measurement we perform, the noise arises only from one mode. Changing the noise of this mode allows us to improve the sensitivity of the measurement. As in the previous section, it is also possible in the general case to perform several simultaneous measurements, and to identify the subspace of modes responsible for the noise.

It is interesting to note that, in the particular case of a measurement where the gains are adapted to have $\langle \hat{M}(\{g_j\})\rangle = 0$, the mode v_0 coincides with w_0. Indeed, v_0 is here orthogonal to w_1 :

$$\begin{aligned} \int_D w_1^*(\vec{r}) v_0(\vec{r}) d^2r &= \sum_j \frac{g_j}{f} \int_{D_j} v_0^*(\vec{r}) v_0(\vec{r}) d^2r \\ &\propto \langle \sum_j g_j \hat{N}(D_j)\rangle \\ &= 0 \end{aligned} \tag{1.154}$$

hence the basis is an eigen-basis of the field. Again, that case is relevant experimentally as it means that one can act on the noise without perturbing the mean field mode. Indeed, in order to implement the theory developed here to complex experimental configurations, it is preferable for the various detection modes to be orthogonal to the mean field (i.e. they do not contribute to the mean electric field). They can then be mixed with the mean field without introducing losses. For instance, one can use the proposal which has be detailed in [Treps04,1], in order to mix two non-classical beams in orthogonal transverse modes, and a mean coherent field, in order to improve the sensitivity of the transverse position measurement of a laser beam. These experimental techniques will be developed in chapter 4.

In this section, we have shown that it was possible to perform one array-detector measurement beyond the quantum noise limit by injecting squeezed light in an identified mode called the *flipped mode*, which corresponds here to the *noise-mode* of detection. Moreover, we have proposed a way to extend this to simultaneous independent measurements.

C.6 Homodyne array detection

A homodyne array detection consists of a combination of identical array detectors in a homodyne detection configuration, as shown in Fig. 1.10e). Such a device has never been implemented experimentally, but could be very interesting as it would combine advantages of both array and homodyne schemes. Indeed, the pixel detectors allows simultaneous spatial measurements in the image, without having to change the local oscillator between each measurement, and the homodyne configuration allows to probe all different quadratures of the incident image [Raymer93]. The shape of the local oscillator and the pixel gain distribution best adapted for a particular type of measurement will be investigated .

D Conclusion

In this first chapter, we have rigourously defined multi-mode quantum state of light, and have presented their general expression when decomposed in a transverse spatial basis. Moreover, we have shown how to selectively measure a particular component of the multi-mode field with different measurement devices. This has notably allowed us to introduce

the concept of noise-mode of detection. This crucial point will provide an understanding of optimal measurements of a given parameter in chapter 3. Our analysis has been so far limited to pure states and a more complete description involving mixed states will be investigated.

CHAPTER 2

Quantum study of optical storage

Contents

High density data storage represents a major challenge for opticians [VanDeNes06,1]. Since the first commercialization of the Compact Disc in 1983, optical techniques have been developed in order to store more and more information on a 12 cm diameter disc, as shown in table 2.1. Such an evolution has been allowed by the modification of two main key parameters : the read-out laser wavelength λ and the numerical aperture N_A of the optical system.

Further developments along this track will now be confronted to several difficulties. First, further decrease of the laser wavelength to the UV domain is not realistic yet, as compact and low-cost UV laser sources are not available. Moreover, further increase of the numerical aperture would require solid immersion lenses or near-field optics, which would compromise the accessibility of the optical media and the robustness of the system for

System	Year	$\lambda\,[\mu m]$	N_A	λ/N_A	Capacity [GB/layer]
Compact Disc	1983	0.785	0.45	1.74	0.65
DVD	1995	0.650	0.60	1.08	4.7
HD-DVD	2006	0.405	0.65	0.62	16
Blu Ray	2006	0.405	0.85	0.48	23

Table 2.1: Evolution and properties of commercial optical disc data storage systems.

commercial use. Furthermore, this modification would not yield noticeable improvement as the size of the focal point in Blu-Ray systems is already almost reaching the diffraction limit.

An alternative approach consists in multiplexing the information by encoding and reading several bits in a single storage location, i.e. within the focussed laser spot[1]. As such, we have proposed two complementary schemes [Delaubert06,2, Hsu06]. First, information is encoded onto the transverse profile of the beam and read-out with a spatial resolving detector such as a CCD camera. Secondly, the information is encoded in the longitudinal phase of the beam and read-out using interferometric measurements. Each one of these schemes is detailed in the two articles reported at the end of this chapter.

We emphasize that both proposals should be considered as proofs of principle as they do not provide a concrete apparatus yet. We did not seek to optimize the shape of the pits, nor their dimension and the detection device. However, we have shown the enormous potential of these schemes for high-density optical data storage. Moreover, note that they are compatible with further modifications of wavelength and aperture.

Encoding and reading details whose size is of the order, or below, the wavelength onto an optical beam is termed *super-resolution*. In such a regime, the non-paraxial beam propagation has to be taken into account. Diffraction plays a major role, signals to be distinguished are small, and noise becomes an important issue.

In our analysis, we concentrated on the influence of quantum noise in optical read-out. The shot noise already represents a few percents of the overall noise in Blu-Ray systems, and will surely be a limiting factor in the next generation of optical data storage equipment. As our analysis does not intrinsically depends on the focussing regime, we have chosen, as a first step, to restrict our study to the paraxial regime. Although the non-paraxial propagation of strongly focussed laser beams, for which the vectorial aspects of light has to be taken into account, has been investigated for decades now, it remains a difficult problem and is still an active field of research [VanDeNes06,1, VanDeNes06,2].

In further development of this work, we will include the non-paraxial propagation of light. Moreover, an experiment is being set-up in order to establish a clear correspondence between diffraction limit and standard quantum noise limit. Indeed, when one asks the simple question : "what is the limiting factor to the imaging of smaller and smaller details in an optical image?", the answer can either be "diffraction" or "quantum noise", according to which research community the question is addressed...

[1]Note that other alternatives are currently investigated, such as multi-layered optical discs VMD (Versatile Multilayer Disc) and holographic medium HVD (Holographic versatile disc).

PHYSICAL REVIEW A **73**, 013820 (2006)

Optical storage of high-density information beyond the diffraction limit: A quantum study

V. Delaubert,[1] N. Treps,[1] G. Bo,[2] and C. Fabre[1]
[1]*Laboratoire Kastler Brossel, UPMC, Case 74, 4 Place Jussieu, 75252 Paris Cedex 05, France*
[2]*Laboratoire Pierre Aigrain, Ecole Normale Supérieure, 24 rue Lhomond, 75231 Paris Cedex 05, France*
(Received 13 September 2005; revised manuscript received 28 November 2005; published 27 January 2006)

We propose an optical readout scheme allowing a proof of principle of information extraction below the diffraction limit. This technique, which could lead to improvement in data readout density onto optical disks, is independent from the wavelength and numerical aperture of the reading apparatus, and involves a multipixel array detector. Furthermore, we show how to use nonclassical light in order to perform a bit discrimination beyond the quantum noise limit.

DOI: 10.1103/PhysRevA.73.013820 PACS number(s): 42.50.Dv, 42.30.Va, 42.30.Wb

I. INTRODUCTION

The reconstruction of an object from its image beyond the diffraction limit, typically of the order of the wavelength, is a hot field of research, though a very old one, as Bethe already dealt with the theory of diffraction by subwavelength holes in 1944, to the best of our knowledge [1]. More recently, a theory has been developed to be applied to the optical storage problem, in order to study the influence of very small variations of pit width or depth relative to the wavelength [1–6]. To date, only a few super-resolution techniques [7] include a quantum treatment of the noise in the measurement, but to our knowledge, none has been applied to the optical data storage problem.

Optical disks are now reaching their third generation, and have improved their data capacity from 0.65 Gbytes for compact disks (using a wavelength of 780 nm), to 4.7 Gbytes for DVDs ($\lambda = 650$ nm), and eventually to 25 GB for the Blu-Ray disks (using a wavelength of 405 nm). In addition to new coding techniques, this has been achieved by reducing the spot size of the diffraction-limited focused laser beam onto the disk, involving higher numerical apertures and shorter wavelengths.

Several further developments are now in progress, such as the use of volume holography, 266 nm reading lasers, immersion lenses, near field systems, multidepths pits [8], or information encoding on angle positions of asymmetrical pits [9]. These new techniques rely on a bit discrimination using small variations of the measured signals. Therefore, the noise is an important issue, and ultimately, quantum noise will be the limiting factor.

In this paper, we investigate an alternative and complementary way to increase the capacity of optical storage, involving the retrieval of information encoded on a scale smaller than the wavelength of the optical reading device. We investigate a way to optimize the detection of subwavelength structures using multipixel array. With an attempt to a full treatment of the optical disk problem being far too complex, we have chosen to illustrate our proposal on a very simple example, leaving aside most technical constraints and complications, but still involving all the essence of the overall problem.

We first explain how the use of an array detector can lead to an improvement of the detection and distinction of subwavelength structures present in the focal spot of a laser beam. We then focus on information extraction from an optical disk with a simple but illustrative example, considering that only a few bits are burnt on the dimensions of the focal spot of the reading laser, and show how the information is encoded from the disk to the light beam, propagated to the detector, and finally detected. We explain the gain configuration of the array detector that has to be chosen in order to improve the signal-to-noise ratio of the detection. Moreover, as quantum noise is experimentally accessible, and will be a limiting factor for further improvements, we perform a quantum calculation of the noise in the detection process. Indeed, we present how this detection can be optimized to perform simultaneous measurements below the quantum noise limit, using nonclassical light.

II. PROPOSED SCHEME FOR BIT SEQUENCE RECOGNITION IN OPTICAL DISKS

We propose an optical readout scheme shown in Fig. 1 allowing information extraction from optical disks beyond the diffraction limit, based on the multipixel detection. Bits, coded as pits and holes on the optical disk, induce phase flips in the electric field transverse profile of the incident beam at reflection. The reflected beam is imaged in the far field of the disk plane, where the detector stands. In the far field, the phase profile induced by the disk is converted into an intensity profile, that the multipixel detectors can, at least partly, reconstruct.

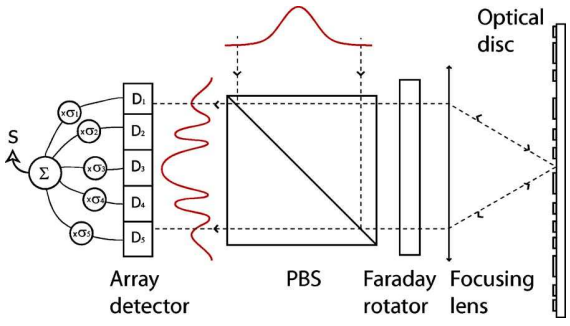

FIG. 1. (Color online) Scheme for information extraction from optical disks, using an array detector.

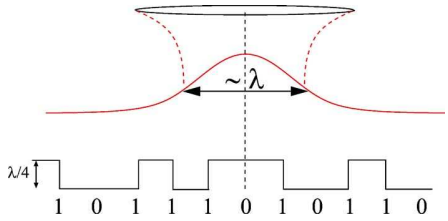

FIG. 2. (Color online) Example of a bit sequence on an optical disk. The spacing between the bits is smaller than the wavelength, the minimum waist of the incident laser beam being of the order of λ. A hole depth of λ/4 insures a π phase shift between fields reflected on a pit and a hole.

Taking into account that a lot of *a priori* information is available—i.e., only a finite number of intensity profiles is possible—we propose to use a detector with a limited number of pixels D_k whose gains can independently be varied depending on which bit sequence one wants to detect. The signal is then given by

$$S = \sum_k \sigma_k N_k, \tag{1}$$

where N_k is the mean photon number detected on pixel D_k, and σ_k is the electronic gain of the same pixel. Ideally, to each bit sequence present on the disk corresponds a set of gains chosen so that the value of the measurement is zero, thus canceling noise from the mean field. Measuring the signal for a given time interval T around the centered position of a bit sequence in the focal spot, and testing, in parallel, all the predefine sets of gain in the remaining time, allows us to deduce which bit sequence is present on the disk.

We will first show that this improvement in a density of information encoded on an optical disk is already possible using classical resources. Moreover, as the measurement is made around a zero mean value, the classical noise is mostly canceled. Hence, we reach regimes where the quantum noise can be the limiting factor. We will demonstrate how to perform measurements beyond the quantum noise limit, using previous results on quantum noise analysis in multipixel detection developed in Ref. [10].

III. ENCODING INFORMATION FROM A DISK ONTO A LIGHT BEAM

We have explained the general principle of readingout subwavelength bit sequences encoded on an optical disk, and now focus on the information transfer from the optical disk to the laser beam, through an illustrative example.

Let us recall that bits are encoded by pits and holes on the disk surface: a step change from hole to pit (or either from pit to hole) encodes bit 1, whereas no depth change on the surface encodes bit 0, as represented in Fig. 2. A hole depth of λ/4 ensures a π phase shift between the fields reflected by a pit and a hole. In this section, we compute the incident field distribution on the optical disk affected by the presence of a bit sequence in the focal spot, and finally analyze the intensity back reflected in the far field, in the detection plane, as sketched in Fig. 1.

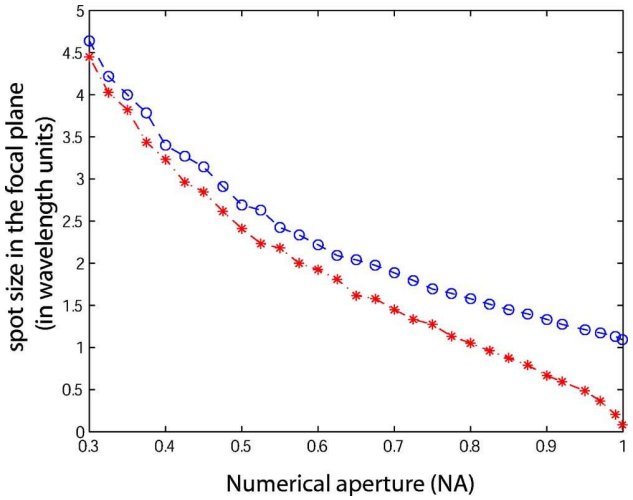

FIG. 3. (Color online) Evolution of the focused spot size of an incident plane wave with the numerical aperture (for λ=780 nm in air medium). The spot size is limited to the order of the wavelength in the nonparaxial case (○), whereas it goes to zero for very high numerical apertures in the paraxial case (∗).

A. Beam focalization

Current optical disk readout devices involve a linearly polarized beam strongly focused on the disk surface to point out details whose size is of the order of the laser wavelength. The numerical aperture (NA) of the focusing lens can be large (0.47 for CDs, 0.6 for DVDs, and 0.85 for BLU RAY disks), and the exact calculation of the field cannot be done in the paraxial and scalar approximation. Thus, the vectorial theory of diffraction has to be taken into account.

The structure of the electromagnetic field in the focal plane of a strongly focused beam has been investigated for decades now [11], as its applications include areas such as microscopy, laser microfabrication, micromanipulation, and optical storage [12–19].

In our case of interest, we can restrict the field calculation to the focal plane, which is the disk plane. Thus Richards and Wolf integrals [20], that are not suitable for a general propagation of the field, but which can provide the field profile in the focal plane for any type of polarization of the incoming beam as long as the focusing length is much larger than the wavelength, can be used to achieve this calculation. These integrals have already been used in many publications dealing with tight focusing processes [21–28]. As highlighted in these references, the importance of the vectorial aspect of the field can easily be understood when a linearly polarized beam is strongly focused, as the polarization of the wave after the lens is not perpendicular to the propagation axis anymore and has thus components along this axis. In order to estimate the limit of validity of the paraxial approximation, we computed focused spot sizes of linearly polarized beams in the focal plane for different numerical apertures, first in the paraxial approximation, and then calculated with Richards and Wolf integrals. The results are compared in Fig. 3 for an incident plane wave in an air medium with λ=780 nm, where the spot size is defined as the diameter

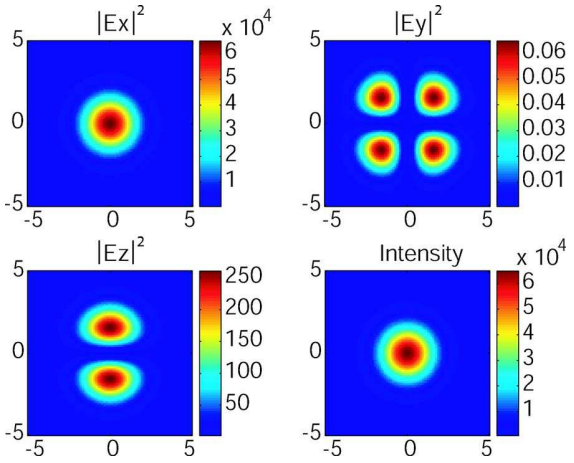

FIG. 4. (Color online) Norm of the different field components and resultant intensity in the focal plane with a linearly polarized incident field along the x axis, focused with a 0.47 numerical aperture.

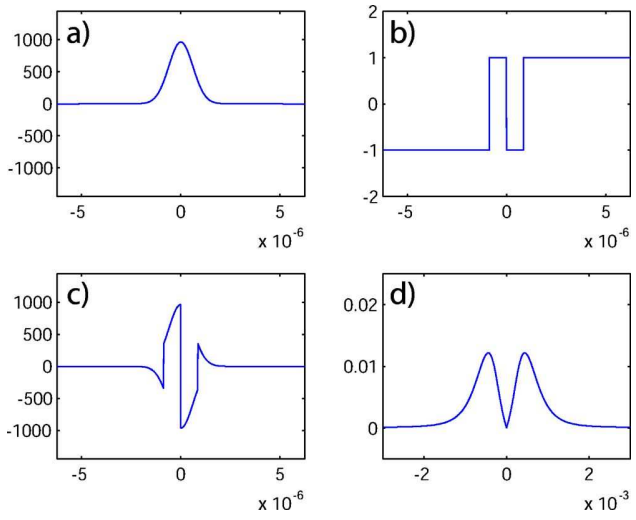

FIG. 5. (Color online) Modifications of the transverse amplitude field profile trough propagation, in the case of a 111 bit sequence in the focal spot: (a) incoming beam profile; (b) 111 bit sequence; (c) corresponding reflected field in the disk plane; (d) far field profile in the detector plane.

which contains 86% of the focused energy, as in Ref. [29]. We see that when the numerical aperture exceeds 0.6, a good prediction requires a nonparaxial treatment. Moreover, whereas there is no theoretical limit to focalization in the paraxial case, we see that nonparaxial effects prevent us to reach a waist smaller than the order of the wavelength. Note that this limit is not fundamental and can be overcome by modifying the polarization of the incoming beam. Quabis and co-workers have indeed managed to reduce the spot area to about 0.1 λ^2 using an incident radially polarized doughnut beam [21,24].

As our aim is to present a demonstration of principle and not a full treatment of the optical disk problem, the following calculations will be done using the physical parameters of the actual compact disks (λ=780 nm and NA=0.47, corresponding to a focalization angle of 27° in air medium). In this case, the paraxial and scalar approximations are still valid. Indeed, Fig. 4, giving the transverse profile of the three field components and the resultant intensity in the focal plane using the former parameters, shows that although the field is not strictly linearly polarized as foreseen before, $E_y \ll E_z \ll E_x$, and we can thus consider that only E_x is different from zero with a good approximation. Note that the exact expression would not intrinsically change the problem, as our scheme can be adapted to any field profile discrimination.

B. Reflection onto the disk

In order to compute the reflected field, we simply assume that bumps and holes are generated in such a way that they induce a π phase shift between them at reflection on the field profile. Note that the holes' depth is usually $\lambda/4$, but precise calculations would be required to give the exact shape of the pits, as they are supposed to be burnt below the wavelength size, and as the field penetration in those holes is not trivial [4–6]. As we have shown that only one vectorial component of the field was relevant in the focal plane, we can directly apply this phase shift to the amplitude profile of this component.

We first envision a scheme with only three bits in the focal spot, which means that 2^3 different bit sequences, i.e., a byte, have to be distinguished from each other, using the information extracted from the reflected field. Note that we neglect the influence of other bits in the neighborhood. A more complete calculation involving this effect with more bits will be considered in a further approach.

The amplitude profiles obtained when the incident beam is centered on a bit of the CD are presented on Fig. 5, for a particular bit sequence. Note that we have chosen the space between two bits on the disk equal to the waist size of the reading beam. The first three curves, respectively, show the field amplitude profile incident on the disk, an example of a bit sequence, and the corresponding profile just after reflection onto the disk. We see that binary information is encoded from bumps and holes on the CD to phase flips in the reflected field.

C. Back propagation to the detector plane

In order to extract the information encoded in the transverse amplitude profile of the beam, the field has to be back propagated to the detector plane. A circulator, composed of a polarizing beam splitter and a Faraday rotator, ensures that the linearly polarized reflected beam reaches the array detector, as shown in Fig. 1. Assuming that the detector is positioned just behind the lens plane, the expression of the detected field is given by the far field of the disk plane, apertured by the diameter of the focusing lens. As the focal length and the diameter of the lens are large compared to the wavelength, we use the Rayleigh Sommerfeld integral to compute the field in the lens plane [30]. As an example, the calculated far field profile when the bit sequence 111 is present in the focal spot is shown on the fourth graph of Fig. 5.

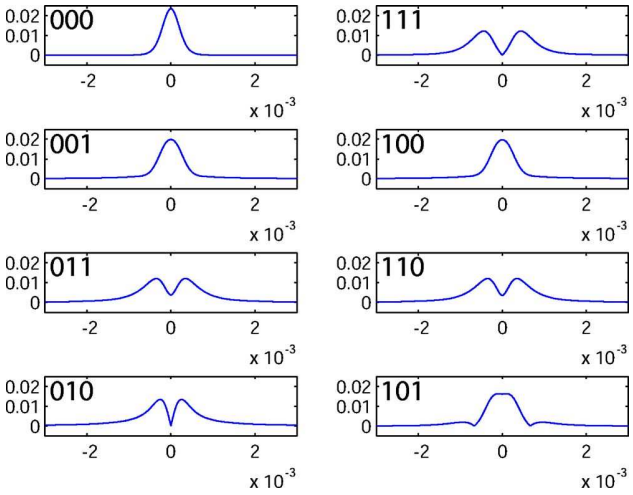

FIG. 6. (Color online) Field profiles in the array detector plane, for each of the 8 bit sequence configuration. Note that they are clearly distinguishable, except for the bit sequences 100 and 001, and 011 and 110, which have the same profile because of the symmetry of the bit sequence relative to the position of the incident laser beam.

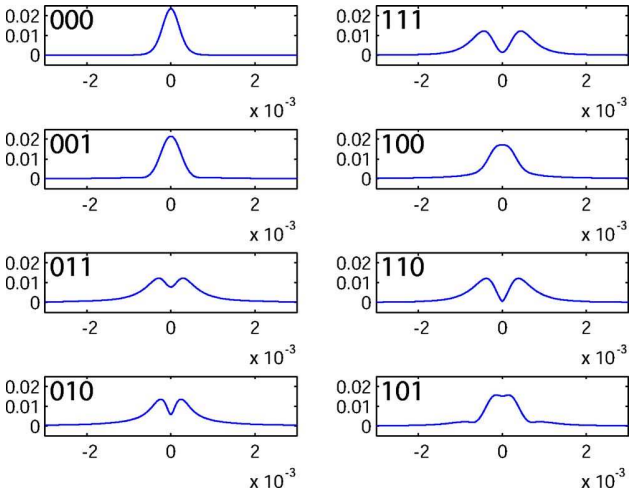

FIG. 7. (Color online) Field profiles in the array detector plane, for each of the 8 bit sequence configuration, when the position of the disk has been shifted of $w_0/6$ relative to the incident beam. The profile degeneracy for 100 and 001, and 011 and 110 is raised. Note that the other profiles have experienced a much smaller shape modification between the two positions of the disk.

The presence of the lens provides a limited aperture for the beam and cuts the high spatial frequencies of the field, which can be a source of information loss, as the difference between each bit sequence can rely on those high frequencies. However, we will see that enough information remains in the low frequency part of the spatial spectrum, so that the 8 bits can be distinguished. This is due to the fact that we have in this problem a lot of *a priori* information on the possible configurations to distinguish.

We see in Fig. 6 that, with the physical parameters used in compact disk readout devices, 6 over 8 profiles in the detector plane are still different enough to be distinguished. At this stage, we are nevertheless unable to discriminate between symmetric configurations, because they give rise to the same far field profile. Therefore, 100 and 001, and 110 and 011, cannot be distinguished. Note that this problem can be solved thanks to the rotation of the disk. Indeed, an asymmetry is created when the position of the disk relative to the laser beam is shifted, thus modifying differently the two previously indistinguishable profiles. As shown in Fig. 7, where the far field profiles are represented after a shift of $w_0/6$ in the position of the disk, the degeneracy has been removed. Moreover, it is important to note that the other profiles experience a small shape modification. This redundant information is very useful in order to remove ambiguities while the disk is rotating.

IV. INFORMATION EXTRACTION FOR BIT SEQUENCE RECOGNITION

In this section, we describe the detection, present some illustrative results, and the way they can be used to increase the readout precision of information encoded on optical disks. We show here that a pixellized detector with a very small number of pixels is enough to distinguish between the 8 bit sequences. Note that for technical and computing time reasons, it is not realistic to use a charge-coupled device (CCD) camera to record the reflected images, as such cameras cannot yet combine good quantum efficiency and high speed.

A. Detected profiles

For simplicity reasons, we limit our calculation to a 5 pixels array detector $D_1,\ldots,D_5$, each of whom has an electronic gain $\sigma_1,\ldots,\sigma_5$, as shown in Fig. 8 The size of each detector has been chosen without a systematic optimi-

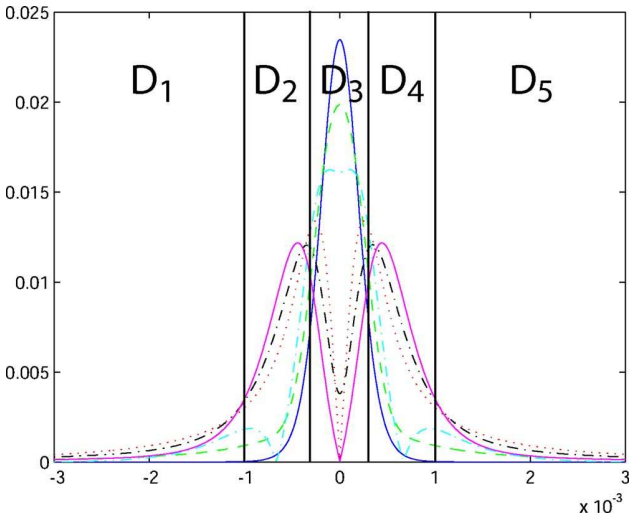

FIG. 8. (Color online) Far field profiles for each bit configuration, and array detector geometry. The 5 detectors $D_1,\ldots,D_5$ have electronic gains $\sigma_1(i),\ldots,\sigma_5,\ldots,(i)$ according to the bit sequence i which is present in the focal spot.

zation, which will be done in a further approach. Gain values are adapted to detect a mean signal equal to zero for each bit configuration present in the focal spot, in order to cancel the common mode classical noise present in the mean field [10]. It means that for each bit sequence i, gains are chosen to satisfy the following relation:

$$\sum_{k=1}^{5} \sigma_k(i) N_k(i) = 0, \tag{2}$$

where $N_k(i)$ is the mean photon number detected on pixel D_k when bit i is present in the focal spot on the disk

$$N_k(i) = \int_{D_k} n_i(x) dx, \tag{3}$$

where $n_i(x)$ is the number of photons incident on the array detector, at position x, when the bit sequence i is present in the focal spot.

As all profiles are symmetrical when the incident beam is centered on a bit, we have set $\sigma_1 = \sigma_5$ and $\sigma_2 = \sigma_4$. In addition, we have chosen $\sigma_3 = -\sigma_1/2$. Using these relations and Eq. (2), we compute gain values adapted to the recognition of each bit sequence. Note that the calculation of each gain configuration requires *a priori* information on the far field profiles, or at least an experimental calibration using a well-known sample.

Now that these gain configurations are set, we can investigate for a bit sequence on the optical disk.

B. Classical results

The expression of the detected signal $S_i(j)$ is given by

$$S_i(j) = \sum_{k=1}^{5} \sigma_k(j) N_k(i), \tag{4}$$

where i refers to the bit sequence effectively present in the focal spot, and j to the gain set adapted to the detection of the bit sequence j. It merely corresponds to the intensity weighted by the electronic gains. Note that for $i=j$—and only in this case if the detector is well chosen—the mean value of the signal $S_i(i)$ is equal to zero, according to Eq. (2). All possible values of $S_i(j)$ are presented for a total number of incident photons $N_{inc}=25$, in Table I where i is read vertically, and corresponds to the bit sequence on the disk, whereas j is read horizontally and refers to the gain set adapted to the detection of bit j. In order not to have redundant information, we have gathered results corresponding to identical far field profiles. A zero value is obtained for only one gain configuration, allowing an identification of the bit sequence present in the focal spot.

The reading process to determine which bit sequence is lit on the disk follows these few steps: the time dependent intensity is first measured on each of the five detectors with all electronic gains set to 1; these intensities are integrated for a time T; the signal is then calculated, using the different gain configurations j; the bit sequence effectively present in the focal spot is determined by the only signal yielding a zero value. Note that the second step just corresponds to the N_k measurements. The integration time T is chosen as the time interval during which the signal leads to the determination of a unique bit sequence. The third step corresponds to the simple calculation of a line in Table I. This can be done in parallel thanks to the speed of data processing on dedicated processors, and the reading rate will thus not be affected compared to current devices. Finally, note that the last step requires a good choice of the parameters in order to be able to distinguish all bit sequences. It means that the noise level has to be smaller than the difference between the two closest values from 0, in order to get a zero mean value for only one bit sequence. Indeed, there must be no overlap between the expectation values when we take into account the noise and thus the uncertainty relative to each measurement. Note that using the zero value as the discriminating factor could be combined with the use of all the calculated values, as each line of Table I is distinct. We just need to know how to weight each data point according to the noise related to its obtention.

TABLE I. Detected signals $S_i(j)$ where i is read vertically and corresponds to the bit sequence on the disk, whereas j is read horizontally and refers to the gain set adapted to the detection of bit j. A zero value means that the tested gain configuration is adapted to the bit sequence.

	000	001/100	010	011/110	101	111
000	0	−34	−204	−254	−77	−303
001/100	15	0	−76	−99	−19	−121
010	23	20	0	−6	16	−13
011/110	24	22	5	0	19	−5
101	19	11	−36	−50	0	−63
111	24	23	9	5	20	0

V. NOISE CALCULATION

A. The shot noise limit

To include the noise in our calculation, we separate classical and quantum noise contributions. The classical noise comprises residual noise of the laser diode, mechanical, and thermal vibrations. The major part of this noise is directly proportional to the signal, i.e., to the number of detected photons. For a detection of the total number of photons N_{inc} in the whole beam during the integration time of the detector, the classical noise contribution $\sqrt{\langle \delta N_{inc}^2 \rangle}$ would thus be written as

$$\sqrt{\langle \delta N_{inc}^2 \rangle} = \beta N_{inc}, \tag{5}$$

where β is a constant factor. And the individual noise variable $\delta N_i(k)$ arising from detection on pixel D_k is given by

$$\delta N_i(k) = \frac{N_i(k)}{N_{inc}} \delta N_{inc}. \tag{6}$$

Using Eqs. (4)–(6) a simple calculation yields the variance of the signal arising from the classical noise

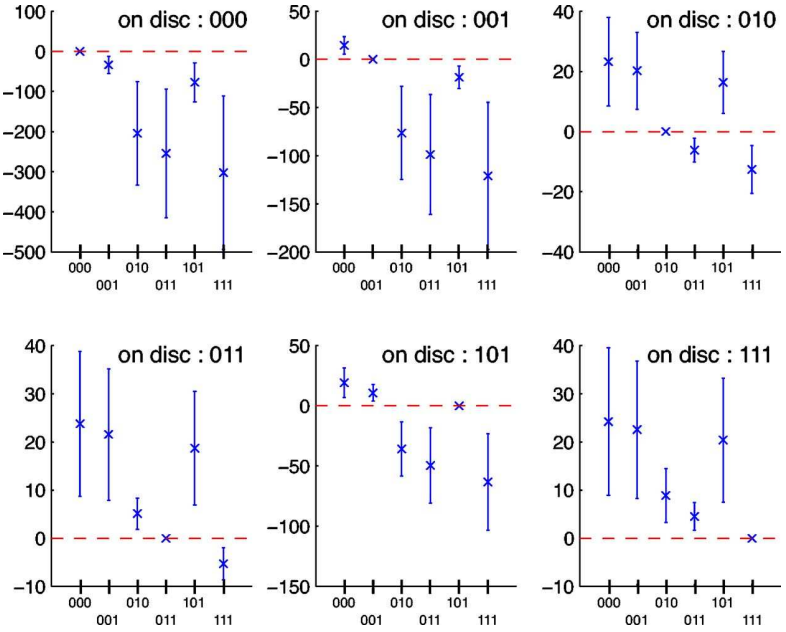

FIG. 9. (Color online) Classical noise (10 dB of excess noise) represented as error bars, for $\lambda = 0.78\ \mu$m, NA=0.47, and 25 detected photons. Each inset corresponds to the 6 signals obtained for the different gain configurations, when one particular bit sequence is present in the focal spot. Each bit sequence present in the focal spot can be clearly identified as only one gain configuration can give a zero value for each inset.

$$\langle \delta \hat{S}_i^2(j) \rangle_{Cl} = \frac{B S_i^2(j)}{N_{inc}}, \tag{7}$$

where the constant $B = N_{inc}\beta^2$ is the classical noise factor, and is chosen so that, when $B=1$ and when all the intensity is detected by one detector, the classical noise term is equal to the shot noise term. Note that classical noise does not deteriorate measurements having a zero mean value. For this reason, we have chosen to discriminate bit sequences by choosing gains such as $S_i(i)=0$, as mentioned earlier.

The calculation of the quantum contribution requires the use of quantum field operators, describing the quantum fluctuations in all transverse modes of the field. By changing the gain configuration of the array detector, not only the signal $S_i(j)$ is modified, but also the related quantum noise denoted $\langle \delta \hat{S}_i^2(j) \rangle_{Qu}$, as different gain configurations are sensitive to noise in different modes of the field. We have shown in Ref. [10] that for a multipixel detection of an optical image, the measurement noise arises from only one mode component of the field, referred to as the *detection mode*, or *noise mode* [31,32]. The expression of the quantum noise is then

$$\langle \delta \hat{S}_i^2(j) \rangle_{Qu} = f_{i,j}^2 N_{inc} \langle \delta \hat{X}_{w_{i,j}}^2 \rangle, \tag{8}$$

where $\delta \hat{X}_{w_{i,j}}$ is the quantum noise contribution of the noise-mode $w_{i,j}(x)$ which is defined for one set of gain j, when the bit sequence i is present in the focal spot, as

$$w_{i,j}(x) = \frac{\sigma_k(j) n_i(x)}{f_{i,j}}, \quad \forall\, x \in D_k \tag{9}$$

and where $f_{i,j}$ is a normalization factor, which expression is

$$f_{i,j}^2 = \frac{\sum_{k=1}^{5} \sigma_k^2(j) N_k(i) dx}{N_{inc}}. \tag{10}$$

The noise mode corresponds in fact to the incident field profile weighted by the gains. The shot noise level corresponds to $\langle \delta \hat{X}_{w_{i,j}}^2 \rangle = 1$.

The variance of the signal can eventually be written as

$$\langle \delta \hat{S}_i^2(j) \rangle = f_{i,j}^2 N_{inc} \langle \delta \hat{X}_{w_{i,j}}^2 \rangle + \frac{B S_i^2(j)}{N_{inc}}. \tag{11}$$

We have first represented the classical noise with an excess noise of 10 dB, as error bars for each result $S_i(j)$, in Fig. 9. We have chosen a representation with a number of detected photons of only 25. Each of the six insets refers to the measurement obtained for a particular bit sequence in the focal spot. The six data points and associated error bars refer to the results obtained when the six gain configurations are tested. One inset thus corresponds to one line in Table I. We can see that with this choice of parameters, the bit sequence effectively present in the focal spot can be determined without ambiguity by the only zero value. The sequence corresponds to the one for which the gains were optimized. We see that the bit sequence discrimination can be achieved even with a very low number of photons. The relative immunity to classical noise of our scheme arises from the fact that measurements are performed around a zero mean value. Thus, given this limit in the minimum necessary photon number and the flux of photons one can calculate the maximum data rate, which is found to be 2×10^7 Mbits/s (this estimation takes into account an integration time T corresponding to $\frac{1}{10}$ of the delay between the readout process of two adjacent bits with a 1 mW laser). This very high value shows that classical noise should not be a limit for data rates in such a scheme.

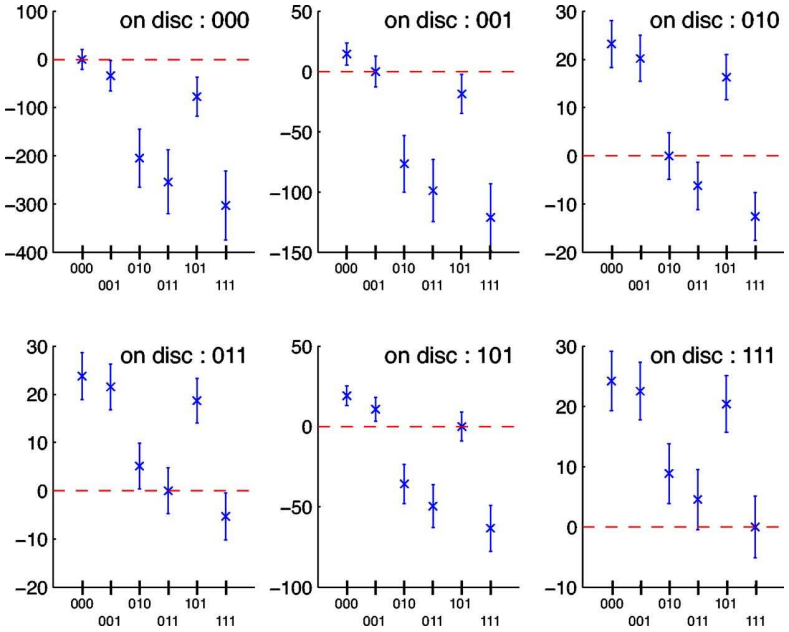

FIG. 10. (Color online) Shot noise represented as error bars, for $\lambda=0.78\ \mu$m, NA $=0.47,25$ detected photons. Some bit sequences cannot be determined without ambiguity because of the noise level.

The effect of quantum noise is very small, but becomes a limiting factor for such a small number of detected photons, or for a large number of bits encoded on the disk in the wavelength size. In order to see independently the effect of each contribution to the noise, we have thus represented in Fig. 10 the shot noise also for 25 detected photons, appearing as the threshold under which it is impossible to distinguish bit sequences because of the quantum noise. Note that for the represented case, the shot noise is the most important contribution, and that it prevents a bit sequence discrimination, as a zero value for the signal can be obtained for several gain configurations in the same inset.

B. Beyond the shot noise limit

When the shot noise is the limiting factor, nonclassical light can be used to perform measurements beyond the quantum noise limit. We have shown in Ref. [10] that squeezing the noise mode of the incident field was a necessary and sufficient condition to a perfect measurement. What we are interested in is improving the measurements that yield a zero value, which are obtained when the gain configuration matches the bit sequence in the focal spot, as $S_i(i)=0$. Using Eq. (11), we see that $w_{i,i}$ has to be squeezed. As no information on the bit present in the focal spot is available before the measurement, in order to improve simultaneously all the bit sequence detections, the six noise modes have to be squeezed at the same time in the incident field. These six transverse modes are not necessarily orthogonal, but one can show that squeezing the subspace that can generate all of them is enough to induce the same amount of squeezing.

The quantum noise with 10 dB of squeezing on the subspace generated by the $w_{i,i}$ is represented as error bars in Fig.

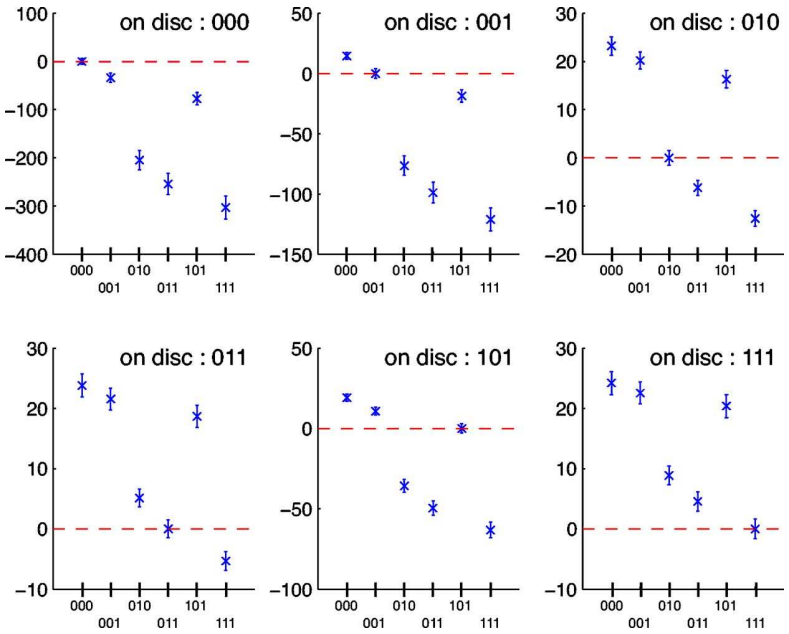

FIG. 11. (Color online) Quantum detection noise represented as error bars, for $\lambda=0.78\ \mu$m, NA$=0.47,25$ detected photons and -10 dB of simultaneous squeezing for all the flipped modes. The ambiguity in the presence of shot noise has been removed and each bit sequence can be identified.

11. The noise of each noise-mode $w_{i,j}$ is computed using its overlap integrals with the generator modes of the squeezed subspace, assuming that all modes orthogonal to the squeezed subspace are filled with coherent noise. In this case, the effect of squeezing, reducing the quantum noise on the measurements, and especially on the measurement for which the gains have been optimized, is enough to discriminate bit sequences that were masked by quantum noise.

VI. CONCLUSION

We have proposed a way of information extraction from optical disks, based on a multipixel detection. We have first demonstrated, using only classical resources, that this detection could allow large data storage capacity, by burning several bits in the spot size of the reading laser. We have presented a proof of principle through a simple example which will be refined in further studies. We have also shown that in shot noise limited measurements, using squeezed light in appropriate modes of the incident laser beam can lead to improvement in bit sequence discrimination.

The next steps are to study in detail how to extract the redundant information when the disk is spinning, and to systematically optimize the number of bits in the focal spot, the number and size of pixels in the array detector. Such a regime involving a large number of bits in the focal spot will ultimately be limited by the shot noise, and will require the quantum noise calculations presented in this paper.

ACKNOWLEDGMENTS

We thank Magnus Hsu, Ping Koy Lam and Hans Bachor for fruitful discussions. Laboratoire Kastler Brossel, of the Ecole Normale Superieure and University Pierre et Marie Curie, is associated to CNRS. This work has been supported by the European Union in the frame of the QUANTIM network (Contract No. IST 2000-26019).

[1] H. A. Bethe, Phys. Rev. **7**, 66 (1944); **8**, 163 (1944).
[2] D. S. Marx and P. Psaltis, J. Opt. Soc. Am. A **14**, 1268 (1997).
[3] D. S. Marx and P. Psaltis, Appl. Opt. **36**, 6434 (1997).
[4] X. Wang, J. Mason, M. Latta, T. C. Strand, D. S. Marx, and P. Psaltis, J. Opt. Soc. Am. A **18**, 565 (2001).
[5] W.-C. Liu and M. W. Kowarz, Appl. Opt. **38**, 3787 (1999).
[6] J. M. Brok and H. P. Urbach, J. Opt. Soc. Am. A **20**, 256 (2003).
[7] I. Sokolov and M. Kolobov, Opt. Lett. **29**, 703 (2004).
[8] M. T. L. Hsu, W. P. Bowen, V. Delaubert, C. Fabre, H.-A. Bachor, and P. K. Lam (unpublished).
[9] P. Török (unpublished).
[10] N. Treps, V. Delaubert, A. Maître, J. M. Courty, and C. Fabre, Phys. Rev. A **71**, 013820 (2005).
[11] A. G. van Nie, Philips Res. Rep. **19**, 378 (1964); **19**, 394 (1964).
[12] M. Lax, W. H. Louisell, and W. B. McKnight, Phys. Rev. A **11**, 1365 (1975).
[13] S. R. Seshadri, J. Opt. Soc. Am. A **19**, 2134 (2002), and references therein.
[14] A. Ciattoni, B. Crosignani, and P. Di Porto, Opt. Commun. **177**, 9 (2000).
[15] Q. Cao and X. Deng, J. Opt. Soc. Am. A **15**, 1144 (1998).
[16] B. T. Landesman and H. H. Barrett, J. Opt. Soc. Am. A **5**, 1610 (1988).
[17] G. Rodriguez-Morales and S. Chavez-Cerda, Opt. Lett. **5**, 430 (2004).
[18] Z. Ulanowski and I. K. Ludlow, Opt. Lett. **25**, 1792 (2000).
[19] T. A. Nieminen, H. Rubinsztein-Dunlop, and N. R. Heckenberg (unpublished).
[20] B. Richards and E. Wolf, Proc. R. Soc. London, Ser. A **253**, 359 (1959).
[21] S. Quabis, R. Dorn, M. Eberler, O. Glöckl, and G. Leuchs, Appl. Phys. B **72**, 109 (2001).
[22] L. Novotny, R. D. Grober, and K. Karrai, Opt. Lett. **26**, 789 (2001).
[23] R. Dorn, S. Quabis, and G. Leuchs, Phys. Rev. Lett. **91**, 233901 (2003).
[24] S. Quabis, R. Dorn, M. Eberler, O. Glöckl, and G. Leuchs, Opt. Commun. **179**, 1 (2000).
[25] C. J. R. Sheppard, J. Opt. Soc. Am. A **18**, 1579 (2001).
[26] P. Török, P. Varga, Z. Laczik, and G. R. Booker, J. Opt. Soc. Am. A **12**, 325 (1995).
[27] K. S. Youngworth and T. G. Brown, Opt. Express **7**, 77 (2000).
[28] Q. Zhan and J. R. Leger, Opt. Express **10**, 324 (2002).
[29] A. E. Siegman, *Lasers* (University Science, Mill Valley, CA, 1986).
[30] M. Born and E. Wolf, *Principle of Optics* (Cambridge University Press, 1959).
[31] V. Delaubert, N. Treps, C. C. Harb, P. K. Lam, and H.-A. Bachor e-print arxiv/ quant-ph/0512151
[32] N. Treps, N. Grosse, W. P. Bowen, M. T. L. Hsu, A. Maître, C. Fabre, H.-A. Bachor, and P. K. Lam, J. Opt. B: Quantum Semiclassical Opt. **6**, S664 (2004).

A Quantum Study of Multibit Phase Coding for Optical Storage

Magnus T. L. Hsu, Vincent Delaubert, Warwick P. Bowen, Claude Fabre, Hans-A. Bachor, and Ping Koy Lam

***Abstract*—We propose a scheme which encodes information in both the longitudinal and spatial transverse phases of a continuous-wave optical beam. A split detector-based interferometric scheme is then introduced to optimally detect both encoded phase signals. In contrast to present day optical storage devices, our phase coding scheme has an information storage capacity which scales with the power of the read-out optical beam. We analyze the maximum number of encoding possibilities at the shot noise limit (SNL). In addition, we show that using squeezed light, the SNL can be overcome and the number of encoding possibilities increased. We discuss a possible application of our phase-coding scheme for increasing the capacities of optical storage devices.**

***Index Terms*—Array detection, interferometer, multimode, optical storage, phase coding, quantum noise limit, split detection, squeezing.**

I. Introduction

THE optical compact disc (CD) was developed in 1979 as a collaboration between two corporations—Sony and Philips. Today, the CD has wide ranging storage applications from the audio–visual to computer industries. The CD system is based on a 780-nm laser (laser spot size of 2.1 μm) with a storage capacity of approximately 670 MB. Since their introduction, there has been increasing demand for greater storage capacities in optical discs; the digital versatile disc (DVD), based on a 650-nm laser system (spot size of 1.3 μm), was introduced. Depending on the format, it can have storage capacities ranging from 4.7 to 17.1 GB. More recently, the HD DVD and Blu-Ray discs, based on a 405-nm laser system, were released. The HD DVD system has a spot size of 0.76 μm and storage capacities of 15–45 GB, while the Blu-Ray disc systems have a smaller spot size of 0.6 μm, with capacities of 25–100 GB [1].

Manuscript received February 14, 2006; revised June 28, 2006. This work was supported in part by the Australian Research Council Centre of Excellence and CNRS France. The work of W. P. Bowen was supported in part by the MacDiarmid Institute for Advanced Materials and Nanotechnology.

M. T. L. Hsu, H.-A. Bachor, and P. K. Lam are with the Australian Research Council Center of Excellence (ARC COE) for Quantum-Atom Optics, Department of Physics, Australian National University, Canberra ACT 0200, Australia (e-mail: magnus.hsu@anu.edu.au; hans.bachor@anu.edu.au; ping.lam@anu.edu.au).

V. Delaubert is with the Australian Research Council Center of Excellence (ARC COE) for Quantum-Atom Optics, Department of Physics, Australian National University, ACT 0200, Australia and also with the Laboratoire Kastler Brossel, Université Pierre et Marie Curie, 75252 Paris, France (e-mail: delaubert@freesurf.fr).

W. P. Bowen is with the Physics Department, University of Otago, Dunedin P.O. Box 56, New Zealand (e-mail: wbowen@physics.otago.ac.nz).

C. Fabre is with the Laboratoire Kastler Brossel, Universite Pierre et Marie Curie, 75252 Paris, France (e-mail: fabre@spectro.jussieu.fr).

Color versions of Figs. 1–3 and 5–7 are available online at http://ieeexplore.ieee.org.

Digital Object Identifier 10.1109/JQE.2006.881634

While nanotechnology allows the fabrication of mechanical surfaces with nanometer size structures, it is the diffraction limit of the read-out optics that prevents data storage densities beyond those of present day systems. The trend of compacting more information into an optical disc, therefore, primarily relies on the use of shorter wavelength lasers to achieve smaller diffraction limited spot sizes. One could envisage that in the not too distant future, such improvement in the storage density would require the use of very short wavelength light beyond the ultra-violet spectrum that cannot be generated with known laser optics.

To date, there have been a number of suggested alternatives for obtaining higher optical storage densities. For example, currently under development are next generation holographic devices, the holographic versatile disc (HVD), which have capacities exceeding 300 GB through the usage of volume storage. An alternative approach depends on the encoding of spatial details beyond the diffraction limit of the read-out laser beam [1]. This approach requires the use of near-field microscopy techniques to resolve subdiffraction limited features.

In this paper, we revisit a well known alternative of using interferometric techniques [2]–[11] to extend optical storage density. We propose to perform multibit phase-front coding of optical beams in an interferometric setup. Our scheme does not require holographic nor near-field optics, instead it utilizes two classes of phase coding—the *longitudinal* and *spatial transverse* phases of an optical beam. We encode information in the longitudinal phase of a beam, which could take discrete values ranging from 0 to π. The total number of encodeable phase values scales with the power of the read-out optical beam. We then introduce an extra encoding degree of freedom, the spatial transverse phase-front profile of the beam. Note that the spatial features of a beam are limited by diffraction. In this paper, dense storage is achieved via small changes in longitudinal phase. We restrict all beam spatial structure to above the diffraction limit, and as a result can describe the beam using the paraxial approximation. In order to resolve the encoded longitudinal phase of the beam, an interferometric scheme is required. To resolve the spatial phase profile of the beam, a multisegment photo-detector [e.g., a charge-coupled device (CCD)] can be used.

This paper is sectioned as follows. We first reduce our analysis of spatial phase-front beam encoding to the situation of a two-pixel array detector, the split detector [12]–[17]. We identify the possible phase profiles symmetric with a split detector and give a modal analysis for these spatial profiles. We also introduce the longitudinal phase of the beam and show how an interferometric scheme based on split detectors can be used to simultaneously obtain information on the longitudinal and spatial phases. A quantum analysis of the measurement noise is then

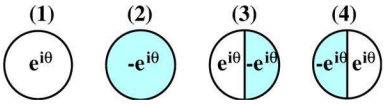

Fig. 1. The four possible phase-front profiles resulting from the transformation on the input $u_0(x)$ beam.

presented. We identify the maximum number of encodeable longitudinal phases at the shot noise limit (SNL). We then show that using squeezed light, one can overcome the SNL and thus the number of encoding possibilities can be further increased. Consequently, we analyze the spectral properties of the signal and noise of the encoded beam. We compare single and consecutive measurement techniques, and show that consecutive measurements provides an improved signal-to-noise ratio (SNR), while ensuring compatibility with squeezed light frequency regimes.

II. Classical Phase Coding

In this paper, we consider the detection of a specific set of possible transverse and longitudinal phase transformations of a TEM_{00} field. To detect such transformations requires a spatially selective detection system such as a CCD array, split detector or specifically configured homodyne detector [18]. Split detectors in particular offer fast response (in the gigahertz regime) and high efficiency. These factors are critical in high bandwidth optical systems. We, therefore, concentrate our analysis on split detectors in this paper.

Restricting our analysis to one-dimension, the set of eigenmodes that best describe split detectors is the flipped eigenmode basis [19]. The normalized beam amplitude function $u_{\mathrm{f}n}(x)$ for the flipped eigenmode (henceforth termed simply the *flipped mode*) of order n is defined by a TEM_{pq} mode with a π phase flip at the center of the mode [19], [20]

$$u_{\mathrm{f}n}(x) = \begin{cases} u_n(x), & \text{for } x > 0 \\ -u_n(x), & \text{for } x < 0 \end{cases} \tag{1}$$

where $u_n(x)$ is the one-dimensional normalized beam amplitude function of a TEM_{pq} mode.

To encode split detector compatible information on the phase-front of a TEM_{pq} beam, π phase flips of this kind should, therefore, be applied. This results in four possible bit values, corresponding to the four possible two-pixel π phase shifts on $u_0(x)$, as illustrated in Fig. 1. A longitudinal phase factor $e^{i\theta}$ is also introduced to increase the total number of encoding possibilities. The phase-coded modes introduced in Fig. 1 are described by the following transformation:

$$u_0(x) \xrightarrow{(1)} e^{i\theta}u_0(x) \tag{2}$$
$$u_0(x) \xrightarrow{(2)} -e^{i\theta}u_0(x) \tag{3}$$
$$u_0(x) \xrightarrow{(3)} e^{i\theta}u_{\mathrm{f}0}(x) \tag{4}$$
$$u_0(x) \xrightarrow{(4)} -e^{i\theta}u_{\mathrm{f}0}(x). \tag{5}$$

In order to resolve the four possible phase-front profiles of (2)–(5), we propose the phase coding scheme shown in Fig. 2. Beam 1 undergoes a phase-front transformation upon traversing

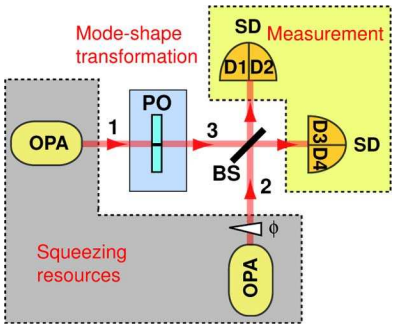

Fig. 2. Two-pixel phase coding scheme. BS: beam-splitter, SD: split-detector. D1, D2, D3, D4: labels for the split detector segments. OPA: optical parametric amplifier, PO: phase object.

a phase object (PO), resulting in transformed beam 3. Subsequently, beams 2 and 3 are combined on a 50:50 beam-splitter and the two output beams are detected using split detectors. Each field can be represented by the positive frequency part of its mean electric field $\mathcal{E}^+e^{-i\omega t}$, where ω is the optical frequency. We are interested in the transverse information described fully by the slowly varying field envelope $\mathcal{E}^+$. For a measurement performed in an exposure time T, the mean field for input beams 1 and 2 are given by

$$\mathcal{E}_1^+(x,t) = i\sqrt{\frac{\hbar\omega}{2\epsilon_0 cT}}\alpha_0(t)u_0(x) \tag{6}$$
$$\mathcal{E}_2^+(x,t) = ie^{i\phi}\sqrt{\frac{\hbar\omega}{2\epsilon_0 cT}}\beta_0(t)u_0(x) \tag{7}$$

where $\alpha_0(t)$ and $\beta_0(t)$ are the coherent amplitudes of the TEM_{00} input beams 1 and 2, respectively. ϕ represents the longitudinal phase of beam 2.

The photocurrent signal for all segments of the split detectors are then calculated. The photocurrent signal is related directly to the mean photon number, given by $n_{x<0} = (2\epsilon_0 cT/\hbar\omega)\int_{-\infty}^{0} dx\mathcal{E}^\dagger\mathcal{E}$ and $n_{x>0} = (2\epsilon_0 cT/\hbar\omega)\int_{0}^{\infty} dx\mathcal{E}^\dagger\mathcal{E}$, for split detector $x < 0$ and $x > 0$ segments, respectively.

We consider four possible combinations for the pair-wise photocurrent addition and subtraction, with the photocurrent signal terms shown in Table I. The table shows that for both combinations $\mathbf{A}$ and $\mathbf{B}$, all four mode transformations have identical signal values of 0 and $\alpha_0(t)^2 + \beta_0(t)^2$, respectively. Thus, the phase-front transformation on the input beam cannot be determined. Combinations $\mathbf{C}$ and $\mathbf{D}$, on the other hand, allow the $u_{\mathrm{f}0}(x)$ and $u_0(x)$ modes to be detected respectively with a sign change for the different phase-front transformation. Moreover, the phase coding scheme is sensitive to the differential longitudinal phase $(\theta - \phi)$.

Note that ϕ has to be calibrated in order to determine the encoded phase θ. ϕ is scanned between 0 and π until an extremum value of $\pm 2\alpha\beta$ is obtained. For example, for combination $\mathbf{D}$, a value of $-2\alpha_0\beta_0$ for $\phi = \phi_{\mathrm{opt}}$ tells us that the encoded mode-shape is $-u_0(x)$ with longitudinal phase $\theta = \pi/2 - \phi_{\mathrm{opt}}$. The maximal signal is obtained for a phase difference of $\phi - \theta = \pi/2$. This interferometric scheme, therefore, enables a unique distinction of all of the four phase-front transforms given in (2)–(5).

TABLE I
PHOTO-CURRENT SIGNAL TERMS

Transformed Mode	Combination **A** $(D_1 - D_2) + (D_3 - D_4)$	Combination **B** $(D_1 + D_2) + (D_3 + D_4)$	Combination **C** $(D_1 - D_2) - (D_3 - D_4)$	Combination **D** $(D_1 + D_2) - (D_3 + D_4)$
$e^{i\theta}u_0(x)$	0	$\alpha_0^2 + \beta_0^2$	0	$2\alpha_0\beta_0\sin(\phi-\theta)$
$-e^{i\theta}u_0(x)$	0	$\alpha_0^2 + \beta_0^2$	0	$-2\alpha_0\beta_0\sin(\phi-\theta)$
$e^{i\theta}u_{\mathrm{f}0}(x)$	0	$\alpha_{\mathrm{f}0}^2 + \beta_0^2$	$2\alpha_{\mathrm{f}0}\beta_0\sin(\phi-\theta)$	0
$-e^{i\theta}u_{\mathrm{f}0}(x)$	0	$\alpha_{\mathrm{f}0}^2 + \beta_0^2$	$-2\alpha_{\mathrm{f}0}\beta_0\sin(\phi-\theta)$	0

TABLE II
PHOTO-CURRENT NOISE

Transformed Mode	Combination **C** $(D_1 - D_2) - (D_3 - D_4)$	Combination **D** $(D_1 + D_2) - (D_3 + D_4)$
$e^{i\theta}u_0(x)$	$-\beta_0\delta\hat{X}_{a_{\mathrm{f}0}}^{(\phi-\theta+\pi/2)} + \alpha_0\delta\hat{X}_{b_{\mathrm{f}0}}^{(\theta-\phi+\pi/2)}$	$-\beta_0\delta\hat{X}_{a_0}^{(\phi-\theta+\pi/2)} + \alpha_0\delta\hat{X}_{b_0}^{(\theta-\phi+\pi/2)}$
$-e^{i\theta}u_0(x)$	$\beta_0\delta\hat{X}_{a_{\mathrm{f}0}}^{(\phi-\theta+\pi/2)} - \alpha_0\delta\hat{X}_{b_{\mathrm{f}0}}^{(\theta-\phi+\pi/2)}$	$\beta_0\delta\hat{X}_{a_0}^{(\phi-\theta+\pi/2)} - \alpha_0\delta\hat{X}_{b_0}^{(\theta-\phi+\pi/2)}$
$e^{i\theta}u_{\mathrm{f}0}(x)$	$-\beta_0\delta\hat{X}_{a_{\mathrm{f}0}}^{(\phi-\theta+\pi/2)} + \alpha_{\mathrm{f}0}\delta\hat{X}_{b_0}^{(\theta-\phi+\pi/2)}$	$-\beta_0\delta\hat{X}_{a_0}^{(\phi-\theta+\pi/2)} + \alpha_{\mathrm{f}0}\delta\hat{X}_{b_{\mathrm{f}0}}^{(\theta-\phi+\pi/2)}$
$-e^{i\theta}u_{\mathrm{f}0}(x)$	$\beta_0\delta\hat{X}_{a_{\mathrm{f}0}}^{(\phi-\theta+\pi/2)} - \alpha_{\mathrm{f}0}\delta\hat{X}_{b_0}^{(\theta-\phi+\pi/2)}$	$\beta_0\delta\hat{X}_{a_0}^{(\phi-\theta+\pi/2)} - \alpha_{\mathrm{f}0}\delta\hat{X}_{b_{\mathrm{f}0}}^{(\theta-\phi+\pi/2)}$

III. QUANTUM PHASE CODING

We would like to quantify the maximum number of encoding possibilities, whose limit is ultimately set by the SNL. The SNL is identified and ways to improve the sensitivity of the measurement using squeezed light are shown. Consider the field operators in the sideband frequency domain, Ω. For brevity, we do not explicitly denote the frequency dependence for the field operators hereon, which are given by

$$\hat{\mathcal{E}}_1^{+} = i\sqrt{\frac{\hbar\omega}{2\epsilon_0 cT}}\left(\alpha_0 u_0(x) + \sum_{n=0}^{\infty}\delta\hat{a}_n u_n(x)\right) \tag{8}$$

$$\hat{\mathcal{E}}_2^{+} = ie^{i\phi}\sqrt{\frac{\hbar\omega}{2\epsilon_0 cT}}\left(\beta_0 u_0(x) + \sum_{n=0}^{\infty}\delta\hat{b}_n u_n(x)\right) \tag{9}$$

where the first terms are the coherent amplitude of the $u_0(x)$ mode. The second terms are the quantum fluctuations $\delta\hat{a} = \hat{a} - \langle\hat{a}\rangle$ and $\delta\hat{b} = \hat{b} - \langle\hat{b}\rangle$, with $\hat{a}$ and $\hat{b}$ being annihilation operators, of beams 3 and 2 in Fig. 2, respectively. Depending on the phase-front transformation on beam 1, the field operator describing beam 3 is given by

$$\begin{aligned}
\hat{\mathcal{E}}_3^{(1)+} &= ie^{i\theta}\sqrt{\frac{\hbar\omega}{2\epsilon_0 cT}}\left(\alpha_0 u_0(x) + \sum_{n=0}\delta\hat{a}_n u_n(x)\right)\\
\hat{\mathcal{E}}_3^{(2)+} &= -ie^{i\theta}\sqrt{\frac{\hbar\omega}{2\epsilon_0 cT}}\left(\alpha_0 u_0(x) + \sum_{n=0}\delta\hat{a}_n u_n(x)\right)\\
\hat{\mathcal{E}}_3^{(3)+} &= ie^{i\theta}\sqrt{\frac{\hbar\omega}{2\epsilon_0 cT}}\left(\alpha_{\mathrm{f}0} u_{\mathrm{f}0}(x) + \sum_{n=0}\delta\hat{a}_{\mathrm{fn}} u_{\mathrm{fn}}(x)\right)\\
\hat{\mathcal{E}}_3^{(4)+} &= -ie^{i\theta}\sqrt{\frac{\hbar\omega}{2\epsilon_0 cT}}\left(\alpha_{\mathrm{f}0} u_{\mathrm{f}0}(x) + \sum_{n=0}\delta\hat{a}_{\mathrm{fn}} u_{\mathrm{fn}}(x)\right)
\end{aligned} \tag{10}$$

where the superscript denotes the transformations corresponding to (2)–(5).

The RF photocurrent for all segments of the split detectors are then calculated similarly to the previous section. The overlap integrals in the expressions for the photocurrent sum and difference operators are simplified using the respective orthogonality properties of the $u_n(x)$ and $u_{fn}(x)$ modes [21]–[23].

The photocurrent noise corresponding to combinations **C** and **D** are shown in Table II, where we have defined the quadrature noise operator as $\delta\hat{X}_a^{\psi} = e^{-i\psi}\delta\hat{a} + e^{i\psi}\delta\hat{a}^{\dagger}$. We assume the phase-front transformation is lossless. Therefore, the photon statistics of the transformed field is unchanged relative to the initial field, so that $|\alpha_{f0}| = |\alpha_0| = |\alpha|$ and $\langle(\delta\hat{X}_{a_{f0}}^{\psi})^2\rangle = \langle(\delta\hat{X}_{a_0}^{\psi})^2\rangle = \langle(\delta\hat{X}_a^{\psi})^2\rangle$. Table II, therefore, suggests that squeezing the input beams 1 and 2 will lead to enhanced noise performances.

We now determine the maximum number of encoding possibilities in our phase coding scheme. The encoding limit is determined by the minimum longitudinal phase difference detectable $\Delta\theta_{\min}$. This corresponds to when the signal and noise variances are equal (i.e., SNR = 1).

The SNR is calculated by taking the ratio of the signal and noise variances, given by $\langle n\rangle^2$ and $\langle\delta\hat{n}^2\rangle$, respectively. The corresponding SNR of the measurement for the $\pm u_0$ and $\pm u_{f0}$ modes are denoted by $\mathcal{R}_{\mathbf{C}}$ and $\mathcal{R}_{\mathbf{D}}$, respectively, and have the same form given by

$$\mathcal{R} = \frac{4\alpha^2\beta_0^2\sin^2(\phi-\theta)}{\alpha^2\langle(\delta\hat{X}_{b_0}^{\psi})^2\rangle + \beta^2\langle(\delta\hat{X}_a^{\psi})^2\rangle}. \tag{11}$$

If the input beams are coherent with $\langle(\delta\hat{X}_a^{\psi})^2\rangle = \langle(\delta\hat{X}_{b_0}^{\psi})^2\rangle = 1$, then $\mathcal{R}^{\mathrm{coh}} = 4\alpha^2\beta_0^2\sin^2(\phi-\theta)/(\alpha^2+\beta_0^2)$. This coherent state SNR serves as a benchmark for which to compare the SNR achievable with squeezing. For quadrature squeezed input beams 1 and 2 (i.e., $\langle(\delta\hat{X}_a^{\psi})^2\rangle, \langle(\delta\hat{X}_b^{\psi})^2\rangle < 1$), we see directly that $\mathcal{R}^{\mathrm{sqz}} > \mathcal{R}^{\mathrm{coh}}$. Squeezed input beams, therefore, increase the SNR achievable for all possible mode transformations.

Note that in the limit $\beta \gg \alpha$, our phase imaging scheme reduces to that of a homodyne measurement with a SNR given by $\mathcal{R}_{\mathrm{hom}} = 4\alpha^2\sin^2(\phi-\theta)/\langle(\delta\hat{X}_a^{\psi})^2\rangle$. The signal and noise contribution arise from the transverse mode defined by the local oscillator mode-shape.

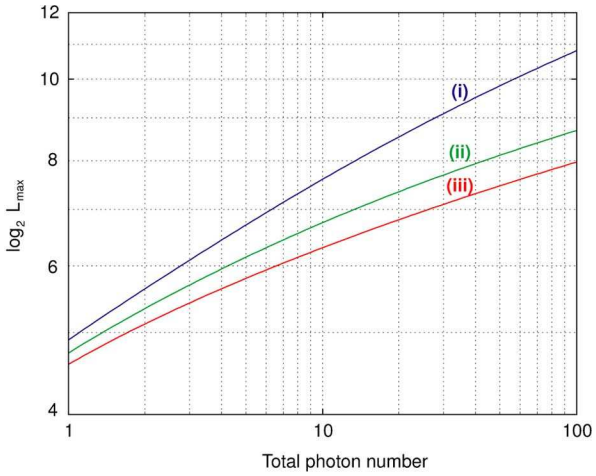

Fig. 3. Maximum $\log_2 L_{\max}$ levels of the phase-front coding scheme as a function of the total mean number of photons/(Hz.s) utilized in the protocol. (i) Both input beams amplitude squeezed, (ii) beam 1 amplitude squeezed and beam 2 coherent, (iii) both input beams coherent.

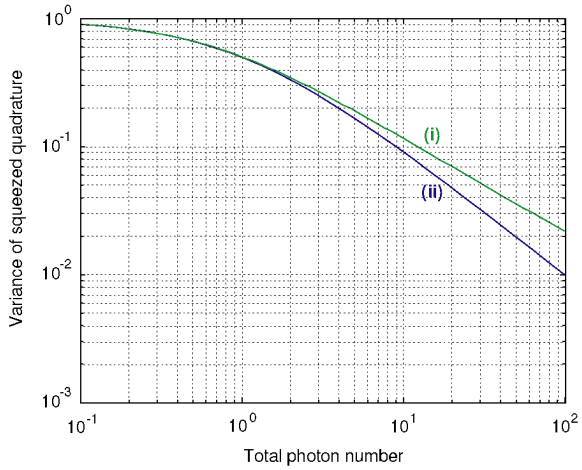

Fig. 4. Shot noise normalized level of squeezing required to achieve the optimum number of encodeable levels as a function of the total mean number of photons per bandwidth–time utilized in the protocol. (i) Beam 1 amplitude squeezed and beam 2 coherent, (ii) both input beams amplitude squeezed.

The minimum longitudinal phase difference detectable (i.e., SNR $= 1$) is given by

$$\Delta\theta_{\min} = \sin^{-1}\sqrt{\frac{\alpha^2\langle(\delta\hat{X}_{b_0})^2\rangle + \langle(\delta\hat{X}_a)^2\rangle\beta_0^2}{4\alpha^2\beta_0^2}} \qquad (12)$$

where we have assumed that the phase difference between beams 2 and 3 have been optimized to $\phi - \theta = \pi/2$. Since the longitudinal phase of beam 3 is determined modulo π, the total number of resolvable phase levels is $\pi/\Delta\theta_{\min}$, which scales with the power of the read-out optical beam α. Note that this contrasts with conventional optical storage devices which are restricted to only two encodeable values (i.e., "0" and "1"), with a SNR proportional to the power of the read-out beam.

Including the four possible transverse encoding combinations, the total number of encodeable levels for our phase coding scheme is, therefore, given by

$$L_{\max} = \frac{4\pi}{\Delta\theta_{\min}}. \qquad (13)$$

We now consider $L_{\max}$ levels for a fixed optical power and show how this can be improved via squeezing. The mean number of photons per bandwidth–time in an optical field $\bar{n}$ can be related to its coherent amplitude α, amplitude $\langle(\delta\hat{X}^+)^2\rangle$ and phase $\langle(\delta\hat{X}^-)^2\rangle$ quadrature noise variances by

$$\bar{n} = \frac{1}{4}(\alpha^2 + \langle(\delta\hat{X}^+)^2\rangle + \langle(\delta\hat{X}^-)^2\rangle - 2). \qquad (14)$$

The first thing to note is that for squeezed states, $\bar{n}$ is non-zero even when $\alpha = 0$. Indeed, as the squeezing increases (for amplitude squeezing $\langle(\delta\hat{X}^+)^2\rangle \to 0$ and $\langle(\delta\hat{X}^-)^2\rangle \to \infty$) $\bar{n}$ increases monotonically. With regards to our phase-front detection scheme, these photons do not contribute to the signal, α and, therefore, for a given optical power, $\bar{n}$, a balance must be obtained between using photons to minimize the noise (maximize the squeezing), and to maximize the signal (maximize α).

In this paper, $L_{\max}$ levels for a fixed optical power was maximized numerically. This was performed over all possible ratios of photons used to minimize the noise, and those used to maximize the signal. The total optical power is the sum of the number of photons in each of the input beams, each individually given by (14). We considered three cases. In the first case, to provide a benchmark, we considered $L_{\max}$ levels when no squeezing was available, and both input beams were coherent. In the second case, squeezing was allowed for beam 1 but beam 2 was coherent. In the third case, both input beams were squeezed. The maximum $L_{\max}$ levels for each of these cases is shown in Fig. 3. We see that by far, the best $L_{\max}$ levels is achieved when both beams are allowed to be squeezed, with $\sim$25% capacity improvement over the coherent state case when 100 photons per bandwidth–time are used. In the case of only one squeezed beam, the capacity improvement is $\sim$10%.

Of course, due to decoherence and inefficiencies, arbitrary levels of squeezing are not available. Therefore, it is interesting to consider not only the maximum $L_{\max}$ levels that can be achieved, but also whether the amount of squeezing required to achieve it are feasible. The amount of squeezing required to achieve the maximum $L_{\max}$ levels for a given total photon number are shown in Fig. 4 for both the one squeezed beam and two squeezed beam cases. In both cases, when less than 10 photons per time are utilized, squeezing levels below 10 dB are required. Although challenging, such levels of squeezing are experimentally achievable. For more than 10 photons per bandwidth–time however, the level of squeezing required to achieve the maximum encodeable levels fast becomes unfeasible. Therefore, utilizing squeezed light in the phase-front detection scheme presented here will only be beneficial when less than 10 photons are available per measurement interval.

Coherent beams can allow a large number of encodeable levels. Assuming similar parameters to CD technology and idealized shot noise limited performance, we can encode up to 5000 levels, for a 1-mW beam ($\lambda = 780$ nm, spot size $= 2.1$ μm) in the limit that $\beta_0 \gg \alpha$, during a 10-μs measurement time (where SNR $= 60$ dB, based on current technology specifications). Therefore, up to 12-bit encoding per site is possible. The capacity of CDs can be potentially increased to 8 GB. For

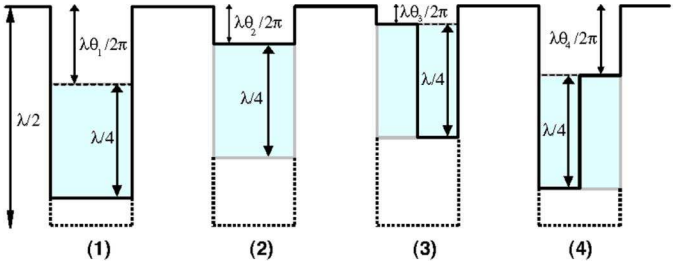

Fig. 5. Examples of bit encoding allowing denser information storage on optical discs. The binary information is encoded in the transverse and longitudinal phases of the reflected read-out laser beam. The depth of the "pit" can range from discrete values between 0 and $\lambda/2$. Hence, $\theta_1 \in (\lambda/4, \lambda/2]$ and $\theta_2 \in (0, \lambda/4]$, where λ is the laser wavelength and θ is the longitudinal phase shift of the laser beam. Note that the "pit" depth is half that of the phase shift experienced by the read-out laser beam due to a round-trip propagation from the optical disc.

lower SNR standards (SNR $= 50$), 19-bit encoding per site can be achieved, giving a capacity increase of up to 13 GB. Squeezing can further improve the maximum encodeable levels in the limit of low laser power. Similar to the multibit encoding schemes of P. Török's group [1], our scheme is a significant improvement over current technology where only one bit per site is encoded.

IV. Potential Application to Optical Storage

In this section, we investigate the compatibility of our phase coding scheme with an optical disc read-out scheme.

A. Optical Disc Scheme

In conventional CDs, the information is encoded in binary format, by burning physical indentations (commonly termed "pits") on the disc. Regions where no physical indentations exist are termed "lands." A transition between "pit" and "land" encodes for "1," whereas no transition encodes for "0" [24]. The reflected beam intensity from a focussed laser beam onto the disc allows bit read-out, as the beam undergoes large diffractive losses when impinging on a "land"–"pit" transition.

We propose to store more than one level on a single "pit" site, by encoding levels as shown on Fig. 5. The information is contained in the longitudinal and transverse phase domains for each "pit." The longitudinal phase is determined by the depth of the "pit," $\lambda\theta/(2\pi)$, while the transverse phase profile is determined from its shape. By assuming that the phase transformation structure is larger than the diffraction limit, and since the longitudinal phase shift is not constrained by the diffraction limit, we can assume that the reflected field has the same transverse profile as in Fig. 1. Note that when the transverse structure is below the diffraction limit, the beam profiles of Fig. 1 cannot be generated [28]. In this situation, two approaches can be used to obtain the transverse profile of the read-out beam: 1) by using Maxwell's equations and/or 2) by performing an initial experimental calibration of all the possible transverse mode profiles, since we posses *a priori* knowledge of the transverse phase structures.

Therefore, the reflection of the read-out beam has one of the four possible transverse mode profiles, $\pm u_0(x)$ or $\pm u_{f0}(x)$, with an additional global phase shift θ. This reflected beam (i.e., beam 3) can then be combined with beam 2 on a 50:50 beamsplitter, as shown in Fig. 2 to perform the phase information decoding.

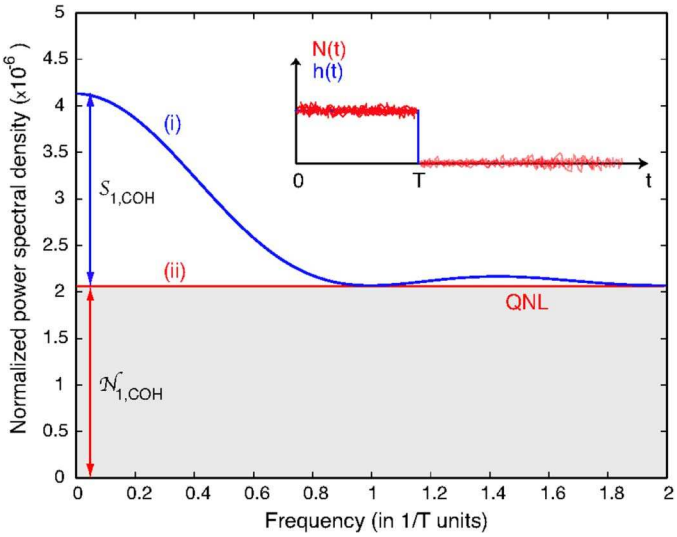

Fig. 6. The normalized (i) signal $\mathcal{S}_1(\nu)$ and (ii) noise $\mathcal{N}_1(\nu)$ PSD for a single measurement in a time interval T. $\mathcal{S}_1(0)$ and $\mathcal{N}_1(0)$ are the maximum signal and noise powers at dc. The inset shows the sequence corresponding to a single top hat measurement window, $h(t)$, with $N(t)$ photons.

Thus far, our analysis has not considered the spectral properties of the read-out signal and noise. Since the optical disc is spinning and the laser read-out time is limited, the spectral power density of a realistic optical disc detection differs from that of an idealized static phase sensing scheme. We examine these issues in the following subsections.

B. Spectral Power Density for a Single Measurement

We first consider the information extraction from a time-limited static disc read-out. N photons are detected in a time interval T, as represented on the inset of Fig. 6, where the integrated photocurrent provides the encoded information.

Using a single top hat function as a time measurement window, the Wiener–Khinchine relation yields the signal power spectral density (PSD), $\mathcal{S}_1(\nu)$. In the case of a double sided power spectrum [25], the signal PSD is given by

$$\mathcal{S}_1(\nu) = T\left[\int_{-\infty}^{\infty} s(\nu')\cdot \mathrm{sinc}(\pi T(\nu'-\nu))d\nu'\right]^2 \quad (15)$$

where ν is the frequency and $s(\nu)$ is the signal linear spectral density in the limit of an infinite time measurement, defined as $s(\nu) = \sqrt{\mathcal{S}(\nu)}$. $\mathcal{S}(\nu)$ is the number of photons per bandwidth–time.

For a single measurement, $s(\nu)$ is given by $s(\nu) = N\delta(\nu)$, where N is the number of photons per time in the signal and $\delta(\nu)$ is a delta function centred at dc. Thus, (15) becomes

$$\mathcal{S}_1(\nu) = N^2 T \mathrm{sin\,c}^2(\pi T\nu) \quad (16)$$

where the signal PSD has a squared cardinal sine distribution with a maximum at dc. Fig. 6 shows the normalized signal and noise PSD.

The noise PSD, $\mathcal{N}(\nu) = \xi(\nu)^2$ is now obtained. We assume that read-out lasers are shot noise limited. Thus, the noise linear spectral density is white and proportional to $\sqrt{N}$, given

by $\xi(\nu) = \sqrt{N}$. The integration time in our measurement is T and the noise PSD is given by

$$\mathcal{N}_1(\nu) = NT\left[\int_{-\infty}^{\infty} \mathrm{sinc}(\pi T(\nu' - \nu))d\nu'\right]^2 = \frac{N}{T} \qquad (17)$$

where the white noise spectrum has an amplitude of $\sqrt{N/T}$. We have chosen $N = 1/T^2$ for Fig. 6 such that the noise power is approximately equal to the maximum signal power.

The typical measurement time of a DVD device is $T = 0.1$ μs, corresponding to $N = 10^{14}$ photons/s for a read-out laser of 20 μW power at a wavelength of $\lambda = 1$ μm. The signal spectrum, therefore, is in the dc to 10 MHz regime. Improvements on the measurement sensitivity beyond the SNL thus requires broad-band squeezing from dc to 10 MHz. Although low frequency squeezing has recently been demonstrated [26], [27], many technical challenges exist.

An alternative solution, compatible with current technology, could be the sampling or modulation of the read-out beam to artificially shift the signal to a higher frequency range. For optical discs rotating at approximately 10 bit/μs (4.32 Mb/s for CDs, and 26.16 Mb/s for DVDs), the sampling or modulation frequencies can be at least 1 GHz, which is compatible with squeezing frequency ranges. However, the disadvantage of such an approach is that the photon number in the signal sidebands is low. The majority of the photons are still distributed in the frequency regime around dc. Thus, the improvement in the SNR may not be significant.

C. Spectral Power Density for Consecutive Measurements

We now propose to perform consecutive "pit" measurements where the center of the signal PSD is shifted to a higher frequency. Two consecutive measurements of the variable $N(t)$ during two time intervals of length T, separated by a delay T', is shown schematically on the inset of Fig. 7.

The difference between two consecutive measurements yields a signal PSD given by the contribution of each individual sine-wave at frequency ν, to the total signal, and averaging over all possible initial phases Θ, giving

$$\mathcal{S}_2(\nu) = \mathcal{S}(\nu)\eta_2(\nu) \qquad (18)$$

where $\eta_2(\nu)$ is given by

$$\eta_2(\nu) = \kappa\left\langle\left(\int_0^T - \int_{T+T'}^{2T+T'} \sin(2\pi\nu t + \Theta)dt\right)^2\right\rangle$$

and where κ is a normalization constant. Note that a similar calculation can be applied to the single measurement case.

The signal and noise PSD for $T' = 0$ are shown in Fig. 7. The signal PSD is shifted to the MHz frequency regime (which is more compatible with routinely obtained experimental squeezing frequency regimes). The signal PSD maximum is at $\nu \sim 0.35/T$ for $T' = 0$. This is also the regime where the bandwidth is maximum. Increasing T' shifts the maximum signal power to lower frequencies and sharpens the distribution. Thus, the bandwidth reduces with increasing T'. For $T' = T$,

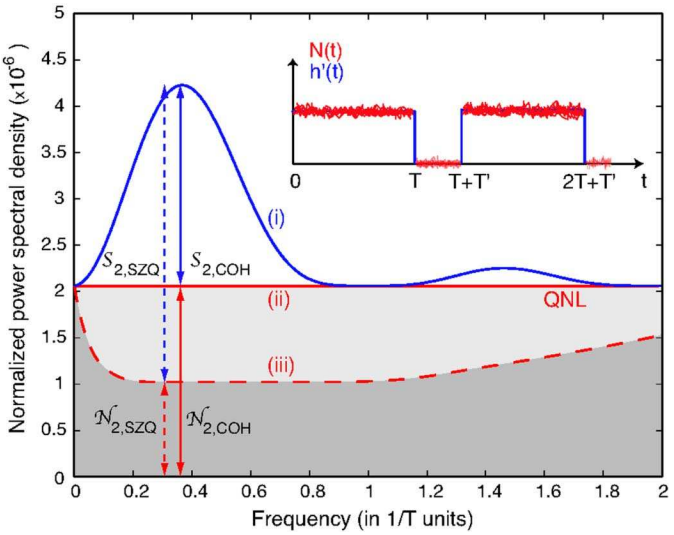

Fig. 7. (i) Normalized signal $\mathcal{S}_2(\nu)$, (ii) shot noise and (iii) squeezed noise $\mathcal{N}_2(\nu)$ PSD for two consecutive measurements of time intervals T separated by a delay $T' = 0$. The maximum signal and noise powers are respectively, $\mathcal{S}_{2,\mathrm{COH}}$ and $\mathcal{N}_{2,\mathrm{COH}}$, for a coherent state read-out laser at $\nu \sim 0.35/T$. In the case of a squeezed read-out laser, the maximum signal and noise powers are denoted by $\mathcal{S}_{2,\mathrm{SQZ}}$ and $\mathcal{N}_{2,\mathrm{SQZ}}$, respectively. The inset shows the sequence corresponding to two consecutive measurements.

the maximum signal power is for example $\sim$1.5 times larger than that for the $T' = 0$ case and occurs at $\nu \sim 0.2/T$, whereas the bandwidth reduces by half. T' can thus be tuned to obtain an optimum for signal power, bandwidth and compatibility with squeezing frequencies.

The SNR of interest in our optical memory scheme corresponds to that of a single frequency ν, as defined in (11). Therefore, our proposed optical memory scheme will require a frequency mixer or bandpass filter centred at ν, where the measurement SNR is maximum.

Differential consecutive measurements is a technique already employed in current optical disc devices, as it allows the cancellation of common-mode classical noise, provided that the phase of the read-out laser is well calibrated in a "pit"-to-"pit" measurement. Furthermore, the maximum of the normalized PSD for consecutive measurements is slightly larger than that for the single measurement case, assuming a coherent state read-out laser with the same parameters. If a broad-band 3-dB squeezed state is used as the read-out laser, the SNR doubles for consecutive measurements. However the SNR improvement for the case of a single measurement is negligible. This is because low frequency noise sources (e.g., acoustic noise) overwhelm the squeezing.

V. Conclusion

We have presented a scheme to perform longitudinal and transverse spatial phase coding of continuous-wave optical beams. We have shown that by performing selective combinations of photocurrent addition and subtraction, the phase-coded signal can be extracted. In order to optimize the phase signal, the longitudinal phase of beam 2 has to be calibrated and optimized such that $\phi = \pi/2 + \theta$. While current CD technologies are limited by a number of different noise sources, such as

thermal-Johnson noise and electronic noise, our analysis assumes shot noise limited performance. The maximum number of encoding possibilities for this regime was calculated, suggesting significant improvement with our phase coding scheme. However, by using squeezed light, the SNL can be overcome and thus the maximum number of encodeable levels increased. We then presented a possible application of our phase coding scheme in increasing the capacities of optical storage devices. We analyzed the performance of single measurement techniques and showed that the signal and noise PSD are centred around dc sideband frequencies. We then analyzed the PSD of differential consecutive measurements and showed that the PSD spectrum is shifted to higher sideband frequencies. In order to extract the phase signal, frequency mixing or narrow bandpass filtering techniques can be used. The differential consecutive measurement technique provides a good SNR while ensuring compatibility with squeezing frequencies.

Our phase coding scheme can be extended to implement a multipixel array detector. Delaubert *et al.* [28] has performed a quantum study of multipixel array detection and shown that it is possible to perform multipixel transverse spatial phase encoding. Possible implementation of a multipixel scheme would require the incorporation of multiple interferometers and the use of multisqueezed beams or a multimode OPO system [29].

ACKNOWLEDGMENT

The authors would like to thank N. Treps and C. C. Harb for discussions.

REFERENCES

[1] P. Török and F.-J. Kao, *Optical Imaging and Microscopy*. New York: Springer-Verlag, 2003.
[2] M. I. Kolobov and P. Kumar, *Opt. Lett.*, vol. 18, pp. 849–851, 1993.
[3] I. V. Sokolov, *J. Opt. B: Quantum Semiclass. Opt.*, vol. 2, pp. 179–183, 2000.
[4] A. F. Abouraddy, B. E. A. Saleh, A. V. Sergienko, and M. C. Teich, *Phys. Rev. Lett.*, vol. 87, p. 123602, 2001.
[5] T. B. Pittman, Y. H. Shih, D. V. Strekalov, and A. V. Sergienko, *Phys. Rev. A*, vol. 52, pp. 3429–3432, 1995.
[6] R. S. Bennick, S. J. Bentley, and R. W. Boyd, *Phys. Rev. Lett.*, vol. 92, p. 033601, 2004.
[7] R. S. Bennink, S. J. Bentley, and R. W. Boyd, *Phys. Rev. Lett.*, vol. 89, p. 113601, 2002.
[8] A. Gatti, E. Brambilla, M. Bache, and L. A. Lugiato, *Phys. Rev. Lett.*, vol. 93, p. 093602, 2004.
[9] A. Gatti, E. Brambilla, and L. A. Lugiato, *Phys. Rev. Lett.*, vol. 90, p. 133603, 2003.
[10] M. I. Kolobov, *Rev. Mod. Phys.*, vol. 71, pp. 1539–1589, 1999.
[11] L. A. Lugiato, A. Gatti, and E. Brambilla, *J. Opt. B: Quantum Semiclass. Opt.*, vol. 4, pp. 176–183, 2002.
[12] T. Santhanakrishnan, N. Krishna Mohan, M. D. Kothiyal, and R. S. Sirochi, *J. Opt.*, vol. 24, pp. 109–112, 1995.
[13] C. A. Putman, B. G. De Grooth, N. F. Van Hulst, and J. Greve, *J. Appl. Phys.*, vol. 72, pp. 6, 12, 1992.
[14] H.-L. Guo, C.-X. Liu, Z.-L. Li, J.-F. Duan, X.-H. Han, B.-Y. Chen, and D.-Z. Zhang, *Chin. Phys. Lett.*, vol. 20, pp. 950–952, 2003.
[15] R. M. Simmons, J. T. Finer, S. Chu, and J. A. Spudich, *Biophys. J.*, vol. 70, pp. 1813–1822, 1996.
[16] F. Gittes and C. F. Schmidt, *Opt. Lett.*, vol. 23, pp. 7–9, 1998.
[17] W. Denk and W. W. Webb, *Appl. Opt.*, vol. 29, pp. 2382–2391, 1990.
[18] M. T. L. Hsu, V. Delaubert, P. K. Lam, and W. P. Bowen, *J. Opt. B: Quantum Semiclass. Opt.*, vol. 6, pp. 495–501, 2004.
[19] C. Fabre, J. B. Fouet, and A. Maître, *Opt. Lett.*, vol. 76, pp. 76–78, 2000.
[20] V. Delaubert, D. A. Shaddock, P. K. Lam, B. C. Buchler, H.-A. Bachor, and D. E. McClelland, *J. Opt. A: Pure Appl. Opt.*, vol. 4, pp. 393–399, 2002.
[21] N. Treps, U. Andersen, B. C. Buchler, P. K. Lam, A. Maître, H.-A. Bachor, and C. Fabre, *Phys. Rev. Lett.*, vol. 88, p. 203601, 2002.
[22] N. Treps, N. Grosse, W. P. Bowen, C. Fabre, H.-A. Bachor, and P. K. Lam, *Science*, vol. 301, pp. 940–943, 2003.
[23] N. Treps, N. Grosse, W. P. Bowen, M. T. L. Hsu, A. Maître, C. Fabre, H.-A. Bachor, and P. K. Lam, *J. Opt. B: Quantum Semiclass. Opt.*, vol. 6, pp. S664–S674, 2004.
[24] E. W. Williams, *The CD-ROM and Optical Disc Recording Systems*. Oxford, U.K.: Oxford Univ. Press, 1996.
[25] L. W. Couch, *Digital and Analog Communication Systems*. New York: Macmillan, 1993.
[26] K. McKenzie, N. Grosse, W. P. Bowen, S. E. Whitcomb, M. B. Gray, D. E. McClelland, and P. K. Lam, *Phys. Rev. Lett.*, vol. 93, p. 161105, 2004.
[27] J. Laurat, T. Coudreau, G. Keller, N. Treps, and C. Fabre, *Phys. Rev. A*, vol. 70, p. 042315, 2004.
[28] V. Delaubert, N. Treps, G. Bo, and C. Fabre, *Phys. Rev. A*, vol. 73, p. 013820, 2006.
[29] L. Lopez, S. Gigan, N. Treps, A. Maître, C. Fabre, and A. Gatti, *Phys. Rev. A*, vol. 72, p. 013806, 2005.

Magnus T. L. Hsu received the B.Sc. (hons.) degree from the University of Adelaide, Adelaide, Australia. He is currently working toward the Ph.D. degree at the ARC COE for Quantum Optics, Department of Physics, Australian National University, Canberra, Australia.

His research interests include quantum optics, quantum imaging and slow light.

Vincent Delaubert received the M.Sc. degree from the Université Paris sud, Orsay, France. He is currently working toward the Ph.D. degree at the Laboratoire Kastler Brossel, Université Pierre et Marie Curie, Paris, France and the ARC COE for Quantum Optics, Department of Physics, Australian National University, Canberra, Australia.

His research interests include quantum imaging and quantum optics.

Warwick P. Bowen received the Ph.D. degree from the Australian National University, Canberra, Australia.

He is a Lecturer in physics at the University of Otago, Dunedin, New Zealand. Prior to that position he worked at the California Institute of Technology, Pasadena. His primary research interests involve taking technology developed in the fields of atom and quantum optics and applying it to other fields such as biophotonics and nanophotonics. He is a Principal Investigator in the MacDiarmid Institute for Advanced Materials and Nanotechnology, University of Otago.

Claude Fabre is a Professor at the Laboratoire Kastler Brossel, Université Pierre et Marie Curie, Paris, France. His research interests include quantum optics and quantum imaging.

Hans-A. Bachor received the Ph.D. degree from the Universität Hannover, Hannover, Germany.

He is currently an Australian Research Council Federation Fellow and the Director for the ARC COE for Quantum-Atom Optics. His research interests include quantum optics, quantum imaging, and laser spectroscopy.

Ping Koy Lam received the B.Sc. degree from the University of Auckland, Auckland, New Zealand, and the M.Sc. and Ph.D. degrees from the Australian National University, Canberra, Australia.

He was previously an Engineer for Sony and Hewlett-Packard. He is presently a Physics Reader and Group Leader of the Quantum Optics Group at the Australian National University. His research interests include nonlinear and quantum optics.

CHAPTER 3

Optimal information extraction from an optical image

Contents

Optical images can convey enormous amounts of information. At the classical level, complicated amplitude and phase distributions are commonly recorded, processed, analyzed and stored. Digital cameras of several mega-pixels are for instance found nearly everywhere at very low price, and image processing has been developed for decades now, allowing for example real-time shape recognition, or "intelligent" analysis for facial identification [Aizawa04].

Moreover, it is well known now that quantum information can be encoded onto optical images [Caves94]. Attempts are currently made to generate such images. Due to the extreme sensitivity to losses of this information, particular care has to be given to the detection process. *Optimal detection* is in this case crucial. *Optimal detection* refers here to the best possible detection performance, given the quantum fluctuations imposed by the random arrival time of the photons in the optical image. Using the results of section 1 C, an optimal detection also corresponds to a detection for which the *noise-mode of detection* identifies with the mode in which lies the information of interest.

Furthermore, this study is of most interest in the quantum imaging field, when the magnitude of the signal to be retrieved in an optical image is comparable to the quantum noise. Optimal detection using coherent light is first investigated. Then, we address the type of non classical light required to improve this detection.

In this chapter, we will first focus on simple optical images related to physical parameters of a Gaussian beam: displacement, tilt, waist-size and waist-position mismatch, and orbital angular momentum. We will show that these properties can be simply described

with the first Hermite Gauss modes previously presented in Fig. 1.1, and will present the quantum operators to which they are related. The understanding of these parameters at the quantum level allow to measure them with the best possible accuracy, and also to potentially convey parallel quantum information.

The second part of this chapter will be dedicated to the determination of the best possible detection of a parameter within an optical image, given the properties of an incident image. We will first consider the simple case of the quantum noise limit imposed on the measurement of the displacement and tilt of a TEM_{00} mode beam. Then, in a much more general context, we will determine the bound to the maximum achievable sensitivity in the estimation of information contained in an optical image in the presence of quantum noise. This limit, based on the Cramer-Rao bound, is valid for any image processing protocol. It is calculated both in the case of a shot noise limited image and of a class of non-classical illumination. We also propose practical experimental implementations allowing to reach this limit.

A Spatial optical information carried by transverse modes

In this section, we detail the physical significance of the first Hermite Gauss modes relative to a bright TEM_{00} beam. A part of the work presented here has been published during the course of this PhD in reference [Hsu04]. We notably show that displacement and tilt, waist-size and waist-position mismatch of a TEM_{00} mode can be simply expressed in terms of Hermite Gauss modes. The corresponding modifications of the TEM_{00} reference beam are represented in Fig.3.1. Finally, we introduce the angular momentum of the beam and will use a description of the field with Laguerre-Gauss modes.

We limit our analysis to a one-dimensional description of the physical parameters, along the x axis. Nevertheless, an identical set of variables could be similarly defined along the other orthogonal direction of the transverse plane, namely along the y axis.

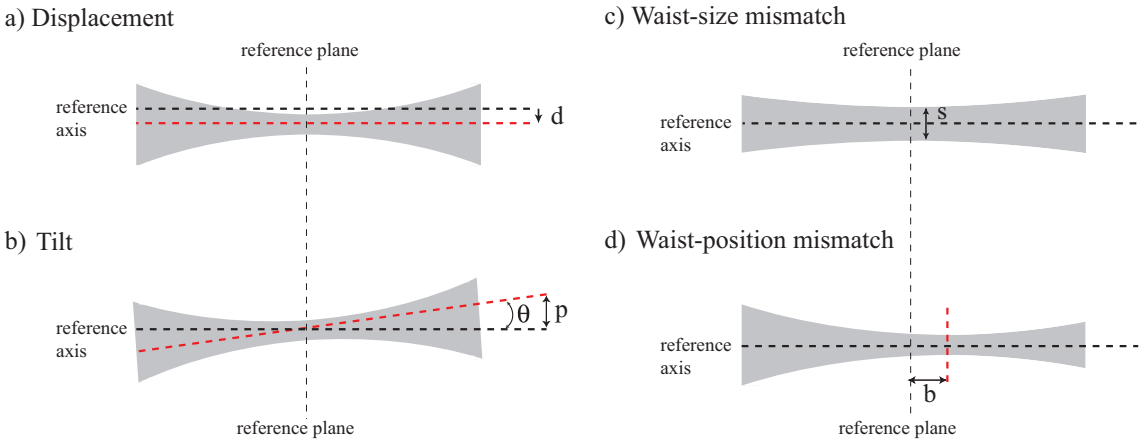

Figure 3.1: Representation of simple spatial modifications of a TEM_{00} gaussian beam, relative to a reference axis (propagation axis), and a reference plane containing the beam waist. a) Displacement d in the transverse plane. b) Tilt or angular displacement θ. c) Waist-size mismatch. d) Waist-position mismatch b.

The detailed understanding of these physical parameters in terms of transverse modes is notably of great importance for the optimization of their detection, as we will detail in section 5 A. This can be applied to any system for which beam alignment and beam focusing have to be finely controlled as, for example, in gravitational wave detectors [Grote02, Chow04, Morrison94, Anderson84].

A.1 Displacement and Tilt of Gaussian beams

A.1.1 Classical description

Displacement and tilt of a single-mode TEM_{00} laser beam are very intuitive notions as they refer to macroscopic properties of the beam, as shown in Fig. 3.1a) and b). We assume here that the beam is constrained in two dimensions, namely the figure plane of the paper, considering that the non represented transverse component remains centered in the same figure plane. A displacement corresponds to a beam translation by a distance d along the transverse direction x, whereas a tilt corresponds to an angular displacement by an angle

θ[1]. Displacement is naturally defined relative to the propagation axis z of a non displaced TEM_{00} beam, i.e. with the beam centered on $x = y = 0$ all along the propagation, as shown in Fig 3.1a). Tilt is defined on the other hand relative to a pivot point centered on the beam waist for simplicity[2], as represented in Fig. 3.1b).

The displaced field can always be expanded into the following development

$$E_d(x) = E(x) + d \cdot \frac{\partial E(x)}{\partial x} + \frac{d^2}{2} \cdot \frac{\partial^2 E(x)}{\partial x^2} + ... \tag{3.1}$$

and, in the regime where the displacement d is much smaller than the beam size, i.e. $d \ll w_0$ where w_0 is the beam waist of the incident TEM_{00} mode, the mean displaced field reduces at first order to[3]

$$E_d(x) \approx E(x) + d \cdot \frac{\partial E(x)}{\partial x} \tag{3.2}$$

We see from this expression that the zeroth order term is not dependent on d, and that the displacement is directly proportional to the first derivative of the field amplitude $\frac{\partial E(x)}{\partial x}$, whose amplitude profile is found to exactly identify with the one of a TEM_{10} mode[4] . A representation in the transverse plane of the decomposition of a displaced beam into its TEM_{00} and TEM_{10} components is given in Fig. 3.2.

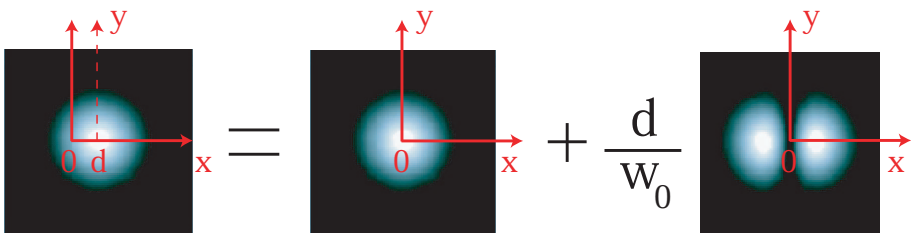

Figure 3.2: Representation of a displaced beam in the transverse plane. The displacement information d is carried by the TEM_{10} component, at first order, and is proportional to its amplitude. w_0 is the beam waist of the incident TEM_{00} mode.

On the other hand, the electric field profile for a tilted beam is given by

$$E_p(x) = e^{\frac{i2\pi x \sin\theta}{\lambda}} E(x \cos\theta) \tag{3.3}$$

where $E(x)$ is the non-tilted electric field profile, λ is the optical wavelength, and where naturally appears the transverse momentum of the beam p, which is given in the limit of small angles by the following expression

$$p = \frac{2\pi \sin\theta}{\lambda} \simeq \frac{2\pi\theta}{\lambda}, \tag{3.4}$$

[1]Note that a rotation of the entire transverse plane of the beam about the propagation axis, i.e. a torque action, corresponds to a different property, namely to *angular momentum*, as we will detail in section 3 A.3.

[2]Choosing the reference point at the waist position is arbitrary. We will see in section 5 A that it can be more appropriate to define the reference for both displacement and tilt in another plane, namely the plane of a moving object, which does not necessarily coincides with the beam waist position.

[3]A discussion on the limit of validity of this assumption is given at the end of this subsection.

[4]This simple calculation relies on the mode expressions given in Eq. 1.60.

Eq. 3.3 can thus be written for small tilt, i.e. for $\theta < \lambda/w_0 \ll 1$[5], as

$$E_p(x) \approx E(x) + ip \cdot xE(x). \tag{3.5}$$

Again, no information about the beam modification is carried in the zeroth order term, as it is not dependent on p. The beam tilt is directly proportional to $xE(x)$, itself proportional to the TEM_{10} mode again in the case of a TEM_{00} reference beam.

Using the expressions $u_n(x)$ of the first Hermite Gauss TEM_{n0} modes given in Eq. 1.60, taken in the plane defined by $z = 0$[6], we can combine Eq. 3.2 and 3.5 into

$$E_{d,p}(x) = A_0 \left[u_0(x) + \left(\frac{d}{w_0} + i\frac{w_0 p}{2} \right) u_1(x) \right], \tag{3.6}$$

where A_0 is the amplitude of the incident TEM_{00} mode[7].

Note that all transverse modes defined here need a reference frame, which is provided by the axis of the detection device. Displacement and tilt are thus measured relative to this reference.

Eq. 3.6 shows that the information about displacement and tilt of a TEM_{00} laser beam can be extracted by measuring the TEM_{10} mode component of the field. Any displacement information[8] is transferred to the "in-phase" amplitude of the TEM_{10} mode relative to the "carrier" (TEM_{00} mode), whereas any tilt information is transferred to the TEM_{10} component "in quadrature" relative to the TEM_{00} mode. The amplitude of these "in phase" and "in quadrature" components present opposite dependence with the beam waist w_0. Indeed, for a given displacement d, a smaller beam yields a larger TEM_{10} component, whereas for a given tilt, it yields a smaller TEM_{10} component. A change in position is more clearly identified when the beam size is small relative to the displacement amplitude, in the near field (NF) of the beam waist. Similarly, a change in tilt is more clearly identified in the far field (FF) of the beam waist, when the beam size in this plane is small. This situation corresponds to a large beam in the near field, due to the expansion properties of gaussian beam, as presented in Eq. 1.53.

In order to estimate the limit of validity of the expansion of a displaced field involving only $u_0(x)$ and $u_1(x)$ given by Eq. 3.6, we calculate the exact decomposition coefficients in the TEM_{n0} basis as a function of beam displacement[9]:

$$c_n(d) = \int_{-\infty}^{\infty} u_0(x-d)u_n(x)dx = \frac{d^n}{w_0^n\sqrt{n!}} exp\left[-\frac{d^2}{2w_0^2}\right] \tag{3.7}$$

where we recall from Eq. 1.60 that $u_0(x-d) = \left(\frac{2}{\pi w_0^2}\right)^{1/4} exp\left[-\frac{(x-d)^2}{w_0^2}\right]$. The results are plotted in Fig. 3.3. For small displacement ($d \ll w_0$), only the TEM_{00} and TEM_{10} modes have significant non-zero coefficients. This means that the TEM_{10} mode initially contributes most to the displacement signal. Moreover, we notice a linear dependence of

[5] $\lambda/w_0 \ll 1$ as we consider the paraxial approximation for which $\lambda \ll w_0$.

[6] Note that in this plane, $u_0(x)$ and $u_1(x)$ have real profiles, which will not be the case in another plane, as we detailed in section 1 A.2.6.

[7] A_0 identifies with the amplitude of the displaced and tilted beam at first order for small value of d and p.

[8] This information can for example be a modulation at RF frequency as we will see in section 5 A.

[9] This expression can be proven using a recurrence relation, and using the modes profiles given in Eq. 1.53.

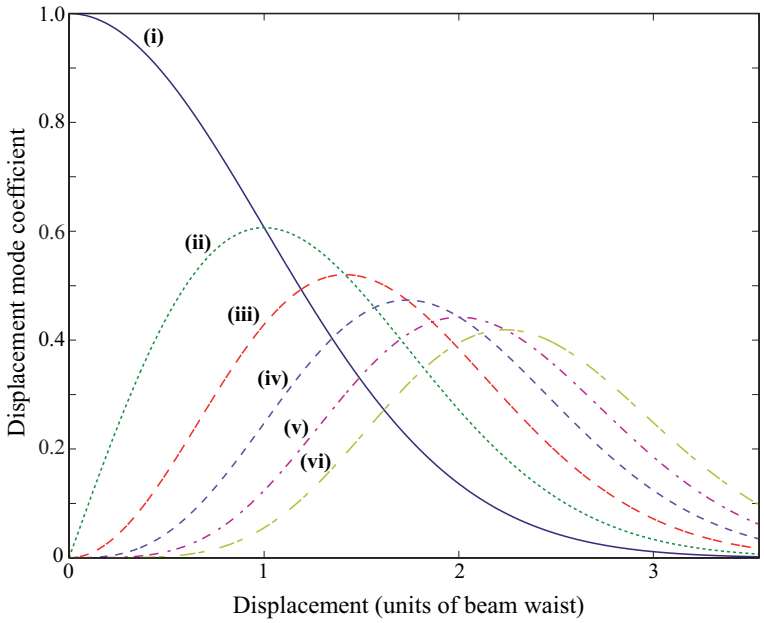

Figure 3.3: Coefficients of the decomposition of the displaced mode in terms of the TEMn0 modes for the (i) TEM_{00}, (ii) TEM_{10}, (iii) TEM_{20}, (iv) TEM_{30}, (v) TEM_{40} and (vi) TEM_{50} mode components.

its coefficient with respect to the displacement amplitude for displacement as large as the waist size. For larger displacement, other higher order modes become significant as their coefficients increase.

We have detailed a classical description of the displacement and tilt of a TEM_{00} mode beam and analyzed the validity of the proposed the expressions with respect to the amplitude of the displacement. The next section is dedicated to the study of their quantum operators analogous: position and momentum.

A.1.2 Quantum operators : position and momentum

In order to give a quantum mechanical description of displacement and tilt of a laser beam, we need to take into account the quantum noise of all the optical modes of the beam, including the vacuum modes.

We can write the positive frequency part of the electric field operator in terms of photon annihilation operators $\hat{a}$. The field operator is then given in its more general form as in Eq. 1.27 by:

$$\hat{\mathcal{E}}^{+}(x) = i\sqrt{\frac{\hbar\omega}{2\epsilon_0 cT}}\sum_{n=0}^{\infty}\hat{a}_n u_n(x). \tag{3.8}$$

For a mean photon number N, defined by $|\langle\hat{a}_0\rangle|^2$ in the small displacement and tilt regime, written in the mean-field basis, the quantum counterpart of equation (3.6), assuming that only u_0 and u_1 are non-vacuum modes, is

$$\hat{\mathcal{E}}^{+}_{d,p}(x) = i\sqrt{\frac{\hbar\omega}{2\epsilon_0 cT}}\left[\sqrt{N}\left(u_0(x)+\left(\frac{d}{w_0}+i\frac{w_0 p}{2}\right)u_1(x)\right)+\sum_{n=0}^{\infty}\delta\hat{a}_n u_n(x)\right], \tag{3.9}$$

where we have introduced the mean value[10] of position and momentum quantum operators of a laser beam, $d = \langle \hat{x} \rangle$ and $p = \langle \hat{p} \rangle$, respectively. Moreover, Eq. 3.8 can be rewritten in terms of its modal quadratures as follows

$$\hat{\mathcal{E}}^{+}(x) = i\sqrt{\frac{\hbar\omega}{2\epsilon_0 cT}} \sum_{n=0}^{\infty} \left[\frac{\hat{X}_n^{+} + i\hat{X}_n^{-}}{2} \right] u_n(x), \tag{3.10}$$

The identification of the TEM_{10} components in Eq. 3.9 and 3.10 yields position and momentum quantum operators are given by[11]

$$\hat{x} = \frac{w_0}{2\sqrt{N}} \hat{X}_1^{+} \tag{3.11}$$

$$\hat{p} = \frac{1}{w_0\sqrt{N}} \hat{X}_1^{-}, \tag{3.12}$$

where we see that position and momentum are linked to the amplitude and phase quadrature of the TEM_{10} mode component of the field, where the quadratures are defined relative to the TEM_{00} mean field phase, as introduced in section 1 A.2.4. Performing measurements of these quantities beyond the standard quantum noise limit will thus require the production of squeezing in the same mode[12]. Section 4 C is dedicated to this generation, also extended to the TEM_{20} mode.

The relation between the squeezing of amplitude or phase quadratures of the very dim TEM_{10} component of a bright TEM_{00} beam and the squeezing of position or momentum variables is illustrated on Fig. 3.4, according to the relative phase Φ between the TEM_{00} and TEM_{10} modes[13]. Such a representation of a bi-mode field in the same diagram is possible as both modes are orthogonal. As they are part of the same multi-mode beam, their relative phase ϕ is very important as it determines whether the state is position or momentum squeezed.

Moreover, a simple calculation shows that position and momentum are conjugate observables and satisfy the following commutation relation [Hsu05]

$$[\hat{x}, \hat{p}] = \frac{i}{N}. \tag{3.13}$$

Position and momentum do not commute, and this is the property we propose to investigate in chapter 5. We will first give a detailed study of their detection using split-detectors or homodyne detectors in section 5 A. We will show that a first consequence of this property is that squeezing a beam in position will result in the production of excess noise on the conjugate observable. Secondly, this will allow the generation of entanglement between these two observables, as detailed in section 5 B.

[10] The related quantum fluctuations are incorporated in the sum of fluctuations operators in all the transverse modes, and in particular in $\delta\hat{a}_1$.

[11] Note that beam position and momentum along the orthogonal directions y are similarly defined with the quadratures components of the TEM_{01} mode.

[12] Producing squeezing in higher order transverse modes is a more difficult task than in the TEM_{00} mode. One can thus wonder what mode has its displacement information in the TEM_{00} mode. In order to measure very small displacement, one could think of using a tailored beam with an available source of TEM_{00} squeezed light. Unfortunately, this mode corresponds to the integral of the TEM_{00} profile, which is the error function $Erf(x) = \int_{-\infty}^{x} exp - \frac{l^2}{w_0^2} dl$. This mode is non zero at infinity and is therefore of difficult use as it generation would require infinite power. Producing squeezing in higher modes is therefore an important breakthrough for any transverse displacement measurement beyond the QNL.

[13] In the experiments presented in chapter 5, we will consider only the case of an amplitude squeezed TEM_{10} mode, as presented in Fig. 3.4a).

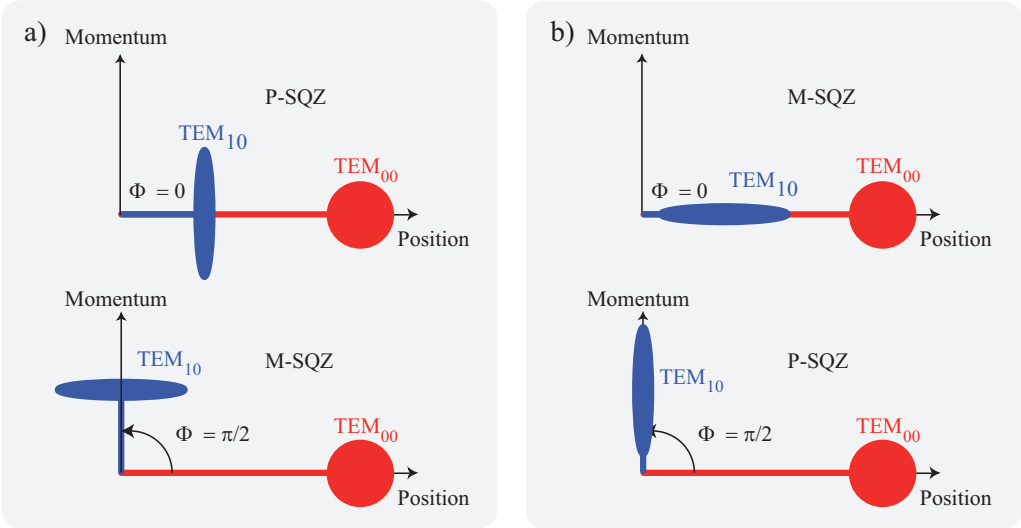

Figure 3.4: Simultaneous 'ball on stick' representation in a position-momentum Fresnel diagram of a bright TEM_{00} component and an a) amplitude and b) phase quadrature squeezed TEM_{10} component. The position axis is oriented with respect to the TEM_{00} mean field. In each case, according to the relative phase Φ between the TEM_{10} and the TEM_{00} components, the beam is position (P-SQZ) or momentum squeezed (M-SQZ).

A.1.3 Displacement and tilt of other beams

Displacement and tilt of other beam profiles can be similarly analyzed. A first remark is that the transverse mode carrying the displacement information is always orthogonal to the mean field. Indeed, Eq. 3.2 is not specific to a TEM_{00} profile. And we can show that for any physical amplitude field distribution[14]

$$\int_{-\infty}^{\infty} E(x)\frac{\partial E(x)}{\partial x}dx = 0, \tag{3.14}$$

which means that $E(x)$ - the mean field - and $\frac{\partial E(x)}{\partial x}$ - which is carrying the displacement information - are orthogonal.

Secondly, Eq. 3.5 defines $xE(x)$ as the mode carrying the tilt information for any field profile. Again, in the general case, mean field mode and mode carrying the tilt information are orthogonal as

$$\int_{-\infty}^{\infty} xE^2(x)dx = 0, \tag{3.15}$$

simply because x and $E^2(x)$ are respectively odd and even functions.

We now propose to show that position and momentum are in the same mode only in the TEM_{00} beam case. As explained previously, Eq. 3.2 and 3.5 are valid for any field profile, as long as displacement and tilt are small enough. At first order, the only mode carrying the displacement is described by $\frac{\partial E(x)}{\partial x}$, whereas the tilt information lies in the

[14]The relation can be obtained using the following integration by parts : $\int_{-\infty}^{\infty} E(x)\frac{\partial E(x)}{\partial x}dx = [E(x)^2]_{-\infty}^{\infty} - \int_{-\infty}^{\infty} E(x)\frac{\partial E(x)}{\partial x}dx$, which implies that $\int_{-\infty}^{\infty} E(x)\frac{\partial E(x)}{\partial x}dx = 0$, as physical distributions always tend towards 0 at infinity.

mode described by $xE(x)$. They are corresponding to the same mode if and only if these two profiles are proportional, i.e.

$$\frac{\partial E(x)}{\partial x} = \beta x E(x) \tag{3.16}$$

where β is a real constant. A simple integration of Eq. 3.16 yields

$$E(x) = E(0)e^{\beta x^2} \tag{3.17}$$

This relation shows that only exponential profiles allow position and momentum as a pair of conjugate variables. Physical modes for which $\beta < 0$ correspond to Gaussian TEM_{00} modes of waist defined by $w_0 = \sqrt{-\beta}$. This proves the previous proposition.

Hence, position and momentum can still be defined in the general case, but they are not carried by the same transverse mode, and they form a pair of conjugate variables only in the TEM_{00} mode case.

We present now the general expression of the displacement and tilt modes for any TEM_{n0} mode, denoted $u_n(x)$ in a one-dimensional description. As the displacement mode is proportional to the first derivative of the mode profile relative to x, we get

$$\frac{\partial u_0(x)}{\partial x} = -\frac{u_1(x)}{w_0} \tag{3.18}$$

$$\frac{\partial u_n(x)}{\partial x} = \frac{\sqrt{n}}{w_0}u_{n-1}(x) - \frac{\sqrt{n+1}}{w_0}u_{n+1}(x), \quad \forall n \geq 1 \tag{3.19}$$

This shows that, in the general case, the displacement mode of a TEM_{n0} mode is a combination of next and previous order Hermite Gauss modes. As for the modes containing the tilt information, whose profile is proportional to $xE(x)$, we get

$$xu_0(x) = \frac{w_0}{\sqrt{2}}u_1(x) \tag{3.20}$$

$$xu_1(x) = \frac{w_0}{\sqrt{2}}u_2(x) \tag{3.21}$$

$$xu_n(x) = \frac{w_0}{\sqrt{2}}u_{n+1}(x) + \frac{n(n-1)w_0}{4\sqrt{2}}u_{n-2}(x), \quad \forall n \geq 2 \tag{3.22}$$

The tilt of the two first modes are contained only in the next order Hermite Gauss mode, but the expression also involves the mode which is two orders below in the general case.

A.2 Waist position and size mismatch

Let us now detail other modifications of a TEM_{00} mode beam: waist-position and waist-size mismatch. They are presented in Fig. 3.1c) and d). Such mismatches can for instance result from imperfect mode-matching with an optical cavity. Being able to identify the transverse modes carrying these properties within the beam can for instance be applied to the design of active mode-matching devices, notably in gravitational wave detectors [Kogelnik64, Morrison94, Penn91, Anderson84].

A.2.1 Waist-size mismatch

We first consider a transformation that would change the waist by a small amount δw such as

$$w_0' = w_0 + \delta w \tag{3.23}$$

Knowing that $\delta w \ll w_0$, we can do a development at the first order of the TEM_{00} mode given by Eq. 1.60 which has undergone such a transformation, denoted $u_0(x, \delta w)$:

$$u_0(x, \delta w) = \left(\frac{2}{\pi w_0^2}\right)^{1/4} e^{-\frac{x^2}{w_0^2}} \left[1 + \frac{\delta w}{w_0}\left(\frac{4x^2}{w_0^2} - 1\right)\right] \tag{3.24}$$

where the first order bracketed terms respectively correspond to the development of the exponential term, and of the pre-exponential factor.

In the first order term, we recognize the expression of the amplitude of $u_2(x)$ given in Eq. 1.60. Eq. 3.24 thus becomes

$$u_0(x, \delta w) = u_0(x) + \frac{\delta w}{\sqrt{2} w_0} u_2(x) \tag{3.25}$$

Similarly to the displacement information given in Eq. 3.6, the waist-size mismatch lies in the "in phase" TEM_{20} component of the field. Let us now present the physical parameter which contributes to the TEM_{20} component "in quadrature" relative to the mean field.

A.2.2 Waist-position mismatch

We now consider a small waist-position mismatch. The waist is now positioned at $z \neq 0$, such as $\delta z \ll 1$[15]. The longitudinal field phase factor given in Eq. 1.60 is now important as it yields the following field at first order in z, in the transverse plane defined by $z = \delta z$

$$u_0(x, \delta z) = \left(\frac{2}{\pi w_0^2}\right)^{\frac{1}{4}} e^{-\frac{x^2}{w_0^2}} \left[1 + i\frac{\delta z}{z_R}\left(1 + \frac{x^2}{w_0^2}\right)\right] \tag{3.26}$$

Using the expression of $u_0(x, 0)$ and $u_2(x, 0)$, we get, at first order in z

$$u_0(x, \delta z) = u_0(x, 0) + i\frac{\delta z}{z_R}\left[\frac{5}{4} u_0(x, 0) + \frac{1}{2\sqrt{2}} u_2(x, 0)\right] \tag{3.27}$$

A.2.3 General relation for mode-mismatch

The results of Eq. 3.25 and 3.27 can be gathered into

$$u_0(x, \delta w, \delta z) = u_0(x, 0) + u_2(x, 0)\left[\frac{\delta w}{\sqrt{2} w_0} + i\frac{\delta z}{2\sqrt{2} z_R}\right] + i\frac{5\delta z}{4 z_R} u_0(x, 0) \tag{3.28}$$

Hence, real and imaginary parts of the TEM_{20} components of a slightly modified TEM_{00} mode beam respectively correspond to waist-size and to a part of the waist-position information[16].

[15] We recall that $z = 0$ corresponds to the reference waist position.

[16] Note that the waist-position information is not entirely comprised into the TEM_{20} component. A quick calculation shows that only $2/27 \simeq 7\%$ of the information is in fact contained in the TEM_{20} component.

A.3 Orbital angular momentum

Let us now consider a small rotation of a beam about its propagation axis. The beam physical property which linked with such a transformation is referred to as *orbital angular momentum*[17] [Mandel95, Mair01, Barnett06, Padgett06]. This torque action is different from the one that has been introduced before, the tilt, which corresponds to an angular displacement relative to an axis of the transverse plane[18]. It also has to be distinguished from the spin angular momentum of circularly polarized light[19].

A.3.1 Rotation of a Hermite Gauss beam about its propagation axis

In order to measure the effect of a beam rotation about its propagation axis, intensity or phase distribution must not have a cylindrical symmetry. For instance, the rotation of a TEM_{00} mode does not yield any modal change, obviously, whereas the rotation of any other TEM_{nm} mode does.

Let us take the example of the rotation of TEM_{10} and TEM_{01} mode beams by a small angle $\delta\theta$ about the propagation axis. Using the expression of the modes given by Eq. 1.53, a simple calculation yields at first order

$$TEM_{10}(\delta\theta) = TEM_{10} + \delta\theta \cdot TEM_{01} \tag{3.29}$$

$$TEM_{01}(\delta\theta) = TEM_{01} - \delta\theta \cdot TEM_{10} \tag{3.30}$$

The modes carrying the rotation information of a TEM_{10} or TEM_{01} beams are thus simply the TEM_{01} and TEM_{10} modes, respectively. Note that these components are in and out of phase relative to the mean field.

The rotation of such beams can thus be measured by extracting the TEM_{01} or TEM_{10} component of the beam, which is orthogonal to the mean field in both cases. Again, squeezing the TEM_{01} or TEM_{10} component of the incident field can potentially allow sub-shot noise rotation measurements of such modes. TEM_{nm} modes are relatively easy to generate (see section 4 A.2), and could therefore be used in order to provide ultra sensitive rotations of a beam. However, more simple beams, related to the orbital angular momentum of a TEM_{00} beam, can be preferred, as we propose to explain now.

A.3.2 Rotation of a Laguerre Gauss beam about its propagation axis

We propose here to introduce another orthonormal basis of the transverse plane, more appropriate[20] for the description of beam rotation about the propagation axis, the Laguerre-Gauss (L-G) mode basis [Siegman86]. A Laguerre-Gaussian (LG) laser beam has an optical vortex in its center, i.e. that its phase representation is twisted like a corkscrew around the propagation axis. We call topological charge the integer number of twists the light does in one wavelength. Optical vortices are for instance used in optical tweezers to manipulate micrometer-sized particles such as cells. Such particles can be rotated in orbits around the axis of an orbital vortex [Paterson01]. Micro-motors have also been created using optical

[17] Angle of rotation ϕ and orbital angular momentum $\hat{L}_z$ define the rotation operator $\hat{\mathcal{R}}_\phi = exp(-\frac{i\hat{L}_z\phi}{\hbar})$.

[18] Tilt with respect to the x and y axis are respectively linked with $\hat{L}_x$ and $\hat{L}_y$.

[19] Note that a conversion from one to the other has been recently demonstrated [Marrucci06].

[20] In opposition with the Hermite Gauss modes, the Laguerre-Gauss modes corresponds to eigenmodes of the orbital angular momentum $\hat{L}_z$.

vortex tweezers [Luo00]. Laguerre-Gaussian modes can be generated experimentally with spiral phase plates [Beijersbergen94], or computer-generated holograms [Basistiy93].

The expression of the Laguerre-Gauss modes is given in cylindrical coordinates (r,θ,z) by

$$\mathrm{LG}_p^l(r,\theta,z) = C_p^l \left(\frac{r\sqrt{2}}{w(z)}\right)^{|l|} L_p^{|l|}\left(\frac{2r^2}{w(z)^2}\right) e^{-\frac{r^2}{w(z)^2}} e^{il\theta} e^{-i(2p+|l|+1)\phi_G(z)} \tag{3.31}$$

where l is the topological charge of the beam, C_p^l is a normalization constant, and $w(z)$, $\phi_G(z)$ have been defined in section 1 A.2.6.

The normalized expressions of the first L-G modes in the plane defined by $z=0$ are

$$\mathrm{LG}_0^0(r,\theta) = \left(\frac{2}{\pi w_0^2}\right)^{\frac{1}{2}} e^{-\frac{r^2}{w_0^2}} \tag{3.32}$$

$$\mathrm{LG}_0^1(r,\theta) = \left(\frac{2}{\pi w_0^2}\right)^{\frac{1}{2}} \frac{\sqrt{2}r}{w_0} e^{-\frac{r^2}{w_0^2}} e^{i\theta} \tag{3.33}$$

$$\mathrm{LG}_0^{-1}(r,\theta) = \left(\frac{2}{\pi w_0^2}\right)^{\frac{1}{2}} \frac{\sqrt{2}r}{w_0} e^{-\frac{r^2}{w_0^2}} e^{-i\theta} \tag{3.34}$$

Let us now consider the rotation of LG_0^1 and LG_0^{-1} mode beams by a small angle $\delta\theta$ about the propagation axis. Using the expression of the modes given by Eq. 3.37, a simple calculation yields at first order[21]

$$\mathrm{LG}_0^1(\delta\theta) = \mathrm{LG}_0^1 + i\delta\theta \cdot \mathrm{LG}_0^1 \tag{3.35}$$

$$\mathrm{LG}_0^{-1}(\delta\theta) = \mathrm{LG}_0^{-1} - i\delta\theta \cdot \mathrm{LG}_0^{-1} \tag{3.36}$$

The modes carrying the orbital angular momentum of a LG_0^1 and LG_0^{-1} beams are thus simply the same modes. However, the rotation signal is in quadrature relative to the mean field. This information can thus still be extracted with a homodyne detection whose local oscillator profile is defined by a LG_0^1 or LG_0^{-1} mode. A calibration of the local oscillator phase can allow a selective extraction of information along a single quadrature. Filling the LG_0^1 or LG_0^{-1} mode of the incident field with squeezed vacuum light can again allow sub-shot noise rotation measurements of LG_0^1 or LG_0^{-1} modes.

In order to establish a simple link with the results obtained with Hermite Gauss modes, we can rewrite the first Laguerre Gauss modes in terms of Hermite Gauss modes as

$$\mathrm{LG}_0^0 = \mathrm{TEM}_{00} \tag{3.37}$$

$$\mathrm{LG}_0^1 = \frac{1}{\sqrt{2}}(\mathrm{TEM}_{10} + i\mathrm{TEM}_{01}) \tag{3.38}$$

$$\mathrm{LG}_0^{-1} = \frac{1}{\sqrt{2}}(\mathrm{TEM}_{10} - i\mathrm{TEM}_{01}) \tag{3.39}$$

TEM_{10} and TEM_{01} modes are thus related to the orbital angular momentum of the first order Laguerre Gauss modes[22].

[21] These relations directly arise from the fact that Laguerre-Gauss modes are eigen-modes of $\hat{L}_z$, and also of $\hat{\mathcal{R}}_\phi$: $\hat{\mathcal{R}}_\phi LG_p^l = exp(-il\phi)LG_p^l$.

[22] We recall that the quadratures of these two modes also carry information on displacement and tilt of

B Quantum limits for information extraction from an optical image

Before considering the general case of the optimal detection of a parameter within an optical image, let us first study the simple case of displacement and tilt measurement of a Gaussian beam. We will come back on more practical aspects of such measurements in section 5 A. A part of the work presented here has been published in reference [Hsu04].

B.1 Displacement and tilt measurements

B.1.1 Quantum limits for displacement and tilt measurements

The position of a light beam can be defined as the mean position of all photons in the beam. Beam displacement is then quantified by the amount of deviation of this mean photon position from some fixed reference axis. We assume here that the displaced beam has a transverse TEM_{00} mode-shape, as presented in section 3 A.1 but this can easily be extended to the displacement of any beam profile. To simplify our analysis, we assume, without loss of generality, a one-dimensional transverse displacement d from the reference axis.

We recall from section 3 A.1 that the normalized transverse beam amplitude function for a displaced TEM_{00} beam is given by

$$\bar{E}(x,d) = u_0(x-d) = \left(\frac{2}{\pi w_0^2}\right)^{1/4} exp\left[-\left(\frac{x-d}{w_0}\right)^2\right]. \tag{3.40}$$

and the transverse intensity distribution normalized to a number of photons, for a beam with a total of N photons, can then be written

$$\bar{n}(x,d) = N u_0^2(x-d). \tag{3.41}$$

This equation essentially describes the normalized Gaussian spatial distribution of photons along one transverse axis of the optical beam. For a coherent TEM_{00} light beam, the photons have Gaussian distribution in transverse position, and Poissonian distribution in time. It is clear that a detector which discriminates the transverse position of each photon will provide the maximum possible information about the displacement of the beam. Such discrimination could, for example, be achieved with an infinite single photon resolving array with infinitesimally small pixels. Although in reality such a detection device is unfeasible, it nevertheless sets a bound to the information obtainable for beam displacement without resorting to quantum resources. This bound therefore constitutes a quantum

a TEM_{00} mode along both x and y axis. At this stage, in order to provide a very general description of the results presented in this chapter, it is tempting to define 4 spatial Stokes parameters (intensity of a TEM_{00} beam, displacement, tilt, and orbital angular momentum), and to represent them in a Poincaré sphere. Such a representation has already been used in continuous variables for the complete description of polarization states [Korolkova02, Bowen02], similarity to the representation of spin variables of atomic systems in the Bloch sphere. However, although our system has great similarity with polarization states, orbital angular momenta expressed with TEM_{10} and TEM_{01} modes are related to a $LG_0^{\pm 1}$ mean field, and not to a bright TEM_{00} beam. Such a representation is therefore not appropriate here.

noise limited displacement measurement. More practical detection schemes can therefore be bench-marked against this limit[23].

Let us now examine an optimum measurement of beam displacement using our idealized array detector. Using Eq. 3.40, the probability distribution of photons along the x-axis of the detector is given by

$$\mathcal{P}(x) = \sqrt{\frac{2}{\pi w_0^2}} exp\left[-2\left(\frac{x-d}{w_0}\right)^2\right]. \tag{3.42}$$

As each photon in the beam impinges on the array, a single pixel is triggered, locating that photon. The mean arrival position of each photon $\bar{x}$ and the standard deviation Δd are given by

$$\bar{x} = \int_{-\infty}^{\infty} x\mathcal{P}(x)dx = d, \tag{3.43}$$

$$\Delta d = \int_{-\infty}^{\infty} x^2\mathcal{P}(x)dx - d^2 = \frac{w_0}{2} \tag{3.44}$$

From the arrival of a single photon we can therefore estimate the displacement of our mode with a standard deviation given by Δd. For N photons, the standard deviation simply becomes $\Delta d_{\mathrm{QNL}} = \Delta d/\sqrt{N}$.

In the case of a coherent illumination, the minimum displacement discernible d_{QNL} taking into account the minimum uncertainty in its determination Δd corresponds to a signal to noise ratio value of 1. This limit is known as the *standard quantum limit*. d_{min} is thus given by[24]

$$\boxed{d_{\mathrm{QNL}} = \frac{w_0}{2\sqrt{N}},} \tag{3.45}$$

which directly shows that the accuracy of a displacement measurement can be enhanced by focussing the beam to a smaller waist, or by increasing the number of detected photons during the measurement, as already explained in section 3 B.1. When the number of detected photons is small, the measurement of the beam position is highly uncertain. This has direct consequences on the resolution of optical images at low photon flux. It is only when N is large enough that a good image resolution is accessible. Experimentally, a few parameters determine N and can be tuned in order to obtain a sufficient resolution. N corresponds to the total number of photons detected in the interval T=1/RBW, where RBW is the resolution bandwidth. Ideally, T is maximized according to the stability of the physical system. For instance in the case of bits read-out in optical disc devices, the RBW roughly corresponds to the scanning frequency. For a 100 μm waist, 1 mW of power at a wavelength of $\lambda = 1$ μm, with $RBW = 100$ kHz, the quantum noise limit is for instance given by $d_{QNL} = 0.2$ nm. Note that during test or characterization procedures, the precision can be increased by averaging with the spectrum analyzer, for instance by reducing the video bandwidth (VBW). The QNL effectively corresponds to the minimum measurable displacement measured on the spectrum analyzer when $VBW = RBW$, without averaging.

[23] We will give a more mathematical proof of the existence and of the value of this bound in the next section using a Cramer Rao bound calculation.

[24] Note that this fundamental limit has already been introduced in [Fabre00, Treps04,1].

We have discussed here only the case of a displacement measurement, but we can similarly define the QNL for momentum measurements as[25]

$$\boxed{p_{\mathrm{QNL}} = \frac{1}{w_0\sqrt{N}}.} \tag{3.46}$$

In the same conditions as the ones defined above, the QNL for momentum measurement is $p_{\mathrm{QNL}} = 4.10^{-2}$ m^{-1}, corresponding to a tilt angle of $\theta_{\mathrm{QNL}} = 7$ $n$rad.

B.1.2 Optimal displacement measurements

One can now wonder if there exists a device allowing an optimal measurement of beam displacement, i.e. a detection whose performances reach the QNL with TEM_{00} coherent illumination.

- Split-detection

The conventional way to measure the displacement of a laser beam is to use a split detector. It is widely used in a large range of applications, as we will detail in section 5 A. As shown in Fig. 3.5a), the difference between the intensity on each side of the split detector yields a photocurrent proportional to the displacement.

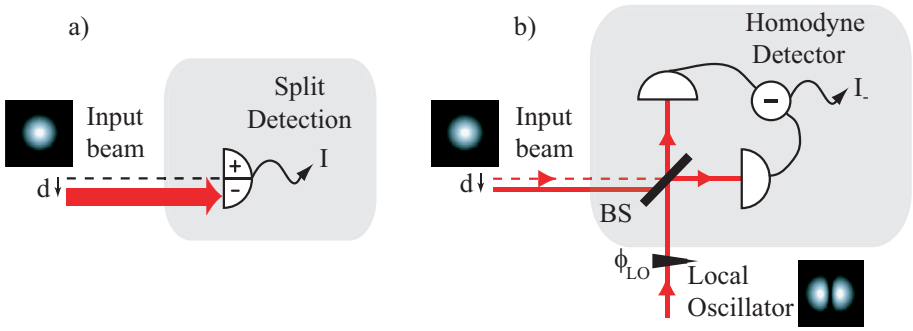

Figure 3.5: Beam displacement detection devices. a) split-detection. b) TEM_{10} homodyne detection.

This detection exactly corresponds to the difference measurement analyzed in section 1 C.5.2. We proved that, in the precise case of the split-detection, the noise-mode of detection is the flipped mode whose profile is presented in Fig. 1.11. However, we have shown in section 3 A.1, that the displacement information was carried by the TEM_{10} mode. As a detection device measures only the information lying in its noise-mode of detection, we expect the split detection to be limited to an efficiency of $\Gamma_{1,f}^2$ relative to the QNL, where $\Gamma_{1,f}$ is the overlap integral between the TEM_{10}, $u_1(x)$ and the flipped mode $u_f(x)$, and is defined by

$$\Gamma_{1,f} = \int_{-\infty}^{\infty} u_1(x)u_f(x)dx = \sqrt{\frac{2}{\pi}}, \tag{3.47}$$

[25] The detection device to be considered in this case is required to be a phase resolving detector positioned in the waist plane, as the tilt information cannot be detected with a traditional array detection. Another possibility is to consider the measurement in the far field of the waist plane, for which the displacement is transferred to a displacement as we will explain in section 4 A.1, and use exactly the same analysis as the one proposed here.

The split-detection is thus $2/\pi \simeq 64\%$ efficient relative to the QNL. The quantum limit on a displacement measurement with a split-detector (SD) is thus given by

$$\boxed{d_{\mathrm{SD}} = \sqrt{\tfrac{\pi}{2}} d_{\mathrm{QNL}} = \sqrt{\tfrac{\pi}{8N}} w_0,} \tag{3.48}$$

which identifies with the limit presented in reference [Treps04,1]. Split-detection is therefore not an optimal detection of optical beam displacement.

- TEM_{10} homodyne detection

Let us now consider a TEM_{10} homodyne detection, i.e. a homodyne detection whose local oscillator is a bright TEM_{10} beam, as illustrated in Fig. 3.5b).

We have shown in section 1 C.4 that the noise-mode of detection of this device was precisely the TEM_{10} mode. This directly proves that this type of detection is an optimal beam displacement device.

We will demonstrate the experimental performances of such a scheme in section 5 A.

B.1.3 Displacement and tilt measurements beyond the QNL

In order to perform measurements beyond the QNL, i.e. for a given T, we have shown in section 1 C that filling the appropriate transverse mode of the input field[26] with squeezed light is a necessary and sufficient condition.

For example, using 3 dB of squeezing in the appropriate component of the beam for a displacement measurement leads to a noise power reduction by a factor 2. We recall that, in the case of a split-detection, the noise-mode of detection is the flipped mode, whereas it is the TEM_{10} mode for the TEM_{10} homodyne detection. The new quantum limit is thus given in each case by

$$d_{\mathrm{SQZ_{SD}}} = \frac{\sqrt{\pi}}{2} d_{\mathrm{QNL}}, \tag{3.49}$$

$$d_{\mathrm{SQZ_{HD}}} = \frac{1}{\sqrt{2}} d_{\mathrm{QNL}}. \tag{3.50}$$

It is important to note that, as imposed by Heisenberg inequality, the measurement of the conjugated observable - the momentum in this case - is degraded[27]. Similar relations can be shown for a tilt measurement with a TEM_{10} homodyne detection.

[26] We have called this mode the *noise-mode of detection* in section 1 C.

[27] We will give an experimental demonstration of this phenomenon in section 5 A.

B.2 Quantum limits in general image processing

B.2.1 Introduction

In this section, we consider the extraction of a piece of information contained in an optical image, by means of space sensitive detectors[28] and information processing, in the case of large photon flux[29]. The information contained in the image is here not restricted to displacement and tilt parameters, and the image itself can be any amplitude and phase distribution in the transverse plane, and is not restricted to a Gaussian profile anymore.

When all the sources of technical noise have been removed, quantum fluctuations still affect the optical measurement and limit its sensitivity, as introduced in chapter 1. We propose here to answer the following broad question: what is the lowest limit imposed by a given distribution of quantum noise to the accuracy of the measurement, independently of the information processing protocol used for the information extraction? We have answered this question in the case of a displacement measurement of a TEM_{00} beam, and propose now to answer it in the general context.

Let us define p as the parameter which carries the information of interest, and which is assumed without loss of generality to be scalar[30]. As we will see, the optimum limit on the determination of p only depends on the statistics of the fluctuations of the incoming light. We use an approach based on the Cramer-Rao Bound (CRB). This tool, widely used in the signal processing community [Refregier02], has already been applied to different domains, such as gravitational wave detection [Nicholson98] or diamagnetism [Curilef05].

One example is when p modifies the total intensity or amplitude of the light beam. It is then well known [Kimble87, SoutoRibeiro97, Gao98, Bachor03] that there exists a standard quantum limit in the sensitivity of the measurement of p when the light beam is in a coherent state, and that it is possible to go beyond this limit using sub-Poissonian or squeezed light. This case has already been studied in section 1 C.

Another example is when the parameter p modifies the distribution of light in the transverse plane but not its total intensity. We will focus on this latter case, for which the parameter p modifies for example the position or direction of a light beam. This configuration has been studied at the quantum level, both theoretically and experimentally using split detectors or homodyne detections, as we have already discussed in section 3 B.1[31]. In many other instances the parameter p affects the image in a complicated way. For example a fluorescent nano-object imbedded in a biological environment modifies the image recorded through a microscope in a complex way because of diffraction. Nevertheless its position can be determined from the information contained in the image with a sensitivity which can be much better than the wavelength [Rohrbach04]. In order to extract the parameter value in such experiments, one needs to use detector arrays or CCD cameras and to combine in an appropriate way the information recorded on the different pixels.

[28] Any detector is included in this category. We still allow here phase resolving array detectors, including homodyne detectors, and do not only restrict our analysis to CCD type detectors.

[29] Note that most of the work presented in this section has been submitted for publication in the format [Delaubert06,4].

[30] The detection systems are assumed to be linear, and the analysis of complex parameters is equivalent to two separate studies of its real and imaginary components.

[31] Section 5 A is also devoted to this configuration and focusses on the experimental part.

Let us now present the field and intensity notations we will use in this section, similarly to the definitions given in section 3 B.1. The mean value of the local complex electric field operator in the image plane, normalized to a number of photons, will be written for a given value of the parameter as

$$\bar{E}(\vec{r},p) = 2\sqrt{N}u_0(\vec{r},p), \tag{3.51}$$

where N refers to the total number of photons detected in the mean field during the integration time of the detector. N is assumed to be independent of p, as stated previously. $u_0(\vec{r},p)$ is the p-dependent normalized transverse distribution of the mean field, complex in the general case. The local mean photon number detected during the same time interval is

$$\bar{n}(\vec{r},p) = \frac{\bar{E}^*(\vec{r},p)\bar{E}(\vec{r},p)}{4} = N|u_0(\vec{r},p)|^2. \tag{3.52}$$

Field or intensity measurements respectively allow an estimation of the distribution of $\bar{E}(\vec{r},p)$ or $\bar{n}(\vec{r},p)$ in the transverse plane. This field and photon number measurements will be respectively denoted $\mathbf{E}(\vec{r})$ and $\mathbf{n}(\vec{r})$ in the following. As a consequence of the quantum fluctuations in the optical measurements, there will be an uncertainty on the estimation of the distributions $\bar{E}(\vec{r},p)$ and $\bar{n}(\vec{r},p)$ from the measurements $\mathbf{E}(\vec{r})$ and $\mathbf{n}(\vec{r})$. Moreover, the way the measurements are performed and the signals are processed has a direct influence on this uncertainty.

Assuming that one knows the dependence of the beam profile with the parameter of interest p, a value of p can be inferred from the previous measurements[32]. Again, the accuracy of this value is directly related to the measurement performance. An evaluation of the measurement uncertainty can thus provide the precision on the determination of the parameter p around its *a priori* value p_0, chosen here for simplicity to be $p_0 = 0$.

This achievable precision on the estimation of the parameter p is limited by the Cramer-Rao Bound. More precisely, one can show that the variance of any unbiased estimator of p cannot be smaller than [Refregier02]

$$\sigma^2_{p_{\min}} = 1/I_F, \tag{3.53}$$

where the Fisher information I_F is related to the maximum information retrievable for any possible measurement, and exclusively depends on the statistics of the studied phenomenon. Instead of giving its abstract definition here, we prefer to define it throughout a commented example in the next section.

We will now use this powerful tool in order to investigate for the quantum limit on the estimation of the parameter p using first intensity measurements, and secondly complex field measurements.

B.2.2 Intensity measurements

- Cramer Rao bound calculation

[32] When the parameter of interest p is an image displacement, one can for example measure the position of the image relative to its center, or relative to the position of a specific detail within the field distribution.

We first assume that p is obtained by processing the information contained in measurements of local intensities, or local number of photons in the entire transverse plane[33]. The best possible local intensity detection device would consist in a set of indexed pixels paving the entire transverse plane, in the limit when their spatial extension approaches 0. Let $\mathbf{n}(\vec{r}) = [n_1, ..., n_k, ...]$ be one measurement of the photon distribution with such a hypothetical detector, where n_k corresponds to the number of photons detected on pixel k. Because of the noise present in the light, the sample $\mathbf{n}$ differs from its statistical mean value $\bar{\mathbf{n}}(p) = [\bar{n}_1(p), ..., \bar{n}_k(p), ...]$, where $\bar{n}_k(p)$ is the mean number of photons incident on pixel k. Let $L(\mathbf{n}|p)$ be the likelihood of the observation of $\mathbf{n}(\vec{r})$. Note that $\mathbf{n}$ corresponds to a single measurement and hence does not explicitly depend on p, contrarily to the average on all the possible realizations.

As presented in the introduction of this chapter, the achievable precision on the estimation of p is limited by the Cramer-Rao Bound (CRB), which corresponds to the inverse of the Fisher information. In the case of intensity measurements when the actual value of p is 0, the Fisher information is given by

$$I_F = -\int \frac{\partial^2}{\partial p^2} l(\mathbf{n}|p)\Big|_{p=0} L(\mathbf{n}|0) d\mathbf{n}, \tag{3.54}$$

where we have introduced the log-likelihood $l(\mathbf{n}|p) = \ln L(\mathbf{n}|p)$. The log-likelihood simply corresponds to the information about the parameter p which is contained into the measured sample $\mathbf{n}(\vec{r})$, taking into account its probability of occurrence[34].

The value of the parameter for which the mean value of first derivative of the log-likelihood $\frac{\partial}{\partial p} l(\mathbf{n}|p)$ is null corresponds the value which maximizes $l(\mathbf{n}|p)$, and thus the information on the parameter. This maximum is reached for $p = p_0 = 0$ if the estimator is unbiased, as represented in Fig. 3.6. In the case of an unbiased estimation, the

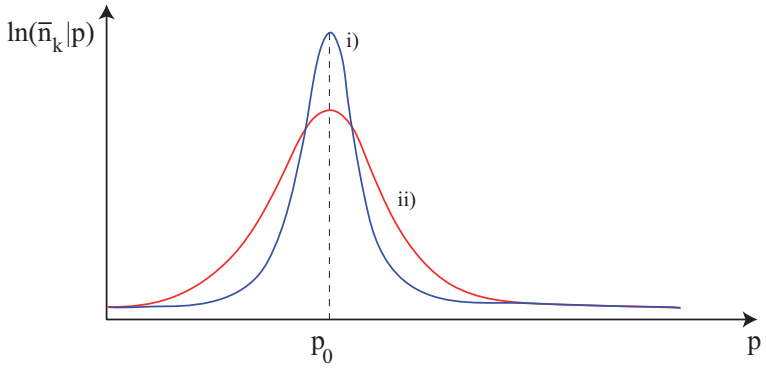

Figure 3.6: Two distributions of the log-likelihood of the mean value of the number of photons incident on pixel k, according to the value of the parameter p. The estimation of p_0 is obviously more precise from i) than ii) because it is narrower and has a larger curvature around its maximum value. Note that both distributions represented are unbiased as their maximum corresponds to $p = p_0$.

second derivative of the log-likelihood taken for the *a priori* value of the parameter, i.e.

[33] Note that such a device does not provide any phase information. The phase will be considered in section 3 B.2.3.

[34] We recall that in information theory, a phenomenon contains all the more information as it is unlikely.

$\frac{\partial^2}{\partial p^2} l(\mathbf{n}|p)\Big|_{p=0}$, directly corresponds to the local curvature of the log-likelihood. When the absolute value[35] of the previous parameter is large, the curve is narrow, the uncertainty on the estimation of p is small, and the information about p contained into the measurement $\mathbf{n}(\vec{r})$ is large. In order to obtain the maximal information retrievable from all possible measurements, all contributions weighted by their probability to occur are summed. In Eq. 3.54, the integration thus spans over all the possible photon distributions that can be detected when the parameter value is $p = 0$[36]. The Fisher information is highly dependent on the quantum noise affecting the measured number of photons, and we need to specify the noise statistics in order to calculate the likelihood of each possible realizations.

Let us first consider coherent illumination, for which the photo-current delivered by each pixel has Poissonian fluctuations [Glauber65, Loudon00]. The probability of measuring n_k photons on pixel k, when the parameter equals p is given by

$$\boxed{\mathcal{P}_{n_k}(k,p) = \frac{\bar{n}_k(p)^{n_k}}{n_k!} e^{-\bar{n}_k(p)}.} \tag{3.55}$$

Restricting our analysis to spatially uncorrelated beams[37], the likelihood $L(n|p)$ of observing the photon distribution $\mathbf{n}(\vec{r}) = [n_1, ..., n_k, ...]$ corresponds to the product of the local probabilities on each pixel given in Eq. 3.55

$$L(\mathbf{n}|p) = \prod_k \mathcal{P}_{n_k}(k,p). \tag{3.56}$$

The log-likelihood is thus

$$\begin{aligned} l(\mathbf{n}|p) &= \sum_k ln\left[\mathcal{P}_{n_k}(k,p)\right] \\ &= \sum_k \Big[-\bar{n}_k(p) + n_k ln\left[\bar{n}_k(p)\right] - ln\left[n_k!\right] \Big]. \end{aligned} \tag{3.57}$$

Taking the limit to infinitely small pixels[38], for which the sum can be replaced by an integral, and for which $\mathbf{n}(\vec{r})$ is a continuous distribution independent of p, the first derivative of the log-likelihood with respect to p can be written

$$\frac{\partial}{\partial p} l(\mathbf{n}|p) = \int \Big[-\bar{n}'(\vec{r},p) + \mathbf{n}(\vec{r}) \frac{\bar{n}'(\vec{r},p)}{\bar{n}(\vec{r},p)} \Big] d^2r, \tag{3.58}$$

where the $'$ denotes a derivative relative to p. Recalling now that we restrict our analysis to images whose total intensity is independent of p, i.e. images for which $\int \bar{n}(p,\vec{r}) d^2r$ is a constant, we get

$$\int \bar{n}'(\vec{r},p) d^2r = 0. \tag{3.59}$$

[35] This second derivative is negative. This explains the minus sign in the expression of the Fisher information.

[36] The photon number distribution can easily be assumed continuous for a large number of incident photon, and the notation $\int ... L(\mathbf{n}|0) d\mathbf{n}$ simply corresponds to a statistical average over all possible photon distributions, when the parameter equals 0.

[37] Spatially uncorrelated beams either correspond to coherent or *locally squeezed* fields.

[38] The type of detection considered here exactly corresponds to the array detector introduced in section 3 B.1 in order to define the best possible detection device.

Using this property of the photon distribution, the first term in Eq. 3.58 cancels, and we get

$$\frac{\partial}{\partial p} l(\mathbf{n}|p) \quad = \quad \int \mathbf{n}(\vec{r}) \frac{\bar{n}'(\vec{r},p)}{\bar{n}(\vec{r},p)} d^2r, \tag{3.60}$$

Moreover, we assume that our estimation of the photon number distribution is unbiased, i.e. the statistical average of sets of photon measurements $\mathbf{n}(\vec{r})$ taken for $p = 0$ identifies with the mean photon distribution $\bar{n}(\vec{r}, 0)$

$$\int \mathbf{n} L(\mathbf{n}|0) d\mathbf{n} = \bar{n}(\vec{r}, 0). \tag{3.61}$$

Using Eq. 3.60, the statistical average of the first derivative of the log-likelihood, taken for $p = 0$ thus becomes

$$\int \frac{\partial}{\partial p} l(\mathbf{n}|p)\Big|_{p=0} L(\mathbf{n}|0) d\mathbf{n} = 0, \tag{3.62}$$

which exactly corresponds to the case described in Fig. 3.6. The maximum of the mean value of the log-likelihood is obtained for $p = 0$.

A second derivation of the log-likelihood, taken for $p = 0$, yields

$$\frac{\partial^2}{\partial p^2} l(\mathbf{n}|p)\Big|_{p=0} \quad = \quad \int \mathbf{n}(\vec{r}) \left[\frac{\bar{n}''(\vec{r},0)}{\bar{n}(\vec{r},0)} - \frac{\bar{n}'(\vec{r},0)^2}{\bar{n}(\vec{r},0)^2} \right] d^2r, \tag{3.63}$$

where $\bar{n}''(\vec{r}, 0)$ is second derivative relative to p of the mean photon distribution when $p = 0$. As stated previously, the Fisher information given by Eq. 3.54 corresponds to the statistical mean value of $-\frac{\partial^2}{\partial p^2} l(\mathbf{n}|p)\Big|_{p=0}$, and thus, using Eq. 3.61,

$$\boxed{I_F^{\text{Poisson}} = \int \left[\frac{\bar{n}'(\vec{r},0)^2}{\bar{n}(\vec{r},0)} - \bar{n}''(\vec{r},0) \right] d^2r.} \tag{3.64}$$

Using Eq.3.59, we show that the integration of the second term over the transverse plane cancels in Eq. 3.64[39]. Recalling from Eq. 3.52 the expression of the photon distribution as a function of the mean field profile, we get

$$I_F^{\text{Poisson}} = N \int \frac{1}{|u_0(\vec{r},0)|^2} \left[\frac{\partial}{\partial p} |u_0(\vec{r},p)|^2 \Big|_{p=0} \right]^2 d^2r, \tag{3.65}$$

Simply expanding the square modulus in Eq. 3.65 yields

$$I_F^{\text{Poisson}} = N \int \left[\frac{\partial}{\partial p} |u_0(\vec{r},p)| \Big|_{p=0} \right]^2 d^2r \tag{3.66}$$

In order to simplify this expression, let us introduce a global positive parameter, denoted a, characterizing the variation of the image intensity with p, defined by the relation

$$\frac{1}{a^2} = \int \left[\frac{\partial}{\partial p} |u_0(\vec{r},p)| \right]^2_{p=0} d^2r. \tag{3.67}$$

[39] The second term of Eq. 3.64 indeed corresponds to the derivative relative to p of Eq. 3.59, which is valid for any p, and in particular for $p = 0$.

Using Eq. 3.67, the expression of the Fisher information becomes

$$I_F^{\text{Poisson}} = \frac{4N}{a^2}. \tag{3.68}$$

The smallest value of p that can be distinguished from the shot noise - i.e. corresponding to a signal to noise ratio (SNR) equal to 1 -, whatever the algorithm used to determine it from the local intensity measurements, provided that it gives an unbiased estimation of p, is finally given by

$$\boxed{p_{\text{min}}^{\text{Poisson}} = \frac{a}{2\sqrt{N}}.} \tag{3.69}$$

This value sets the standard quantum noise limit for intensity measurements of p, imposed by the random time arrival of photons on the detector. It is inversely proportional to the square root of the number of photons and depends on the parameter a defined in Eq. 3.67.

We now consider a non-classical illumination, still with identical mean intensity, but with local sub-Poissonian quantum fluctuations described by a noise variance $\sigma_+^2 < 1$ (assumed to be the same over the entire transverse plane). One can show that the CRB leads to[40]

$$p_{\text{min}}^{\text{sub-Poisson}} = \frac{a\sigma_+}{2\sqrt{N}}. \tag{3.70}$$

Let us now compare these results with the ones obtained in section 3 B.1 in the case of displacement measurements.

Using Eq.3.69 in the case of any amplitude detection of a coherent TEM_{00} beam, the parameter a corresponds to the beam waist w_0. The smallest displacement d_{min} that can be distinguished from the quantum noise is thus given by

$$d_{\text{min}} = \frac{w_0}{2\sqrt{N}} \tag{3.71}$$

which identifies with the quantum noise limit given in Eq. 3.45.

As we have already stressed, the limits given by Eq. 3.69 and 3.70 are valid for any measurement strategy. But a practical way enabling us to reach such an absolute limit in the general case remains to be found. This is what is presented in the next section.

- Array Detection performance

Let us assume that an image processor calculates a given linear combination of the local intensity values recorded by the pixels of an array detector, as represented in Fig. 3.7. Assuming that the pixels are small compared to the characteristic variation length of the image, the mean value $S(p)$ of the computed signal can be written as an integral over the transverse plane as follows

$$S(p) = \int g(\vec{r})\bar{n}(\vec{r},p)d^2r, \tag{3.72}$$

[40] The proof has been obtained by P. Réfrégier but has not been published yet.

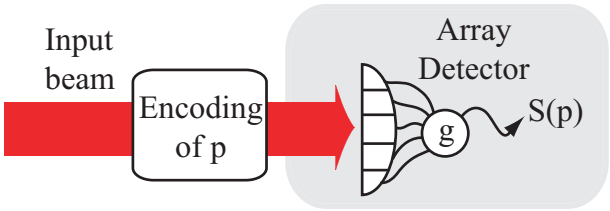

Figure 3.7: Array detector as an optimal detection of a parameter p within an optical image. This optical parameter has been encoded on the beam intensity via a physical interaction with a phase object, typically a phase mask or a nano-particle. g refers to the pixel gain distribution. $S(p)$ is the p-dependent processed signal.

where $g(\vec{r})$ is the local gain on the pixel localized at position $\vec{r}$, which can either be positive or negative. Assuming that p is small, we can write the modulus of the mean field profile as[41]

$$|u_0(\vec{r},p)| = |u_0(\vec{r},0)| + \frac{p}{a}v(\vec{r}) \tag{3.73}$$

where a is the same parameter as the one already introduced in Eq. 3.67, and where v is a normalized[42] transverse function[43]. Choosing the gains such as $S(p=0)=0$[44], i.e. such as $\int g(\vec{r})\bar{n}(\vec{r},0)d^2r = 0$, so that the signal can be written, at first order, as

$$S(p) = \frac{2Np}{a}\int g(\vec{r})|u_0(\vec{r},0)|v(\vec{r})d^2r. \tag{3.74}$$

For a coherent illumination, as the local quantum fluctuations are uncorrelated, the noise variance ΔS^2 on $S(p)$ is equal to the shot noise on each pixel weighted by the squared gain function $g^2(\vec{r})$, as explained in section 1 C.5.2. Moreover, as p is small, the noise is independent of p at first order, and we get

$$\Delta S^2 = N\int g^2(\vec{r})|u_0(\vec{r},0)|^2 d\vec{r}, \tag{3.75}$$

It is then possible to optimize the gain factor $g(\vec{r})$ in order to get the highest possible Signal-to-Noise Ratio (SNR) defined by

$$\mathrm{SNR} = \frac{S(p)^2}{\Delta S^2} \tag{3.76}$$

Using Cauchy-Schwartz inequality, one can show[45] that the highest SNR value for the

[41] This simply corresponds to a first order Taylor development of $|u_0(\vec{r},p)|$.

[42] The normalization means here that the integration of its squared modulus over the transverse plane equals 1, i.e. $\int |v(\vec{r})|^2 d^2r = 1$.

[43] The function $v(\vec{r})$ satisfies the following relation $\frac{v(\vec{r})}{a} = \frac{\partial}{\partial p}|u_0(\vec{r},p)|_{p=0}$. Note that such a mode, whose transverse envelope corresponds to the derivative of the mean field profile, has already been introduced in the particular case of displacement and tilt measurements in section 3 A.

[44] Note that this corresponds to a difference measurement, introduced in section 1 C.5.2

[45] Cauchy-Schwartz inequality for two square-integrable functions $f(\vec{r})$ and $h(\vec{r})$ is given by $\left|\int f(\vec{r})h(\vec{r})d^2r\right|^2 \leq \int f^2(\vec{r})d^2r \int h^2(\vec{r})d^2r$. Transposing this inequality in order to maximize the signal given by Eq. 3.74, with $f(\vec{r}) = g(\vec{r})|u_0(\vec{r},0)|$ and $h(\vec{r}) = v(\vec{r})$ yields $\left|\int g(\vec{r})|u_0(\vec{r},0)|v(\vec{r})d^2r\right|^2 \leq \int g^2(\vec{r})|u_0(\vec{r},0)|^2 d^2r \int v^2(\vec{r})d^2r$. The first factor of this maximal value is proportional to the noise given in Eq. 3.75, and the second factor equals 1.

present measurement strategy is given by

$$\mathrm{SNR} = \frac{4Np^2}{a^2}, \tag{3.77}$$

and is obtained[46] for an optimal value of the gain distribution given by

$$g_{\mathrm{opt}}(\vec{r}) = \beta \frac{v(\vec{r})}{|u_0(\vec{r},0)|}, \tag{3.78}$$

where β is an arbitrary constant. The minimum measurable value of p - corresponding to comparable signal and noise, i.e. SNR=1 - is given by

$$\boxed{p_{\mathrm{min}} = \frac{a}{2\sqrt{N}},} \tag{3.79}$$

which identifies with the standard CRB, previously obtained in Eq. 3.69. The present measurement strategy is therefore *optimal* as it allows us to reach the CRB[47], with the certainty that no other measurement strategy can do better. Note that we have not proven that it is the unique way to reach the CRB[48].

Let us now propose practical solution to perform measurement beyond the quantum limit described above, with the use of non classical light. As the only non classical state included in the determination of the limit given in Eq. 3.70 corresponds to the use of a very particular light field[49], we also consider here the use of single mode squeezed states[50], which can be generated experimentally as shown in section 4 C.

In order to maximally reduce the measurement noise obtained with an array detector below the shot noise limit, we know from section 1 C.5.2 that the *noise-mode of detection* - which corresponds to the mean amplitude profile multiplied by the gain distribution - has to be filled with squeezed vacuum. Using Eq.3.78, the noise-mode of detection $u_I$is thus given by[51]

$$u_I(\vec{r}) = a \frac{u_0(\vec{r})}{|u_0(\vec{r})|} \frac{\partial}{\partial p} |u_0(\vec{r},p)| \Big|_{p=0} \tag{3.80}$$

Using a bimodal field described in its eigen-basis[52] composed of a bright mode $u_0(\vec{r},0)$ in a coherent state carrying the mean field, and a squeezed vacuum state in the appropriate mode $u_I(\vec{r})$[53], the detected noise power is modified into

$$\Delta S^2 = N\sigma_+^2, \tag{3.81}$$

[46] The equality case in Cauchy-Schwartz inequality is reached when both functions $f(\vec{r})$ and $h(\vec{r})$ are proportional, i.e. here that $g(\vec{r})|u_0(\vec{r})|$ and $v(\vec{r})$ are proportional.

[47] The only restriction relative to the most general case is the assumption of small values of the parameter p.

[48] There is in fact not unicity as one can for instance already use several value of β for the gain configuration.

[49] The only non classical light whose fluctuations are spatially uncorrelated corresponds to the case of a locally squeezed beam.

[50] We recall that such states are always spatially correlated, to some extend.

[51] Note that this mode is normalized such as $\int |u_I(\vec{r})|^2 d^2r = 1$.

[52] See section 1 B.2.2.

[53] Note that we also know from section 1 C.5.2 that mean field - $u_0(\vec{r},0)$ - and noise-mode of detection - $u_I(\vec{r})$ - are orthogonal for a difference measurement. They can thus be chosen as the first two modes of the eigen-basis.

when the noise variance on the amplitude quadrature of the flipped mode is given by σ_+^2. The minimum measurable p value becomes

$$p_{\min} = \frac{a\sigma_+}{2\sqrt{N}}. \tag{3.82}$$

Note that the fact that the performance obtained here identifies with the non classical bound presented in Eq. 3.70 can only be qualified of "coincidence" at this stage. We have indeed not yet derived the quantum limit in presence of single mode squeezed light in the general case, and the bound could potentially be lower than the one obtained with uncorrelated beams.

Nevertheless, this result also provides information about the context of spatially uncorrelated illumination. A beam with local squeezing would also give the same performance and reach in this case the associated non-classical CRB presented in Eq. 3.70. Indeed, as all the transverse modes of such a field are squeezed, and thus in particular the appropriate one $u_I(\vec{r})$, the noise-mode of detection, the result would be identical, and the squeezing present in all the other modes would not contribute to the measurement noise.

As a conclusion, the result proposed with the single mode squeezed state is obviously of more experimental relevance, and still allows to reach the same sub-QNL performances with minimal resources. Practically, in order to have the best precision of a measurement of the parameter p, one can use the proposed scheme with first, maximum available power in the incident beam[54], as $p_{\min}$ is inversely proportional to the square root of the beam intensity, secondly with a beam profile tending to minimize the parameter a defined in Eq. 3.67, and finally with a squeezed vacuum state in the component of the *noise-mode of detection*.

B.2.3 Field measurements

- Cramer Rao bound calculation

We now assume that the information about p is extracted from the knowledge of the local complex field, i.e. *local amplitude and phase*, obtained by interferometric techniques[55]. We will assume that this field is monochromatic. The best possible detection would here access the local complex field on k-indexed areas paving the entire transverse plane, in the limit when their spatial extension approaches 0. Using similar notations as in the previous section, we denote $\mathbf{E}(\vec{r}) = [E_1, ..., E_k, ...]$ a single measurement of the field distribution, hence independent of p, where E_k corresponds to the complex field detected on area k. Again, because of the noise present in the light, the sample $\mathbf{E}(\vec{r})$ differs from its statistical mean value $\bar{E}(\vec{r}, p) = \left[\bar{E}_1(p), ..., \bar{E}_k(p), ...\right]$, where $\bar{E}_k(p)$ refers to the mean complex field measured on pixel k. Let $L(\mathbf{E}|p)$ be the likelihood of the observation of each possible realization $\mathbf{E}(\vec{r}) = [E_1, ..., E_k, ...]$.

As explained in the introduction of this chapter, the maximal precision on p can again be calculated from the CRB, which, for a field measurement, is the inverse of the following

[54] The incident beam power still has to be compatible with the properties of the detection device (saturation, damage threshold for instance), with the specificity of the sample from which the information is extracted (if a biological sample is studied, shining a high power beam onto it can alter or even destroy it), and with safety requirements.

[55] Note that we do not restrict here to a single quadrature measurement, potentially allowing any kind of field detection.

Fisher information

$$I_F = -\int \left[\frac{\partial^2}{\partial p^2} l(\mathbf{E}|p)\right]_{p=0} L(\mathbf{E}|0) d\mathbf{E}, \tag{3.83}$$

where the integration is taken on all the possible field distributions.[56]

We now need to specify the photon statistics in order to do the calculation of the Fisher information. We assume that the local field fluctuations in the transverse plane can be described by a generalized Gaussian probability density function independent from the mean field. The probability of measuring a field $\mathbf{E}_k$ on pixel k, when the parameter equals p, is given by

$$\boxed{\mathcal{P}_{k,p}(E_k) = \frac{e^{-\frac{1}{2}\left(E_k - \bar{E}_k(p)\right)^T \Gamma_k(p)^{-1}\left(E_k - \bar{E}_k(p)\right)}}{2\pi\sqrt{|\Gamma_k(p)|}}} \tag{3.84}$$

where the exponent T refers to a transposition of the fields written as Fresnel vectors[57] $\bar{E}_k(p) = \begin{pmatrix} \bar{X}_k^+(p) \\ \bar{X}_k^-(p) \end{pmatrix}$ and $E_k = \begin{pmatrix} X_k^+ \\ X_k^- \end{pmatrix}$, where $\bar{X}_k^+(p)$ is the statistical average of amplitude quadrature measurements on pixel k, denoted X_k^+. Similar notations are used for the phase quadrature X^-. $\Gamma_k(p)$ is the local covariance matrix on pixel k, and $|\Gamma_k(p)|$ is its determinant. Assuming in the following that the field fluctuations are homogeneous in the transverse plane, and independent of the parameter p, the covariance matrix neither depends on $\vec{r}$, nor on p, and we will simply denote it as Γ. Moreover, we will only consider fields whose amplitude and phase quadratures respectively have fluctuations described by the variances σ_+^2 and σ_-^2, and whose covariance matrix has the following expression[58]:

$$\Gamma = \begin{pmatrix} \sigma_+^2 & 0 \\ 0 & \sigma_-^2 \end{pmatrix}. \tag{3.85}$$

Such a covariance matrix either corresponds to coherent fields for which $\sigma_+^2 = \sigma_-^2 = 1$, or *locally squeezed* beams, for which we will assume $\sigma_+^2 < \sigma_-^2$. We can describe here classical and some range of non-classical illuminations with the same formulation[59]. With such illuminations, the probability introduced in Eq.3.84 can now be expanded into

$$\mathcal{P}_{k,p}(E_k) = \frac{1}{2\pi\sigma_+\sigma_-} e^{-\left[\frac{\left(X_k^+ - \bar{X}_k^+(p)\right)^2}{2\sigma_+^2} + \frac{\left(X_k^- - \bar{X}_k^-(p)\right)^2}{2\sigma_-^2}\right]}, \tag{3.86}$$

[56] Again, we can consider that the different field distributions range continuously in the transverse plane, when the amplitude of the field is not too small.

[57] The quadratures are defined relative to the mean field, as presented in section 1 A.2.4. As the mean field is p-dependent, the phase reference for the definition of the quadrature is continuously rotating in the Fresnel diagram when the parameter p is varied. This was summarized by arguing that "the phase reference was following the mean field".

[58] In order to simplify our expressions, we consider that the noise properties are conserved when the parameter p varies. This is not the case in general as the quadratures are rotating when the parameter p varies. We should therefore have included a p-dependence of the noise factors, or for instance have applied a rotation to the covariance matrix relative to the reference $p = 0$. This will have no consequence on the generality of our final results, as noise quadratures will be evaluated precisely for the reference value of the parameter $p = 0$, as shown by Eq.3.91.

[59] Note that, as in the previous section, the calculation does not include the case of single mode squeezed states, which are spatially correlated.

The likelihood $L(\mathbf{E}_1, ..., \mathbf{E}_k, ...|p)$ of observing the field distribution $\mathbf{E}(\vec{r}) = [\mathbf{E}_1, ..., \mathbf{E}_k, ...]$ corresponds to the product of the local probabilities, as we only consider non spatially correlated beams[60]:

$$L(E_1, ..., E_k, ...|p) = \prod_k \mathcal{P}_{k,p}(E_k). \tag{3.87}$$

The log-likelihood is thus given by

$$l(E_1, ..., E_k, ...|p) = \sum_k ln\left[\mathcal{P}_{k,p}(E_k)\right]. \tag{3.88}$$

Taking the limit of infinitely small pixels, for which the sum can be replaced by an integral, one finally obtains

$$l(\mathbf{E}|p) = -\int \left[\frac{\left(X^+(\vec{r}) - \bar{X}^+(\vec{r},p)\right)^2}{2\sigma_+^2} + \frac{(X^-(\vec{r}) - \bar{X}^-(\vec{r},p))^2}{2\sigma_-^2} + ln(2\pi\sigma_-\sigma_+) \right] d^2r,$$

whose first derivative relative to p is[61]

$$\frac{\partial l(\mathbf{E}|p)}{\partial p} = \int \left[\frac{\left(X^+(\vec{r}) - \bar{X}^+(\vec{r},p)\right)}{\sigma_+^2} \frac{\partial \bar{X}^+(\vec{r},p)}{\partial p} + \frac{\left(X^-(\vec{r}) - \bar{X}^-(\vec{r},p)\right)}{\sigma_-^2} \frac{\partial \bar{X}^-(\vec{r},p)}{\partial p} \right] d^2r.$$

Assume that our estimation of the photon number distribution is unbiased, i.e. the statistical average of sets of field measurements $\mathbf{E}(\vec{r})$ taken for $p = 0$ identifies with the mean field distribution $\bar{E}(\vec{r}, 0)$, i.e.

$$\int \mathbf{E}(\vec{r}) L(\mathbf{E}|0) d\mathbf{E} = \bar{E}(\vec{r}, 0). \tag{3.89}$$

This can be similarly shown for each quadrature, and the statistical average of the first derivative of the log-likelihood, taken for $p = 0$ thus becomes

$$\int \frac{\partial}{\partial p} l(\mathbf{E}|p)\Big|_{p=0} L(\mathbf{E}|0) d\mathbf{E} = 0, \tag{3.90}$$

which again exactly corresponds to the case described in Fig. 3.6. The maximum of the mean value of the log-likelihood is obtained for $p = 0$. We now need to calculate the second derivative in order to estimate the local curvature of the log-likelihood around $p = 0$.

The second derivative of the log-likelihood, taken for $p = 0$, yields

$$\begin{aligned} \frac{\partial^2 l(\mathbf{E}|p)}{\partial p^2}\Big|_{p=0} &= \frac{1}{\sigma_+^2} \int \left[\left(X^+(\vec{r}) - \bar{X}^+(\vec{r},0)\right) \frac{\partial^2 \bar{X}^+(\vec{r},p)}{\partial p^2}\Big|_{p=0} - \frac{\partial \bar{X}^+(\vec{r},p)}{\partial p}\Big|_{p=0}^2 \right] d^2r \\ &+ \frac{1}{\sigma_-^2} \int \left[\left(X^-(\vec{r}) - \bar{X}^-(\vec{r},0)\right) \frac{\partial^2 \bar{X}^-(\vec{r},p)}{\partial p^2}\Big|_{p=0} - \frac{\partial \bar{X}^-(\vec{r},p)}{\partial p}\Big|_{p=0}^2 \right] d^2r \end{aligned}$$

As the Fisher information corresponds to the statistical average of $-\frac{\partial^2 l(\mathbf{E}|p)}{\partial p^2}$ over all possible measurements, when $p = 0$, we get

$$I_F^{\text{Gauss}} = \frac{1}{\sigma_+^2} \int \frac{\partial X^+(\vec{r},p)}{\partial p}\Big|_{p=0}^2 d^2r + \frac{1}{\sigma_-^2} \int \frac{\partial X^-(\vec{r},p)}{\partial p}\Big|_{p=0}^2 d^2r. \tag{3.91}$$

[60] The states to which we have restricted our analysis - coherent and *locally squeezed* beams - are precisely not spatially correlated.

[61] Note that the last integrated term diverges but vanishes as it is independent of p.

Two terms canceled as the statistical average of the measured quadratures $X^{\pm}(\vec{r})$ corresponds to the amplitude quadrature mean value for $p = 0$, $\bar{X}^{\pm}(\vec{r}, 0)$, as explained in Eq. 3.89.

Recalling from Eq. 3.51 that $\bar{E}(\vec{r}, p) = 2\sqrt{N}u_0(\vec{r}, p)$, the definition of the quadratures given in section 1 A.2.4 yield $\bar{X}^{+}(\vec{r}, p) = 2\sqrt{N}u_0(\vec{r}, p)$ and $\bar{X}^{-}(\vec{r}, p) = 0$[62]. It is interesting to note that with this definition of the quadratures, the information about the parameter p is entirely comprised in the amplitude quadrature of the incident field.

Hence, the second term of the Fisher information given in Eq.3.91 cancels, and introducing the global positive parameter - denoted b - characterizing the variation of the image field with p

$$\frac{1}{b^2} = \int \left[\frac{\partial}{\partial p} u_0(\vec{r}, p)\right]_{p=0}^{2} d^2r, \tag{3.92}$$

we finally obtain the Fisher information

$$I_F^{\text{Gauss}} = \frac{4N}{b^2\sigma_+^2}. \tag{3.93}$$

The smallest value of p that can be distinguished from the quantum noise using any field detection of the optical beam is thus given by

$$\boxed{p_{\text{min}}^{\text{Gauss}} = \frac{b\sigma_+}{2\sqrt{N}}.} \tag{3.94}$$

This value sets the *quantum noise limit*[63] for field measurements of p, imposed by the quantum fluctuations of the light beam, and therefore valid for any measurement strategy. It is again inversely proportional to the square root of the number of photons, and depends on the variation of the field profile with the parameter p towards b, which is defined in Eq. 3.92. Moreover, Eq. 3.94 shows that squeezing the amplitude quadrature of the incident field improves the CRB through the factor σ_+ without the counterpart of measuring excess noise σ_- on the orthogonal quadrature[64].

- Homodyne Detection performance

As in the intensity case in section 3B.2.2, we propose a scheme in order to reach this limit in the case of a small parameter p, and for which the mean value of the complex electric field can be written at first order around $p = 0$[65]

$$E(\vec{r}, p) = 2\sqrt{N}\left[u_0(\vec{r}, 0) + \frac{p}{b}u_E(\vec{r})\right], \tag{3.95}$$

where b has been introduced in Eq. 3.92, and where $u_E(\vec{r})$ is a normalized transverse function defined such as $\frac{\partial}{\partial p}u_0(\vec{r}, p)\Big|_{p=0} = \frac{u_E(\vec{r})}{b}$[66].

Let us consider a balanced homodyne detection[67], whose local oscillator (LO) is defined

[62] We recall that the amplitude and phase quadratures are respectively defined relative to the real and imaginary parts of the factor in front of the mean field profile $u_0(\vec{r})$. The reference of the amplitude quadrature is following the mean field.

[63] We can define the related *quantum noise limit* when $\sigma_+ = 1$, corresponding to $p_{\text{min}}^{\text{Gauss}} = \frac{b}{2\sqrt{N}}$.

[64] For instance for a minimum squeezed state, we recall that $\sigma_+ = 1/\sigma_-$.

[65] This simply corresponds to a Taylor development of the mean field profile at first order around $p = 0$: $u_0(\vec{r}, p) = u_0(\vec{r}, 0) + p\left.\frac{\partial u_0(\vec{r}, p)}{\partial p}\right|_{p=0}$.

[66] $u_E(\vec{r})$ is normalized such as $\int |u_E(\vec{r})|^2 d^2r = 1$. This can easily be shown using the definition of b in Eq. 3.92.

[67] The homodyne detection and its properties have been presented in section 1 C.4.

by the following complex field operator

$$E_{LO}(\vec{r}) = 2\sqrt{N_{LO}}u_E(\vec{r})e^{i\theta_{LO}}, \tag{3.96}$$

where N_{LO} corresponds to the number of photons detected in the entire LO beam during the integration time. The setup is schematized on Fig. 3.8. The LO is much more intense

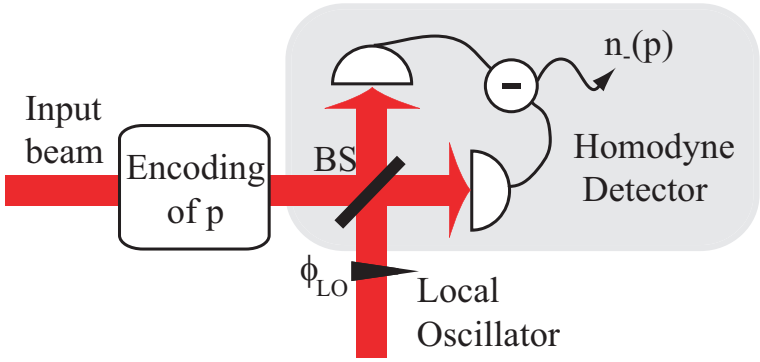

Figure 3.8: Balanced homodyne detection as an optimal detection of an parameter p within an optical image. This optical parameter has been encoded on local amplitude and phase of the beam via a physical interaction with a phase object, typically a phase mask or a nano-particle. $n_-(p)$ is the p-dependent homodyne detection signal. ϕ_{LO} is the local oscillator phase. BS : 50/50 beamsplitter.

than the image, i.e. $N_{LO} \gg N$. θ_{LO} is the global local oscillator phase. The mean intensity difference $n_-(p)$ between the two homodyne detectors is given in terms of number of photons by[68]

$$n_-(p) = \frac{1}{4}\int \left[E^*_{LO}(\vec{r})E(\vec{r},p) + E^*(\vec{r},p)E_{LO}(\vec{r})\right] d^2r. \tag{3.97}$$

Note the great similarity with Eq. 3.72. Incident field amplitude and local oscillator field play here identical roles of incident intensity and electronic gain, respectively. Though detectors do not resolve the spatial distribution of the beams and no processing of the spatial information is made, the balanced homodyne technique directly provides an "analog" computation of the quantity of interest.

Using Eq. 3.95 and 3.96, the signal given in Eq. 3.97 becomes

$$n_- = 2\sqrt{NN_{LO}}\left[\frac{p}{b}\cos(\theta_{LO}) + |\gamma|\sin(\theta_{LO})\right]. \tag{3.98}$$

where γ is the overlap integral between $u_0(\vec{r},0)$ and $u_E(\vec{r})$, which are not orthogonal in the general case[69]. γ is defined by

$$\gamma = \int u_0^*(\vec{r},0)u_E(\vec{r})d^2r. \tag{3.99}$$

[68] Note the great similarity with Eq. 3.72. Incident field amplitude and local oscillator field play here identical roles to incident intensity and electronic gain, respectively.

[69] $u_0(\vec{r},0)$ and $u_E(\vec{r})$ are orthogonal if the mean field profile is real for $p=0$, i.e. if $u_0(\vec{r},0)$ is real. Indeed, in this case $\gamma = b\int u_0(\vec{r},0)\left.\frac{\partial u_0(\vec{r},p)}{\partial p}\right|_{p=0} d^2r = \frac{b}{2}\int \left.\frac{\partial |u_0(\vec{r},p)|^2}{\partial p}\right|_{p=0} d^2r = 0$, as the global beam intensity is not modified by p and $\int |u_0(\vec{r},p)|^2 d^2r$ is a constant.

The local oscillator phase can be tuned to $\theta_{LO_{\text{opt}}} = 0\,[\pi]$ in order to maximize the first term of Eq.3.98, and hence the information about p that can be extracted.

For a coherent illumination, the noise power on the homodyne signal, denoted $\langle \hat{n}_-^2 \rangle$, corresponds to N_{LO}, i.e. to the shot noise of the LO, as shown by Eq. 1.126. The SNR of the homodyne measurement is thus given by

$$\text{SNR} = \frac{n_-^2}{\langle \hat{n}_-^2 \rangle} = \frac{4Np^2}{b^2}. \tag{3.100}$$

The minimum measurable value of p - corresponding to a SNR of 1 - with a homodyne detection is given by

$$\boxed{p_{\text{min}} = \frac{b}{2\sqrt{N}}}. \tag{3.101}$$

This is the Cramer Rao Bound.

Similarly to section 3 B.2.2, let us now propose practical solution to perform measurement beyond the quantum limit described in Eq. 3.101, with the use of non classical light. Again, as the only non classical state included in the determination of the limit given in Eq. 3.94 corresponds to light field which is very difficult to produce, we also consider here the use of single mode squeezed light.

Hence, when the component of the image selected by the LO is in a non classical state, i.e. allowing a squeezed u_E mode, which appears here as the *noise-mode of detection*[70], with a noise variance on the amplitude quadrature equal to σ_+^2 within the incoming beam, we get

$$p_{min} = \frac{b\sigma_+}{2\sqrt{N}}, \tag{3.102}$$

when u_E and u_0 are orthogonal.

Note that the fact that the performance obtained here again identifies with the non classical bound presented in Eq. 3.94 can only be qualified of "coincidence" at this stage. We have indeed not yet derived the quantum limit in presence of single mode squeezed light in the general case, and the bound could potentially be lower than the one obtained with uncorrelated beams.

Nevertheless, again, this result also provides information about the context of spatially uncorrelated illumination. A beam with local squeezing, yet unphysical, would also give the same performance and reach in this case the associated non-classical CRB presented in Eq. 3.94. Indeed, as all the transverse modes of such a field are squeezed, and thus in particular the appropriate one $u_E(\vec{r})$, the noise-mode of detection, the result would be identical, and the squeezing present in all the other modes would not contribute to the measurement noise.

As a conclusion, the result proposed with the single mode squeezed state is obviously of more experimental relevance, and still allows to reach the same sub-QNL performances with minimal resources.

[70] See section 1C.

B.2.4 Comparison

In the previous sections, we have presented two optimum signal processing techniques for the extraction of information contained in an optical image. They are optimum in the sense that they potentially[71] allow to reach the associated quantum limit imposed by the statistics of the measured light beam, namely the Cramer-Rao Bound. We have also shown that they could perform measurements beyond this limit with the use of single mode squeezed light within the incident beam.

Let us now compare the limits obtained for intensity and field measurements. The two expressions of the Fisher information about the parameter p that can be deduced from such detections are presented in Eq. 3.70 and 3.94. They only differ by the parameters a and b. We can thus compare intensity and field detection performances simply by comparing these two positive parameters. Recalling that the mean field profile is a complex function, we can write

$$u_0(\vec{r},p) = |u_0(\vec{r},p)|e^{i\theta_0(\vec{r},p)}, \tag{3.103}$$

where $\theta_0(\vec{r},p)$ is the phase distribution of the mean field. The first derivative of Eq. 3.103 relative to p, taken for $p=0$ yields

$$\left.\frac{\partial u_0(\vec{r},p)}{\partial p}\right|_{p=0} = \left.\frac{\partial |u_0(\vec{r},p)|}{\partial p}\right|_{p=0} e^{i\theta_0(\vec{r},0)} + i|u_0(\vec{r},0)| \left.\frac{\partial \theta_0(\vec{r},p)}{\partial p}\right|_{p=0} e^{i\theta_0(\vec{r},0)} \tag{3.104}$$

Similarly to the definition of a and b in Eq. 3.67 and 3.92, we define a real positive number c by the relation

$$\frac{1}{c^2} = \int |u_0(\vec{r},0)|^2 \left|\left.\frac{\partial \theta_0(\vec{r},p)}{\partial p}\right|_{p=0}\right|^2 d^2r \tag{3.105}$$

Then, the squared modulus of Eq. 3.104, integrated over the transverse plane, yields

$$\frac{1}{b^2} = \frac{1}{a^2} + \frac{1}{c^2} \tag{3.106}$$

The first conclusion is that $a \geq b$, i.e. that the CRB for field measurements is smaller than the one for intensity measurements. Moreover, it is interesting to note that each term given in Eq.3.106 exactly corresponds to the maximum information that can be extracted from field, intensity, and phase measurements[72], respectively. Indeed, multiplying Eq. 3.106 by $4N$ yields

$$I_F^{\text{field}} = I_F^{\text{intensity}} + I_F^{\text{phase}}. \tag{3.107}$$

It is not surprising to see that the information that can be extracted from field measurements, in which all quadratures can be accessed, corresponds to the sum of the information given by intensity and phase measurements. The case $a = b$ thus obviously corresponds to a parameter which is only affecting the intensity.

[71] The CRB is effectively reached when the detection process is done without any losses, i.e. for perfect detection efficiencies, perfect mode-matching...

[72] The information about the dependence of the phase of the mean field with respect to the parameter p is contained in c, as shown in Eq. 3.105.

Although field measurements give more precision on the parameter p, both detection schemes previously presented are still useful: the intensity scheme is simple to implement experimentally, and is not restricted to monochromatic light, whereas the amplitude scheme does not need pixellized detectors.

This work provides limits as well as optimal schemes for any coherent illumination. However, it does not account for all quantum field illumination, as we have restricted our analysis to spatially uncorrelated beams. In some future work, we will include spatial correlations in the transverse plane of the incident beam, i.e. single mode squeezed states, and will investigate the modifications of the CRB. The non classical performance of our schemes will thus be compared to the best possible measurement using the same non classical source. This will apply to the optimal extraction of any information from any quantum field in the transverse plane.

C Conclusion

In this chapter, we have presented simple physical parameters that can be encoded onto the transverse plane of an optical beam. We have notably introduced the displacement and tilt of a TEM_{00} reference beam, which are key elements of this thesis. Moreover, we have identified the bound under which such transverse parameters cannot be distinguished from the quantum noise, in any type of detection. Furthermore, we have proposed practical solutions to optimally extract any transverse information with classical resources. Finally, we have shown that measurements beyond this bound were accessible with the use of squeezed light in an appropriate mode which identifies with the noise-mode of detection introduced in the previous chapter.

CHAPTER 4

Transverse modes manipulation

Contents

There has been a growing interest during recent years in spatial quantum optical effects, usually called quantum imaging effects [Lugiato02, Kolobov 99, Gigan06], as the generation of spatial correlations or spatial squeezing in the transverse plane of laser beams may open the way to new applications in many different areas. Among them are laser physics, quantum information, and potentially astrophysics and biophotonics. Some pertinent examples are the measurement of small transverse displacement and tilt of a TEM_{00} laser beam below the quantum noise limit [Treps02], detection of weak phase images [Lugiato02], quantum teleportation of optical information [Sokolov01], transverse spatial quantum correlation for transmission of images [Gigan06] and noiseless image amplification [Kolobov95, Lopez07,2]. Multiple spatial modes can also provide advantages in regard to the complexity of quantum information protocols [Caves94] and can allow parallel transfer of quantum information through an optical network. In single photon optics, this has created considerable interest in the use of modes with different angular momentum [Zeilinger00, Oemrawsingh04, Langford04, Barnett06]. An advantage of continuous wave light beams is that close to perfect modulation and detection schemes are available, which is a requirement for the effective use of squeezed and entangled light in quantum information protocols.

An infinite number of orthonormal basis are available to describe the spatial properties of laser beams. The most commonly used are the Hermite-Gauss and the Laguerre-Gauss

basis. In this chapter, we will concentrate on the H-G modes, but a similar study could be undergone with any another set of modes. The higher order H-G modes are particularly interesting with a cartesian description of the transverse plane, as they are directly related to simple spatial properties of Gaussian beams, as we have detailed in the previous chapter in section 3 A. We recall that the real and imaginary parts of the TEM_{10} mode represent small changes in tilt and position of a TEM_{00} beam, whereas the real and imaginary parts of the TEM_{20} mode correspond to a small waist-size and waist-position mismatch.

Using the results obtained in the previous chapter, we know how to extract a spatial information from an image, even in the case of a multi-mode quantum illumination, and can thus potentially determine the spatial parameters of an object with which the beam has interacted better than what could be done with classical light. In order to be compatible with the use of squeezed light, note that the interaction with the object must not induce losses on the optical beam. This is for example the case for the imaging of a phase object.

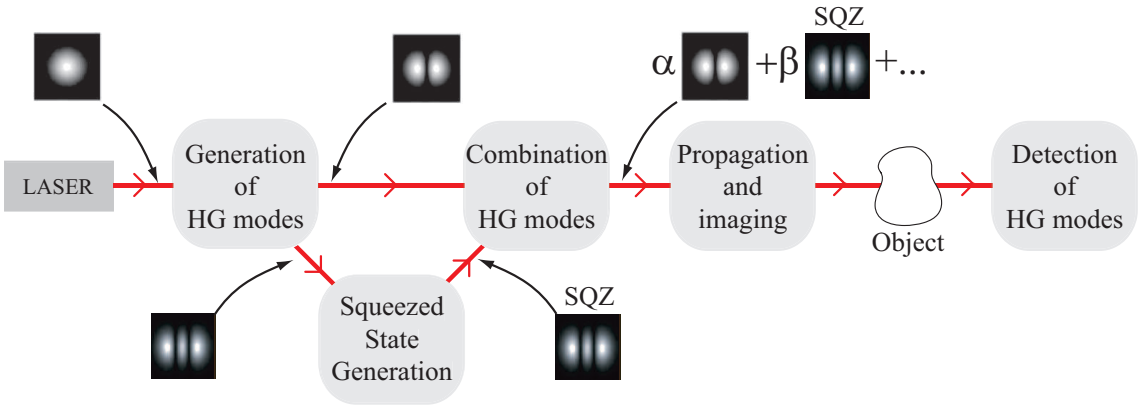

Figure 4.1: Quantum Imaging with Hermite Gauss modes. Five major steps are required and are detailed in this chapter. The scheme allows the generation of a multi-mode beam with squeezed components (SQZ), as illustrated by the transverse mode profiles, in order to retrieve spatial parameters of an object, with an accuracy better than the QNL.

However, we have not detailed yet the production and the manipulation of such a beam. This is what we propose to detail in this chapter, following the general quantum imaging scheme presented in Fig. 4.1. Some of this work has been accepted for publication [Lassen07].

First, we will give some properties about the propagation of Hermite Gauss modes, then present some devices that allow us to selectively produce these modes or excite the physical property of interest developed in section 3A. In order to scale the manipulation of such transverse modes, we will show how to combine them, and especially how to achieve the combination without modifying the non-classical properties of each beam. We will not come back on the selective detection of the information lying in each transverse mode, as this has already been detailed in section 1 C.

Then, we will concentrate on the second harmonic generation (SHG) of higher order transverse modes. And finally, we will present how the results obtained in the SHG section in the classical regime can be used to generate squeezing in higher Hermite Gauss modes.

A Basic manipulations of Hermite Gauss modes

A.1 Propagation of Hermite Gauss modes

A.1.1 Gouy phase shift

As we already briefly introduced in section 1 A.2.6, Hermite Gauss modes not only differ by their amplitude functions but also by their phase dependence, due to the Gouy phase $\psi_G(n,m,z)$ [Siegman86]. It is responsible for the existence of a phase shift between modes of different order during their propagation.

$$\psi_G(n,m,z) = (n+m+1)\phi_G(z) = (n+m+1)\arctan\left(\frac{z}{z_R}\right) \tag{4.1}$$

In order to give an idea of its importance, let us give two examples. For a beam at λ =1064 nm focused to $w_0 = 100\mu$ m, the Rayleigh range corresponds to $z_R = \pi w_0^2/\lambda \simeq 3$ mm. A phase shift as large as 45° is thus accumulated between two modes of consecutive order for a propagation over 3 mm. However, the Gouy phase shift can be neglected for collimated beams, for which the Rayleigh range z_R is large. Indeed, for a for a beam waist of $w_0 = 2$ mm, z_R =$\simeq$ 13 m, and less than 10° phase shift is obtained between two consecutive modes for a propagation over 2 meters.

The Gouy phase shift has a direct consequence on the displacement and tilt defined in Eq. 3.6. For a TEM_{00} beam, the displacement is proportional to the real part of the TEM_{10} component of the field, whereas the tilt is defined relative to imaginary part of the TEM_{10} component, but only in the reference plane. Nevertheless, knowing the coefficients of the decomposition in a particular plane, here in $z = 0$, a field can simply be propagated using the mode expansion as long as the paraxial approximation is still fulfilled[1]. Taking into account the phase shift accumulated between the TEM_{00} and the TEM_{10} modes, Eq. 3.6 can be rewritten as

$$E_{d,p}(x,z) = A_0 e^{i\frac{kx^2}{2R(z)}} e^{-i\phi_G(z)} \left[|u_0(x,z)| + \left(\frac{d}{w_0} + i\frac{pw_0}{2}\right) |u_1(x,z)| e^{-i\phi_G(z)} \right], \tag{4.2}$$

where we have used the complete expression of the Hermite Gauss modes given in Eq. 1.60.

Hence, displacement and tilt generated in $z = 0$ do not correspond to the real and imaginary parts of the TEM_{10} mode at position z anymore. Denoting as $d_{\text{app}}(z)$ and $p_{\text{app}}(z)$ the real and imaginary parts of the TEM_{10} component at position z, respectively, we get, using Eq. 4.2

$$\frac{d_{\text{app}}(z)}{w(z)} = \frac{d}{w_0}\cos\left[\phi_G(z)\right] + \frac{pw_0}{2}\sin\left[\phi_G(z)\right] \tag{4.3}$$

$$\frac{p_{\text{app}}(z)w(z)}{2} = -\frac{d}{w_0}\sin\left[\phi_G(z)\right] + \frac{pw_0}{2}\cos\left[\phi_G(z)\right] \tag{4.4}$$

[1] Indeed, the mean value of Eq. 1.27, shows that there exists a unique decomposition of the field as

$$E(x,z) = A_0 \sum_n c_n u_n(x,z)$$

, where $u_n(x,z)$ are the full expressions of the transverse modes which are satisfying the paraxial propagation equation, and where the coefficient c_n are independent of z. With these notations, Eq. 3.6 corresponds to $E(x,0) = A_0 \sum c_n u_n(x,0)$, and coefficients c_0 and c_1 can be identified in both cases.

$d_{\text{app}}(z)$ and $p_{\text{app}}(z)$ can be seen as "apparent" displacement and tilt at position z. A split-detector is for example only sensitive to the amplitude of the field and only measures an apparent displacement, as we will show in section 5 A.

We now focus on the consequences of the Gouy phase shift between two particular planes, which are called near-field and far-field. We define the near field (NF) as the plane $z = 0$[2]. The far field (FF) corresponds to $z \to \infty$. These definitions are common in Fourier optics, as the transformation of an optical image from NF to FF corresponds to the Fraunhofer diffraction regime and is described by a Fourier Transform [Born97].

The expression of the Gouy phase shift given in Eq. 4.1 immediately implies that a TEM_{nm} mode accumulates a $(n+m+1)\pi/2$ Gouy phase shift between NF and FF. A π phase difference is hence for instance accumulated between a TEM_{00} and a TEM_{20} mode, between NF and FF. A direct consequence of this is the modification of a multi-mode beam profile during propagation. This phenomenon is well known and corresponds to the diffraction of the image. The only fields which are stable during propagation are the modes solution of the paraxial propagation equation, as presented in section 1 A.2.

Let us now come back to the displacement and tilt of a TEM_{00} mode, and the way they are modified in such a Fourier transformation. Knowing that a TEM_{10} mode accumulates a $\pi/2$ phase difference relative to the TEM_{00} mode during the propagation between NF and FF. It shows that tilt and displacement information now respectively correspond to imaginary and real parts of the TEM_{10} component. A split-detector far from the reference plane, i.e. the one where displacement and tilt are produced, will be sensitive to the tilt but not to the displacement, whereas it was only sensitive to the displacement in the reference plane (NF). A measurement of the displacement in the FF yields the value of the tilt in the NF. These two variables, both related to the TEM_{10} component of a TEM_{00} mode beam, are therefore linked by Fourier Transform [Hsu05].

One can then wonder whether there also exists such a Fourier relation between waist-size and waist-position mismatch, the pair of variables related to the TEM_{20} component of a TEM_{00} mode beam. Recalling that a TEM_{20} accumulates a π phase shift relative to a TEM_{00} mode between NF and FF, it is obvious from Eq. 3.28 that waist-size and waist-position are not inverted by Fourier Transform. The inversion between both variables is obtained here between the NF and the plane which is such as $2\arctan(z/z_R) = \pi/2$, i.e. $z = z_R$.

For a TEM_{00} beam, displacement and tilt are thus the only variables contained in Hermite Gauss modes that are Fourier Transform of each other.

A.1.2 Imaging in terms of Hermite Gauss modes

In the previous section, we have presented the free propagation of an optical image in terms of the evolution of its Hermite Gauss components. We now consider a general imaging setup, and analyze in particular the image modification when transmitted through a lens, still in terms of individual Hermite Gauss modes evolution.

[2]Note that the near field can be defined more generally relative to a reference object or plane, and could also be taken elsewhere on the propagation axis. We have chosen here $z = 0$ as the expressions are simpler in this plane, but the properties which are discussed are completely transposable to any reference transverse plane situation.

Setting up an imaging experiment with Gaussian beams adds a degree of complexity relative to geometrical optics. The position of the beam waists and their size is here of great importance.

Let us first consider the most simple case of the imaging of a planar intensity or phase mask onto a detector. For ideal performance of the imaging setup, the beam wave-front must match the mask and the detector properties. The beam used to convey the information must therefore be imaged such that it has a waist, i.e. a planar wave-front in the mask and in the detector planes.

In such a case, the most convenient ways to proceed are to build "2f-2f" or "f_1-f_1-f_2-f_2" setups, as presented in Fig. 4.2. In these two simple configurations, the object and image

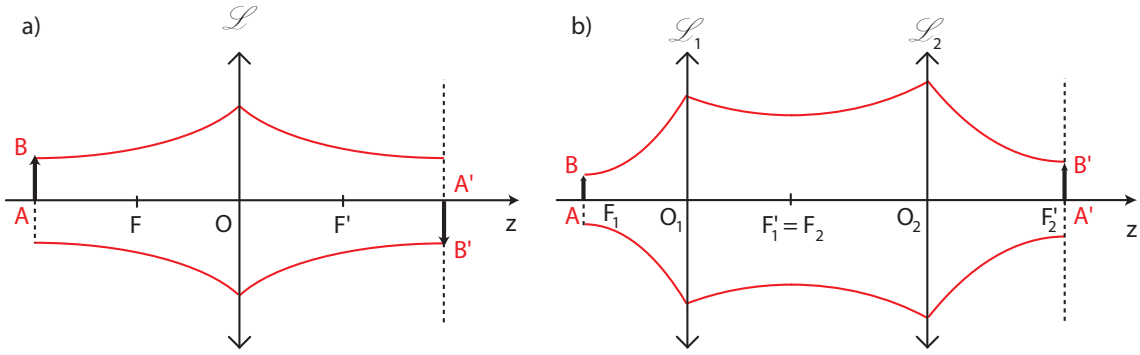

Figure 4.2: The two most simple imaging setups, a)"2f-2f" and b) "f_1-f_1-f_2-f_2" configurations. In both cases, object AB and image A'B' planes are situated at waists position, and the magnifying factor equals 1.

planes are both situated at waists position. In the first case, the magnifying factor equals 1 whereas it can be tuned in the second configuration by the ratio f_1/f_2.

General imaging properties using ABCD matrices have been very clearly detailed in reference [GiganPhD04], and we therefore propose only the resolution of a simple example, that will be useful to understand the imaging setup demonstrated in section 5 A. The most important feature of imaging a given object plane with gaussian beams is that there exists no simple relation between the position of the images and the position of the waists.

Let us consider the configuration presented in Fig. 4.3. We want to answer the following question: what is the Gouy phase shift accumulated from the plane defined by the waist w_0 to the plane defined by the waist w_0', between a TEM_{00} and a TEM_{10} components, initially in phase in the plane containing w_0? As represented in Fig. 4.3, it is always possible to choose a fictitious object plane anywhere on the optical axis before the lens, and calculate its image using geometrical optics. Both planes, referred as NF and NF' in Fig. 4.3, are optically conjugated through the lens. As a consequence, the intensity distributions in both planes identify up to a scaling factor. It is easy to show in this case that the expression of the ABCD matrix used to propagate the field from plane NF to plane NF' is such that $B = 0$ and $C = -1/f$ [Gigan05]. The field distribution in plane NF' can then be shown to be related to the field in plane NF by [Siegman86, Gigan05]

$$E(\vec{r}') = -ME(M\vec{r})e^{i\frac{kCM\vec{r}'^2}{2}} \tag{4.5}$$

There is thus an additional curvature in the image plane NF' with respect to the field

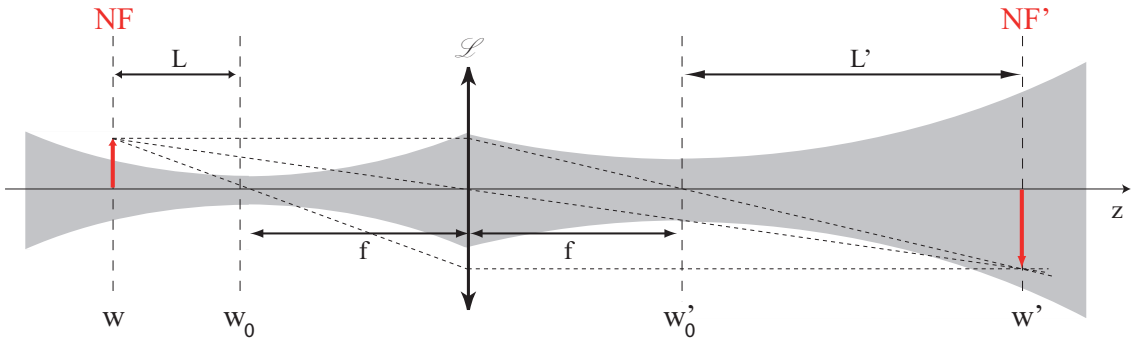

Figure 4.3: Example of imaging setup where gaussian beam profile and geometrical optics are simultaneously represented. An object in plane NF(near field) is imaged in NF' using a lens of focal lens f. The beam waists before and after the lens are respectively denoted w_0 and w'_0.

distribution in plane NF. However, knowing that our optical systems are typically such as $M \simeq 1$, $f \simeq 0.1m$, $w \simeq 100\mu m$, $\lambda \simeq 1\mu m$, the curvature is small as the exponential term is of the order of 0.1 rad[3]. In our experiments[4], we can thus neglect this curvature, and we will assume that the image in plane NF' has exactly the same modal decomposition as the one in plane NF. This means that no mode-dependent phase shift has been accumulated during the propagation through the lens from NF to NF'[5].

This property can then be used to deduce all phase shifts between modes in any plane on each side of a lens. In particular, we can now answer the question regarding the phase shift $\Delta\phi_{01}$ accumulated between TEM_{00} and TEM_{10} modes from w_0 waist plane to w'_0 waist plane in Fig. 4.3. Starting from the plane containing w_0, the phase shift between TEM_{00} and TEM_{10} components in plane NF corresponds to the Gouy phase shift $\arctan(L/z_R)$ by back propagation of the beam (see Fig. 4.3). Then using the previous property, we know that no phase shift is accumulated between planes NF and NF'. Finally, a phase shift of $\arctan(L'/z'_R)$ is accumulated between NF' and the plane containing w'_0. z_R and z'_R are respectively the beam Rayleigh ranges before and after the lens. In the end, the phase shift accumulated between both waist plane between TEM_{00} and TEM_{10} components is

$$\Delta\phi_{01} = arctan(L/z_R) + arctan(L'/z'_R).$$

This method, illustrated here in a particular case, is useful to deduce the beam Gouy phase shift modification after a lens, and will be used in section 5 A.

Let us give another important imaging scheme for the need of section 5 A. We have seen earlier in this section that displacement and tilt were Fourier transform of each other. This property is illustrated in Fig. 4.4, where the far field (FF) is classically accessed in a "f-f" configuration with a lens of focal length f. In configuration a), a pure displacement

[3]This value is not so small and one has to be careful about the validity of the approximation for large beams or large magnifying factors.

[4]See section 5 A.

[5]Note that taking into account the additional curvature of the beam would add a mode-dependent phase shift between the two field distributions, resulting from the decomposition of $E(\vec{r}')$ given in Eq. 4.5 in the Hermite Gauss basis.

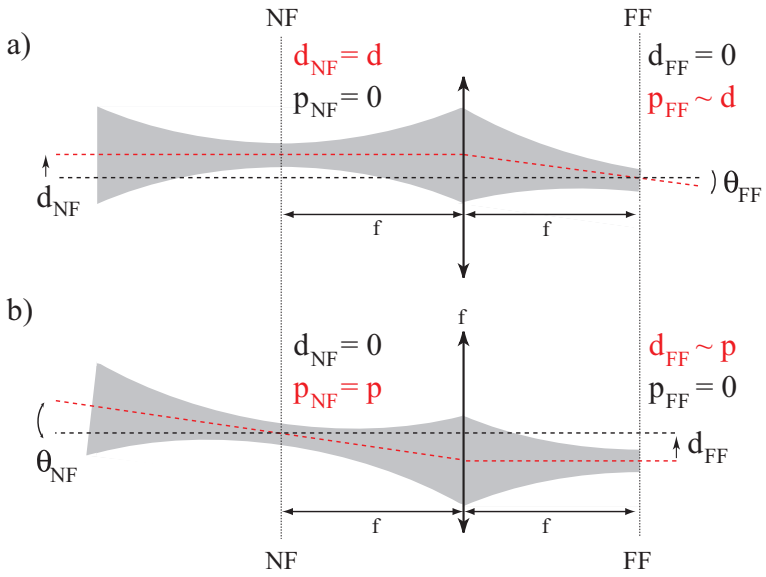

Figure 4.4: Correspondence between a) displacement in the near field (NF) and tilt in the far field (FF), and b) tilt in the near field (NF) and displacement in the far field (FF). Displacement and tilt are Fourier Transform of each other.

in NF plane translates into a pure tilt in plane FF. Similarly, in configuration b), a pure tilt translates into a pure displacement. Using measurements in the FF, we can infer the value of the Fourier related component using the following expressions[6]

$$\frac{p_{FF} w_{FF}}{2} = -\frac{d_{NF}}{w_{NF}} \tag{4.6}$$

$$\frac{d_{FF}}{w_{FF}} = \frac{p_{NF} w_{NF}}{2} \tag{4.7}$$

where the relation between w_{NF} and w_{FF} can simply be deduced from ABCD matrix calculation.

A.2 Generation of higher order modes

We now introduce some devices that allow selective and controllable generation of spatial modes. We will first present "universal" mode converters, i.e. techniques that potentially converts any mode into any other mode. Then, we will concentrate on the selective generation of higher order Hermite Gauss modes. Finally, we will present devices that allow the production of controllable displacement and tilt. For each apparatus, efficiency, simplicity and cost are of course the main issues, and will be investigated.

[6] These relations can be shown using the previous results. In the imaging scheme shown in Fig. 4.4, NF' - the conjugated plane with NF by the lens - is positioned at infinity after the lens. We know that no differential phase shift exists between the TEM_{00} and TEM_{10} components between the planes NF and NF'. In order to back-propagate the field to the plane denoted FF, a Gouy phase shift equal to $\pi/2$ is accumulated between TEM_{00} and TEM_{10} components. This shows that the displacement generated in plane NF is carried by the imaginary component of the TEM_{10} mode in plane FF and appears as a tilt in this plane. Similar relation exists for the tilt in plane NF.

A.2.1 "Universal" mode-conversion devices

The first "universal" device one could mention is the hologram mask. Its advantages are its wide range of applications, its very low price, and the way it can easily be duplicated[7]. A picture of an example of hologram is presented in Fig. 4.5a) [Arlt98]. This pattern

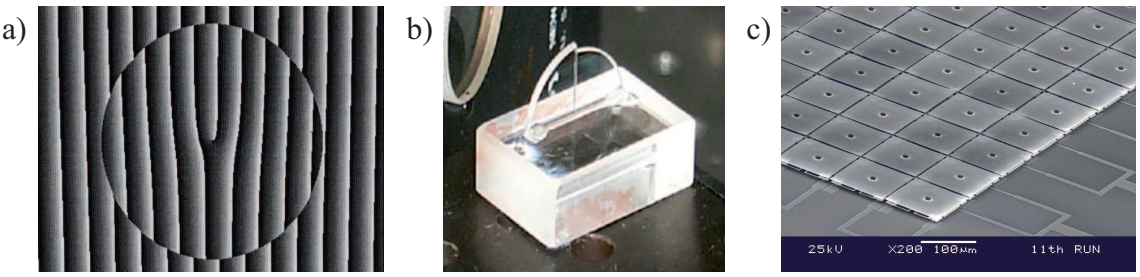

Figure 4.5: "Universal" mode-converting devices. a) hologram mask, b) phase mask, c) spatial modulator.

converts an incident TEM_{00} mode into a LG_0^1 mode in its first order diffracted pattern. Such a hologram can be generated by interfering the illumination mode and the mode that one wants to generate. The drawback of such a mode converting device is mainly its specificity. One hologram indeed corresponds to a single mode generation, for a very particular illumination mode, for which the hologram has been processed. For instance if the waist of the incident TEM_{00} mode is slightly modified, the purity of the converted mode drops rapidly. Moreover, when the mode-conversion of non classical beams is considered, the loss caused by the holograms can be a limiting factor.

A second interesting mode-converting device is the phase mask. The first advantage of such a pure phase object is its very high efficiency, as a non classical beam does not necessarily suffers from losses when transmitted through the mask. An example of phase mask is given in Fig. 4.5b). This wave-plate converts a TEM_{00} mode into a flipped gaussian mode. This conversion has been studied in detail in reference [Delaubert02], and will be used in the experiments presented in chapter 5. Nevertheless, similarly to hologram masks, such devices are limited to a very specific use, and must be changed each time the illumination mode profile or the desired profile changes.

The most flexible "universal" device remains the phase modulator, although it is also the most complex one to use, and obviously the most expensive. A picture of an example of spatial phase modulator is presented in Fig. 4.5c). It consists of an array of a large number of micro-controlled mirrors[8] [MISA], than can either be used in reflection or transmission - depending on designs - in order to produce any mode, according to the preprogrammed phase profile provided by the tunable mirrors. Such a system is perfect from classical imaging applications, but the losses, close to 50%, are still a limiting factor for its implementation in quantum imaging.

[7] Most holograms masks can be generated simply by photocopying a pre-existing mask.

[8] This type of micro-element technology is referred to as the MEMS (MicroElectroMechanical Systems) technology.

A.2.2 Hermite Gauss mode generation using a misaligned optical cavity

Let us now focus on the selective generation of Hermite Gauss modes. We propose a simple scheme to convert a TEM_{00} input beam into a pure TEM_{n0} beam by using an optical cavity.

We consider a TEM_{00} beam incident on a ring cavity[9], as illustrated in Fig. 4.6a). When the beam is perfectly aligned and mode-matched into the cavity, the transmission

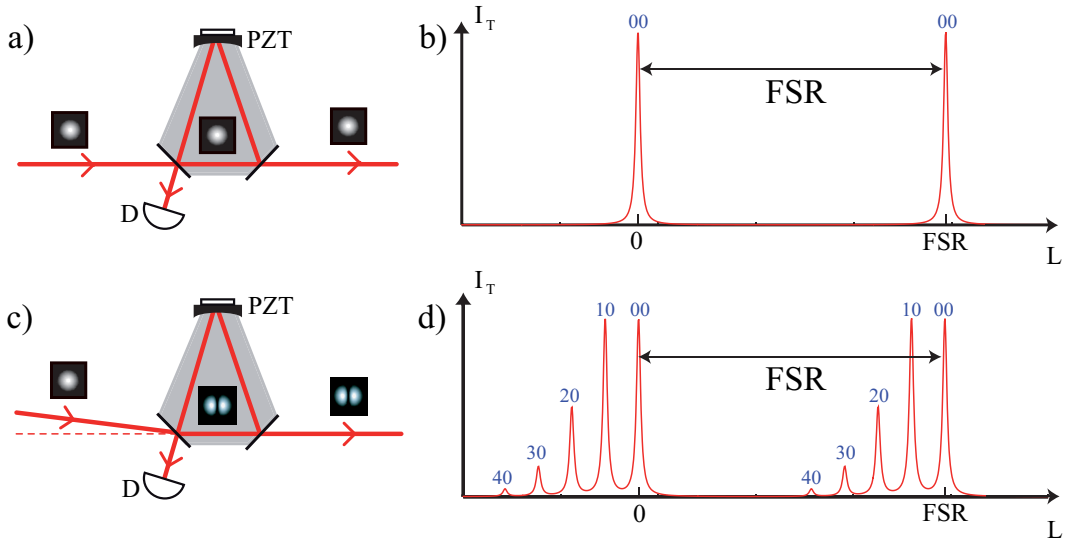

Figure 4.6: Hermite Gauss mode-converting device. A misaligned cavity is locked at resonance to the desired Hermite Gauss mode. a) Cavity aligned to the TEM_{00} mode. b) Transmitted intensity I_T as a function of the cavity length L, when the cavity is aligned. c) Cavity misaligned in order to maximize the TEM_{10} mode peak. d) Transmitted intensity as a function of the cavity length, when the cavity is misaligned. The numbers above each peak corresponds to the TEM_{n0} mode resonant for this cavity length. FSR:free spectral range. D:locking detector. PZT:piezoelectric device.

as a function of the cavity length is given by the well-known Airy function, as represented in Fig. 4.6b). A TEM_{00} output mode is obtained when the cavity length is locked to the maximum of the peaks. Experimentally, this locking is achieved with the Pound Drever Hall technique [Drever83]. The error signal is generated from the measurement of the reflected beam on the input coupler of the cavity and retro-acted on a mirror-mounted piezoelectric stack inside the cavity[10].

When the beam is misaligned relative to the previous configuration, the displaced or tilted beam projects onto several transverse modes of the optical cavity, as shown in Fig. 4.6c)and d). The transmission as a function of the cavity length is hence composed of several peaks, each one of them corresponding to the resonance of a particular transverse mode inside the cavity. Locking the cavity length to any of the peaks allows the generation of the corresponding mode. Moreover, if the cavity is designed in order to prevent any mode

[9]Note that a ring-cavity can also be used as a mode combiner, as explained in section 4 A.3.3.

[10]Note that the generation of the error signal requires the encoding of a phase modulation at RF frequency Ω on the input beam, for instance with an EOM (Electro-Optic-Modulator), and to demodulate the measured signal with the locking detector at the same frequency Ω.

degeneracy, each peak can be clearly separated from the others, and the output mode can easily be more than 99% pure. Furthermore, for an impedance-matched cavity[11], the relative height of each resonance peak directly corresponds to the coefficient of the decomposition of the displaced or tilted input TEM_{00} beam, as presented in section 3 A.1. The maximum of the coefficient of each TEM_{n0} mode as a function of the displacement presented in Fig. 3.3 can thus directly give us the best conversion efficiency achievable with this method. Hence, the conversion of a TEM_{00} into a TEM_{00} is 100% efficient, as expected, whereas the conversion into TEM_{10} and TEM_{20} modes is only $0.60^2 = 36\%$ and $0.50^2 = 25\%$ at best.

Note that the efficiencies presented here can be improved with different methods. For instance, for the generation of a TEM_{10} output mode, a special wave-plate can be inserted into the beam before the cavity [Delaubert02]. It converts the TEM_{00} beam into a *flipped mode*, which is a TEM_{00} with a π phase flip in the center of the beam, as already presented in Fig. 1.11. The TEM_{10} coefficient of the flipped mode decomposition equals 0.8. Therefore, without misaligning the beam, the conversion efficiency of the combination of wave-plate and cavity can be improved to $0.8^2 = 64\%$. This technique will be used in section 5 B. Another example is to de-focus the input beam inside the cavity in order to increase the TEM_{20} component. The relation between de-focusing and TEM_{20} mode is explained in section 3 A.2.

The advantages of the mode conversion with a ring cavity are the purity of the output mode, and the simplicity of use when one often needs to change the output field from one mode into another. The propagation axis of the output beam is never modified as it is defined by the cavity axis. No realignment it thus required between the operation of the cavity on resonance in different modes. As we will present in chapter 5, this device will be particularly useful for our experiments. However, the low efficiency does not allow the conversion or the transmission of non-classical fields, and will therefore be limited to modification of coherent beams.

Let us briefly mention that the production of a tunable combination of transverse modes, which cannot be achieved with the cavity technique, is possible by means of second harmonic generation of TEM_{n0} pump modes, as presented in section 4 B.

A.2.3 Displacement and tilt modulators

The generation of displacement of a beam is an easy task with the use of a mirror mounted on a piezoelectric material (PZT). At low frequency, i.e. at frequencies below the mechanical resonance of the PZT device, typically below 20 kHz in our experiments, a pure displacement[12] of the beam can be achieved when the angle of incidence of the beam is around 45°. However, at higher frequencies, using the accidental resonances of the PZT in the MHz regime, we noticed that a combination of displacement and tilt was generated on the beam. This result is presented in section 5 A. The latter combination is intrinsic to the PZT device and cannot be modified.

However, it can be useful to be able to either generate a pure beam displacement, or

[11] A cavity is said impedance-matched if the reflectivity of its mirrors potentially allows 100% of the light to be transmitted through. Experimentally, transmission of around 90% can typically be achieved in the fundamental mode of the cavity.

[12] Note that although it does not generate any tilt, such a method adds a global phase shift to the beam.

to control the amount of displacement and tilt generated. A scheme for the production of tunable displacement and tilt is presented in Fig. 4.7.

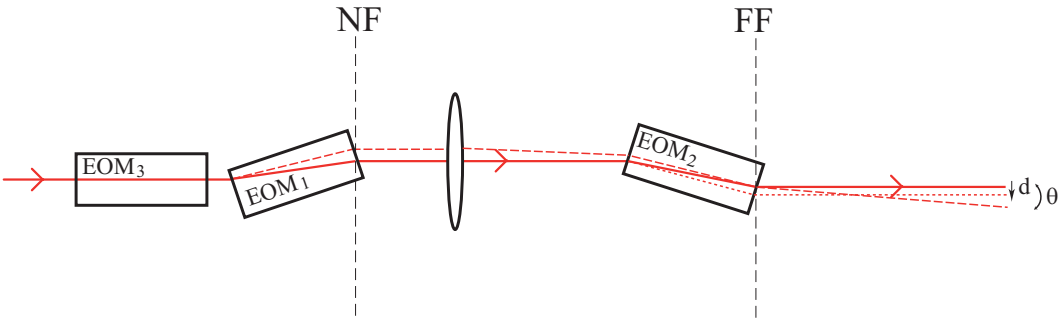

Figure 4.7: Tunable beam displacement and tilt generator. The modulation of a beam using an electro-optic modulator (EOM), when the angle of incidence is non zero, generates a pure displacement of the output beam. The combinations of two identical devices in Fourier related planes allows a tunability of displacement and tilt independently. A third EOM (EOM_3) can be used at the very beginning of the setup in order to compensate for the phase shift induced by the EOM_1 and EOM_2. Cases of pure displacement d and pure tilt θ are represented in dotted lines. The solid line is the beam path when no voltage is applied to the EOMs. NF:near field. FF:far field.

Such a device has first been implemented in reference [Treps02], and relies on the properties of electro-optic modulators (EOM). The refractive index of an EOM crystal can be modulated at RF frequency. This feature is usually used in order to produce a phase modulation on an optical beam whose direction of propagation corresponds to the crystal axis. When the input beam is tilted, the modulation of the refractive index also results in a pure displacement of the output beam. The displacement can thus be tuned at RF frequency by changing the amplitude of the modulation.

Moreover, the combinations of two identical devices in Fourier related planes allows a simultaneous tunability of displacement and tilt independently. Indeed, the production of pure displacement in one plane will result in a pure tilt in its far field. The displacement of this controllable tilted beam is then achievable using the same method.

Furthermore, a third EOM (EOM_3) can be used at the very beginning of the setup in order to compensate for the phase shift induced by EOM_1 and EOM_2.

Such a tunable displacement and tilt generator has not been demonstrated yet, and that only a pure displacement generator has been set up [Treps02].

A.3 Combination of higher order modes

A.3.1 Beam-splitter

The most simple combination of Hermite Gauss modes is obviously the one using a simple beam-splitter. Such a combination gives rise to mode-to-mode interferences at the output of the beam-splitter, i.e. that a state in a given mode of the first beam will only interfere with the state which has the same transverse profile within the second incident beam. Both outputs of the beam-splitter depend on the relative phase between the two input beams.

The use of a 50/50 beam-splitter can be appropriate in quantum optics experiments in order to combine two beams with identical profiles. This is for instance what is used in a homodyne detection. It is also used in order to produce single-mode quadrature entanglement from two squeezed beams in quadrature.

However, when only one the input state in the mode of interest is a non-vacuum state, the other one being vacuum, it is obvious here that the only action of the beam-splitter will be to add vacuum fluctuations. This typically corresponds to a beam attenuation, whatever the beam-splitter ratio. As squeezed states are not robust to loss, we will try not to make use of beam-splitters in such a case. Still, this has for example been done in reference [Treps02], in order to combine a bright TEM_{00} and a dim squeezed flipped mode. Only a few percent loss was induced on the squeezed beam, whereas almost all the intensity of the coherent TEM_{00} was lost in the process. We now present ways to combine different beams without losses, in order to prevent squeezed states from any loss during combination operation similar to the one described in the example above. We will first present how the addition of a second beam-splitter can allow a lossless combination of modes.

A.3.2 Special Mach-Zehnder

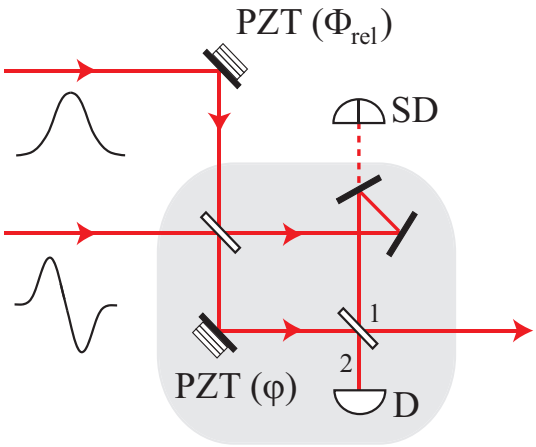

Figure 4.8: Special Mach Zehnder interferometer for lossless combination of Hermite Gauss beams of opposite parity. The particularity of the interferometer is to present one additional mirror in one arm. This insures an additional π phase shift between both arms only for the odd modes. Both input beams - here TEM_{00} and TEM_{10} modes - are combined without losses. The interferometer is locked using a locking detector (D) and a PZT in one arm of the interferometer, PZT (φ). The relative phase Φ_{rel} between both input beams is locked using a split detector (SD) and a PZT before the interferometer.

We consider the special Mach-Zehnder (MZ) interferometer represented in Fig. 4.8. Its particularity is to present an additional mirror in one arm of the interferometer.

Such a device allows the lossless combination of beams whose transverse profiles have opposite parity. We will typically use such an interferometer to combine a TEM_{00} mode, whose profile is even with respect to the transverse axis, with a TEM_{10} or a *flipped mode*, whose profiles are odd.

In order to explain this property, let us use the following notations for the mean value of the two input fields

$$E_{in,e}(x) = A_e u_e(x) \tag{4.8}$$
$$E_{in,o}(x) = A_o u_o(x) e^{i\phi_{rel}}, \tag{4.9}$$

where the indexes e and o respectively refer to *even* and *odd* modes $u_e(x)$ and $u_o(x)$. A_e and A_o are the field amplitudes, and ϕ_{rel} is the relative phase between the two input fields in the plane defined by the first beam-splitter.

It is then easy to show that the mean field expressions at the two output ports are given by

$$E_{out,1}(x) = \frac{1}{2}\left[iA_e u_e(x)\left(1+e^{i\varphi}\right) - A_o u_o(x) e^{i\phi_{rel}}\left(1+e^{i\varphi}\right)\right] \tag{4.10}$$
$$E_{out,2}(x) = \frac{1}{2}\left[A_e u_e(x)\left(1-e^{i\varphi}\right) + iA_o u_o(x) e^{i\phi_{rel}}\left(1-e^{i\varphi}\right)\right] \tag{4.11}$$

where φ is the relative phase between both arm of the interferometer, and where we have used that the reflection of an odd mode on a mirror is equivalent to the transformation $u_o(-x) \rightarrow -u_o(x)$, whereas it has no effect on an even mode $u_e(-x) \rightarrow u_e(x)$. The presence of an odd number of mirrors in the interferometer therefore insures, only for odd modes, an additional phase shift between both arm of the interferometer propagating inside the special MZ.

Taking $\varphi = 0[2\pi]$ in Eq. 4.10 and 4.11 yields

$$E_{out,1}(x) = iA_e u_e(x) - A_o u_o(x) e^{i\phi_{rel}} \tag{4.12}$$
$$E_{out,2}(x) = 0 \tag{4.13}$$

which exactly corresponds to a lossless combination of both beams, as the integrality of both input fields is going through the same output port of the interferometer. Note that this due to the presence of the extra mirror. Otherwise, the two beams would have been re-separated at the output of the interferometer, the even beam going out through port 1, and the odd beam going through port 2.

In order to implement this interferometer, a few experimental considerations have to be taken into account. First, the interferometer needs to be as small as possible, in order to maximize its stability, with arms of comparable length. The best operation is achieved with collimated beams, for which a small discrepancy in the arm lengths has not critical consequences on the mode matching of the beams on the second beam-splitter of the interferometer[13].

We now consider a single input field, which has been carefully mode-matched on both beam-splitters. In order to lock the interferometer, i.e. to lock ϕ to $0[2\pi]$, the error signal can be taken on the output port 2 of the interferometer with a normal detector. It will be locked to a dark fringe, leaving all the intensity in the first output port. The modulation to be used to create the error signal has to be generated on the same PZT as the one which is used to control the phase difference between both arms[14]. The phase modulation

[13] This is of particular importance for the combination of a TEM_{00} mode with a flipped mode, as the latter mode evolves very rapidly during propagation due to its high order components [Delaubert02].

[14] Any modulation produced before the interferometer is of no use here, as it will be present in both arms of the interferometer and does not allow the generation of the MZ.

is generated with an accidental resonance of the PZT at RF frequency Ω, typically around 1 MHz[15]. The error signal is generated by demodulating the intensity measured on the locking detector at Ω, similarly to the Pound Drever Hall locking technique [Drever83]. The interferometer is now locked in order to transmit the first beam, with up to 98% efficiency.

A way to align the second input beam on the first beamsplitter with the other mode has now to be found. Both modes are orthogonal as they have opposite parity, and it is therefore impossible to use the usual method of maximization of the interference fringes. In each particular case, we found to transform one of the beam profiles to fit the other one, without misaligning the beam[16]. At this stage, both beams are combined at the output of the interferometer, but the relative phase between them, denoted Φ_{rel} in Fig. 4.8, has not been fixed.

The locking of the relative phase between both input beams Φ_{rel} again requires special attention. As both beams are orthogonal, no interference signal can be generated with a normal "bucket" detector in order to infer Φ_{rel}. However, both beams are not orthogonal anymore with respect to a split-detection, as both beams interfere on each half of the overall beam. The error signal is hence directly generated without using any modulation, and retro-acted on a mirror mounted PZT placed on one beam before the interferometer. The split-detector can be set without blocking the output beam by using the "leakage" of a mirror of the interferometer, as represented in Fig. 4.8. A dichroic mirror can for instance replace one mirror. The angle of the dichroic mirror can be tuned in order to allow only 1% of the light to go through, in order to minimize the losses. Note that both lockings are independent, which is easier to manage experimentally.

The combination technique presented here is rather easy to implement, and does not require any special component[17]. However, it does not allow to combine any pair of modes.

A.3.3 Ring cavity

An optical ring-cavity, similar to the one presented in section 4 A.2.2, can be used to combine any orthogonal modes. The combination scheme is presented in Fig. 4.9, in the case of the combination of TEM_{00} and TEM_{10} modes. First, the cavity is locked to resonance on one of the input beam mode, which is transmitted through the cavity, as explained in section 4 A.2.2. If the cavity is designed in order to prevent degeneracy between the resonance peaks of both modes, the second beam will be totally reflected by the cavity, and will therefore be combined with the other transmitted beam. Note that this condition is always achievable as long as both modes are orthogonal. No other restriction, for example on the parity of the mode, is introduced here. Moreover, the combination does not have any influence on the relative phase of the two output beams and has to be locked independently.

[15] Note that this requires one signal generator to be dedicated only to the locking of the MZ, as the resonance depends on the mount and the mirror.

[16] In the case of the combination of a bright TEM_{00} with a squeezed flipped mode, we temporarily removed the flipped mode waveplate to perform alignments, as detailed in section 5 A. As for the combination of a bright TEM_{00} mode with a dim squeezed TEM_{10} mode, we locked the ring cavity which was generating the TEM_{00} mode temporarily on the TEM_{10}, as explained in section 5 B.

[17] The split-detector is not even indispensable as one could use a normal detector and block one half of the beam. The error signal would only be halved.

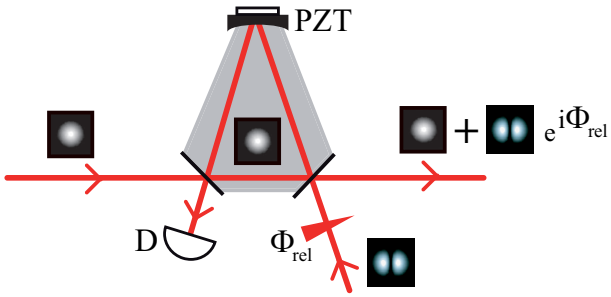

Figure 4.9: Optical ring-cavity for orthogonal modes combination. It is illustrated her for the combination of TEM_{00} and TEM_{10} modes. The cavity is locked to the resonance of the TEM_{00} mode, and the first TEM_{00} beam is transmitted through. The second one is totally reflected if the cavity is designed to prevent degeneracy between its resonances on the TEM_{00} and TEM_{10} modes. A lossless combination of both orthogonal modes is achieved. The relative phase $\Phi_r el$ is not fixed by this combination. D: locking detector. PZT: piezoelectric device used for locking the cavity length.

Such a lossless combining device has already been demonstrated in reference [Treps03, Treps04,1]. It is important to note that losses are experienced mainly on the transmitted beam, and are of the order of 10%. The combination of a coherent beam with a squeezed beam will thus be performed preferentially with a transmitted coherent beam and a reflected squeezed beam.

In our experiments, we have preferred to use the Mach Zehnder technique mainly because of the cost of making cavities[18], but we could also have used ring-cavities for our beams combinations. An important advantage given by the cavity compared to the Mach-Zehnder interferometer is its stability for alignments. Indeed, the cavity axis itself provides a reference, and allows to decouple the experiment parts before and after the combination. Changing a beam alignment before the Mach-Zehnder basically required to rebuild the entire interferometer...

As a conclusion, we have presented all the main basic elements for the realization of quantum imaging experiments with Hermite Gauss modes. The generation of squeezing in these modes is the only missing part to the scheme presented in Fig. 4.1. In order to understand how to produce these quantum correlations in the transverse, let us first present the second harmonic generation of Hermite Gauss modes, that will allow us to develop the fundamental properties of the parametric interaction in the transverse plane.

[18] In order to reduce the cost, non tunable cavities could be designed for specific combination of modes, like for instance coated prisms whose shape would have been optimized for this purpose.

B Second Harmonic Generation with higher order Hermite Gauss modes

Second harmonic generation (SHG), also called parametric up-conversion or frequency doubling, is based on the second order susceptibility $\chi^{(2)}$ of nonlinear crystals, where a wave at frequency ω is converted into a wave at frequency 2ω. Optical SHG was first proposed by Khokhlov in 1961 [Khokhlov61] and demonstrated in the same year by Franken *et al.* [Franken61]. In the case of continuous wave (CW) laser sources, SHG is now routinely achieved with very high conversion efficiencies. More than 80% power conversion is possible using enhancement cavities, [Paschotta94]. Frequency doubling is now widely used to generate wavelengths from the far UV to the far IR [Yu03, Patel66]. The most common application is the generation of coherent green light at 532 nm by up-converting a Nd:YAG laser at 1064 nm[19]

As for quantum applications of SHG, it has been used for the production of squeezed light [Kurz92, Ralph95, Serkland97] and is now proposed to generate harmonic entanglement [Grosse06].

The fundamental requirements for insuring efficient power conversion are high pump intensity, tight pump focusing, high second order nonlinearity and low losses in the crystal at both wavelengths involved in the frequency doubling. Moreover, the fundamental pump and second harmonic generated fields must preserve their phase relation over the length of the nonlinear crystal as we already discussed in the introduction of this chapter. The last requirement is also known as the nonlinear phase-matching condition and is achieved experimentally by taking advantage of the birefringence of the nonlinear crystal, or by manufacturing a periodic poling of the non linear material [Grynberg97].

A full analysis of the SHG efficiency, assuming a Gaussian spatial profile, i.e. a TEM_{00} pump mode, has been described in the work by Boyd and Kleinman in 1968 [Boyd68]. But no general extension of this analysis to higher order transverse mode has - to our knowledge - been proposed. In the last few years, there has been a growing attention in spatial nonlinear and quantum optical effects, as the introduction of spatial features in the transverse plane of laser beams may lead to parallel information processing and multichannel operations [Caves94]. At the same time, SHG experiments are no longer limited to single mode operation. The operation of optical cavities resonant on the TEM_{00} mode is indeed now being extended to the SHG of complex optical images [Lopez07,1]. The basic principles of SHG of optical images, i.e. a field comprising several transverse modes, can for instance help understanding the transfer of spatial correlations during the nonlinear process. There is indeed a limit to the focusing of an optical image into the crystal above which the local quantum information is lost in the frequency doubled image [Lopez05]. Moreover, as SHG is the reciprocal process of optical parametric amplification (OPA), also called parametric down-conversion, understanding the higher order mode conversion in SHG enables the optimization of the second harmonic pump profile in order to pump the OPA cavity efficiently [Lassen06, Lopez07,2].

In this section, we propose a study of second harmonic generation with higher order Hermite Gauss modes, both experimental and theoretical. This work has been submitted for publication [Delaubert07]. We present here only results for the TEM_{00}, TEM_{10}, and

[19] Commercial lasers of up to 18W are now available at this wavelength [Coherent].

TEM_{20} modes. Nevertheless, the experimental method as well as the theoretical calculations can easily be extended to any transverse mode. We will first present our single pass SHG experimental setup with TEM_{n0} pump modes. Secondly, we will concentrate on the thin crystal approximation, which is valid experimentally as long as the beam is not too strongly focused in the crystal. This simple case will allow us to introduce the basic concepts of SHG with non trivial pump profile. We will then consider the up-conversion process beyond the thin crystal approximation, hence taking into account the propagation of the field inside the crystal. We will notably show the high sensitivity of the profile of the second harmonic (SH) generated field relative to the crystal temperature, the frequency of the laser, and the focusing of the pump beam into the crystal. Finally, we will propose potential applications making use of this phenomenon.

B.1 Single pass SHG experiment

We consider a single pass parametric up-conversion experiment using TEM_{n0} pump modes, as represented in Fig. 4.10. The TEM_{00} pump beam at a wavelength of 1064 nm is produced

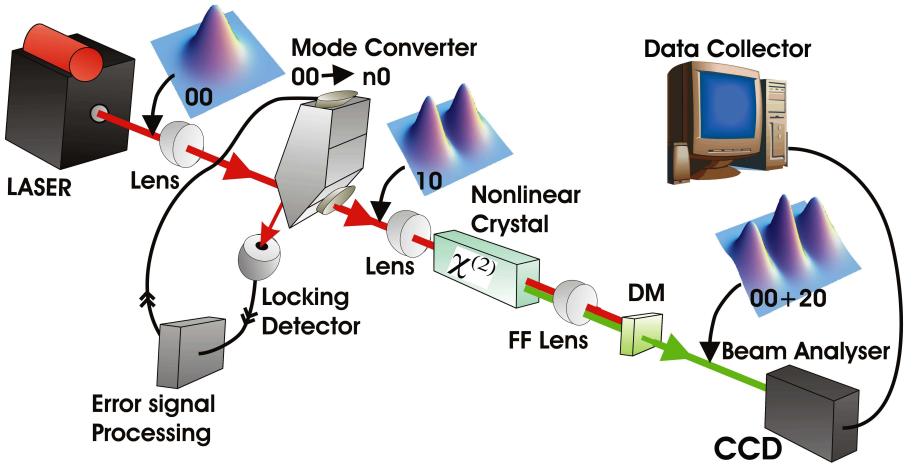

Figure 4.10: Scheme for single pass SHG measurement, illustrated in the case of a TEM_{10} pump mode.

by a diode-pumped monolithic Nd:YAG ring laser. We then generate a TEM_{n0} pump mode, successively here the TEM_{00}, TEM_{10} and TEM_{20} mode, by misaligning a ring cavity designed to prevent any transverse mode degeneracy and locked to the resonance of the TEM_{n0} mode, as detailed in section 4 A.2.2. This mode converting device thus delivers a pure transverse TEM_{n0} output mode, which is then focused into a bulk 5x5x20 mm^3 lithium niobate ($LiNbO_3$ 7% MgO doped) type I nonlinear crystal[20]. In type I phase-matching, the fundamental pump and SH fields are orthogonally polarized with respect to each other. The generated green SH beam at 532 nm is easily filtered out from the remaining transmitted fundamental beam with a dichroic element, and read-out with a CCD camera in the far field of the center of the crystal. The influence of four experimental parameters can be investigated with this setup : pump mode, laser frequency, crystal

[20]The experiment has been first operated in Canberra, and then reproduced in Copenhagen by Mikael Lassen in the same conditions.

temperature and pump focusing into the crystal. The beam focusing of the pump into the crystal, defined by the ratio $l/2z_R$, can be tuned by changing the focusing lens before the crystal. z_R is the Rayleigh range of the pump beam and l is the crystal length.

B.2 Thin crystal approximation

We now focus on to the de-focused case (!), namely the thin crystal approximation, which is valid experimentally as long as the beam is not too strongly focused in the crystal, i.e. as long as $z_R \gg l$. Ideally, it corresponds to a beam of very large waist, which is therefore roughly collimated.

In this section, we calculate the transverse profile of the SH modes when the nonlinear crystal is pumped with a collimated TEM_{n0} beam, where $n = 0, 1, 2$. We then give an estimation of the SHG efficiency in each pump case and compare them to experimental results.

B.2.1 Transverse profile of the generated SHG modes

For a type I non linear interaction, both fundamental fields (signal and idler) are necessarily degenerate in frequency and have the same polarization. Moreover, the polarization of the second harmonic field is orthogonal to this common orientation. The SHG process combines two fundamental photons to generate one SH photon with twice the energy. The transverse profile of the SH mode therefore corresponds locally, i.e. in one specific crystal plane, to the decomposition of the square of the fundamental pump mode profile into the SH basis[21].

Two sets of Hermite-Gauss modes will be required to describe the second harmonic generation. A first basis $\{u_n\}$ will be used to describe the fundamental modes at a wavelength λ, and the second one $\{v_n\}$ will be used to describe the second harmonic modes, at a wavelength of $\lambda/2$. We denote w_0 the waist of the TEM_{00} mode of the first basis. The waist of the TEM_{00} mode of the SH basis is chosen to be $w_0/\sqrt{2}$. This particular choice can be simply understood with Eq.1.53. In order to maximize the parametric interaction between two beams at different wavelengths, the best possible spatial overlap is needed. Both beams must in particular have the same Rayleigh range during their propagation inside the crystal. Without taking into account the dispersion of the crystal material, the two Rayleigh ranges match with this particular choice of waists as $z_R = \frac{\pi w_0^2}{\lambda} = \frac{\pi (w_0/\sqrt{2})^2}{\lambda/2}$. As a direct consequence, beam sizes and phase automatically match all along the beam propagation for two TEM_{00} defined in these two basis, thus maximizing the spatial interaction between both beams.

The SH field is composed of $n+1$ mode components[22] which are all even since the TEM_{n0} pump squared profile is necessarily even. Moreover, $2n$ is their highest order as the squared TEM_{n0} profile does not project onto higher order modes[23].

[21] It is important to note that this statement is valid only for type I interaction, and that other relations can exist between fundamental and SH field in type II interaction. For instance, intra-cavity type II SHG allows an input image to be perfectly transferred from the fundamental to the SH frequency, i.e. without quadratic effect [Scotto03].

[22] Note that even if the field has several components, it does not necessarily imply that the it is a quantum multi-mode field according to the definition we have given in section 1 B.

[23] This property can easily be shown by recalling that the expression of the TEM_{n0} involves a Hermite polynomial of order n.

In the thin crystal approximation, the normalized profile of the generated SH field, in the case of a TEM_{n0} pump and restricting ourselves to a one-dimensional description of the phenomenon, can be written as

$$\mathcal{E}_n(x) = \sum_{i=0}^{n} \Gamma_{n2i} v_{2i}(x), \tag{4.14}$$

where v_{2i} denotes the even SH mode of order $2i$ and Γ_{n2i} describes the spatial overlap between the squared pump and the SH modes in the transverse plane[24]. Its expression is given by

$$\Gamma_{n2i} = \int_{-\infty}^{\infty} \frac{u_n^2(x)}{\alpha_n} v_{2i}(x) dx, \tag{4.15}$$

where u_n denotes the fundamental modes and α_n corresponds to the normalization of the squared pump, i.e. $\alpha_n^2 = \int_{-\infty}^{\infty} u_n^4(x) dx$.

The common case of using a pump with a TEM_{00} mode profile yields $\Gamma_{00} = 1$. It corresponds to a perfect spatial overlap as the profile of the generated SH mode is also a TEM_{00} mode [Paschotta94]. For non TEM_{00} pump modes, the overlap coefficients can be calculated from Eq. 4.15. In the case of a TEM_{10} pump mode, they are given by $\Gamma_{10} = 0.58$ and $\Gamma_{12} = 0.82$. For a TEM_{20} pump mode, we get $\Gamma_{20} = 0.47$, $\Gamma_{22} = 0.44$ and $\Gamma_{24} = 0.77$. The presence of several non zero coefficients implies that for all cases, except a TEM_{00} pump mode, the generated profiles do not correspond to the pump intensity distribution. This is shown in Fig.4.11 in the particular cases of TEM_{10} and TEM_{20} pump modes, where we have included theoretical expectation and 1D and 2D experimental transverse profiles obtained with collimated pump beams, i.e. in the thin crystal approximation. We see a good agreement although the local pump power was quite low in these operating conditions. Indeed, the pump beam waist was large (1200 μm) and the available pump power in the TEM_{10} and TEM_{20} modes was limited to 80 mW and 55 mW, respectively. It is important to note that the profiles represented in Fig.4.11 can either be fitted with a the squared profile of the infrared pump modes, or by the green mode profile defined by Eq. 4.14, but cannot be fitted using a single SH mode profile.

The temperatures reported as insets in Fig. 4.11 correspond to phase matching crystal temperatures, i.e. to the best SH conversion efficiency. Note that they do not match. We will find the explanation for this phase matching temperature shift later on in section 4 B.3. Moreover, if tuning the crystal temperature had notable effect on the efficiency itself, no noticeable SH profile was witnessed.

B.2.2 Conversion efficiency

Still in the thin crystal approximation, we can compare the SHG efficiency η_n for different TEM_{n0} pump profiles by comparing the integrated power of the SH field over the transverse plane, for a given pump power. As the amplitude of the SH field is proportional to the square of the fundamental field, it simply yields

$$\eta_n = \frac{\int_{-\infty}^{\infty} u_n^4(x) dx}{\int_{-\infty}^{\infty} u_0^4(x) dx} \tag{4.16}$$

[24] A similar overlap integral has been introduced by Schwob *et. al* in order to describe the multi-mode properties of the field in the transverse plane of an optical parametric amplifier [Schwob98].

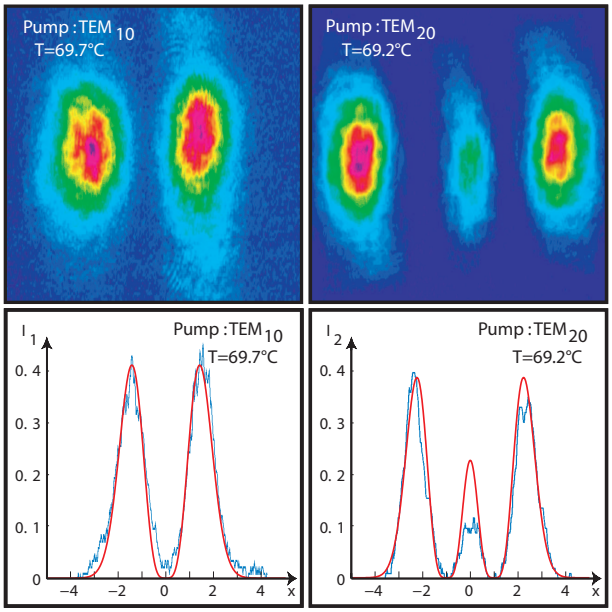

Figure 4.11: SH profiles generated in the crystal far field with TEM_{10} and TEM_{20} collimated pump modes, i.e. in the thin crystal approximation. The cross-section traces contain both the data and theory fits. Pump modes and optimal phase matching temperatures are reported on each inset.

where $u_n(x)$ refers to the profile of the TEM_{n0} pump mode, and where we have normalized the efficiency relative to the TEM_{00} pump mode case. For given TEM_{10} and TEM_{20} pump powers, we get $\eta_1 = 3/4$ and $\eta_2 = 41/64$. A comparison between theoretical and experimental results is presented in Table 4.1. The measured green powers have also been normalized to the TEM_{00} pump mode case, and have been obtained with collimated pump beams of identical properties, 55 mW and 1.2 mm of diameter.

Collimated Pump	TEM_{10}	TEM_{20}
Exp.	0.73 ± 0.04	0.56 ± 0.06
Th.	0.75	0.64

Table 4.1: SHG conversion efficiency for TEM_{10} and TEM_{20} mode pumps, normalized to the TEM_{00} pump mode case. Theory in the thin crystal approximation and experimental results obtained for collimated pumps are presented. The relatively high uncertainties are mainly due to the low power of the detected SH modes.

Theoretical model and experiment show very good agreement, taking into account the uncertainties in our experiments, which are mainly due to the relatively low power of the generated SH beams (less than 1 μW). In the regime considered here, the absolute SH conversion efficiency is very small because the local intensity is law in a large collimated beams. Efficient SHG is rather achieved with a pump tightly focused into the crystal, as we will see in the next section.

Moreover, the results presented in Table 4.1 show that the SHG efficiency is a decreas-

ing function of the pump mode order. This property is due to the lower local intensity in higher order modes. Indeed, as discussed in section 1 A.2.6, the transverse mode extension increases with the order of the mode, which implies a lower local intensity as the modes are normalized.

The study of the thin crystal approximation, although not relevant for experimental applications because of the very low efficiency, has allowed us to introduce the basic concepts of type I second harmonic generation. We now propose to consider a more general case.

B.3 Beyond the thin crystal approximation

We now consider the case of a focused pump into the nonlinear crystal. Because of the different evolution of each H-G component of the generated SH field, a local field description and a propagation of the SH modes along the crystal is necessary. We therefore propose to develop a similar approach to the one adopted by Boyd and Kleinman in 1968 [Boyd68] which was limited to the TEM_{00} mode. We will extend their analysis to the second harmonic generation of higher order modes[25].

The major difference with Boyd and Kleinman derivation is the great importance of the Gouy phase shift accumulated by the different H-G modes during the mode propagation [Siegman86]. Consequently, all of the SH components are not simultaneously phase matched with the pump along the length of the nonlinear crystal[26]. Since the birefringence of the crystal material is highly temperature dependant, phase matching for each mode occurs at different crystal temperatures. We therefore expect different temperature dependence for the generation of each SH modes, and thus also to see a modification of the global SH profile when the crystal temperature is varied. It is interesting to note that this effect, although due to mode interference in the crystal, does not need any cavity or interferometer to be observed. This will be of great importance for potential application of this effect as detailed in section 4 B.4.

B.3.1 Generalization of Boyd and Kleinman's approach to higher order modes

In this analysis, we restrict ourselves to the SHG of the three first Hermite Gauss modes, namely the TEM_{00}, TEM_{10} and TEM_{20} modes. Moreover, we make one approximation and two hypotheses. First, we consider negligible loss in the crystal for both the fundamental and second harmonic fields. This approximation allows a simplification of the calculations, and does not intrinsically modify the results, as we expect to have similar losses for all transverse modes[27]. Secondly, we consider that the beam propagation axis z corresponds to the optical axis of the Type I nonlinear crystal and therefore omit any walk-off effect of

[25] Note that another analysis on the SHG of higher order modes has been conducted by Lue and Sun in 1987 [Lue87] using another approach, but does not provide a description of the profile of the output SH field.

[26] In the thin crystal approximation, this phase shift was negligible because this phase shift is all the more important as the beam is focused, and has no effect on collimated beams, as detailed in section 1 A.2.6.

[27] Although it has indeed not noticeable effects on the classical behavior of the second harmonic generation, we will see in section 4 C that losses have to be taken into account to efficiently model quantum effects in such systems. In our experiments, losses originate from GRIIRA (GReen Induced Infra-Red Absorption), and probably also from direct infrared absorption in the nonlinear crystal.

the beams. Finally, we consider that the beam waist of the input beam is centered in the crystal. This corresponds to the optimum case and is generally adopted in the experiments.

Starting from a TEM_{00}, TEM_{10} or TEM_{20} mode propagating along the z axis, we can show (see appendix B) that the respective SHG intensity $I_{2\omega_0,00}$, $I_{2\omega_0,10}$ and $I_{2\omega_0,20}$, at frequency $2\omega_0$, outside the crystal of length l, can be written along one direction of the transverse plane denoted x as

$$I_{2\omega_0,00}(s,\xi,\Delta k) = \kappa_I e^{-4s^2}\left[H_{0,0}(\xi,\Delta k)\right]^2, \tag{4.17}$$

$$I_{2\omega_0,10}(s,\xi,\Delta k) = \kappa_I \frac{e^{-4s^2}}{4}\left[H_{1,0}(\xi,\Delta k)+(8s^2-1)H_{1,2}(\xi,\Delta k)\right]^2, \tag{4.18}$$

$$I_{2\omega_0,20}(s,\xi,\Delta k) = \kappa_I \frac{e^{-4s^2}}{4}\left[\frac{3}{4}H_{2,0}(\xi,\Delta k)-\frac{1}{2}(8s^2-1)H_{2,2}(\xi,\Delta k) + \frac{1}{4}(64s^4-48s^2+3)H_{2,4}(\xi,\Delta k)\right]^2, \tag{4.19}$$

where κ_I is a constant independent of the transverse position parameter $s = xz_R/w_0z$, of the focusing parameter $\xi = l/2z_R$ and of the phase mismatch Δk. $H_{n,2p}(\xi,\Delta k)$ integrates the nonlinear effects on the crystal length, and is defined by

$$H_{n,2p}(\xi,\Delta k) = \frac{1}{2\pi}\int_{-\xi}^{\xi}\frac{(1+i\tau)^{n-p}\,e^{-i\frac{l\Delta k\tau}{2\xi}}}{(1+i\tau)^{n-p+1}}d\tau, \tag{4.20}$$

where τ is defined by $\tau = (z-f)/z_R$, and where $z = f$ corresponds to the position of the beam waist. We recall that l is the crystal length. The indexes n and $2p$ respectively refer to the TEM_{n0} pump mode and to the even TEM_{2p0} SH mode thereby generated. Each term in Eq. 4.17, 4.18 and 4.19 accounts for the contribution of an even SH mode to the total SHG. The expression of the SHG intensity is hence very similar to the one given in Eq. 4.14, with additional correcting terms taking into account propagation effects in the crystal. The same modes as in section 4 B.2 appear naturally here. Because of the Gouy phase shift, their propagation strongly depends on the beam focusing towards ξ, and on the crystal temperature towards Δk. These effects between the fundamental TEM_{n0} and the SH TEM_{2p0} modes are described by the function $H_{n,2p}(\xi,\Delta k)$. Again, as detailed in section 4 B.2, only a few even modes contribute to the SH beam, and the SH beam profile always differs from the pump profile, except in the case of a TEM_{00} pump mode.

The SHG powers $P_{2\omega_0,00}$, $P_{2\omega_0,10}$ and $P_{2\omega_0,20}$ can simply be obtained by integrating the previous intensity distribution given in Eq. 4.17, 4.18 and 4.19 and are given by

$$P_{2\omega_0,00}(\xi,\Delta k) = \frac{\kappa_P}{\xi}|H_{0,0}(\xi,\Delta k)|^2 \tag{4.21}$$

$$P_{2\omega_0,10}(\xi,\Delta k) = \frac{\kappa_P}{\xi}\left[\frac{1}{4}|H_{1,0}(\xi,\Delta k)|^2+\frac{1}{2}|H_{1,2}(\xi,\Delta k)|^2\right] \tag{4.22}$$

$$P_{2\omega_0,20}(\xi,\Delta k) = \frac{\kappa_P}{\xi}\left[\frac{9}{64}|H_{2,0}(\xi,\Delta k)|^2+\frac{1}{8}|H_{2,2}(\xi,\Delta k)|^2+\frac{3}{8}|H_{2,4}(\xi,\Delta k)|^2\right] \tag{4.23}$$

where κ_P is a constant independent of the focusing and phase matching parameters, ξ and Δk. We propose now to analyze the influence of the focusing parameter and the crystal temperature T, which is directly related to the phase mismatch Δk.

B.3.2 Sensitivity to experimental parameters

- Influence of the beam focusing

In order to find the best SHG achievable experimentally, i.e. the optimum regime, we have plotted P_0, P_1 and P_2 as a function of the beam focusing in Fig.4.12, using Eq. 4.21, 4.22 and 4.23. These curves are all normalized to the maximum achievable SHG power in the case of a TEM_{00} pump. Moreover, this representation corresponds to optimal phase matching conditions, i.e. for the value of Δk that maximizes the SHG power.

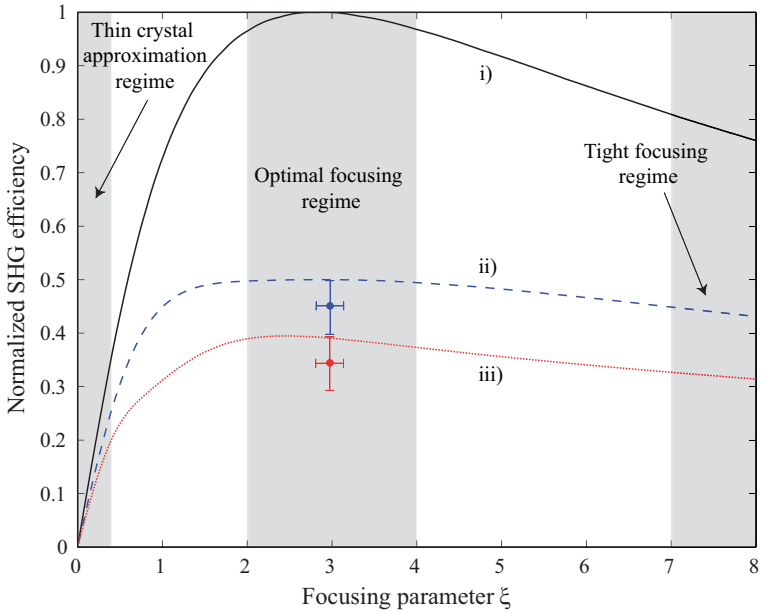

Figure 4.12: SHG efficiency as a function of the focusing parameter ξ, in optimal phase matching conditions, for i) TEM_{00}, ii) TEM_{10} and iii) TEM_{20} pump modes. All curves are normalized to the best conversion efficiency obtained for the TEM_{00} case. We have represented the three most relevant regimes to our analysis : 'thin crystal approximation regime' corresponding to collimated beams, 'optimal focusing regime', and 'tight focusing regime'. Two experimental points corresponding to the measurements presented in Table 4.2 are represented in the optimal focusing region.

The maxima are respectively obtained for $\xi_{opt0} = 2.84$, $\xi_{opt1} = 2.7$ and $\xi_{opt2} = 2.5$. Note that $\xi_{opt0} = 2.84$ exactly corresponds to the value cited in the work by Boyd and Kleinman [Boyd68][28]. The maximum SHG efficiency achievable with a TEM_{10} and a TEM_{20} pump modes, relative to the TEM_{00} case, for a given pump power are respectively 50% and 40%. These drops in conversion efficiency relative to the TEM_{00} case are easily explained by the smaller local intensity in higher order modes, as we already explained in section 4 B.2.

All efficiency curves, shown in Fig. 4.12, are rather flat around the optimal value, allowing an operating range between $\xi = 2$ and $\xi = 4$ in which close to maximum conversion efficiency can be obtained experimentally. This 'optimal focusing regime' is hence

[28] It has been shown very recently in reference [Lastzka06] that generating a position dependent refractive index in order to compensate for the Gouy phase shift inside the crystal could slightly improve the non linear efficiency, and that the optimal focusing parameter was in this case $\xi'_{opt0} = 3.32$. We can also wonder how the calculations presented here are modified in a periodically poled material.

Optimally Focused Pump	TEM_{10}	TEM_{20}
Expt.	0.45 ± 0.05	0.34 ± 0.05
Th.	0.5	0.4

Table 4.2: Comparison between theory (Th.), and experimental SHG efficiency results (Expt.) in the optimal focusing case ($z_R = l/6$ and $w_0 = 35\mu m$). These results are normalized related to the TEM_{00} case.

comprised between z_R values of $l/4$ and $l/8$.

The case $\xi \ll 1$ corresponds to $z_R \gg l$, i.e. to the 'thin crystal approximation regime'. This is obviously not the optimum regime as it corresponds to a large waist w_0 and therefore to a smaller local intensity. In the opposite regime corresponding to a very tight focusing, i.e. to $\xi \gg 1$, the efficiency drops because of de-focusing and because of the the importance of the phase shift between fundamental and SH beams at both ends of the crystal. When this phase shift exceeds $\pi/2$, the parametric interaction is indeed partly leading to a down-conversion of the SH power.

We have also performed experimental measurements of the SHG efficiency in the optimal focusing regime ($z_R = l/6$ and $w_0 = 35\mu m$) for TEM_{10} and TEM_{20} pump modes, and compared the results with our theoretical predictions in Table 4.2. We have also represented the two points in Fig. 4.12. The results show good agreement.

As we have seen earlier, the SH field profile can be composed of several components, and we have therefore studied the modal decomposition of the output SH field. The results calculated with Eq. 4.21, 4.22 and 4.23 are represented in Fig. 4.13, and respectively comprise a) 1, b) 2 and c) 3 SH components. This demonstrates the sensitivity of the SH profile with the beam focusing. We will study the profile of the mode itself in the next section. Note that at low pump focusing, we get the square of the values obtained earlier from Eq. 4.15, i.e $\Gamma^2_{10} = 0.34$ and $\Gamma^2_{12} = 0.67$ for a TEM_{10} pump mode, and $\Gamma^2_{20} = 0.22$, $\Gamma^2_{22} = 0.19$ and $\Gamma^2_{24} = 0.59$ for a TEM_{20} pump mode.

- Influence of the crystal temperature

So far, we have studied the influence of the beam focusing on the SHG efficiency, where we have assumed perfect phase matching. On the contrary, we will now detail the influence of the phase mismatch Δk, in optimal focusing conditions.

We have plotted in Fig. 4.14 the normalized SHG efficiency as a function of the crystal temperature, still for a a) TEM_{00}, b) TEM_{10} or c) TEM_{20} pump mode. The variation of the crystal temperature T is related to the variations of the phase mismatch Δk via the temperature dependence of the ordinary and extraordinary refractive index n_o and n_e [Smith76] by $\Delta k = 2k_{\omega_0} - k_{2\omega_0} = \frac{4\pi}{\lambda_0}\left[n_e(\omega_0, T) - n_o(2\omega_0, T)\right]$, where ω_0 and λ_0 respectively refer to the frequency and wavelength of the fundamental field.

Experimental results, presented as dots and error bars, show good agreement with theoretical curves, presented as solid lines. In the case of the TEM_{00} pump mode, the phase matching curve corresponds to the common 'sinc function'[29]. As for higher order

[29]This 'sinc function' distribution is only symmetrical for SHG operation in the thin crystal approximation. Here however, we are using focused beams. This accounts for the fact that this distribution is not

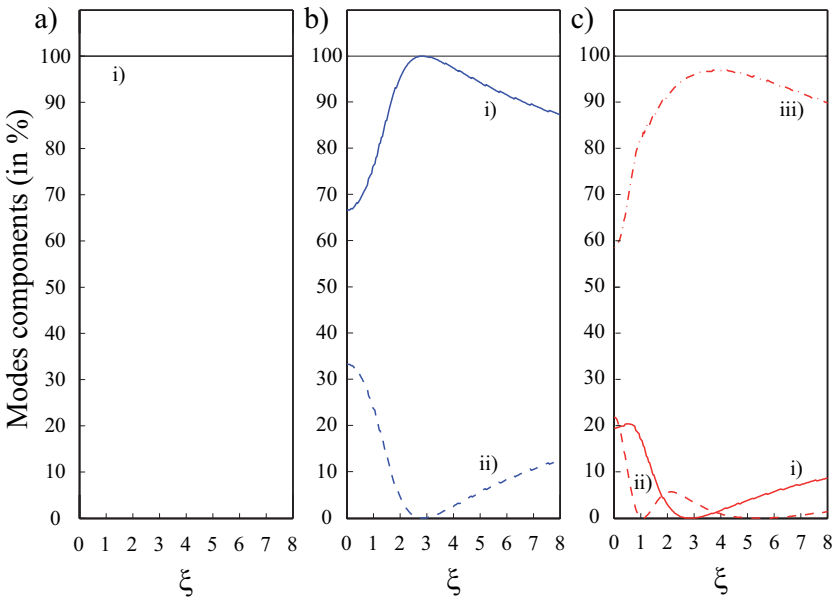

Figure 4.13: Modal decomposition of the SH field as a function of the focusing parameter ξ, in optimal phase matching conditions, for a) TEM_{00}, b) TEM_{10} and c) TEM_{20} pump modes. Mode components are represented in percentage of the overall power. In all insets, trace i) corresponds to a TEM_{00} SH component, whereas traces ii) and iii) respectively refer to TEM_{20} and TEM_{40} SH components.

pump modes, we have represented with dotted lines the different contributions of the TEM_{n0} SH components as a function of the crystal temperature, using Eq. 4.21, 4.22 and 4.23. Due to Gouy phase shift, the propagation along the crystal length leads to different phase matching conditions for each SH mode. This explains why the overall phase-matching curves correspond to a sum of shifted 'sinc functions', and are all the more asymmetric as the pump mode order is high. This property of asymmetry is also clearly visible on the experimental results. Note that the optimal overall phase-matching condition corresponds in each case to the generation of the SH mode of highest order in the decomposition of the SH beam. The general agreement is good between experimental and theoretical curves. Discrepancy mainly arises from the overall SH conversion efficiency due to the difficulty to reach the optimal focusing regime experimentally.

In order to have a better description of the modal composition according to the crystal temperature, we have plotted the percentage of the TEM_{00}, TEM_{20} and TEM_{40} SH components in the overall generated SH field in Fig. 4.15. Note the high dependence of the composition of the SH field with the crystal temperature. We will come back on this property in section 4 B.4.

We have seen that the profile of the SH mode should strongly depend on the pump focusing and on the crystal temperature, but we have not given a representation of this profile yet, nor have we confronted this to the experiment. This is what we propose to present now.

We now concentrate on the influence of the crystal temperature on the spatial SH beam

centered on $\Delta k = 0$ and slightly asymmetric.

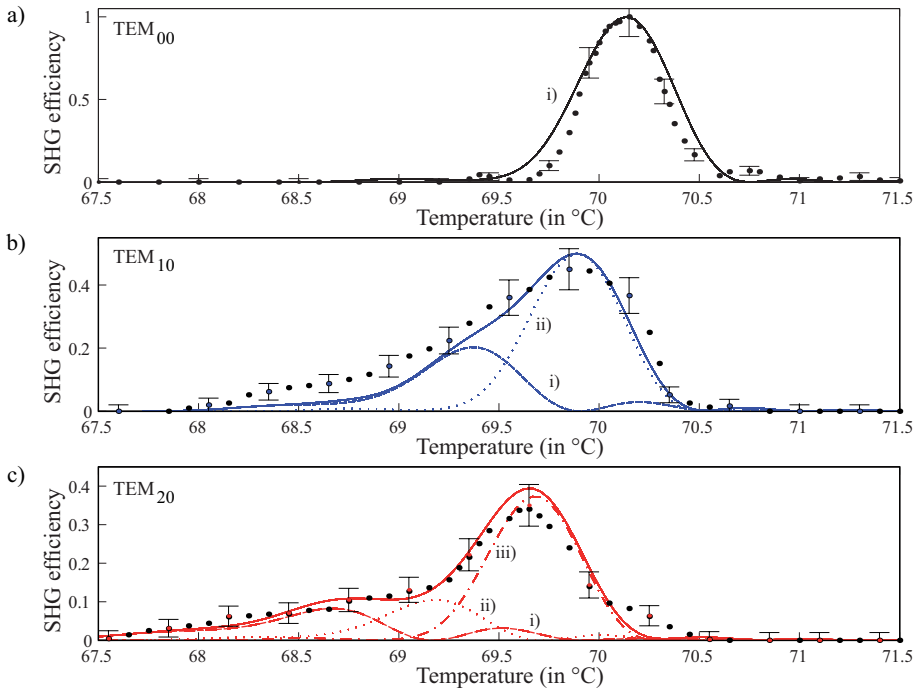

Figure 4.14: SHG efficiency as a function of the phase matching temperature, in optimum focusing conditions, for TEM_{00}, TEM_{10} and TEM_{20} pump modes. Experimental data are represented by black dots with error bars, whereas analytical model is represented by a solid line. The decomposition of the SH mode is also shown for each temperature with dotted lines. Traces i), ii) and iii) hence respectively correspond to the TEM_{00}, TEM_{20} and TEM_{40} SH components. All traces are normalized to the best efficiency in the TEM_{00} case.

profile in optimal focusing conditions[30]. Experimental results are again obtained with the setup presented in Fig. 4.10. The generated SH profiles at 532 nm, normalized to their maximum, are presented for different crystal temperatures in Fig. 4.16 (a) and (b) for a TEM_{10} and TEM_{20} pump mode, respectively. The power of the TEM_{10} and TEM_{20} pump beams are 80 mW and 55 mW, respectively.

We have compared these experimental results with the expected generated profiles in the same experimental conditions, using Eq.4.17, 4.18 and 4.19. They are in excellent agreement as shown in the cross-sections in Fig. 4.16. As accounted by Fig. 4.15, the profile of the mode is highly temperature dependent. In the case of a TEM_{10} pump, the SH field can thus be tuned from a predominantly TEM_{00} mode to a predominantly TEM_{20} profile. Note that changing the crystal temperature allows reproducible control over the coefficients of the linear combination between the TEM_{00} and TEM_{20} modes. Similarly, for the TEM_{20} pump mode, we find that the SH field is a temperature dependant linear combination of the TEM_{00}, TEM_{20} and TEM_{40} modes. For even higher order pump modes, there is an increasing mode profile sensitivity with the crystal temperature.

[30]We have not detailed the influence of the focusing parameter here. It is experimentally difficult to vary this parameter continuously, and would require to modify the focal length of the lenses between each focusing regime.

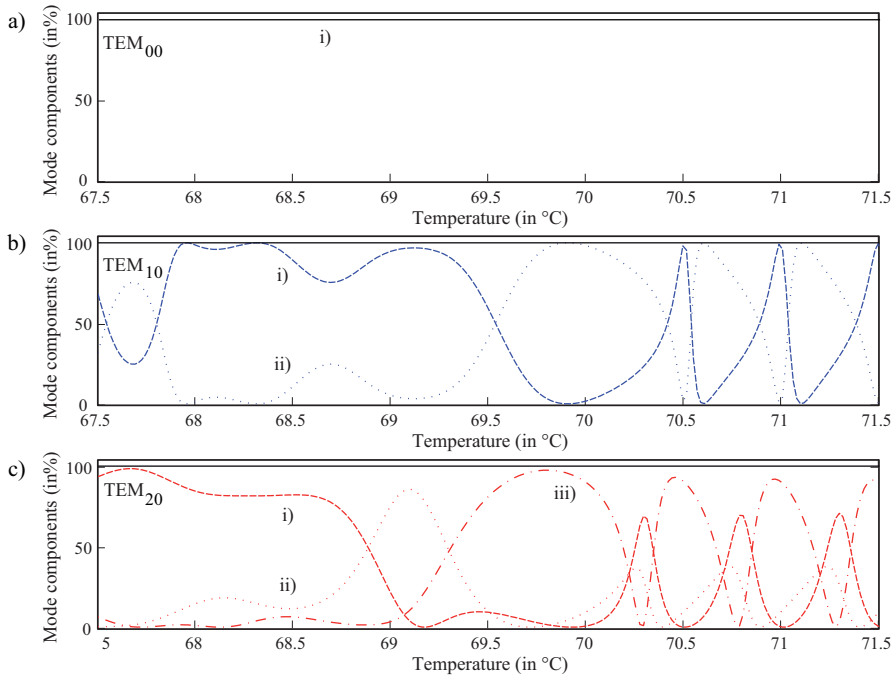

Figure 4.15: Mode components of the SH fields as a function of the phase matching temperature, in optimum focusing conditions, for a) TEM_{00}, b) TEM_{10} and c) TEM_{20} pump modes. Traces i), ii) and iii) respectively correspond to the TEM_{00}, TEM_{20} and TEM_{40} SH components.

The results we have presented here, taking into account the full propagation of the modes in the crystal, show a very good agreement, in conversion efficiencies as well as in mode profiles. This proves that transverse mode coupling can be understood in terms of mode overlaps, and that a full quantitative description can be obtained in the general case.

B.4 Potential applications

The single pass SHG described above show very interesting properties. It offers a highly stable device delivering a temperature tunable optical beam profile.

The consequence of this result is of most importance. It shows that mode coupling between different transverse modes is possible in a $\chi^{(2)}$ second order nonlinear interaction, and that the ratio between the generated SH components can be adjusted continuously via changes in the crystal temperature. We have used this effect in reverse to pump an OPA and selectively generate squeezed light in a desired higher order spatial mode, as explained in section 4 C[31].

Moreover, this effect arises from interferences in the crystal, but does not need any cavity or moveable mirrors to be controlled. It is therefore intrinsically stable. This opens the way to other applications, such as a very accurate temperature sensors [Delaubert07].

[31] The best non-classical properties on optical beams have lately been reported with periodically poled material, such as PPKTP [Hetet06, Schnabel06, Furusawa07], and we will investigate whether our results presented here with bulk material can be generalized.

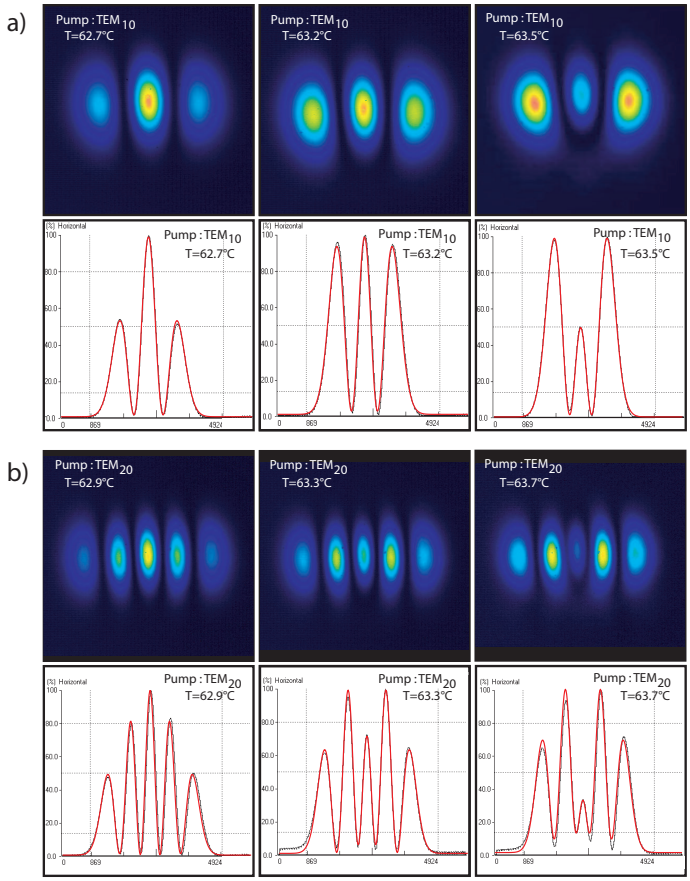

Figure 4.16: Two-dimensional SH profiles generated in the crystal far field for three phase matching temperatures. (a) TEM_{10} and (b) TEM_{20} pump mode. The cross-section traces contain both the data and theory plots calculated with Eq. 4.18 and 4.19 using experimental parameters.

Note that D. Pulford has developed a numerical model allowing studies with any transverse pump distribution. This model already shows perfect agreement with the analytical results present in this chapter.

Furthermore, the continuous variation of the spatial profile of the output field could be of great interest for trapping, un-trapping, or continuously displacing particles in an optical beam. A ring-shaped input beam would be implemented, like a LG_1^0 beam , as defined in Eq. 3.35. When the crystal temperature is continuously varied, several rings can surely be generated, moving in or out from the center of the beam. Further optimization of the input profile for best trapping performances could again be investigated using the numerical model. Similar optical manipulation is currently performed using interference between several optical beams whose frequency is continuously varied [MacDonald02].

C Generation of higher order Hermite Gauss modes squeezing

The production of squeezed light by parametric down-conversion was first achieved by Wu et al. in 1986 [Wu86]. More recently, squeezed noise power variances of -7 dB [Lam99, Suzuki06], and even -9.5 dB [Furusawa07], at sideband frequencies down to sub-kHz frequencies [McKenzie04] and up to the GHz regime [Senior07] have been demonstrated. Note that the squeezed optical mode was limited until recently to the TEM_{00} mode, and that we propose here to present the first generation of squeezed light in higher order Hermite Gauss modes. Most of the work presented here has been work published or accepted for publication [Lassen06, Lassen07].

C.1 Theoretical analysis of TEM_{n0} mode Optical Parametric Amplification

C.1.1 Introduction

Optical Parametric Amplification exactly corresponds to the reverse process of the Second Harmonic Generation presented in section 4 B. A *pump* photon of energy $\hbar\omega_p$ down-converts into two photons, *signal* and *idler*, of energy $\hbar\omega_s$ and $\hbar\omega_i$, respectively. Frequencies necessarily satisfy the energy conservation relation : $\omega_p = \omega_s + \omega_i$[32]. Moreover, in order to have a significant effect, the nonlinear interaction must satisfy the phase-matching conservation relation : $k_p = k_s + k_i$. In the continuous wave regime, in order to enhance the effect, the nonlinear crystal used for the down-conversion is usually inserted into an optical cavity[33]. When only a pump beam is used, the system is referred to as an *Optical Parametric Oscillator* (OPO), whereas when an additional *seed* beam at fundamental frequency, the signal, it is called *Optical Parametric Amplifier* (OPA). We will concentrate on latter case, restricted to a type I interaction, as in section 4 B, for which signal and idler are degenerate at frequency ω_0. As they cannot be distinguished, signal and idler will be described by the same quantum operator $\hat{A}_0$. The pump field at frequency $2\omega_0$ is orthogonally polarized and will be described by $\hat{B}_P$. According to the relative phase between both beams, the signal beam is either amplified or de-amplified. Locking this phase to de-amplification, the output fundamental beam is amplitude squeezed [Bachor03]. We propose to use this effect in order to produce amplitude squeezed higher order modes.

C.1.2 Multi-mode description of the parametric interaction

Let us now present a multi-mode description of the Optical Parametric Amplification of a TEM_{n0} seed beam, in order to understand the effect of the pump profile on the threshold value. We will limit this theoretical analysis to the thin crystal approximation, which can already provide very interesting results.

[32] This relation is at the origin of the numerous applications of optical parametric systems as frequency converters [Zhang:95].

[33] According to the number of fields resonant in the cavity, the system is said to be singly, doubly or triply resonant, knowing that it is at least resonant for one of the fundamental fields. Note that in order to access high field intensities inside the crystal, the input fields can be pulsed.

Using a one-dimensional transverse definition of the field, as introduced in section 1 A.2, for which we have kept the time dependance, we can write[34]

$$\hat{A}_0(x,t) = \sum_{n=0}^{\infty} \hat{a}_n(t) u_n(x), \tag{4.24}$$

$$\hat{B}_P(x,t) = \sum_{n=0}^{\infty} \hat{b}_n(t) v_n(x), \tag{4.25}$$

where $\hat{a}_n(t)$ corresponds to the annihilation operators of the fundamental signal and idler modes $\{u_n\}$. $\hat{b}_n(t)$ and $v_n(x)$ refer to the same parameters for the pump beam. We will consider that the mode profiles are real. We recall that the transverse modes basis are different as their modes are defined relative to different reference waists[35].

Taking into account a lossless parametric interaction inside the crystal, and using the notation conventions presented in Fig. 4.17, the equations of motion of the intra-cavity fields can be written [Walls95, BowenPhD03]

$$\frac{\partial \hat{A}_0}{\partial t} = -\gamma_0 \hat{A}_0 + \Lambda \hat{A}_0^{\dagger} \hat{B}_P - \sqrt{2\gamma_{0,ic}} \hat{A}_{0,ic,in} \tag{4.26}$$

$$\frac{\partial \hat{B}_P}{\partial t} = -\gamma_P \hat{B}_P - \frac{\Lambda}{2} \hat{A}_0^2 - \sqrt{2\gamma_{P,oc}} \hat{B}_{P,oc,in} \tag{4.27}$$

where $\gamma_0 = \gamma_{0,ic} + \gamma_{0,oc}$ is the total resonator decay rate for the fundamental beam. $\gamma_{0,ic}$ and

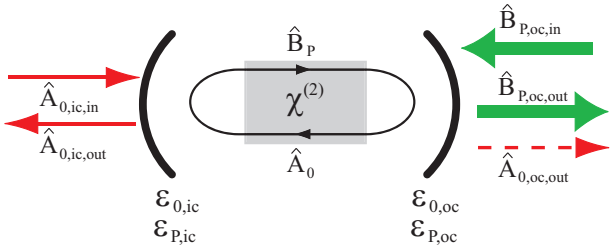

Figure 4.17: Schematic of an Optical Parametric Amplifier. A non linear $\chi^{(2)}$ crystal is inserted into a doubly (signal-idler) resonant cavity, which acts as a double pass system for the pump. ϵ refer to the cavity mirror transmission. Subscripts 0 and P respectively correspond to fundamental and second harmonic beams, and ic and oc refer to input and output coupler.

$\gamma_{0,oc}$ respectively correspond to decay rates at the same frequency, due to the transmission of the input and output coupler. They are related to the respective mirror transmissivity $\epsilon_{0,ic}$ and $\epsilon_{0,oc}$, and the resonator round trip time τ by $\gamma_{0,ic} = \epsilon_{0,ic}/2\tau$ and $\gamma_{0,oc} = \epsilon_{0,oc}/2\tau$. Same notations apply for the pump with $\gamma_P = \gamma_{P,ic} + \gamma_{P,oc}$. Λ describes the non linear coupling strength. It is related to the nonlinearity of the material, but also on of the beam focusing and phase mismatch. We have studied a similar dependance in section 4 B.

[34] We do not write here the pre-factor $i\sqrt{\hbar\omega_0/2\epsilon_0 cT}$ as these relations directly apply to the photon numbers operators.

[35] If the waist of the fundamental TEM_{00} mode is w_0, the waist of the second harmonic TEM_{00} mode is $w_0/\sqrt{2}$.

We consider here a doubly resonant optical cavity, resonant for signal and idler, i.e. $\epsilon_{0,ic}$ and $\epsilon_{0,oc}$ are close to 0[36] and no cavity detuning. Moreover, we have chosen a double pass system for the pump, i.e. $\epsilon_{P,ic} = 0$ and $\epsilon_{P,oc} \simeq 1$, which is seeded via the input coupler with $\hat{A}_{0,ic,in}$, and pumped via the output coupler via $\hat{B}_{P,oc,in}$, as represented in Fig. 4.17. The output fields are denoted $\hat{A}_{0,ic,out}$ and $\hat{A}_{0,oc,out}$ for the reflected and transmitted fundamental fields. The transmitted field is represented with a dotted line, and will correspond to the dim squeezed beam when the system is operated below threshold. The reflected pump is denoted $\hat{B}_{P,oc,out}$.

By decomposing the previous fields on the TEM_{pq} basis, as presented in Eq. 4.24 and 4.25, we get

$$\frac{\partial \hat{a}_n}{\partial t} = -\gamma_0 \hat{a}_n + \Lambda \sum_{i,j} \Gamma'_{nji} \hat{a}_j^\dagger \hat{b}_i - \sqrt{2\gamma_{0,ic}} \hat{a}_{n,ic,in} \tag{4.28}$$

$$\frac{\partial \hat{b}_n}{\partial t} = -\gamma_P \hat{b}_n - \frac{\Lambda}{2} \sum_{i,j} \Gamma'_{ijn} \hat{a}_i \hat{a}_j - \sqrt{2\gamma_{P,oc}} \hat{b}_{n,oc,in} \tag{4.29}$$

where Γ'_{ijn} is an overlap integral defined by[37]

$$\Gamma'_{ijn} = \int_{-\infty}^{\infty} v_n(x) u_i(x) u_j(x) dx. \tag{4.30}$$

The resonator has a much higher finesse for the fundamental field than for the second harmonic field, as $\gamma_0 \ll \gamma_P$. The evolution of the second harmonic thus occurs rapidly compared to the one of the fundamental field. In this case, we can assume that $\frac{\partial \hat{b}_n}{\partial t} = 0$. Substituting $\hat{b}_n$ in the previous equation yields,

$$\frac{\partial \hat{a}_n}{\partial t} = -\gamma_0 \hat{a}_n + \frac{\Lambda}{\gamma_P} \sum_{i,j} \Gamma'_{nji} \hat{a}_j^\dagger \left[\frac{\Lambda}{2} \sum_{k,l} \Gamma'_{kli} \hat{a}_k \hat{a}_l + \hat{b}_{i,in} \right] - \hat{a}_{n,in} \tag{4.31}$$

where we have introduced the notations $\hat{a}_{n,in} = \sqrt{2\gamma_{0,ic}} \hat{a}_{n,ic,in}$ and $\hat{b}_{n,in} = \sqrt{2\gamma_{P,oc}} \hat{b}_{n,oc,in}$.

Let us now consider that a single mode is resonant inside the cavity : the $\mathrm{TEM}_{n_0 0}$ mode. This is experimentally achievable if the cavity length and the mirror reflectivity has been chosen so that no other transverse mode can simultaneously resonate with the $\mathrm{TEM}_{n_0 0}$ mode, as explained in section 4 A.2.2 for example. $\hat{a}_{n_0}$ is therefore the only fundamental operator which has a non zero mean value.

- TEM_{10} fundamental mode resonant in the cavity

Restricting ourselves to the mean value of the operators, denoted $\langle \hat{a}_n \rangle = a_n$, in Eq. 4.31 we get, for $n_0 = 1$

$$\frac{\partial a_1}{\partial t} = -\gamma_0 a_1 + \frac{\Lambda}{\gamma_P} \sum_i \Gamma'_{11i} a_1^* \left[\frac{\Lambda}{2} \Gamma'_{11i} a_1^2 + b_{i,in} \right] - a_{1,in} \tag{4.32}$$

[36] The reflectivity is a crucial parameter for the design of the cavity, as it is related to the escape efficiency, as we will later in section 4 C.2.4.

[37] It is not surprising here to find a very similar expression to Eq. 4.15 for the spatial factor describing the parametric interaction. We will relate both later on.

Using the notations introduced in Eq. 4.15 in section 4 B.2, we get $\Gamma'_{nni} = \alpha_n \Gamma_{ni}$[38]. Eq. 4.32 becomes

$$\frac{\partial a_1}{\partial t} = -\gamma_0 a_1 + \frac{\Lambda'^2}{2\gamma_P} a_1^* a_1^2 + \frac{\Lambda'}{\gamma_P} a_1^* b'_{in} - a_{1,in} \tag{4.33}$$

where $b'_{in} = \Gamma_{10} b_{0,in} + \Gamma_{12} b_{2,in}$, and $\Lambda' = \alpha_1 \Lambda$. We can show[39] that this field operator corresponds to the component whose profile is proportional to $u_1^2(x)$. .

Eq. 4.33 is very similar to the equation of motion describing the parametric interaction in the single TEM_{00} mode case [BowenPhD03]. The first difference is the modification of the nonlinear coupling strength $\Lambda' = \alpha_1 \Lambda$, which has been multiplied by $\alpha_1 < 1$. This factor corresponds to the drop in local intensity, because of the spatial extension increases with the number of the mode. This has direct consequences on the ideal impedance matching of the cavity[40]. The second difference is the way the input pump field has been decomposed into its modal components to yield b'_{in}. This has a direct effect on the threshold value, which is determined from Eq. 4.33 by the following condition

$$b'^{\circ}_{in} \geq \frac{\gamma_0 \gamma_P}{\Lambda'} \tag{4.34}$$

This result shows that pumping the OPA with a beam whose normalized profile is given by $\Gamma_{10} v_0(x) + \Gamma_{12} v_2(x)$, $v_0(x)$ or $v_2(x)$, yields a threshold respectively given by $(\gamma_0 \gamma_P / \alpha_1 \Lambda)^2$, $(\gamma_0 \gamma_P / \alpha_1 \Gamma_{10} \Lambda)^2$, or $(\gamma_0 \gamma_P / \alpha_1 \Gamma_{12} \Lambda)^2$.

The normalized mode profile $\Gamma_{10} v_0(x) + \Gamma_{12} v_2(x)$, or $u_1^2(x)/\alpha_1$, is therefore the optimum pump profile for a TEM_{10} fundamental mode operation, as already explained in Eq. 4.14. Indeed, as explained in section 4 B, in order to pump efficiently the crystal for a TEM_{n0} signal mode, we have shown that the transverse profile of the pump mode had to locally match the square of the signal mode.

Note that even in the optimum case, since the threshold is directly related to the local intensity in the crystal, it is increased for higher order signal mode operations. Indeed, higher order mode intensity is more spread out in the transverse plane than for the TEM_{00} mode, as discussed in section 1 A.2.6. Therefore the best conversion efficiency is expected to happen for a TEM_{00} mode pump and a TEM_{00} signal beam resonant inside the cavity. We call P°_{thr} the threshold value corresponding to this operation. Coming back to the OPA operation with a fundamental TEM_{10} mode in the thin crystal approximation, pumping in the optimal SH mode, in the TEM_{00} or TEM_{20} SH mode respectively increases the threshold relative to P°_{thr} by a factor of $1/\alpha_1^2 \simeq 1.3$, $1/\Gamma_{10}^2 \alpha_1^2 \simeq 4$ and $1/\Gamma_{12}^2 \alpha_1^2 \simeq 2$.

---

[38] We recall that $\Gamma_{ni} = \int_{-\infty}^{\infty} \frac{u_n^2(x)}{\alpha_n} v_i(x) dx$, where $\alpha_n^2 = \int_{-\infty}^{\infty} u_n^4(x) dx$, and that for $n = 1$, only Γ_{10} and Γ_{12} are different from zero and fulfill $\Gamma_{10}^2 + \Gamma_{12}^2 = 1$.

[39] Any pump spatial profile $b(x)$ can be decomposed into $b(x) = b_0 v_0(x) + b_2 v_2(x)$. Its projection on the "mode" $u_1^2(x)$ yields $\int b(x) u_1^2(x) dx = \alpha_1 [\Gamma_{10} b_0 + \Gamma_{12} b_2]$. This proves that the component which is effectively taking part in the interaction is defined by $b'_{in} = \Gamma_{10} b_{0,in} + \Gamma_{12} b_{2,in}$. This result is in perfect agreement with Eq. 4.14.

[40] We prefer not to give all the details here and propose to refer to [BowenPhD03] and analyze the effect of a modification of Λ. In a word, the value of the coupling strength determines the optimal value of the output coupler transmissivity, in order to have the highest possible escape efficiency. It is difficult to quantify the modification of the squeezing level without going into details, but we can already expect an effect on the escape efficiency, if the output coupler is not changed from one TEM_{n0} mode operation to the other. The measured squeezing should decrease with the order of the mode, as changing the output coupler would require to realign the entire experiment each time.

- TEM$_{n0}$ fundamental mode resonant in the cavity

We now concentrate on the case $n_0 = n$, in the same conditions, for which we can show that the equation of motion describing the evolution of the TEM$_{n0}$ mode inside the cavity is given by

$$\frac{\partial a_n}{\partial t} = -\gamma_0 a_n + \frac{\alpha_n^2 \Lambda^2}{2\gamma_P} a_n^* a_n^2 + \frac{\alpha_n \Lambda}{\gamma_P} a_n^* b_{in}^{(n)} - a_{n,in} \tag{4.35}$$

where $b_{in}^{(n)} = \alpha_n \sum_k \Gamma_{nk} b_{k,in}$. We can again show that this field operator corresponds to the component whose profile is proportional to $u_n^2(x)$.

Eq. 4.35 shows exactly the same properties as Eq. 4.33, the modification of the nonlinear coupling strength Λ, which has been multiplied by $\alpha_n < 1$. The threshold value is also defined by the following condition

$$b^{(n)\circ}_{in} \geq \frac{\gamma_0 \gamma_P}{\Lambda} \tag{4.36}$$

The normalized optimum pump mode is given by $\sum_k \Gamma_{nk} v_k(x)$, or $u_n^2(x)/\alpha_n$. Pumping the OPA with a beam whose normalized profile is given by $v_k(x)$ yields a threshold given by $(\gamma_0 \gamma_P / \alpha_n \Gamma_{nk} \Lambda)^2$.

We now focusing on the OPA operation with a resonant fundamental TEM$_{20}$ mode. Pumping in the optimal mode, in the TEM$_{00}$, TEM$_{20}$ or TEM$_{40}$ SH mode respectively increases the threshold relative to P°_{thr} by a factor of $1/\alpha_2^2 \simeq 1.6$, $1/\Gamma_{20}^2 \alpha_2^2 \simeq 7$, $1/\Gamma_{22}^2 \alpha_2^2 \simeq 8.3$ or $1/\Gamma_{24}^2 \alpha_2^2 \simeq 2.7$.

The multi-mode description of an OPA operated with a TEM$_{n0}$ mode in the thin crystal approximation has allowed interesting predictions on the threshold values for a given pump profile. We have identified the optimal pump profile and shown the effect of the lower local intensity in higher order modes, quantitatively on the threshold value, and qualitatively on the squeezing level. These theoretical results will be important to understand the experimental ones presented in the next section.

We have limited here our study to the thin crystal approximation but the full calculation, corresponding more closely to the experimental case, will be investigated[41].

C.2 Experimental demonstration of higher order Hermite Gauss mode squeezing

Most of the work presented in this section has been published in reference [Lassen06].

C.2.1 Experimental setup

The experimental setup is schematized in Fig. 4.18. The laser source is a dual output laser delivering two coherent TEM$_{00}$ output beams, 195 mW of infrared power at 1064 nm, and 950 mW of green at 532 nm, using a cw solid-state monolithic YAG laser and an internal frequency doubler [Innolight]. The infrared and green beams are respectively used to seed and pump the OPA cavity.

[41] The formalism used for this derivation will be similar to the one presented in reference [Lopez05].

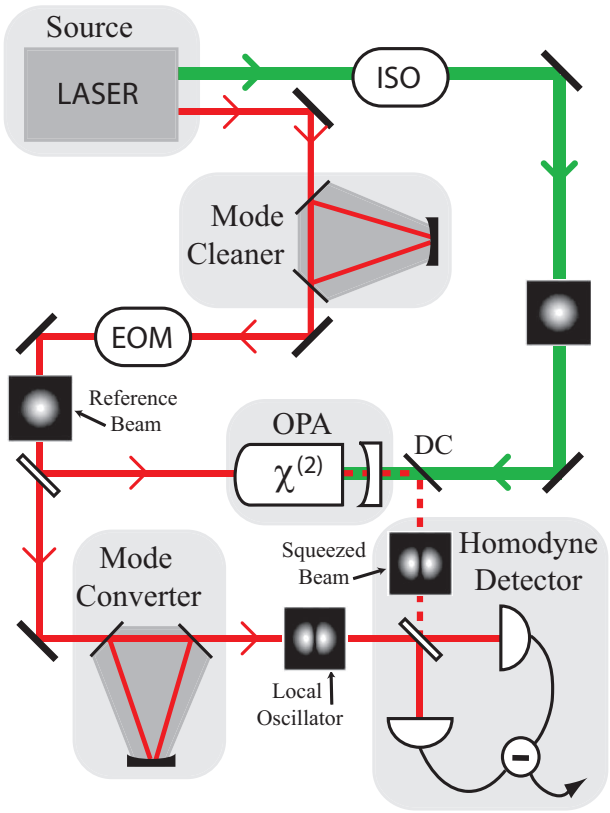

Figure 4.18: Experimental setup to generate higher order transverse mode squeezing, illustrated in the case of the TEM_{10} mode. An OPA is seeded with a misaligned TEM_{00} beam. The cavity is locked to the fundamental TEM_{n0} mode and pumped with a second harmonic TEM_{00} beam. The TEM_{n0} squeezed beam is analyzed using a homodyne detection, whose TEM_{n0} local oscillator is created from a misaligned ring cavity.

The infrared beam is first filtered through a mode-cleaning cavity[42] (non represented in Fig. 4.18), which filters out the intensity and frequency noise of the laser above the bandwidth of the ring-cavity, and also defines a high quality spatial mode. A bandwidth of 2.5 MHz is measured and a transmission greater than 90% is obtained for the TEM_{00} mode. The infrared TEM_{00} output beam is then misaligned into the OPA cavity in order to excite higher order H-G modes[43]. The cavity is then locked to resonance on the TEM_{n0} mode.

The green output beam, used as a TEM_{00} pump[44], passes through an optical isolator (ISO: isolation > 40 dB) and is carefully mode-matched (95%) into the OPA cavity. Below threshold, the seed is either amplified or de-amplified depending on the relative phase between the pump and the seed. The phase of the pump beam is stably locked to de-amplification in order to generate an amplitude quadrature squeezed beam.

[42] We have already detailed such a cavity in section 4 A.2.2.

[43] As explained in section 4 A.2.2, this is analogous to seeding the OPA directly with a TEM_{n0} mode, but has the advantage of using much less resources.

[44] We will comment later on the influence of the pump profile, using the results of section 4 C.1. This does obviously not correspond to optimal pump profile in the case of an OPA operation with any TEM_{n0} mode.

The OPA is a hemilithic cavity as represented in Fig. 4.18. This type of cavity has high intrinsic frequency stability. The crystal is a bulk 2x2.5x6.5 mm^3 lithium niobate ($MgO:LiNbO_3$) type I nonlinear crystal doped with 7% of magnesium. Its back surface is polished so that it has a 8 mm radius of curvature and is high reflectance coated for both wavelengths. The output coupler has 96% reflectivity for 1064 nm and 10% reflectivity for 532 nm, has a radius of curvature of 25 mm, and is placed 23 mm from the front-end of the crystal. The cavity is therefore near concentricity with a waist of 24 μm for the 1064 nm cavity and 19 μm for the non-resonant 532 nm pump[45]. The OPA has a finesse of 165 with a free spectral range of 10 GHz and a bandwidth of 70 MHz.

The dim TEM_{n0} squeezed beam generated at the output of the OPA is separated from the pump beam with a dichroic mirror (DC). The squeezed beam is then analyzed with a particular homodyne detection, for which the local oscillator (LO) is a TEM_{n0} mode. As explained in section 1 C.4, such a device selectively extracts from the squeezed beam the information contained in the TEM_{n0} component. The LO is created with a ring cavity, used as a mode transferring cavity locked to the TEM_{n0} mode, as explained in section 4 A.2.2.

In order to ensure the stability of the system, 6 locking loops are implemented in the experiment. We use the Pound Drever Hall locking technique, where a phase-modulation is imparted on the optical beams with an electro-optic modulator (EOM). The generated error-signals are then fed back to the cavities through piezo-electric elements (PZT) [Drever83]. All cavities in the experiment are held at resonance at the same time. The experiment stays locked for longer than 20 minutes. The main limiting factor is temperature fluctuations in the laboratory.

In order to have large parametric interaction we need the best possible mode overlap between pump and seed modes. To achieve this, different issues have to be addressed such as mode-matching and alignment of pump and seed into the cavity. A useful tool for optimizing the parametric interaction - and at the same time the possible amount of squeezing to be extracted - is to measure the classical gain factor of the seed.

C.2.2 Optimization of the pump profile

We focus here on the particular question of the pump profile, which has already been proven to play an important role in the theoretical section 4 C.1. We have shown that the optimal pump profile was complicated in the general case, and composed of several SH TEM_{n0} modes. Although generating such a complicated mode is in principle possible by using holograms [Vaziri02] or forcing a laser cavity to emit in these mode [Lassen05, Schwarz04], we choose, as a first step, to simply use the TEM_{00} green mode delivered by the laser.

In order to improve the setup for optimal pump operation in the TEM_{10} case only, we propose the scheme presented in Fig. 4.19. The scheme involves two ring cavities as the ones presented in section 4 A.2.2. The first one is used to generate a pure SH TEM_{20} component, by misaligning the input TEM_{00} beam, and locking the cavity to the resonance of the TEM_{20} mode. The reflected beam is then mixture of mainly TEM_{00} and TEM_{10}

[45] This design has been changed for a longer cavity in the latest experiment presented in section 5 B. As our experiments require the resonance of a single transverse mode inside the cavity, it is preferable to operate the OPA cavity as far as possible from any multi-mode cavity, like the concentric or the confocal configuration.

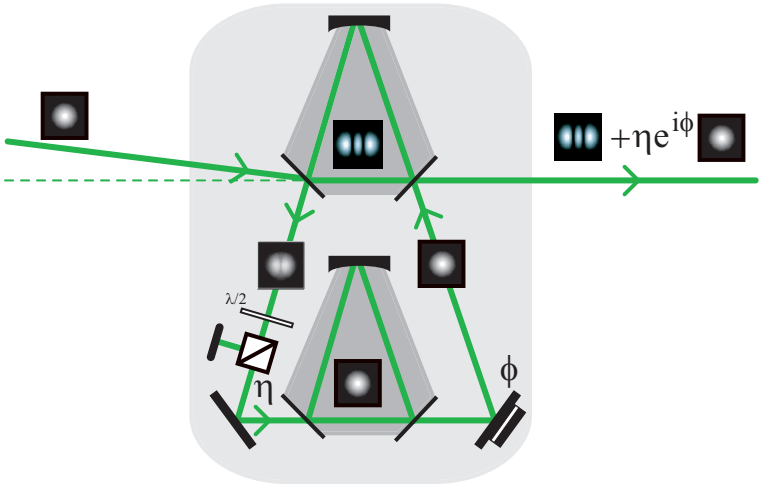

Figure 4.19: Proposition to generate an optimal pump mode for a TEM_{10} operation of the OPA cavity with two ring cavities. An incident green TEM_{00} mode is misaligned in order to couple into the TEM_{20} component of the first ring cavity. The cavity is locked to the TEM_{20} mode. The reflected field is then filtered with a second ring cavity in order to produce a pure TEM_{00} mode. The amplitude ratio η and the relative phase Φ can be varied using a variable attenuator and a piezoelectric device, respectively.

modes. We use a second cavity used as a spatial filter in order to produce a pure TEM_{00} mode, which is sent back on the first cavity and perfectly reflected. The amplitude ratio η between the two output components is controlled by an attenuator in the TEM_{00} arm, which simply consists of a polarizing beam-splitter and a half waveplate. The relative phase Φ between the two components is tuned with a PZT in the TEM_{00} arm. The output field is thus proportional to $v_2(x) + \eta e^{i\Phi} v_0(x)$. Even if the results given in the theoretical section were limited to the thin crystal approximation, they give a good idea of the value of the parameters. Moreover, we have seen in section 4 B that even beyond the thin crystal approximation, the same two modes allowed a full description of the parametric properties. It seems therefore reasonable to believe that the optimal pumping profile can be obtained with the setup presented in Fig. 4.19.

Nevertheless, we have performed the experiments only with a TEM_{00} at this stage, as the implementation of an optimal pump is resource demanding. The TEM_{00} pump mode was always aligned with the cavity axis and mode-matched to the TEM_{00} mode of the cavity[46]. We therefore expect the increase of the oscillation threshold as predicted in the theoretical section. In the cases relevant to our experiment, when the signal mode resonant in the OPA is a TEM_{10} mode, pumping with a SH TEM_{00} mode increases the threshold

[46] We have checked that this configuration was giving maximal gain. Since our OPA is not a cavity for the pump beam, the output coupler has only 10% reflectivity for 532 nm, we can envision three different cases for pumping the OPA efficiently, knowing that we are restricted to a TEM_{00} pump mode operation, as discussed in the previous section. Firstly, we can match the pump profile to the TEM_{00} mode defined through the infrared mode. Secondly, we can de-focus the pump. Finally, we can misalign the pump to match with one lobe (one side) of the infrared mode, in the TEM_{10} mode case for instance. In each case we have tuned the crystal temperature to maximize the gain, and we find in the end that the most efficient option is to pump with a TEM_{00} mode aligned with the cavity axis.

relative to the TEM_{00} case by a factor 4. As for a TEM_{20} signal mode, pumping with a SH TEM_{00} mode increases the threshold by a factor 7.

In order to confront this values with experimental results, we have maximized the classical amplification factor by tuning the relative phase between pump and seed, the pump power, and the crystal temperature[47]. The measured amplification gain curves for TEM_{00}, TEM_{10} and TEM_{20} H-G modes are presented in Fig. 4.20. The gain corresponds to the ratio between the OPA output power when the non-linearity is on and off, i.e. when the pump is used or not.

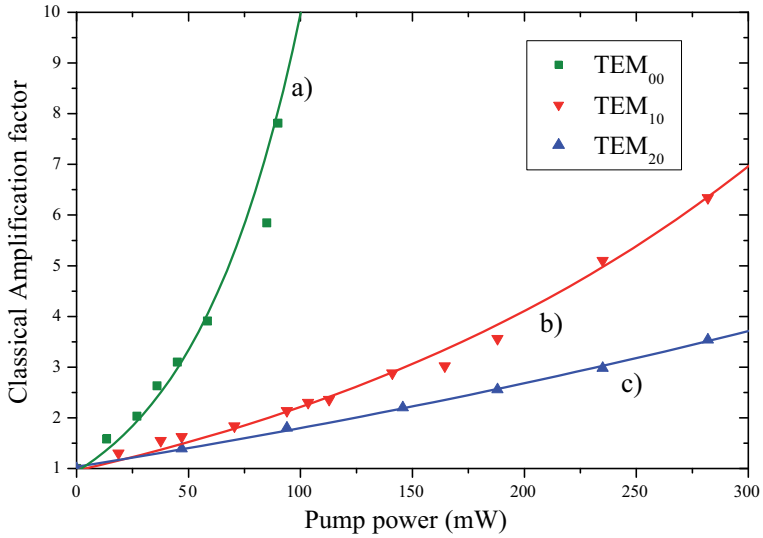

Figure 4.20: Experimental measurements of classical amplification curves for the OPA operation in the a) TEM_{00}, b) TEM_{10} or c) TEM_{20} mode. Solid lines correspond to exponential fits.

We measured a maximum amplification of 300, 23, 5 for the TEM_{00}, TEM_{10} and TEM_{20} H-G modes, respectively. The best measured de-amplification factors are 0.30, 0.56 and 0.70 for the TEM_{00}, TEM_{10} and TEM_{20} H-G modes, respectively. On the one hand, the de-amplification of 0.30 for the TEM_{00} indicates that the system is close to ideal operation, since the theoretical value for de-amplification from a back seeded OPA at threshold is 0.25 [Bachor03].

The oscillation threshold of the system is reached for 260 mW of pump power when the OPA is resonant for the TEM_{00} signal mode. However, the threshold for higher order modes cannot be accessed experimentally because the system oscillates on the TEM_{00} mode as soon as the pump power reaches 300 mW, even for crystal temperatures optimized for an operation on the TEM_{10} and TEM_{20} modes. Nevertheless, we can use the gain curves to infer the threshold values for the TEM_{10} and TEM_{20} modes. A linear fit of the curves at low pump power gives the relative gain slopes between each case, yielding an estimation of the relative threshold. We find thresholds for the TEM_{10} and TEM_{20} OPA operation of approximately 1000 mW and 1600 mW, respectively. These values can be compared with the theoretical calculation presented in section 4 C.1, taking into ac-

[47] We noticed at this stage that the optimum phase matching temperature was shifted between OPA operation in different TEM_{n0} modes. We will come back on this property in the next section.

	TEM_{00}	TEM_{10}	TEM_{20}
Experimental	1	3.9 ± 0.5	6.2 ± 0.8
Theoretical	1	4	7

Table 4.3: Threshold comparison between experimental results and theory in the thin crystal approximation. The threshold for the different modes is normalized with respect to the TEM_{00} threshold power.

count the imperfect spatial overlap between the infrared mode resonant in the cavity and the TEM_{00} pump mode, and the lower local intensity for higher order modes. This comparison is presented in Table 4.3, and shows a very good agreement between theory and experimental measurements.

C.2.3 Optimization of the phase matching condition

We now concentrate on the phase matching condition, which is obtained by tuning the crystal temperature.

The birefringence of the crystal is highly temperature dependent, as discussed in section 4 B where we studied this effect in the same material. Accurate heating of the crystal can therefore be used to achieve optimal phase-matching for the different modes at approximately 62°C, as shown in Fig. 4.21. This figure shows the classical gain factor measured as a function of the crystal temperature, in the case of infrared TEM_{00}, TEM_{10} or TEM_{20} mode OPA operation, still using the best available pumping option detailed in the previous section. The optimal temperature is specific to each TEM_{n0} signal mode operation of the

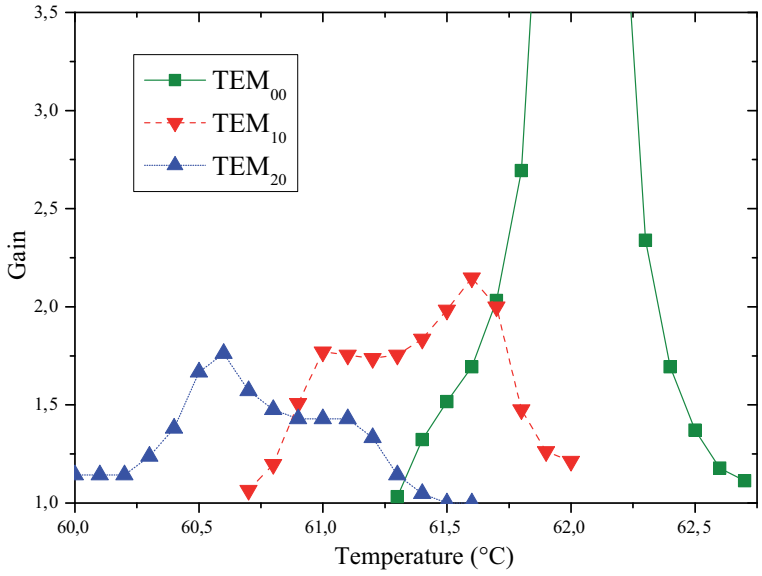

Figure 4.21: Classical gain factor as a function of the crystal temperature for OPA operation with a TEM_{00}, a TEM_{10} and a TEM_{20} signal modes. The optimal phase-matching temperature are 62.1°C, 61.6°C and 60.6°C for the TEM_{00}, TEM_{10} and TEM_{20} H-G modes, respectively.

OPA, mainly because of the different Gouy phase-shift between H-G modes, as explained

in section 4 B. Indeed, a temperature shift between optimal phase matching condition clearly appears in Fig. 4.21. The temperature has thus to be re-optimized for each experiment. We find that the optimal phase-matching temperatures are 62.1°C, 61.6°C and 60.6°C for the TEM_{00}, TEM_{10} and TEM_{20} modes, respectively. The width (FWHM) for optimal phase-matching temperature is approximately 1°C for all phase-matching curves.

In order to have a full understanding of the link with the results obtained for second harmonic generation in the single pass experiment, we have operated the OPA cavity as a SHG by blocking the green pump beam and by increasing the power of the infrared seed beam. Even if the OPA cavity is not designed for SHG, a green beam is generated as SHG systems do not have an operation threshold. The intensity of the SH beam as well as some profiles are given in Fig. 4.22 as a function of the crystal temperature, when the system is operated with an infrared TEM_{10} mode. The phase-matching curve

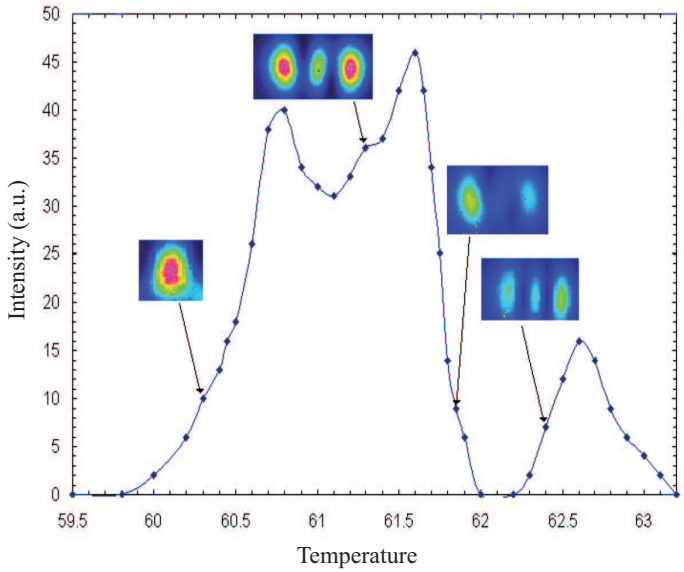

Figure 4.22: SHG operation of the OPA cavity. The intensity of the SH beam is plotted as a function of the crystal temperature, when the seed beam is a TEM_{10} infrared mode. Some profiles of the generated SH beams are also presented. Phase-matching curve for the nonlinear crystal and different SHG TEM modes as a function of temperature.

is more complicated than the one presented in Fig. 4.16b) as the crystal is inserted here into the OPA cavity[48]. We clearly notice on the profile presented in Fig. 4.22 that the output SH profile is temperature dependent. Indeed, a predominant TEM_{00} component can be obtained for T=60.3 °C, whereas a predominant TEM_{20} component can be obtained for T=61.3 °C. For an OPA operation with a given pump profile, the phase-matching temperature has thus to be optimized in order to match the temperature for which the system operated as an SHG would generate a SH beam whose profile would be identical to the pump profile. For example, in the case of the infrared TEM_{10} mode OPA operation with a green TEM_{00} pump mode, the temperature should be set to 60.3 °C, as shown

[48] Indeed, phase reflections on the cavity mirrors and standing wave effect have to be taken into account in order to model the curve presented in Fig. 4.22. These properties modulate the single pass phase-matching curve because of interference effects [Juwiler99]. The cavity parameters are usually chosen not to create destructive interferences at the optimal phase matching temperature.

by Fig. 4.22. However, as the intensity of the generated SH mode at this temperature is rather low, the effective non linearity in the OPA operation with a TEM_{00} will not be as high as the operation with a pump profile given by a TEM_{20} profile, as shown by Fig. 4.22. Note that it is difficult to compare the temperature axis between the different experiments as the presence of the intense pump power modifies the properties of the system for the results presented in Fig. 4.21[49]. Nevertheless, these results still explain clearly the way to proceed experimentally to adjust the crystal temperature, and link the properties of SHG and OPA with higher order H-G modes.

C.2.4 TEM_{00}, TEM_{10} and TEM_{20} squeezing

Amplitude squeezed states are generated at the output of the OPA when the phase of the pump beam is locked to de-amplification, as explained in section 4 C.2.1. The OPA cavity is operated with its best pump and phase matching parameters, as detailed in the previous sections. Experimental squeezing curves in the TEM_{00}, TEM_{10} and TEM_{20} modes are successively obtained using a homodyne detection whose local oscillator has the same profile as the squeezed mode. Scanning the phase of the local oscillator beam allows measurements of the amplitude (squeezed) and phase (anti-squeezed) quadratures of the input beam. The results presented in Fig. 4.23 are recorded with a spectrum analyzer with a resolution bandwidth of 300 kHz and video bandwidth of 300 Hz at a detection frequency of 4.5 MHz.

All traces are normalized to the quantum noise level (QNL), which corresponds to trace ii), and which is measured by blocking the squeezed beam before the homodyne detector. Trace i) is obtained by scanning the phase of the LO, and trace iii) by locking the LO phase to the squeezed amplitude quadrature. The smooth line is the theoretical fit of the noise variance assuming the experimental parameters. We measured -4.0 ± 0.2 dB of squeezing and $+8.5 \pm 0.5$ dB of anti-squeezing for the TEM_{00} mode, -2.6 ± 0.2 dB of squeezing and $+5.4 \pm 0.4$ dB of anti-squeezing for the TEM_{10} mode, and -1.5 ± 0.3 dB of squeezing and $+2.7 \pm 0.4$ dB of anti-squeezing for the TEM_{20} mode. To our knowledge, this is the first demonstration of higher order transverse mode squeezing using an OPA. These values have been corrected for electrical noise, which is 9.1 ± 0.1 dB below the QNL, and is mostly due to the amplifiers in the photo-detectors.

In order to perform these measurements, we used the following pump powers which were maximizing the amount of squeezing: 100 mW for the TEM_{00} mode and 300 mW for TEM_{10} and TEM_{20} modes. We were unable to pump the OPA with higher power, as the system was starting to oscillate on the TEM_{00} mode at 300 mW, even when the cavity was locked to another mode, as discussed in the previous section.

The values obtained above are the values detected with the homodyne detection. Nevertheless, they do not exactly correspond to the squeezing coming out of the OPA, i.e. to the squeezing that would be measured with perfect detection efficiency. In order to fully characterize our squeezing source, we propose to infer this squeezing value by correcting our experimental results for propagation η_{prop}, photo-detection η_{det}, and homodyne detection η_{hd} efficiency.

[49] We thought about taking the results of Fig. 4.22 in presence of the pump, but on the orthogonal polarization to the one we use to generate parametric interaction. However, the generated SH profiles were too dim to be easily separated from the intense reflected pump, even if they were orthogonally polarized.

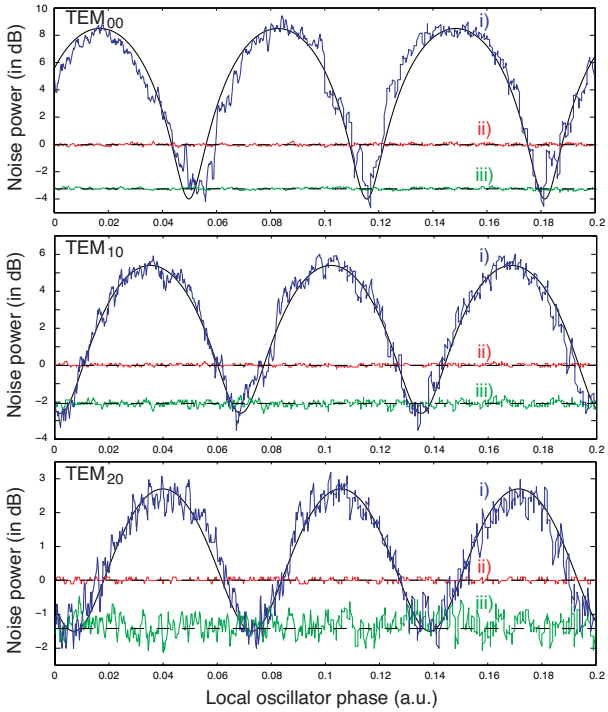

Figure 4.23: Experimental squeezing traces on the a) TEM_{00}, b) TEM_{10} and c) TEM_{20} modes, recorded by homodyne detection. i) Scan of the relative phase between the LO and the squeezed beam. ii) Quantum noise limit. iii) Phase of the LO locked to the squeezed amplitude quadrature.

The total detection efficiency of our detection system after the output of the OPA cavity is hence given by $\eta_{\rm tot} = \eta_{\rm prop}\eta_{\rm det}\eta_{\rm hd}$, where $\eta_{prop} = 0.97 \pm 0.02$ is the propagation efficiency, taking into account the losses at reflection on the optics, $\eta_{det} = 0.96 \pm 0.03$ is the photo-detector (Epitaxx ETX500) efficiency, and η_{hd} is the homodyne detection efficiency, measured to be $\eta_{hd}(TEM_{00}) = 0.98 \pm 0.01$, $\eta_{hd}(TEM_{10}) = 0.95 \pm 0.01$ and $\eta_{hd}(TEM_{20}) = 0.91 \pm 0.01$ for the different modes. The homodyne detection efficiency depends on the transverse mode of interest. This dependence is due to three main factors. First, higher order modes have larger spatial extension and are more apertured by the optics[50]. Moreover, the fringe visibility drops for higher order modes compared to the TEM_{00} case because of the additional transverse degree of freedom that has to be adjusted. Finally, a small mode mismatch has more dramatic effects on the fringe visibility for a complex intensity distribution. The total detection efficiency for our experiment are then $\eta_{\rm tot}(TEM_{00}) = 0.91 \pm 0.04$, $\eta_{\rm tot}(TEM_{10}) = 0.88 \pm 0.04$ and $\eta_{\rm tot}(TEM_{20}) = 0.85 \pm 0.04$ for the different modes. From these efficiencies, we can directly infer the squeezing and anti-squeezing values just at the output of the OPA using Eq. 1.68. The values are reported in Table 4.4.

An upper limit of the squeezing and anti-squeezing values, generated at the output of the OPA cavity, can also be calculated using the characteristics of the OPA operation, namely the escape efficiency $\eta_{\rm esc}$, the threshold $P_{\rm thr}$, and the pump power P. The noise

[50] Our TEM_{00} beam had a waist of approximately 2 mm. This large diameter, corresponding to a collimated beam, was chosen in order to facilitate mode matching with the local oscillator.

	TEM_{00}		TEM_{10}		TEM_{20}	
	SQZ	A-SQZ	SQZ	A-SQZ	SQZ	A-SQZ
a) Measured	-4.0	+8.5	-2.6	+5.4	-1.5	+2.7
b) Inferred just after OPA	-4.7	+8.9	-3.1	+5.8	-1.8	+3.0
c) Calculated just after OPA	-7.6	+11.0	-6.8	+9.1	-5.4	+6.5

Table 4.4: TEM_{n0} mode squeezing (SQZ) and anti-squeezing (A-SQZ) a) Measured with the homodyne detection, and corrected only for electronic noise. b) Inferred from the previous values by taking detection and propagation losses into account. c) Calculated using Eq. 4.37, i.e. taking the cavity escape efficiency and relative pump power into account.

variance on the amplitude and phase quadratures can hence be written as [Bachor03]

$$\langle \delta \hat{X}^{\pm^2} \rangle = 1 \pm \eta_{\text{esc}} \frac{4\sqrt{P/P_{\text{thr}}}}{\left(1 \mp \sqrt{P/P_{\text{thr}}}\right)^2}, \tag{4.37}$$

The expression of the escape efficiency is $\eta_{\text{esc}} = \epsilon/(\epsilon + \mathcal{L})$, where $\mathcal{L}$ is the intra-cavity loss and ϵ is the transmittance of the output-coupler. The estimated intra-cavity loss for our OPA is approximately $\mathcal{L} = 0.0043$, considering a material absorption of 0.1%/cm and scattering at the mirror and crystal. This gives a cavity escape efficiency of approximately $\eta_{\text{esc}} = 0.89$. The calculated squeezing and anti-squeezing for the different modes, using Eq 4.37 are shown in Table 4.4c). The high discrepancy with the previous inferred values suggests that there exists additional losses inside our system. A direct manifestation of this intra cavity loss is the impurity of the squeezed states produced with our system, as shown by Fig. 4.23.

A common extra possible loss factor is caused by the existence green induced infra-red absorption (GRIIRA) [Furukawa01] inside the crystal. However, according to Furukawa *et al.*, no effect of GRIIRA should be seen in our setup as we have chosen a 7% MgO doped $LiNbO_3$ crystal for this purpose.

Another possibility is the presence of direct infrared loss inside the crystal. However, this parameter is difficult to measure experimentally.

Moreover, we notice a discrepancy between the results obtained with operation on different modes. We can propose two explanations for this phenomenon. First, it seems reasonable to measure less and less non classical properties when the pump has less and less overlap with the ideal pump mode. Indeed, this overlap coefficient respectively equals 1, 0.58 and 0.47 for the TEM_{00}, TEM_{10} and TEM_{20} mode operation. Secondly, as we pointed out in section 4 C.1, the nonlinear coupling parameter Λ decreases with the order of the mode. As a consequence, the escape efficiency no longer corresponds to the ideal value for the squeezing extraction out of the cavity.

We have demonstrated the generation of squeezed light in the TEM_{00}, TEM_{10} and TEM_{20} modes. To our knowledge this is the first demonstration of higher order transverse mode squeezing. Losses in the material limit us presently to noise suppressions below the QNL of -4 dB, -2.6 dB and -1.5 dB. However, we believe that there is a potential for further improvement. First, optimal pumping could be tested experimentally, using for example the setup proposed in Fig. 4.19 in the case of the TEM_{10} mode. And secondly, a complete study of the influence of the effect of the modification of the nonlinear coupling parameter

could determine the ideal output coupler for a specific mode operation.

Moreover, the recent squeezing results obtained with periodically poled materials [Furusawa07] are very promising, and encourages us to investigate the compatibility of such nonlinear material with the generation of squeezing in higher order modes.

D Conclusion

In this chapter, we have presented in detail how to selectively manipulate transverse modes within an optical field. We have in particular focused our analysis on the Hermite Gauss modes basis. All the key elements required for the implementation of a full quantum imaging experiment have been demonstrated, namely the selective production, combination, and separation of transverse modes with very high efficiency, i.e. without altering the quantum state of the modes. The study of parametric interaction between these modes in SHG and OPA configuration has also allowed the first demonstration of squeezing in these modes.

These ”building blocks” are assembled together in the two experiments presented in the next chapter.

CHAPTER 5

Quantum Imaging with a small number of transverse modes

Contents

Using the transverse spatial properties of laser beams, we are now able to produce all the required basic elements for higher order continuous laser quantum optics experiments. The key components developed in the previous chapters are the ability to generate the H-G modes selectively with high efficiency and the availability of simple and fully efficient modulation and detection techniques. The first practical quantum imaging schemes with continuous variables in the transverse plane of a laser beam, using the basis of H-G modes, are now accessible.

In a first section, we will present an optimal detection of beam displacement and tilt using the concepts developed earlier in this thesis.

Moreover, the previous results potentially open the way to parallel quantum information processing in the transverse plane, as first suggested by Caves and Drummond in 1994 [Caves94]. Indeed, a very similar general scheme as the one described in Fig. 4.1 could be used. No object is involved here, but modulations are encoded on the transverse modes. This process can be performed with electro-optic spatial modulators, which would selectively encode modulations into the H-G modes. The information can then be extracted using homodyne detections with adapted transverse profiles for the local oscillator. We can thus encode and detect parallel quantum information in the transverse plane of continuous wave light beams. However, each quantum channel would be independent at this stage. It is well known that, in order to implement quantum information and communication protocols, one of the key elements is the production of entanglement. This element was missing until now. We propose to demonstrate all the major steps required for such entanglement in a second section.

A Experimental demonstration of optimal small displacement and tilt measurements

Efficient techniques for performing optical beam displacement measurements are crucial for many applications. When an optical beam is reflected from, or transmitted through, an object that is moving, the mechanical movement can be translated to a movement of the optical beam. Characterization of the transverse position of this beam then yields an extremely accurate measurement of the object movement. Some example applications that use these techniques are: Atomic force microscopy, where a beam displacement measurement is used to characterize the vibration of a cantilever, and the force the cantilever experiences [Santhanakrishnan95, Putman92]; inter-satellite position stabilisation, where a displacement measurement allows a receiving satellite to orient itself to an optical beam sent by another satellite, thus allowing a reduction of non-common mode positional vibrations between satellites [Borah06, Nikulin01]; and optical tweezers, where the position of particles held in optical tweezers can be detected and controlled by measuring the position of the beam [Guo03, Simmons96, Gittes:98, Denk90]. An understanding of the fundamental limits imposed on these opto-mechanical positional measurements is therefore an important step.

Recently our group has been investigated the possibility, both theoretical [Fabre00] and experimental [Treps02, Treps03, Treps04,1], to use quantum resources to enhance optical displacement measurements. Optical beam displacement below the standard quantum noise limit has been demonstrated[1]. Much of the interest has been on how multi-mode squeezed light can be used to enhance the outcome of split detector and array detector measurements. This is an important question since split detectors and arrays are the primary instruments presently used in displacement measurements and imaging systems.

In spite of the successes in using multi-mode squeezed light to achieve displacement measurements beyond the standard quantum noise limit (QNL), we have shown in section 3 B.1.1 that split detection is not an optimum displacement measurement, as it extracts, at best, only $\sim$ 80 % of the signal. In this section, we propose a detailed theoretical and experimental comparison of split-detection and TEM_{10} homodyne detection. We will demonstrate the performances of the TEM_{10} homodyne detection and its advantages. This technique has the potential to enhance many applications presently using split detectors to measure displacement. Furthermore, we will demonstrate that the QNL for optical displacement measurement can be surpassed by introducing a squeezed TEM_{10} mode into the measurement process. This work has been published in references [Delaubert06,1, Delaubert06,3].

A.1 Displacement and tilt measurements

A.1.1 Split-detection

- Theory

[1] Note that displacement of mechanical resonator with other detection devices can also be measured below the standard quantum noise limit imposed to the motion of the oscillator. For example, Knobel *et. al.* have reported a sensitivity of the displacement of a micro-resonator about 100 lower than the QNL using single electron transistor [Knobel03].

The conventional way to measure the displacement of a laser beam is to use a split detector. As illustrated in Fig. 5.1a), the difference between the intensity on each side of the split detector yields a photocurrent proportional to the displacement. Nevertheless,

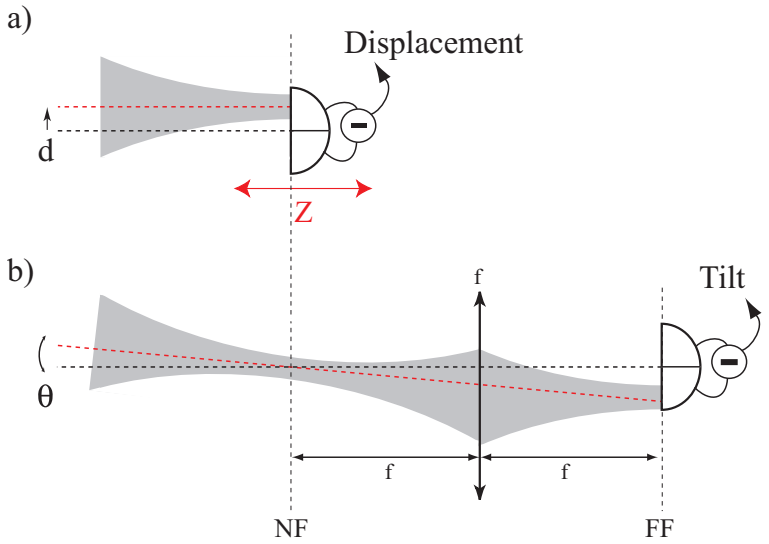

Figure 5.1: Measuring displacement and tilt of a Gaussian beam with a split detector. Taking a reference plane where displacement and tilt components are needed, displacement can be measured directly with a split detection in the near field (NF) of the reference plane, whereas tilt can be accessed in its far field (FF).

such a detection device only accesses the beam position in the detector plane, and is totally insensitive to the orientation of the propagation axis of the beam, i.e. tilt, as presented in section 3 A.

Let us now consider the evolution of the field operator of Eq. 3.9 under propagation along the z axis, we get

$$\begin{aligned}\hat{\mathcal{E}}^{+}(x,z) &= i\sqrt{\frac{\hbar\omega}{2\epsilon_0 cT}}\left[\sqrt{N}u_0(x,z)+\sqrt{N}\left(\frac{d}{w_0}+i\frac{w_0 p}{2}\right)u_1(x,z)e^{i\phi_G(z)}\right.\\ &\left.+\sum_{i=0}^{\infty}\delta\hat{a}_n u_n(x,z)e^{in\phi_G(z)}\right],\end{aligned} \tag{5.1}$$

where $u_n(x,z)$ is the Hermite Gauss TEM_{n0} mode, $\phi_G(z)$ is the Gouy phase shift, which equals $\arctan(z/z_R)$, where z_R is the Rayleigh range of the beam. N is the number of photons detected in the mean field during the integration time T. The displacement and tilt ratio varies along z because of the Gouy phase shift, i.e. diffraction, up to be perfectly inverted in the far field where $\phi_G(\infty)=\pi/2$. As explained in section 4 A.1.1, this Fourier Transform relation is a well known result in classical optics, for which a displacement in the focal plane of a simple lens is changed into an inclination relative to the propagation axis, and can be easily understood with transverse modes. Therefore, if the exact amount of tilt and displacement is needed in a particular transverse plane, for instance at $z=0$, displacement can be measured in this plane (or in its near field), whereas tilt can only be accessed in its far field, as presented in figure (5.1b).

The field presented in Eq. 5.1 is detected via a split detector whose position is varied along the z axis. The photocurrent is directly proportional to the difference of intensity incident on the two halves of the detector

$$\hat{I}_-(z) = \int_0^\infty \hat{\mathcal{E}}^+(x,z)\hat{\mathcal{E}}^{+\dagger}(x,z)dx - \int_{-\infty}^0 \hat{\mathcal{E}}^+(x,z)\hat{\mathcal{E}}^{+\dagger}(x,z)dx, \tag{5.2}$$

where the center of the split-detector itself is chosen as the reference frame, i.e. as the origin of the transverse axis x. The beam displacement is thus measured relative to the position of the split-detector. Any perturbation modifying this position will create artificial beam displacement. Consequently, we have performed our measurements at an RF frequency (4 MHz as presented later on), far from the usual mechanical or thermal instabilities in optical set-ups, that would potentially generate noise on the detector position.

Replacing $\hat{\mathcal{E}}^+(x,z)$ with the previous expression yields, for very small displacement and tilt

$$\begin{aligned}\hat{I}_-(z) = \frac{\hbar\omega}{2\epsilon_0 cT}\Bigg[&2Nc_1\left(\frac{d}{w_0}\cos\phi_G(z) + \frac{w_0 p}{2}\sin\phi_G(z)\right)\\ &+\sqrt{N}\sum_{p=0}^{\infty} c_{2p+1}\delta\hat{X}_{2p+1}^{-(2p+1)\phi_G(z)}\Bigg],\end{aligned} \tag{5.3}$$

where $\delta\hat{X}_n^\phi = \delta\hat{a}_n e^{-i\phi} + \delta\hat{a}_n^\dagger e^{i\phi}$ refers to the noise of the quadrature of the $\mathrm{TEM}_{n,0}$ mode defined by the angle ϕ, and[2]

$$\begin{aligned}c_n &= \int_0^\infty - \int_{-\infty}^0 u_n(x)u_0(x)dx\\ &= \int_{-\infty}^\infty u_n(x)u_f(x)dx,\end{aligned} \tag{5.4}$$

where u_f is the flipped mode, which is a TEM_{00} mode whose transverse profile has a π phase shift at the origin for $z = 0$ [Delaubert02], as already introduced in Fig. 1.11. Its decomposition in the TEM_{pq} basis during propagation is given by[3]

$$u_f(x,z) = \sum_{p=0}^{\infty} c_{2p+1}u_{2p+1}(x,z)e^{i(2p+1)\phi_G(z)}, \tag{5.5}$$

and the fluctuations of its amplitude quadrature operator are found to be

$$\delta\hat{X}_f^+ = \sum_{p=0}^{\infty} c_{2p+1}\delta\hat{X}_{2p+1}^+, \tag{5.6}$$

where $\delta\hat{X}_{2p+1}^+$ corresponds to the fluctuations of the amplitude quadrature of the mode $u_{2p+1}(x,z)$.

Experimentally, we measure the displacement for different split detector positions. This displacement is induced by a modulating device generating at $z = 0$ displacement and tilt modulations of amplitude d and p, respectively. A measurement at the modulation

[2] Note that the coefficient c_1 identifies with the overlap integral $\Gamma_{1,f}$ defined in Eq. 3.47.

[3] As the flipped mode profile is odd, its decomposition in the Hermite Gauss mode basis only involves odd modes.

frequency, using a spectrum analyzer yields the modulation signal as well as the noise at this frequency. As usual in quantum optics, all equations are directly transposable into the frequency domain. Using Eq. 5.3, the variance measured by a spectrum analyzer at the precise modulation frequency is given by

$$V_{SD}(z) = \kappa N \left(\frac{\hbar\omega}{2\epsilon_0 cT}\right)^2 \left[\frac{8N}{\pi}\left(\frac{d}{w_0}\cos\phi_G(z) + \frac{pw_0}{2}\sin\phi_G(z)\right)^2 + \langle\left(\sum_{p=0}^{\infty} c_{2p+1}\delta\hat{X}_{2p+1}^{-(2p+1)\phi_G(z)}\right)^2\rangle\right], \tag{5.7}$$

where κ is a constant depending only on the electronic gains of the spectrum analyzer, $T = 1/RBW$ is the integration time and $c_1 = \sqrt{2/\pi}$. The first and second bracketed terms in Eq. 5.7 respectively correspond to modulation signal and noise. In the plane of the modulating device (i.e. for $z = 0$), the noise term can be written $\langle\delta\hat{X}_f^{+^2}\rangle$ and corresponds to the noise of the amplitude quadrature of the flipped mode. We see that the flipped mode comes out as the only mode contributing to the noise in this particular plane, and corresponds to the *noise-mode of detection*, as explained in section 1C. This result was first introduced in reference [Treps02]. Note that this is not true all along the propagation axis. For a coherent incoming beam, this noise term defines the shot noise level, and is equal to 1. Note that using non classical resources for which $\langle\delta\hat{X}_f^{+^2}\rangle < 1$ in the detection plane results in noise reduction. This case will be discussed in section 5A.2.

The Signal to Noise Ratio (SNR) for a coherent beam is found from Eq. 5.7

$$SNR_{SD} = \frac{8N}{\pi}\left(\frac{d}{w_0}\cos\phi_G(z) + \frac{pw_0}{2}\sin\phi_G(z)\right)^2.$$

As stated in section 3 B.1, the SNR has a quadratic dependence in displacement d and momentum p. This expression allows the dependence of the measured signal with the split-detection during the beam propagation. Note that for pure displacement, it is in agreement with the minimal measurable displacement value obtained in Eq. 3.48. Indeed, for a SNR value of 1, corresponding to comparable signal and noise, also called the *standard quantum limit* below which a signal cannot be distinguished from the noise, $d_{\mathrm{SD}} = \sqrt{\frac{\pi}{8N}}w_0$.

Let us now present the experimental results.

- Experiment

We have performed split detection measurements of displacement and tilt of a Gaussian beam, by moving the position of the detector along the propagation axis, as shown in Fig. 5.2. Displacement and tilt are produced by a piezoelectric element (PZT) modulated at 4 MHz. A modulation signal at such a high frequency has two main advantages. The first one is to operate far from mechanical instabilities, as stated previously. The second one is to be insensitive to the technical noise of our laser source, which is shot noise limited above 1 MHz. Each measurement along the propagation axis refers to a different quadrature of the modulation (i.e. a different mixture of displacement and tilt modulation). The results are normalized to the shot noise and taken with a 4.2 mW incident beam, ensuring $7dB$ of clearance between the shot noise and the electronic noise level. From these measurements, we can infer the displacement and tilt relative amplitude modulation in the PZT plane

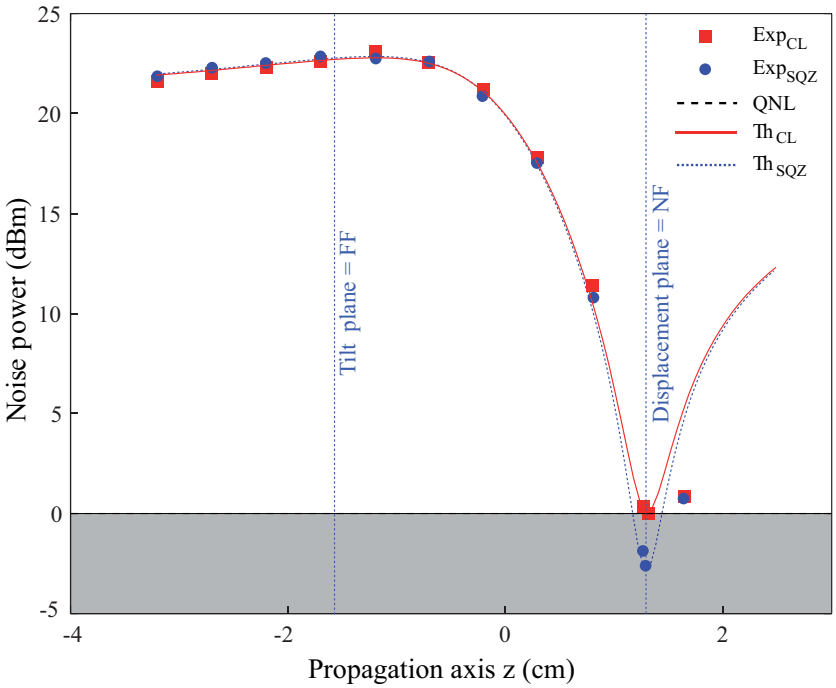

Figure 5.2: Modulation measurement normalized to the shot noise along the propagation axis of a tilted and displaced beam, using a split detector. The modulation was produced by a PZT at 4 MHz, the near field image is located 1.6 cm after the waist plane which is taken as the reference position $z = 0$. The modulation detected in this plane (NF) corresponds to the displacement modulation and represents only 10 % of the overall modulation strength. The tilt information lies in its far field (FF). Classical and non-classical experimental and theoretical results are presented.

where the waist is 106 μm. The displacement signal, accessible in the near field of the PZT, is found to be much smaller than the tilt signal, and even so that it cannot clearly be distinguished from the shot noise. This unusual behavior of the piezoelectric material arises from the operation regime, where the modulation is generated via an accidental mechanical resonance of the PZT. The theoretical curve has been plotted for a coherent illumination, using Eq. 5.7 for 10% displacement modulation, and 90% tilt modulation, ratio determined with the more accurate results presented in the section 5 A.1.2. There is a very good agreement with the experimental data. The last experimental point in Fig. 5.2 lies below the theoretical prediction, as the beam started to be apertured by the split detector, leading to a smaller measured modulation. Note that for technical reasons, our experimental setup is slightly different from the simplest setup presented on Fig. 5.1, where the reference plane coincides with the beam waist position. The waist size is $65\mu m$ after the lens, corresponding to a Rayleigh range of 1.3 cm. As shown on Fig. 5.2, the waist position lies at 1.6 cm for the near field of the PZT in our imaging setup, and we have used the imaging properties of Hermite Gauss modes developed in section 4 A.1.2.

We have shown in this section how to retrieve displacement and tilt information from a gaussian beam with a split detector, and have taken experimental results which will be used as a reference in the following sections.

A.1.2 Homodyne detection with a TEM_{10} mode local oscillator

We have proved theoretically in section 3 B.1.1 that split detection was non optimal to retrieve displacement information, as it is only sensitive to the flipped mode instead of the TEM_{10} mode component of the input field. In order to extract all the displacement and tilt information with up to 100% efficiency, we have proposed a homodyne detector involving a TEM_{10} mode local oscillator, which selects the TEM_{10} mode component of the field. We now first detail the theoretical detected signal dependence with the local oscillator phase.

In the homodyne detection scheme, two beams are mixed on a 50 : 50 beam-splitter. The first one is the signal beam containing the displacement and tilt modulations, whose field operator is given by Eq. 3.9. The second one is the local oscillator (LO), whose field operator is

$$\hat{\mathcal{E}}^{+}_{LO}(x) = i\sqrt{\frac{\hbar\omega}{2\epsilon_0 cT}}\left[\sqrt{N_{LO}}u_1(x) + \sum_{i=0}^{\infty}\delta\hat{a}_{LO_n}u_n(x)\right],$$

where N_{LO} denotes the number of photons detected that can be detected in the LO beam during the time interval T. This definition of the LO profile, namely its axis and spatial extension, sets a spatial reference for beam displacement and tilt measurements, similarly to the position of the split detector in the previous section. Since displacement and tilt modulations are very small and the local oscillator is much brighter than the signal beam (i.e. $N_{LO} \gg N$), the usual calculation of the intensity difference between the two homodyne detectors at the modulation frequency gives

$$\hat{I}_{-} = \frac{\hbar\omega}{2\epsilon_0 cT}\left[2\sqrt{NN_{LO}}\left(\frac{d}{w_0}\cos\phi_{LO} + \frac{w_0 p}{2}\sin\phi_{LO}\right) + \sqrt{N_{LO}}\delta\hat{X}_1^{\phi_{LO}}\right], \quad (5.8)$$

where ϕ_{LO} is the local oscillator phase. Similarly to Eq. 5.7, the variance of the intensity difference at the displacement and tilt modulation frequency is therefore

$$V_{\mathrm{HD}}(\phi_{LO}) = \kappa N_{LO}\left(\frac{\hbar\omega}{2\epsilon_0 cT}\right)^2\left[4N\left(cos(\phi_{LO})\frac{d}{w_0} + sin(\phi_{LO})\frac{pw_0}{2}\right)^2 + \langle\delta\hat{X}_1^{\phi^2_{LO}}\rangle\right], \quad (5.9)$$

where the constant κ is identical to the split detection part as long as the spectrum analyzer settings have not been changed. The first bracketed term corresponds to the modulation signal. The second one refers to the noise of the TEM_{10} component of the detected field, and its variation with the local oscillator phase ϕ_{LO} is given by $\langle\delta\hat{X}_1^{\phi^2_{LO}}\rangle = \langle\delta\hat{X}_1^{+^2}\rangle\cos^2\phi_{LO} + \langle\delta\hat{X}_1^{-^2}\rangle\sin^2\phi_{LO}$, where $\langle\delta\hat{X}_1^{+^2}\rangle$ and $\langle\delta\hat{X}_1^{-^2}\rangle$ are the noise of the amplitude and phase quadrature of the TEM_{10} mode, respectively. Scanning the local oscillator phase allows to measure all the quadratures of the displacement and tilt modulation. We have omitted the Gouy phase shift in the previous expression, as it can be incorporated as a constant term in the local oscillator phase. This phase is still defined so that $\phi_{LO} = 0$ corresponds to a displacement measurement in the PZT plane.

Again, we find that the TEM_{10} mode of the incoming beam contributes to the noise, as it matches the local oscillator transverse shape. All the other modes contributions cancel out since they are orthogonal to the local oscillator. The TEM_{10} mode is thus the *noise-mode* of the homodyne detection, and precisely matches the information to be extracted. This is in this sense an optimal beam displacement and tilt detection device, as explained

in section 3 B. It shows that no other device can perform better measurement of the same parameters.

For a coherent incoming TEM_{10} mode, the previous noise term defines the shot noise level, and is equal to 1. Using squeezed light in the TEM_{10} mode component of the incoming beam would result in noise reduction, and will be discussed in the section 5A.2.

The SNR for a coherent incoming beam can be derived from Eq. 5.9 in the homodyne detection case

$$\mathrm{SNR}_{\mathrm{HD}} = 4NT\left(\frac{d}{w_0}\cos\phi_{\mathrm{LO}} + \frac{pw_0}{2}\sin\phi_{\mathrm{LO}}\right)^2. \tag{5.10}$$

Comparing the split and homodyne detections schemes yields certain similarities between Eq.(5.7) and (5.9). First, a variation of the local oscillator phase ϕ_{LO} in the homodyne scheme is equivalent to a propagation along the z axis inducing a Gouy phase shift ϕ_G in the split detection case. Secondly, an additional $2/\pi$ geometry factor in the split detection case arises from the imperfect overlap between the flipped mode and the TEM_{10} mode, as discussed in section 3 B.1.1. The comparison between the two SNRs in the coherent case yields a theoretical efficiency ratio given by

$$R_{th} = \frac{\mathrm{SNR}_{\mathrm{SD}}}{\mathrm{SNR}_{\mathrm{HD}}} = \frac{2}{\pi}\frac{N_{\mathrm{SD}}}{N_{\mathrm{HD}}}, \tag{5.11}$$

where N_{SD} and N_{HD} refer to the number of photon in the displaced and tilted beam, for the split detection and the homodyne detection case, respectively. As explained earlier, for identical signal beams powers, this means that the split detection is only $2/\pi = 64\%$ efficient compared to the homodyne detection. Using the homodyne detection thus corresponds to an improvement of $(100-64)/64 = 56\%$.

Eventually, the intensity factor before the bracketed term in Eq. 5.9 and Eq. 5.7 can be much bigger in the homodyne detection case, as it corresponds to the local oscillator intensity instead of the input beam intensity in the split detection case. It is thus easier to have more electronic noise clearance in the homodyne case for weak signals. This is of particular interest when the intensity of the input beam is limited, for instance if it interacts with an intensity sensitive medium which has a low damage threshold.

In this section, we have shown - still theoretically - how to retrieve displacement and tilt using a homodyne detector with a TEM_{10} local oscillator. Moreover, we have proved a 56% theoretical improvement of this scheme compared to the split detection.

A.2 Displacement measurement beyond the standard quantum noise limit

When the information to be retrieved is below - or of the order of - the quantum noise, non classical resources (i.e. squeezed laser beams) can help extracting the information. For each type of detection (i.e homodyne- and split detection), the only transverse mode component within the incident field which contributes to the noise has been identified in the previous sections. The noise modes of the split and homodyne detection are the flipped mode and the TEM_{10} mode, respectively. Since displacement and tilt of a TEM_{00} beam lies in the TEM_{10} component of the beam, noise mode and information encoded are matched for the homodyne detection only.

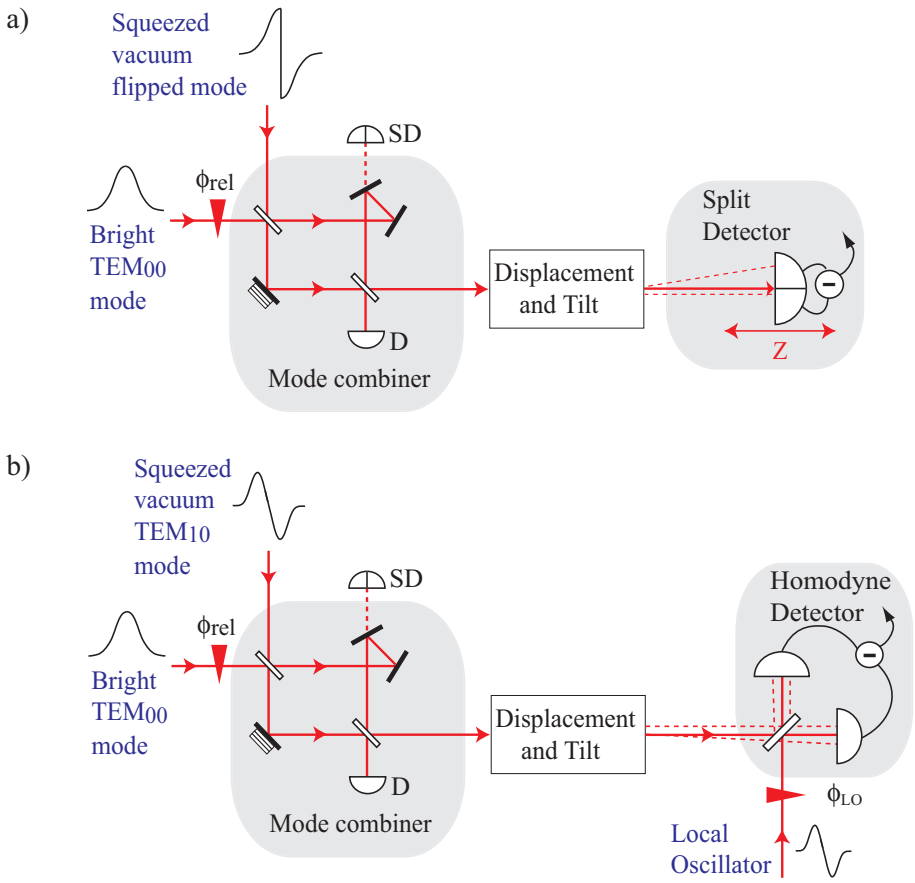

Figure 5.3: Schematic of displacement and tilt modulation measurement beyond the quantum noise limit. a) With a split detector and b) with a homodyne detector. Prior to the modulation generated via a PZT at a few MHz, a bright TEM_{00} beam is combined without losses with a squeezed vacuum noise mode. This was done with a special Mach-Zehnder which has an additional mirror in one arm. A mirror leakage is used to lock the relative phase between both input modes. All different combinations of displacement and tilt modulations are accessible when a) the position of the split detector along the propagation axis z is varied, and b) when the local oscillator phase ϕ_{LO} is scanned.

Sub shot noise measurements with both schemes can be performed using the setups shown in Fig. 5.3, by filling the noise mode of the input beam with squeezed light. A mode combiner has to be used to merge the signal beam - in our case a bright TEM_{00} beam - with the noise mode of detection, filled with squeezed vacuum. Note that it has to be a vacuum mode, or a very dim field not to contribute to the signal, but only to reduce the quantum noise properties[4]. The combination of beams cannot be done with a sheer beamsplitter as the squeezing is not robust to losses. Instead, we used a special Mach-Zehnder interferometer with an additional mirror in one arm, as already introduced in section 4

[4]Note that even if the combination of the reference TEM_{00} beam with the squeezed beam is made before the displacement of the beam, the displacement involved is so small compared to the beam waist that the non-classical properties of the beam are unchanged at first order in d/w_0. We can therefore consider in the following that noise reduction useful for the detection corresponds to the squeezing of the input field with an excellent approximation.

A.3.2. This mirror has no effect on even transverse profiles, but induces an additional π phase shift to odd transverse profiles. Therefore, thanks to this asymmetry, orthogonal even and odd modes, which are incident on the two input ports of the Mach-Zehnder, interfere constructively on the same output port without experiencing any losses. The integrality of the bright beam and the squeezing of the squeezed vacuum mode - a) flipped mode or b) TEM_{10} mode - are thus preserved at the output of the interferometer. Note that other devices can be used for the mode combination, such as an optical ring-cavity, as explained in section 4 A.3.3.

In order to make a direct comparison of the performances of the split detection and the homodyne detection, we have built the experimental setup sketched in Fig. 5.4, where both schemes are tested in the same operating conditions. In addition to a simple comparison involving only classical resources, we designed the experience in order to allow measurements beyond the QNL. At this stage, we were unable to produce directly a squeezed TEM_{10} mode, as the experiment on higher order mode squeezing (see section 4 C) has been demonstrated after the one presented here. We have therefore chosen to generate a squeezed flipped mode, which also corresponds to a squeezed TEM_{10} mode having experienced 36 % losses. Indeed, the amount of squeezing in the amplitude quadrature of the

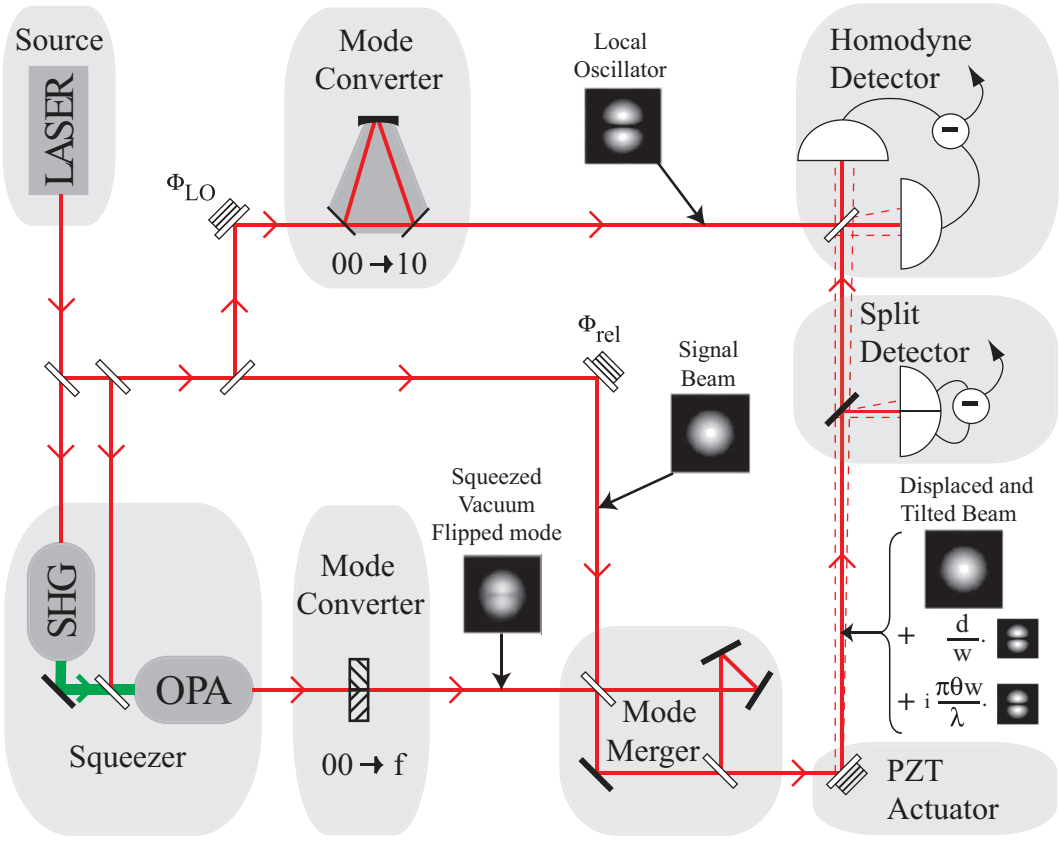

Figure 5.4: Experimental scheme to measure displacement and tilt with a split detector and a homodyne detector in the same operating conditions. f: flipped mode.

TEM_{10} component of the flipped mode can be deduced from

$$\langle \delta \hat{X}_1^{+^2} \rangle = \frac{2}{\pi} \langle \delta \hat{X}_f^{+^2} \rangle + \left(1 - \frac{2}{\pi}\right), \tag{5.12}$$

as all the modes except the flipped mode are filled with coherent light. This expression can be obtained by changing the basis for the description of the field, as explained in section 1 A.2.5. If the flipped mode is a classical coherent state, $\langle \delta \hat{X}_f^{+^2} \rangle = 1$, which also implies that the TEM_{10} component is coherent $\langle \delta \hat{X}_1^{+^2} \rangle = 1$, as expected. In the end, if we start with 3.6 dB of squeezing in the amplitude quadrature of the flipped mode as discussed below, we get 2 dB of squeezing in the TEM_{10} mode, which is exactly what can be measured experimentally by using the homodyne detection with a TEM_{10} local oscillator.

We used the following experimental procedure. First we generated a 3.6 dB squeezed TEM_{00} mode from a monolithic optical parametric amplifier (OPA) pumped by a frequency doubled YAG laser delivering 600 mW at 1064 nm, and seeded by a TEM_{00} mode[5]. This very low power (μW) squeezed beam then experiences a mode conversion into the flipped mode thanks to a special wave-plate made of two half wave-plates whose optical axis have been rotated 90° relative to each other [Delaubert02]. A beam incident on such an optical element yields a π phase shift on half of its transverse profile.

Thanks to the special Mach-Zehnder interferometer formerly presented, we combine this beam with a bright TEM_{00} beam, therefore preserving their potential non classical properties. To achieve this experimentally, we first mode matched both input beams of the interferometer without the special wave-plate, reaching 99.5 % visibility on the first beam-splitter of the interferometer. The squeezed beam, although very dim, is still bright enough to be mode matched with the other bright TEM_{00} beam. The interferometer is then aligned on the OPA beam without the wave-plate with 98 % visibility and then the wave-plate is slid in the center of the beam to a maximum visibility of 97.8 %. Note that we purposely introduced a leakage in one of the mirrors to lock the relative phase ϕ_{rel} between the two input modes with a split detector (SD), as drawn in Fig. 5.3). In the end, the global mode combiner efficiency is still higher than 97%.

The multi-mode squeezed beam hereby generated is then displaced and tilted with a PZT, as presented in section 5 A.1.1, and the information is detected with either one of the split or homodyne detection schemes. Let us first briefly concentrate on the results obtained with the split-detector, in presence of the squeezed flipped mode. We see in Fig.5.2 that we were able to measure a modulation below the QNL. These measurements precisely correspond to detection in the near field of the mode converting wave-plate - which is also the far field of the PZT - as the flipped mode is not stable with propagation, and the squeezing degrades very quickly along the z direction.

We now focus on the TEM_{10} homodyne detection. The TEM_{10} local oscillator is produced with a misaligned ring cavity locked to resonance on the TEM_{10} mode represented in Fig. 5.4, and has already been presented in section 4 A.2.2. We recall that the cavity has been designed such that it delivers a pure transverse output mode (i.e. high order modes are not simultaneously resonant in the cavity). We mode matched this local oscillator beam to the signal beam by previously locking the ring cavity to the TEM_{00} mode resonance, reaching a visibility of 98.9 % with the TEM_{00} input mode.

The experimental results, obtained with the spectrum analyzer in zero-span mode at 4 MHz, are presented in Fig. 5.5(a) and Fig. 5.5(b), when the TEM_{10} local oscillator phase is scanned and locked for displacement ($\phi_{\mathrm{LO}} = 0$) and tilt ($\phi_{\mathrm{LO}} = \pi/2$) measurement.

[5]This operation of this monolithic OPA is not presented in this thesis, as it has already been very clearly described in reference [BuchlerPhD01].

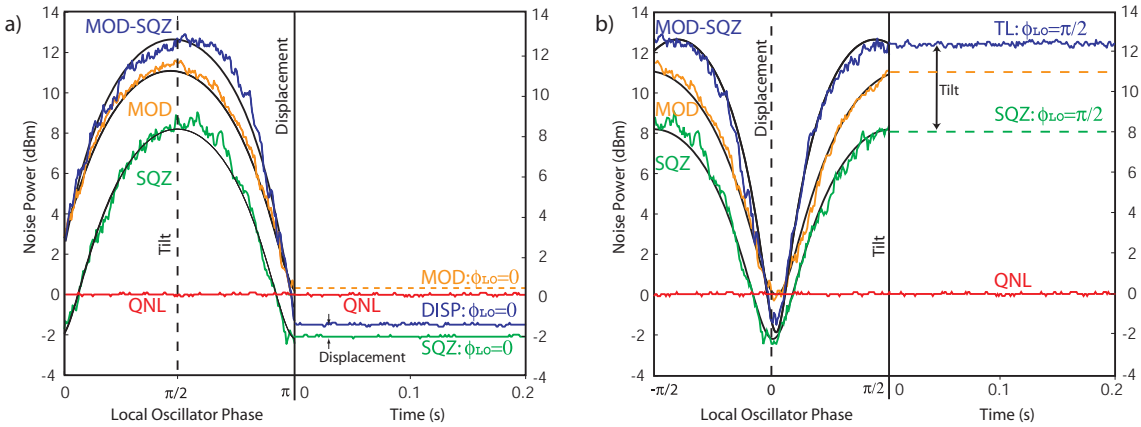

Figure 5.5: Demonstration of sub-shot noise measurements of (a) displacement and (b) tilt modulations using spatial homodyne detector. The figures show an example with 90% of tilt, and 10% of displacement modulations. Left hand side of the figures shows the scanning of the local oscillator phase ϕ_{LO} that continuously access the pure displacement (at $\phi_{\mathrm{LO}} = 0$ and π) to pure tilt (at $\phi_{\mathrm{LO}} = \pi/2$ and $3\pi/2$) information of the beam. QNL: quantum noise limit. SQZ: quadrature noise of squeezed light with 2 dB of squeezing and 8 dB of anti-squeezing on the TEM_{10} mode, but without any modulation signal. MOD: measured modulation with coherent light. MOD-SQZ: measured modulation with squeezed light. Right hand side of the figures shows the corresponding locked local oscillator phase to the (a) displacement or (b) tilt measurement. SQZ: at $\phi_{\mathrm{LO}} = 0$ the squeezed noise level is 2 dB below the shot noise and at $\phi_{\mathrm{LO}} = \pi/2$ there is 8 dB of anti-squeezing noise. DISP: MOD-SQZ curve locked to $\phi_{\mathrm{LO}} = 0$ for displacement measurement. TL: MOD-SQZ curve locked to $\phi_{\mathrm{LO}} = \pi/2$ for tilt measurement. Displacement measurement is improved by the 2 dB of squeezing, while the tilt measurement is degraded by the 8 dB of anti-squeezing.

The electronic noise is $11.7dB$ below the shot noise level. All traces are corrected for this noise. Without the use of squeezed light, the displacement modulation cannot clearly be resolved, as in the split detection case. Improvement of the SNR for displacement measurement beyond the quantum noise limit is achieved when the squeezed quadrature of the TEM_{10} mode is in phase with the displacement measurement quadrature (i.e. in phase with the incoming TEM_{00} mode). Since we are dealing with conjugate variables, improving the displacement measurement degrades the tilt measurement of the same beam, as required by the anti-squeezing of the other quadrature. The displacement measurement is improved by the 2 dB of squeezing, whereas the tilt measurement is degraded by the 8 dB of anti-squeezing. Theoretical curves calculated with 2 dB of noise reduction and 8 dB of anti-squeezing, and 90 % of tilt modulation and 10 % of displacement modulation - continuous curves in Fig. 5.5(a) - are in very good agreement with experimental data. In our experiment, we have a TEM_{00} waist size of $w_0 = 106$ μm in the PZT plane, a power of 170 μW, RBW = 100 kHz and VBW= 100 Hz, corresponding to a QNL of $d_{\mathrm{QNL}} = 0.6$ nm. The measured displacement lies 0.5 dB above the squeezed noise floor, yielding a displacement modulation 0.08 times larger than the QNL. As the modulation has a square dependence on the displacement d, we get $d_{exp} = \sqrt{0.08} d_{\mathrm{QNL}} = 0.15$ nm. This would correspond to a trace only 0.3 dB above the QNL (trace MOD:$\phi_{\mathrm{LO}} = 0$ in

Fig5.5a))[6]. The ratio between displacement and tilt modulations can be inferred from the theoretical fit in figure 5.5, giving a measured tilt of 0.13 μrad.

We have in this section demonstrated measurements of a pair of quantum conjugate variables - displacement and tilt - with a homodyne detector involving a TEM_{10} mode local oscillator, and performed sub shot noise displacement measurements.

A.3 Comparison of TEM_{10} homodyne and split-detection for displacement and tilt measurements

Split-detection and homodyne detection efficiencies would ideally be compared exactly in the same regime. However, the optimum operating regimes for both schemes are not compatible. Indeed, on the one hand, in the split detection case, the incident beam power must be "intense" in order to have enough clearance relative to the electronic noise level, i.e. several mW for our split detection device. On the other hand, in the homodyne detection case, the local oscillator has to be the "intense" beam, and is the one whose power must ensure an electronic noise clearance. Its power must thus be of the order of the mW for our homodyne detectors. In this case the power of the incident displaced and tilted beam should beat least 10 times less than the power of the LO beam, i.e. its power cannot exceed about $100\mu W$. In order to provide a comparison, we use Eq.5.11 which takes into account the power discrepancy between both experiments. Note however that all other parameters are identical, as shown by the symmetry of the system shown in Fig.5.4.

The experimental efficiency ratio can be accessed by the ratio of maximum modulation power relative to the shot noise $\mathrm{Mod_{SD}}$ and $\mathrm{Mod_{HD}}$, respectively detected with the split-detection and the homodyne detection:

$$R_{exp} = \frac{\mathrm{Mod_{SD}}}{\mathrm{Mod_{HD}}}. \tag{5.13}$$

The two experimental curves presented in Fig. 5.2 and 5.5a) (MOD) read $\mathrm{Mod_{SD}} = 23dB$ and $\mathrm{Mod_{HD}} = 11.3dB$, for beam powers of $P_{\mathrm{SD}} = 4.2mW$ and $P_{HD} = 170\mu W$, respectively. Using Eq. 5.11 and 5.13, we can compare our theoretical prediction and the experimental efficiency ratio with the following ratio:

$$\frac{R_{exp}}{R_{th}} = 1 \pm 0.05, \tag{5.14}$$

where the uncertainty is mainly due to the determination of the maximum modulation values. We therefore report an efficiency improvement of 56%, in perfect agreement with the theoretical value calculated earlier.

Let us now compare the advantages or drawbacks of both detection devices. Although we have proven that the homodyne scheme is more efficient, it is not always the most convenient or the most appropriate to operate in some experimental setups.

The main advantage of the split-detector is obviously its simplicity for a single displacement measurement and its compatibility with incoherent illumination. When the beam to

[6]It is important to note that even if the signal is smaller than the QNL, it still yields a measurable trace above the QNL. The use of squeezed light only allows to better resolve this modulation signal from the noise of the QNL, but similar resolution could be obtained by averaging the traces. Squeezed light is therefore mostly useful when the phenomenon of interest is non stationary and when this averaging process cannot be used, i.e. when the noise level itself fluctuates.

be analyzed is intense enough to be distinguished from the electronic noise, such a simple device has to be preferred. However, as soon as both conjugated variables are investigated, several split-detections are required, potentially involving a displacement of the detector itself in between two consecutive measurements. There are additional limitations to the use of a split detector due to its gap and to its finite size, which are imposing constraints when the variation of the modulation on the propagation axis is measured. The accessible range to a good detection on the z axis is small, as the beam can neither be too small (because of the gap), nor too large because of the finite size of the detector).

When it comes to ultra-sensitive measurements, the gain in efficiency provided by the homodyne scheme relative to the split-detection is a simpler technique than the use of non classical light with a split-detector. In order to perform measurements beyond the QNL, one has to carefully image the squeezed flipped mode onto the sample with which the beam is interacting, and also onto the detector, as the flipped mode is not stable in propagation. As a 56% improvement roughly corresponds to the use of 3dB of squeezing, homodyne detection with coherent[7] illumination should be preferred in this case. Another advantage of the homodyne device is to allow measurements of displacement and tilt of a beam without changing the position of the detector, just by varying the local oscillator phase, which has to be carefully mode-matched to the incoming beam. High measurement rates of both variables can thus be achieved. Moreover, weak signals that would have been drowned in the electronic noise of a split-detector are measurable as the noise clearance is determined by the intense local oscillator[8]. Nevertheless, using this detection device requires coherent illumination as it relies on interference measurement. Additionally, implementing a local oscillator beam is sometimes impossible, typically when the source of the beam to be analyzed cannot be accessed.

In order to further improve the measurement sensitivity, for instance when the signal is so weak that it cannot be distinguished from the quantum noise, a non classical beam with a squeezed TEM_{10} component can be generated. The homodyne detection noise will be reduced either for displacement or tilt measurement, according to the relative phase between squeezed beam and carrier beam. Such detection can for instance be applied to track the position and orientation - at high frequency not to have thermal and mechanical perturbations - of a phase object or a biological sample - we recall that the use of non classical light is limited to transparent propagation media, as the squeezing rapidly decays with losses.

As a conclusion, we have demonstrated the generation of position-squeezed and momentum-squeezed beams and their optimal detection with a TEM_{10} homodyne detection. We now propose to use this knowledge to combine two of these non-classical beams on a beam-splitter in order to generate entanglement between position and momentum of macroscopic bright optical beams.

[7] The term "coherence" means here temporal coherence, i.e. that local oscillator and signal beams must be generated with the same source.

[8] The total available power for the experiment can of course be a limiting factor, which would limit the performances in the same way as in the split-detection case.

B Spatial entanglement

In 1935, Einstein, Podolsky and Rosen introduced the notion of entanglement, and what are now referred to as *EPR states*, in order to answer the following question : 'Can quantum-mechanical description of physical reality be considered complete?'[Einstein35]. In their demonstration, involving the position and momentum of particles, they presented a paradox that could be solved only by invoking the non completeness of Quantum Mechanics.

States realizing the EPR paradox have now been produced in many laboratories, as detailed in section 1A.3.4. Position-momentum entanglement has already been demonstrated in the discrete regime with atoms [Parkins00, Riedmatten06] and quantum correlations have been observed between near and far-field corresponding to the position and momentum observables of photon pairs in the regime of a few incident photons [Howell04]. However, to date, no such states have been generated with optical beams in the continuous variable regime.

The aim of the work presented in this chapter is to generalize the former continuous variable quadrature entanglement experiments [Ou92, Bowen03, Jing06] to the spatial domain, similarly to what has been done in the polarization domain [Bowen02, Korolkova02, Zambrini03, Josse04, Laurat06], in order to produce entanglement of position and momentum conjugate observables, as first considered by Einstein, Podolsky and Rosen in 1935 [Einstein35]. This theoretical proposition using two bright optical beams was first introduced by M.T.L. Hsu *et al.* in 2005 [Hsu05], and was termed *spatial entanglement of bright optical beams*. Here, by *spatial entanglement*, they referred to the entanglement of spatial observables, namely position and momentum, involving a complete detection of the beams in the transverse plane. This has be to distinguished from previous use of this term, where it referred to quadrature entanglement between restricted spatial areas of optical images [Gatti99, Navez01, Gatti03], or local areas of a Bose-Einstein condensate [Heaney06].

In this section, we will first discuss the latter proposal, then focus on its experimental implications, and will finally present the latest experimental results towards the generation of spatial entanglement of bright optical beams.

B.1 Theory

B.1.1 Heisenberg inequality relation

As introduced in section 3A, position and momentum of a bright TEM_{00} mode laser beam are simply related to the TEM_{10} quadratures components of the beam by

$$\hat{x} = \frac{w_0}{2\sqrt{N}}\hat{X}_1^+ \tag{5.15}$$

$$\hat{p} = \frac{1}{w_0\sqrt{N}}\hat{X}_1^-, \tag{5.16}$$

It is important to note that the quadratures of the TEM_{10} mode are defined relative to the quadratures of the bright TEM_{00} carrier beam, which corresponds here with the mean field (to a first order approximation) as explained in section 3A.1.2. This is of particular importance when the TEM_{10} mode beam of interest is not strictly a vacuum state, as it is the case in our experiment.

We recall that these position and momentum variables are conjugate observables which satisfy the following commutation relation

$$[\hat{x}, \hat{p}] = \frac{i}{N}. \tag{5.17}$$

This commutation relation is similar to the position-momentum commutation relation for a single photon, apart from the $1/N$ factor. This factor is related to the precision with which one can measure beam position and momentum. Rewriting the Heisenberg inequality using the commutation relation gives

$$\Delta^2\hat{x}\Delta^2\hat{p} \geq \frac{1}{4N}. \tag{5.18}$$

The $1/N$ factor is to be related to the result presented in section 3B.1 showing that both the sensitivity of beam position and beam momentum of a coherent beam scales as $\sqrt{N}$. We see from Eq. 5.18 that for a small number of incident photons N, the measurement of position and momentum of the beams are highly uncertain. However, as N becomes large, the uncertainty product $\Delta^2\hat{x}\Delta^2\hat{p}$ approaches zero, so that even without quantum resources[9], x and p can be known simultaneously with very high precision.

B.1.2 Entanglement scheme

Position and momentum observables of a TEM_{00} beam do not commute and hence satisfy a Heisenberg inequality. One consequence of this has been presented in section 5A, when we showed that using squeezed light in order to improve the accuracy of a position measurement was simultaneously altering the associated momentum measurement.

Another interesting consequence is that EPR entanglement for the position and momentum of TEM_{00} beams is possible. Entanglement can be generated by mixing two beams, each containing two components - a bright TEM_{00} mode, and a dim vacuum-squeezed TEM_{10} mode. As with previous experiments generating quadrature entanglement [Ou92, Bowen03, Jing06], these two beams can be combined on a 50/50 beamsplitter, from now on to be referred to as the *entanglement beam-splitter*. For clarity, we will only discuss in the theoretical section the particular case of the orthogonal combination of two position-squeezed beams, as defined in section 3A[10]. However, it is easy to show that all the results still hold as long as the relative phases ϕ_{rel_1} and ϕ_{rel_2} between the dim squeezed TEM_{10} and bright coherent TEM_{00} components are identical, and that both squeezed TEM_{10} components interfere in quadrature on the entanglement beam-splitter, as shown in Fig.5.6. A schematic of the *spatial entanglement* scheme is presented in Fig.5.7. The setup involves the interferences of four fields, in analogous to the setup for polarization entanglement [Bowen02].

As discussed in section 1A.3.4, the production of entanglement requires two orthogonal squeezed states. Both position squeezed beams must therefore be in quadrature, i.e. $\pi/2$ shifted relative to each other, when they interfere on the beam-splitter. A summary of all the different phases involved in the experiment, and the values they have to be locked to, is given in Fig. 5.8. In addition to the relative phases between the TEM_{00} and

[9] Quantum resources means here sub-QNL sources and ideal detection devices.

[10] We recall that a light beam is said to be position-squeezed if its position can be determined to an accuracy beyond the standard quantum limit. Such beams are composed of a coherent bright TEM_{00} mode

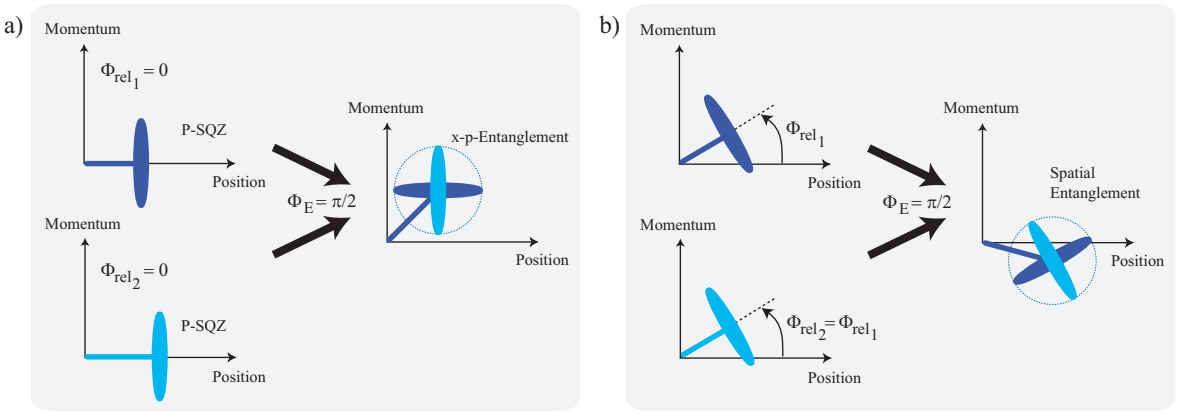

Figure 5.6: Fresnel representation of the TEM_{10} component for spatial entanglement, a) in the particular case of the orthogonal combination of two position-squeezed beams (x-p entanglement), and b) in the more general case of any orthogonal combination of two beams, for which the relative phase ϕ_{rel} between the TEM_{00} carrier mode and the squeezed TEM_{10} component is non zero. The orthogonality of the two non classical beams on the entanglement beam-splitter corresponds to $\phi_E = \pi/2$. Similarly to the definition used in Fig. 3.4, the horizontal axis of the Fresnel diagrams corresponds here to the TEM_{00} phase reference, and therefore designates the position axis, whereas the vertical axis refers to the momentum of the beam.

TEM_{10} components (ϕ_{rel_1} and ϕ_{rel_2}), and the relative phase between the two non-classical beams interfering on the entanglement beam-splitter (ϕ_E), we also present the local oscillator phases required for amplitude $\hat{X}^+$ and phase $\hat{X}^-$ quadrature measurements at the homodyne detection $\left(\phi_{LO_x}(\hat{X}^+), \phi_{LO_x}(\hat{X}^-), \phi_{LO_y}(\hat{X}^+), \text{and} \phi_{LO_y}(\hat{X}^-)\right)$.

B.1.3 Inseparability criterion

In order to generate x-p entanglement, we consider beams with zero mean position and momentum. Nevertheless, the quantum noise of the position and momentum of both beams can already yield a signature of entanglement as shown below[11]. The electric field operators for the two input beams at the beam splitter are given by

$$\hat{\mathcal{E}}_1^{(+)}(x) = i\sqrt{\frac{\hbar\omega_0}{2\epsilon_0 cT}}\left(\sqrt{N}u_0(x) + \sum_{n=0}^{\infty}\delta\hat{a}_n u_n(x)\right) \tag{5.19}$$

$$\hat{\mathcal{E}}_2^{(+)}(x) = i\sqrt{\frac{\hbar\omega_0}{2\epsilon_0 cT}}\left(\sqrt{N}u_0(x) + \sum_{n=0}^{\infty}\delta\hat{b}_n u_n(x)\right) \tag{5.20}$$

where $\hat{a}_n$ and $\hat{b}_n$ correspond to the annihilation operators of the n^{th} mode of the first and second input beams, respectively. N is the number of photons detected in each of the two beams during the measurement time. In both equations, the first bracketed term describes

component and a squeezed vacuum TEM_{10} mode component whose squeezed quadrature is in phase with the TEM_{00} component.

[11] Note that the use of entangled beams carrying a displacement and momentum signal, i.e. a modulation, would however be necessary for a teleportation protocol.

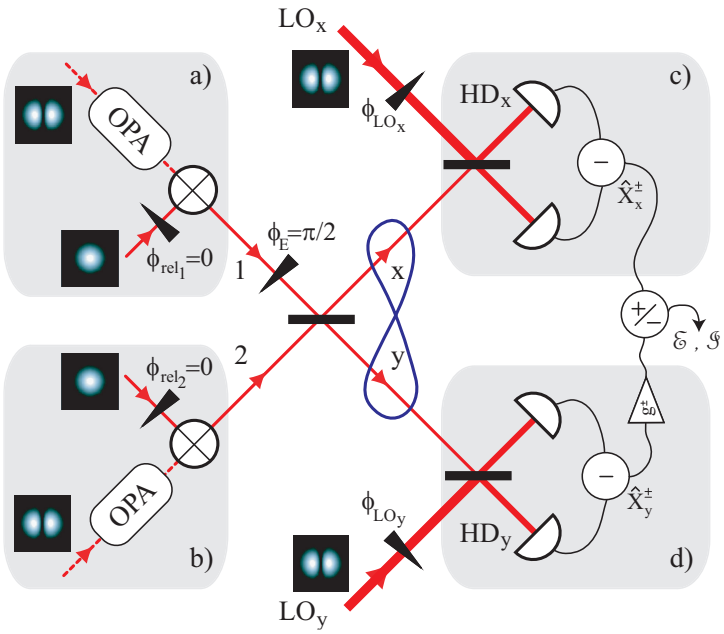

Figure 5.7: Scheme for position-momentum entanglement between two bright TEM_{00} beams. Two position-squeezed beams a) and b), denoted 1 and 2, are combined on a 50/50 beam-splitter. The two output beams, denoted x and y, are entangled when beams 1 and 2 are in quadrature, i.e. when $\phi_E = \pi/2$. The entangled beams are analyzed with two homodyne detections (HD_x and HD_y). Amplitude ($\hat{X}^+$) and phase ($\hat{X}^-$) quadratures are alternatively accessible for both beams, for determined phases of the local oscillators beams (ϕ_{LO_x} and ϕ_{LO_y}). The appropriate combination of both homodyne signals yields the degree of EPR paradox $\mathcal{E}$ or the degree of inseparability $\mathcal{I}$. $\bigotimes$: lossless mode combiner (special Mach Zehnder for instance).

the coherent amplitude of the TEM_{00} beam, and the second one the quantum fluctuations present in all modes. For position squeezed states, only the TEM_{10} mode is occupied by a vacuum squeezed mode, and all other modes are occupied by vacuum fluctuations. Knowing that both beams are combined in quadrature on the 50/50 beam-splitter, we get

$$\hat{\mathcal{E}}_x^{(+)} = \frac{1}{\sqrt{2}}\left(\hat{\mathcal{E}}_1^{(+)} + i\hat{\mathcal{E}}_2^{(+)}\right) \tag{5.21}$$

$$\hat{\mathcal{E}}_y^{(+)} = \frac{1}{\sqrt{2}}\left(\hat{\mathcal{E}}_1^{(+)} - i\hat{\mathcal{E}}_2^{(+)}\right) \tag{5.22}$$

To demonstrate the existence of entanglement, we seek quantum correlation and anti-correlation between the position and momentum quantum noise operators. The position fluctuation operators corresponding to beams x and y are given, respectively, by

$$\delta\hat{x}_x = \frac{w_0}{2\sqrt{2N}}\left(\delta\hat{X}_{a_1}^+ + \delta\hat{X}_{b_1}^-\right) = \frac{1}{\sqrt{2}}\left(\delta\hat{x}_1 + \frac{w_0^2}{2}\delta\hat{p}_2\right) \tag{5.23}$$

$$\delta\hat{x}_y = \frac{w_0}{2\sqrt{2N}}\left(\delta\hat{X}_{a_1}^+ - \delta\hat{X}_{b_1}^-\right) = \frac{1}{\sqrt{2}}\left(\delta\hat{x}_1 - \frac{w_0^2}{2}\delta\hat{p}_2\right) \tag{5.24}$$

a)

Beam	Component	Ent-BS
1	TEM_{00}	0
	TEM_{10}	0
2	TEM_{00}	$\pi/2$
	TEM_{10}	$\pi/2$

b)

Beam	$\hat{X}^+$ Measurement	$\hat{X}^-$ Measurement
x	0	0
LO_x	0	$\pi/2$
y	0	0
LO_y	0	$\pi/2$

Figure 5.8: Relative phases for the entanglement setup a) before the beam-splitter : the TEM_{00} and TEM_{10} components of beams 1 are in phase, but both are in quadrature with the TEM_{00} and TEM_{10} components of beams 2, b) after the beam-splitter : for amplitude quadrature $\hat{X}^+$ measurement, local oscillators x and y, LO_x and LO_y are required to be in phase with beams x and y, respectively, whereas they are required to be in quadrature for phase quadrature $\hat{X}^-$ measurement.

The momentum fluctuation operators corresponding to beams x and y are given by

$$\delta\hat{p}_x = \frac{1}{w_0\sqrt{N}}\left(\delta\hat{X}^-_{a_1} + \delta\hat{X}^+_{b_1}\right) = \frac{1}{\sqrt{2}}\left(\delta\hat{p}_1 + \frac{2}{w_0^2}\delta\hat{x}_2\right) \tag{5.25}$$

$$\delta\hat{p}_y = \frac{1}{w_0\sqrt{N}}\left(\delta\hat{X}^-_{a_1} - \delta\hat{X}^+_{b_1}\right) = \frac{1}{\sqrt{2}}\left(\delta\hat{p}_1 - \frac{2}{w_0^2}\delta\hat{x}_2\right) \tag{5.26}$$

It is not surprising to find here a direct link with the *inseparability criterion* introduced in section 1A.3.4, which can be written in its product form as [Hsu05]

$$\mathcal{I}(\hat{x},\hat{p}) = \sqrt{\frac{\langle(\hat{x}_x+\hat{x}_y)^2\rangle\langle(\hat{p}_x-\hat{p}_y)^2\rangle}{|[\hat{x},\hat{p}]|^2}} \tag{5.27}$$

Using Eq. 5.23, 5.24 and 5.25, 5.26, the degree of inseparability for the quantum fluctuations of the observables of both beams thus becomes

$$\mathcal{I}(\delta\hat{x},\delta\hat{p}) = \frac{4N}{w_0^2}\sqrt{\langle\delta\hat{x}_1^2\rangle\langle\delta\hat{x}_2^2\rangle} = \sqrt{\langle\delta\hat{X}^{+^2}_{a_1}\rangle\langle\delta\hat{X}^{+^2}_{b_1}\rangle} < 1 \tag{5.28}$$

where we have chosen to combine two position squeezed beams, i.e. $\langle\delta\hat{X}^{+^2}_{a_1}\rangle < 1$ and $\langle\delta\hat{X}^{+^2}_{b_1}\rangle < 1$, position noise anti-correlations and momentum noise correlations are created[12] and $\mathcal{I}(\delta\hat{x},\delta\hat{p}) < 1$. We have proved here as in reference [Hsu05] that continuous variable EPR entanglement between two beams could be achieved. This is what we propose to demonstrate experimentally in the next sections.

B.2 Experimental setup

B.2.1 Optical layout

A complete diagram of the optical layout is presented in Fig. 5.9. Let us now present the main elements of this setup.

- The dual output laser source

[12] Combining two momentum squeezed beams for which $\langle\delta\hat{X}^{-^2}_{a_1}\rangle < 1$ and $\langle\delta\hat{X}^{-^2}_{b_1}\rangle < 1$, would result in position noise correlations and momentum noise anti-correlations are created.

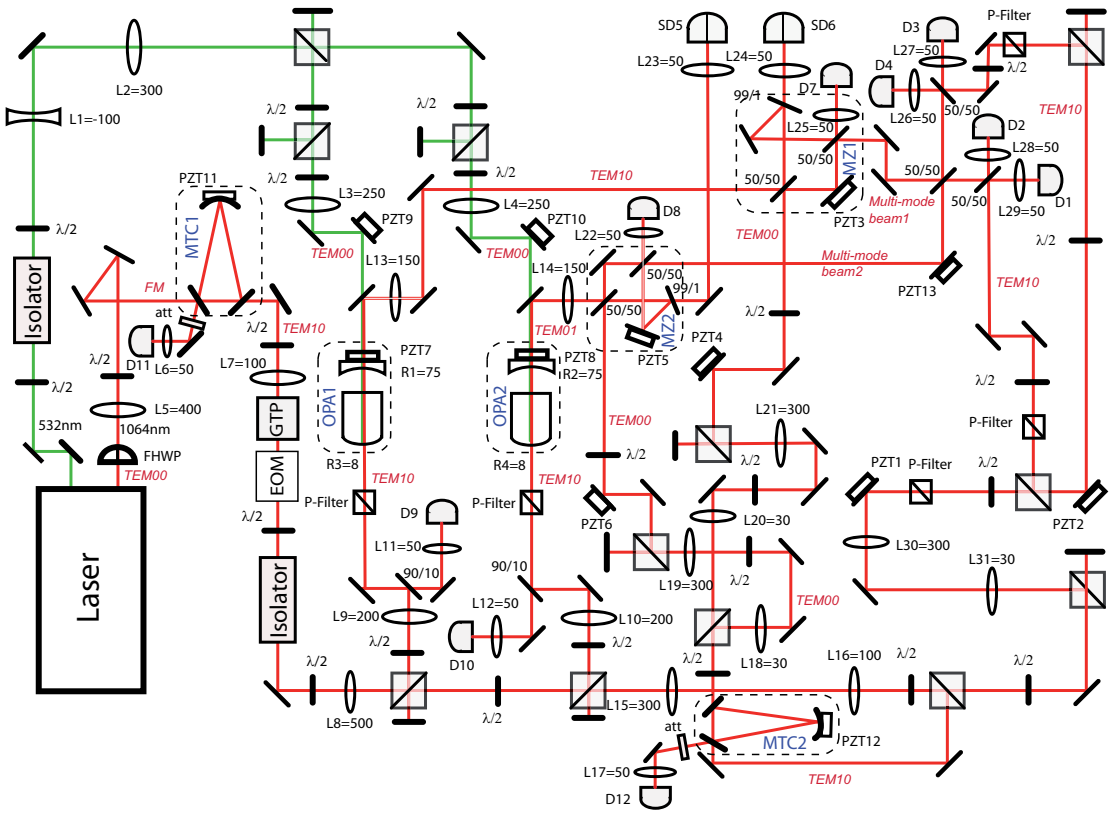

Figure 5.9: Experimental setup for spatial entanglement. D: detector, SD: split-detector, L: lens (focal length in mm), R: radius of curvature (in mm), FHWP: flipped mode half-waveplate, GTP: Glen-Thomson polarizer, EOM: electro-optic modulator, att: attenuator, P-Filter: polarization filter, PZT: piezoelectric device.

The laser source that has been used for this experiment is the same dual-output Diabolo laser as the one used in section 4C. This device delivers two coherent output TEM_{00} beams, 195 mW of infrared power at 1064 nm, and 950 mW of green at 532 nm[13].

- The two Optical Parametric Amplifiers (OPA)

In order to produce the two TEM_{10} squeezed beams, we use two optical parametric amplifiers (OPA) seeded with TEM_{10} modes at 1064 nm, and pumped with TEM_{00} beams at 532 nm. A picture of a single OPA is represented in Fig. 5.10. The hemilithic OPA cavity design has been improved from the one presented in section 4C. The oven and the 2x2.5x6.5 mm^3 $LiNbO_3$ crystal - 7% MgO doped - are still identical. However, the optical length of the cavity has been increased to 90 mm, and the output coupler mount has been completely re-designed by Jiri Janousek, in order to increase the stability of the system. The PZT is spring-loaded in order to increase the resonance frequency of the mount, which results in an increase of the locking bandwidth from around 20 kHz to 60 kHz. A complete study of the influence of pre-loading on the PZT resonance can be found in reference [BowenPhD03]. With these cavity characteristics, the waist size of the infrared beam is 16 μm, and is located in the middle of the crystal.

[13]Note that this laser can have different power ratios according to the reflecting property of the beam-splitter used inside the laser box to pump the second harmonic generation cavity.

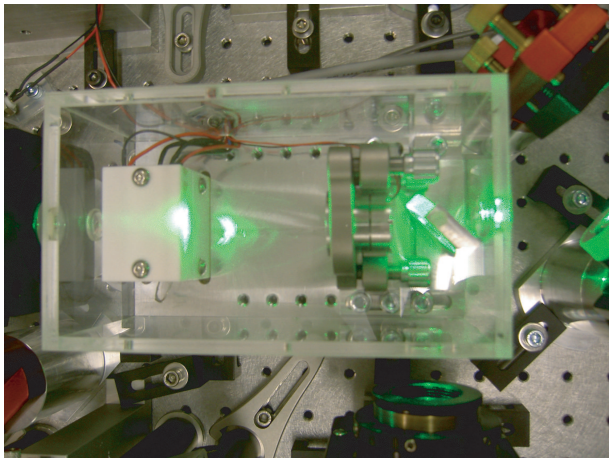

Figure 5.10: Picture of one of the two identical Optical Parametric Oscillators. On the left-hand side, only a white MACOR container maintaining the crystal in its oven is visible. The output coupler and the spring-loaded piezoelectric stack are located in the optical mount on the right part of the picture.

In this setup, we seed the OPA cavity with a TEM_{10} mode, rather than misaligning a TEM_{00} seed beam. The TEM_{10} beam is generated by a misaligned ring cavity with TEM_{00} input, locked to the resonance of the TEM_{10} mode. As explained in section 4A.2.2, we have introduced a special wave-plate, referred to as a *flipped mode waveplate*, in order to improve the conversion efficiency from the TEM_{00} laser output mode into a TEM_{10} mode. This mode transferring cavity (MTC_1) acts also as a mode cleaning cavity, thus delivering a pure TEM_{10} output mode, shot noise limited above 1.5 MHz. The infrared TEM_{10} mode thereby produced is used not only to seed both OPAs, but also as local oscillators for both homodyne detections, and also to create the two carrier TEM_{00} beams using another mode transferring cavity, as we will explain later.

As described in section 4C, we lock the OPA cavity on resonance with the TEM_{10} mode[14], and then we use a TEM_{00} pump beam. We found that a good compromise between

[14]We should mention here an experimental complication that arose. Unlike the mode converting ring cavities which we presented in section 4A.2.2 which have non degenerate x and y axes, the linear OPA cavity has close to cylindrical symmetry. As a consequence, TEM_{10} and TEM_{01} modes can be simultaneously resonant in the OPA cavity. This causes dramatic effects on the orientation of the two lobes of the output mode, when either the seed or the cavity itself is not perfectly aligned. This effect was clearly occurring for OPA_2, but not for OPA_1 (was it better aligned, or were the crystal and output coupler fortunately not of cylindrical symmetry?). We noticed that even a small amount of coupling in the TEM_{01} component (it is difficult to estimate the minimum amount of this component we were producing) was inducing a clear - visible to the eye - rotation of the beam, and thus a large drop in the efficiency of the whole setup which needed to be operated with pure TEM_{10} modes. We also noticed that this rotation effect was very sensitive to the crystal temperature. A temperature change of 0.05 degrees only could have such large effects as the drop of the visibility with the TEM_{10} local oscillator by more than 20%. A possible explanation is that the x-y degeneracy is raised when the crystal temperature is changed, due to the anisotropy in the crystal itself. For some crystal temperature regions, both TEM_{10} and TEM_{01} resonance peaks are separated enough, and both modes are not simultaneously resonant anymore. The solution we found was to operate the OPA in this non degenerate temperature range. The trade-off was that this temperature was not perfectly corresponding to the optimum phase matching temperature. Nevertheless, we noticed that it was preferable to operate the OPA with less de-amplification and a pure mode, than at best de-

the amount of squeezing and the noise induced by a high power pump, was to operate OPAs with the following power : P_{pump_1}=90 mW and P_{pump_2}=200 mW. The discrepancy between the two pump powers arises from the impossibility to run OPA_2 at exact phase matching temperature, as discussed in the previous footnote. In this regime, amplification and de-amplification were respectively 4 and 0.44 for OPA_1, and 3.5 and 0.57 for OPA_2. The phase matching crystal temperatures were found to be 61.45°C and 59.60°C, respectively. In order to produce amplitude squeezed TEM_{10} beams, we locked the phase of the green pump to de-amplification. Note that for the following parts of the experiment where we required two squeezed beams of identical power[15], we adjusted both seed beam powers so that the squeezed beam powers were equal to P_{SQZ_1}=P_{SQZ_2}=320 μW[16]. The generated squeezing and anti-squeezing spectra of both OPAs can be found in Fig. 5.11a)[17]. Each spectrum analyzer trace of 2000 points corresponds to the average of 50 traces, and was taken with a sweep time of 100 ms, a resolution bandwidth RBW=300 kHz, and a video bandwidth VBW=300 Hz[18]. The large modulation peaks visible on the spectra correspond to beating between phase modulations generated for locking purposes[19]. In order to characterize our sources, we have also represented in Fig. 5.11b) the purity, i.e. the product $\langle \delta\hat{X}^{+^2} \rangle \langle \delta\hat{X}^{-^2} \rangle$, of the states produced by OPA_1 and OPA_2 as a function of frequency, where the squeezing and anti-squeezing spectra are corrected for losses after the output of the OPAs, and taken from Fig. 5.11a).

- The two TEM_{00} carrier beams

The reference for position and momentum of each beam is provided by two TEM_{00} carrier beams. They are simply generated and filtered[20] with a second mode transferring cavity (MTC_2), identical to the first one (MTC_1), whose operation has already been described in section 4A.2.2. The cavity converts the TEM_{10} mode coming from the MTC_1 into a TEM_{00} mode beam, which is then equally split into two carrier beams and sent to the two Mach-Zehnders. The power of the carrier beams is chosen to be $P_{carrier_1}$=$P_{carrier_2}$=1.6 mW, in order to be large relative to the squeezed TEM_{10} beam power[21].

- The two special Mach-Zehnders

amplification and a non-pure mode. This technical problem explains the discrepancy between the optimal operating conditions of both OPAs. Note that a solution to prevent this phenomenon to occur, would be to manufacture the crystal or the output coupler purposely with slightly different radius of curvature along the x and y axis, in order to force the non-degeneracy along identifiable directions.

[15] This requirement is crucial for the locking of the two position squeezed beams in quadrature, in order to produce good entanglement.

[16] This power was the smallest power compatible with the stability of all the locking loops.

[17] Note that the curves presented here are not raw data, as they have been taken with the entire setup on the optical table. The losses induced by the Mach-Zehnder interferometer - 98% visibility -, the homodyne detection - 96% visibility -, the 96% photo-detection efficiency, and foremost the 50% loss on the entanglement beam-splitter have been corrected. We have also corrected the traces for electronic noise, which was around 5 dB below the shot noise level.

[18] These spectrum analyzer settings have been kept for all the traces presented in this section, and will therefore not be mentioned again.

[19] A list of the modulation frequencies is given in table B.2.2. The peak at 4 MHz arises, for example, from a beating between the 16 MHz and 12 MHz modulations.

[20] The output mode of the laser needs to be spatially and spectrally filtered and could not have been used directly here.

[21] Ideally, the power of the carrier beams would be much larger, but the carrier beams must also have little power compared to the local oscillator beams. The beams power are all chosen limited by the saturation of the homodyne detectors.

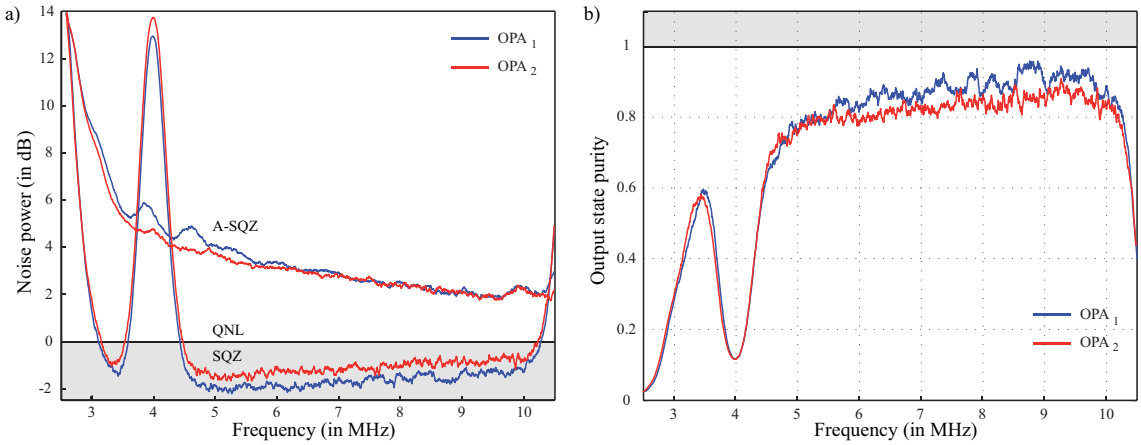

Figure 5.11: a) Squeezing and anti-squeezing spectra of OPA_1 (blue trace), and OPA_2 (red trace). The spectra have been back inferred from measurements using the whole setup, and have been corrected for electronic noise. b) Purity of the states generated at the output of OPA_1 (blue trace), and OPA_2 (red trace). Both curves have been corrected for losses after the output of the devices. Resolution and video bandwidth were set to 300 kHz and 300 Hz respectively.

Each Mach Zehnder interferometer has one additional mirror in one of the arms, in order to combine without loss the TEM_{00} carrier beam and the squeezed TEM_{10} beams, as explained in section 4A.3.2. We recall that this method relies on the different parity of the two transverse modes to be combined, in this case the TEM_{00} and TEM_{10} modes. Similarly to what has done in section 5 A, each interferometer is first aligned on the squeezed TEM_{10} beam[22], as we want to minimize losses on this particular beam. For both interferometers, a fringe visibility of 98 % was achieved[23]. We then aligned the TEM_{00} carrier beam with the TEM_{10} squeezed beam on the first beam-splitter of the interferometer. As both beams would not interfere on the beam-splitter as they are orthogonal, we temporarily locked the mode transferring cavity (MTC_2) to the TEM_{10} mode in order to perform the alignment of the carrier beams[24]. Note that the relative phase between the two beams circulating in each arm is not imposed yet. However, as explained in section 4A, this relative phase determines which spatial quadrature of the beam is squeezed. In order to lock this relative phase, denoted ϕ_{rel} in Fig.5.7, we have replaced one of the mirrors by a dichroic mirror in one arm of the interferometer. This dichroic mirror has been preferred to a weak transmission mirror as it allows tunable transmission relative to the angle of incidence of the beam [25]. We therefore managed to tune the dichroic angle in order to have only 1% of the light transmitted through, in order not to alter the squeezing circulating in the interferometer. This low power beam is then incident on a split-detector to lock the relative phase between

[22]Note that we increased the seed power in order to have a better accuracy during all alignments, as the TEM_{10} beams coming out of the OPAs are very dim (320 μW).

[23]This visibility dropped to less than 80 % in MZ_2 when the crystal temperature was not well optimized, because of the problem we mentioned earlier in OPA_2.

[24]This required in practise to change slightly the alignment of the input beam of MTC_2.

[25]This angle value was around 22°, and does not correspond to angles for which coatings are conventionally made.

TEM_{00} and TEM_{10} beams[26]. Strictly speaking, the generation of two position-squeezed beams would require an adjustment of the locking system [27] so that the TEM_{00} and TEM_{10} components of each beam are in phase in the plane defined by the entanglement beam-splitter. However, as stated earlier, the generation of spatial entanglement, that is, entanglement of two spatial quadratures of the beam, is possible as long as the relative phases between the two components of each beams are identical, i.e. $\phi_{\mathrm{rel}_1} = \phi_{\mathrm{rel}_2}$. As all beams are collimated to a beam radius of about 2 mm, Gouy phase shifts between the two different components[28] only occur between the split-detectors and the focusing lens which are used to match the size of the beams to the two pixel detectors. We have therefore carefully positioned both split-detectors at the same distance away from their focusing lens.

Two non classical beams with identical properties have thus been separately generated[29].

- The entanglement beam-splitter

Both non classical beams are combined on the 50/50 entanglement beam-splitter. In order to perform the alignment of these two beams, the TEM_{00} components are blocked, and the TEM_{10} components are aligned. We obtained a fringe visibility of 98%. The two output beams thereby generated are entangled when the relative phase between the two position-squeezed beams, denoted ϕ_{E}, is locked to $\phi_{\mathrm{E}} = \pi/2$. This phase was locked using DC locking with the difference between the sum of the homodyne detectors : $[D_1 + D_2] - [D_3 + D_4]$, as reported in table B.2.2.

- The two TEM_{10} homodyne detectors

Both homodyne detections have a bright TEM_{10} local oscillator, which is aligned to the entangled beams when all but one TEM_{10} component are blocked. The power of the local oscillators was set to P_{LO_1}=P_{LO_2}=6 mW, in order to be simultaneously large relative to the power of the squeezed TEM_{10} and TEM_{00} beams, without reaching the saturation of the homodyne detectors. Both homodyne detections were limited to a fringe visibility of 96% at this stage of the experiment. The local oscillator beams were slightly spatially distorted because of the number of optics they had to go through before interfering on the homodyne beam-splitter[30].

B.2.2 Electronic layout

One of the major difficulties encountered in the experiment was the simultaneous stability of the 13 locking loops. We have presented the specifications of each of them in table B.2.2. It lists the detectors, names of the locking servo, DC locking or AC locking system using Pound Drever Hall (PDH) technique [Drever83, Pound46] with a high frequency modulation, and piezoelectric device, referenced according to the notations introduced in Fig. 5.9.

[26] Note that a conventional detector does not allow such a locking as both beams are orthogonal for complete transverse detection. This justifies the necessity of the use of a measuring device for which both modes are not orthogonal.

[27] We will come back to the details of this locking method later on in section 5B.2.2.

[28] This phenomenon is detailed in section 1A.2.6.

[29] We will often improperly term them position-squeezed beams for simplicity in the following section, even if the relative phase between the TEM_{00} and TEM_{10} components is not necessarily zero.

[30] This problem has been solved recently by adding another mode-cleaning ring cavity common to both local oscillator beams. This allowed to reach a fringe visibility of 98 %.

Detector	Name	AC/DC	modulation for PDH	PZT
$D_1 - D_2$	LO$_y$ ($\hat{X}^+$)	AC	360 kHz	PZT$_1$
	LO$_y$ ($\hat{X}^-$)	DC	$\emptyset$	
$D_3 - D_4$	LO$_x$ ($\hat{X}^+$)	AC	177 kHz	PZT$_2$
	LO$_x$ ($\hat{X}^-$)	DC	$\emptyset$	
$[D_1 + D_2] - [D_3 + D_4]$	Ent	DC	$\emptyset$	PZT$_{13}$
SD$_{5_{\text{right}}}$-SD$_{5_{\text{left}}}$	SD$_2$	DC	$\emptyset$	PZT$_6$
SD$_{6_{\text{right}}}$-SD$_{6_{\text{left}}}$	SD$_1$	DC	$\emptyset$	PZT$_4$
D$_7$	MZ$_1$	AC	373.6 kHz	PZT$_3$
D$_8$	MZ$_2$	AC	317.4 kHz	PZT$_5$
D$_9$	OPO$_1$	AC	16 MHz	PZT$_7$
	Green$_1$	AC	1 MHz	PZT$_9$
D$_{10}$	OPO$_2$	AC	16 MHz	PZT$_8$
	Green$_2$	AC	1 MHz	PZT$_{10}$
D$_{11}$	MTC$_2$	AC	12 MHz	PZT$_{11}$
D$_{12}$	MTC$_1$	AC	16 MHz	PZT$_{12}$

Table 5.1: List of locking loops and their related information. For each servo loop, we list a correspondence between locking detectors, names to which we refer every locking loop, type of locking (AC or DC) with the modulation frequency used for Pound Drever Hall (PDH) locking if relevant, and PZTs. All the notations used in the table have been introduced in Fig.5.9. The mention ($\hat{X}^+$) or ($\hat{X}^-$) refers to the quadrature which is measured by the homodyne detections, respectively amplitude and phase quadratures.

The notation ($\hat{X}^+$) or ($\hat{X}^-$) refers to the quadrature which is measured by the homodyne detections, the amplitude and phase quadratures respectively. As we will explain later, the inseparability measurements require us to successively measure correlations and anti-correlations between homodyne detection signals when the phases of the local oscillator are locked to the phase and amplitude quadratures, respectively. In order to make clear the combinations of the signals recorded by the homodyne detectors, and then used either for locking or measuring quantum correlations Fig. 5.12 has been included. The different locking systems can be grouped into 4 categories.

The first category is the conventional PDH locking [Drever83] using an external phase modulation reflected by an optical cavity (MTC$_1$, MTC$_2$, OPO$_1$, OPO$_2$, Green$_1$, Green$_2$).

The second one corresponds to dark - or bright - fringe locking in a low finesse interferometer [Bachor03]. A technique very similar to PDH locking is used, where a high frequency phase modulation is applied, in one arm of the interferometer, on the same PZT that is used to lock the interferometer (MZ$_1$, MZ$_2$, LO$_x$ ($\hat{X}^+$), LO$_y$ ($\hat{X}^+$)).

The third one corresponds to half-fringe locking in a low finesse interferometer [Bachor03]. The error signal is here directly generated with the subtraction of the DC intensities from the output ports of the interferometer (Ent, LO$_x$ ($\hat{X}^-$), LO$_y$ ($\hat{X}^-$)). Note that the locking of the relative phase between the two non-classical beams before the entanglement beam-splitter requires excellent symmetry in the setup between the intensity of the beams in each half of the setup. Indeed, the error signal (Ent) resulting from the combination

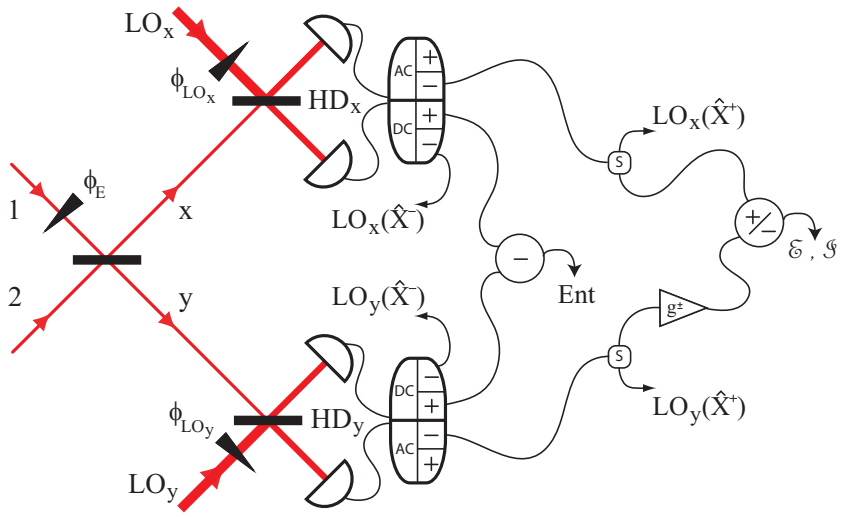

Figure 5.12: Cabling of homodyne detections in order to lock and perform entanglement measurements ($\mathcal{E}$,$\mathcal{I}$). Five locking loops are monitored using sum and differences of homodyne DC and AC signals : LO_x and LO_y either locked on amplitude ($\hat{X}^+$) or phase ($\hat{X}^-$) quadratures, and relative phase between the two beams incident on the entanglement beam-splitter (Ent).

$[D_1 + D_2] - [D_3 + D_4]$ will be centered on a zero value only if the power of both local oscillators, both carrier beams, and both squeezed beams are carefully matched.

The last category involves split-detectors and deserves special attention. The subtraction of the DC intensity between right and left parts of the split-detectors provides an error signal that can be used to lock the relative phase ϕ_{rel} between the two incident beams, namely the TEM_{00} carrier and the TEM_{10} squeezed beams. Such an error signal allows to lock the relative phase to $\phi_{\mathrm{rel}} = \pi/2$, i.e. to lock the two modes in quadrature *in the split-detector plane*. The generation of two position-squeezed beams would require us to lock the TEM_{00} and TEM_{10} components in phase *in the entanglement beam-splitter plane*[31]. We would either need to apply a DC offset to the error signal in order to modify the locking point in the relative phase, or find an imaging system on the split-detectors which is not introducing any Gouy phase shift. Nevertheless, as we have stated earlier in section 5B.1.2, it is not necessary to produce two-position squeezed beams. As long as the relative phases between the TEM_{00} and TEM_{10} components are identical, i.e. that the imaging systems on the split-detectors are rigourously identical, spatial entanglement can be fully observed. We have therefore simply locked the two components of each beam in quadrature in the split-detectors plane.

[31] Because of the Gouy phase shift, both TEM_{00} and TEM_{10} modes accumulate different phase shift when propagating from the detector plane to the entanglement beam-splitter plane, as we have discussed earlier in section 4A.1.1.

B.3 Experimental results

B.3.1 TEM_{10} mode quadrature entanglement

Before presenting the full operating system, we have first demonstrated TEM_{10} quadrature entanglement. To our knowledge, this is the first experiment of quadrature entanglement for higher order Hermite Gauss modes.

The schematic of this experiment corresponds exactly to the one presented in Fig. 1.4 with TEM_{10} modes replacing the TEM_{00} modes. To match this scheme with our setup represented in Fig. 5.7, we simply blocked both carrier beams, and left everything else unchanged. This experiment provides an important step towards the generation of spatial entanglement, as it provides a calibration of the entanglement source.

We first investigated the degree of inseparability of the two beams generated at the output of the entanglement beam-splitter. This involves the measurement of $\Delta^2\hat{X}^+_{x+y} = \langle\left(\delta\hat{X}^+_x + \delta\hat{X}^+_y\right)^2\rangle/2$ and $\Delta^2\hat{X}^-_{x-y} = \langle\left(\delta\hat{X}^-_x - \delta\hat{X}^-_y\right)^2\rangle/2$, for two incident amplitude squeezed beams, as explained in section 1A.3.4. $\Delta^2\hat{X}^+_{x+y}$ corresponds to the quantum noise measured with the sum of the two homodyne detections subtracted AC outputs, when both homodyne detections locked to amplitude quadratures, whereas $\Delta^2\hat{X}^-_{x-y}$ corresponds to the quantum noise measured with the difference of the two homodyne detections subtracted AC outputs, when both homodyne detections locked to phase quadratures. The cabling to perform these successive measurements is shown in Fig. 5.12 (in both cases, $g^{\pm} = 1$). The results normalized to the shot noise are presented in Fig. 5.13. $\Delta^2\hat{X}^+_{x+y}$ and

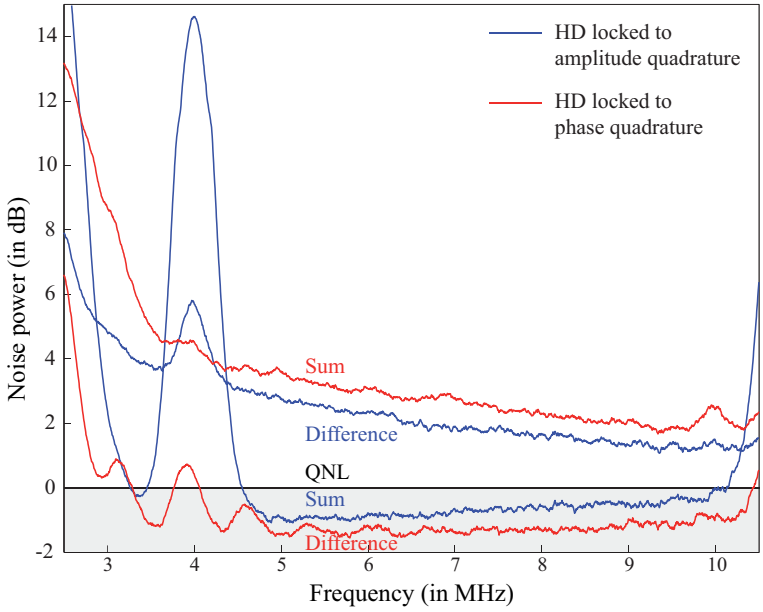

Figure 5.13: Noise spectrum of sum and difference of homodyne detection (HD) signals when the HD are locked to amplitude (blue) or phase (red) quadratures. $\Delta^2\hat{X}^+_{x+y}$ and $\Delta^2\hat{X}^-_{x-y}$ correspond to the red and blue curves below the quantum noise limit (QNL), respectively.

$\Delta^2\hat{X}^-_{x-y}$ correspond to the blue and red curves below the quantum noise limit (QNL), respectively. This noise reduction below the quantum noise limit is the signature that the

two beams generated after the entanglement beam-splitter are indeed entangled. We have also measured $\Delta^2\hat{X}^+_{x-y}$ and $\Delta^2\hat{X}^-_{x+y}$, which correspond to the blue and red curves above the quantum noise limit (QNL). They show excess noise as expected from measurements of orthogonal quadratures of sub-QNL entities[32].

Let us now quantify the entanglement produced between the two quadratures of the TEM_{10} modes. We have presented the two most commonly used criteria in section 1A.3.4, and propose to apply them to our experimental results.

We first concentrate on the inseparability criterion. The results are presented in Fig. 5.14. The blue trace shows the measured[33] degree of inseparability using the product

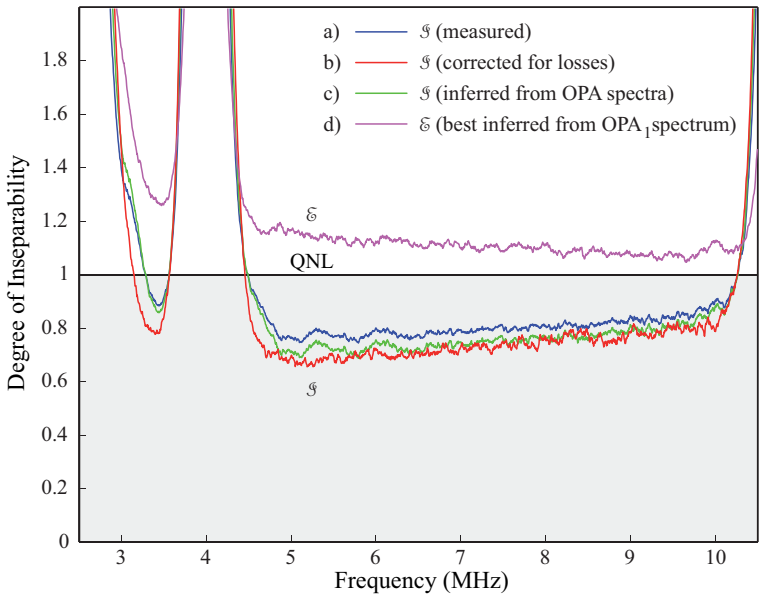

Figure 5.14: Degree of inseparability $\mathcal{I}$, a) measured, b) corrected for losses, c) inferred from OPA_1 and OPA_2 spectra, and degree of EPR paradox $\mathcal{E}$, d) inferred assuming two spectra similar to OPA_1. The degree of inseparability of the beams produced experimentally is clearly below 1, i.e. the quantum noise limit (QNL) that would be obtained with coherent incident fields. However, the states produced do not show any EPR paradox, as $\mathcal{E}$ is always above 1.

form[34], i.e. $\mathcal{I} = \sqrt{\Delta^2\hat{X}^+_{x+y}\Delta^2\hat{X}^-_{x-y}}$. The best measured inseparability value is $\mathcal{I} = 0.76 \pm 0.02$ and is obtained at around 5 MHz. We have also plotted in Fig. 5.14 the degree of inseparability, corrected for losses, in green. The trace is calculated using Eq. 1.77, with a detection efficiency on a single beam given by $\eta = 0.81$. This estimation of the detection efficiency is calculated as follows $\eta = \eta_{MZ}.\eta_{Ent}.\eta_{HD}.\eta_{det}$, where $\eta_{MZ} = (0.98)^2$ is the trans-

[32] The results presented here are preliminary and are being improved. The modulation peak at 4 MHz is clearly visible only on the two curves taken when the homodyne detections were locked to the amplitude quadratures. This shows that at least one locking loop was not perfectly optimized and could potentially be improved. As a consequence, the two corresponding traces are not as far apart from each other, compared to the traces taken when the homodyne detections were locked to the phase quadratures.

[33] This value has just been corrected for electronic noise, and taken directly from the traces shown in Fig. 5.13.

[34] We could have plotted any of Duan or Mancini's inseparability criteria, as both states produced by the OPAs are alike.

mission of the Mach-Zehnders as the fringe visibility of both interferometers was 98%, $\eta_{\text{Ent}} = (0.98)^2$ is the entanglement beam-splitter efficiency as the fringe visibility between the two squeezed beam was 98%, where $\eta_{\text{HD}} = (0.96)^2\%$ is the homodyne detections efficiency as the fringe visibility with the local oscillator was 96%[35], and where $\eta_{\text{det}} = 0.96$ is the photo-detection efficiency[36]. The degree of inseparability corrected for losses, which corresponds to the blue trace b), goes down to $\mathcal{I} = 0.71 \pm 0.02$. This value can be compared with the value inferred from the spectra of OPA_1 and OPA_2 presented in Fig. 5.11a), using Eq. 5.28. The calculated red trace c) is only slightly below the previous one, meaning that our system, and especially the locking of the different phases, is reliable.

Let us now try to apply the EPR criterion to our setup. The measurement of this quantity requires the optimization of a gain parameter $g^{\pm}$ using a variable attenuator[37]. Before such an optimization, we have inferred the best values of $\mathcal{E}$ that could be generated using our two sources, given their non classical properties. We have seen in section 1A.3.4 that not only the squeezing level was important but also the purity of the two squeezed states used to generate the entanglement. We have therefore calculated the spectrum d) shown in Fig. 5.14, using Eq. 1.80, and assuming that both sources had the squeezing and anti-squeezing properties of OPA_1, given in Fig.5.11a). The values of $\mathcal{E}$ are all clearly above 1, with a lowest value of 1.1 ± 0.02 being found at around 9.5 MHz. As explained in section 1A.3.4, the degree of EPR paradox $\mathcal{E}$ is more restrictive when it comes to quantify entanglement. In particular, it is very sensitive to the purity of the states used to generate the entanglement. Unfortunately, as shown on both spectra presented in Fig. 5.11b), the states generated by our OPAs are far from pure at the best squeezing performances of the device. The best purity is found at around 9 MHz and equals 1.2 ± 0.1 for OPA_1. However, at this frequency, the squeezing is low, and not sufficient to give a value of the degree of EPR paradox below 1. The OPAs are now being re-designed in order to produce more squeezing with PPKTP crystals.

We have been able to generate TEM_{10} quadrature entanglement, and characterized the quantum correlations between the two output beams using the inseparability criterion, yielding a measure of the degree of inseparability of $\mathcal{I} = 0.76 \pm 0.02$.

B.3.2 Towards spatial entanglement

The major difficulty of the spatial entanglement experiment is the TEM_{10} entanglement source, and has already been demonstrated in the previous section. The operation of the entire experiment as shown in Fig. 5.9 requires the addition of the two TEM_{00} carrier beams. Two position-squeezed beams now need to be combined on the entanglement beam-splitter, instead of two amplitude squeezed TEM_{10} mode beams. This addition greatly increases

[35] As stated earlier, this relatively low fringe visibility has been brought up to 98% in the current apparatus by the addition of a mode-cleaning cavity on the local oscillator path. Indeed, this latter was distorted because of the high number of lenses it was going through.

[36] It is very difficult to estimate the absolute value of the photo-detector efficiency, as it would require an absolute power meter. The number provided here is an estimation of the efficiency of the ETX-500 photo-diodes we used in our setup.

[37] This method allows a direct measurement of the degree of EPR paradox, in real time, on the spectrum analyser, but is difficult to implement, as it requires to re-measure the shot noise level for each attenuation value in order to find the optimum configuration. A data acquisition system can also be used to record individual homodyne detection signals, and the optimal gain can be found by post processing the data.

the complexity of the experiment, as it requires the implementation of one additional mode converting ring cavity, two Mach-Zehnder interferometers and the locking of the two relative phases between TEM_{00} and TEM_{10} components. However, it is important to realize that we do not expect any modification to the correlations between the measured signals on the homodyne detectors compared to the experiment detailed in the previous section! Indeed, the TEM_{00} mode is orthogonal to the TEM_{10} local oscillator, and should therefore not modify the non-classical properties lying in the TEM_{10} component of the field. We have first demonstrated that the homodyne detection of a single position-squeezed beam (in presence of the TEM_{00} carrier beam) gives identical noise reduction below the QNL to the homodyne detection of a single squeezed TEM_{10} mode beam. This comparison is shown in Fig. 5.15. Both spectra, after normalization to the shot noise, show perfect

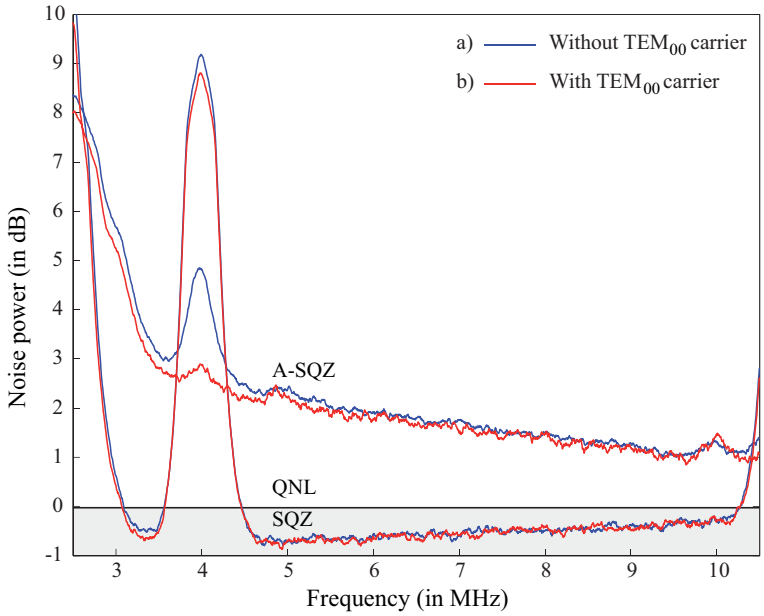

Figure 5.15: Squeezing (SQZ) and anti-squeezing (A-SQZ) noise spectra, normalized to the shot noise (QNL), of a single TEM_{10} beam a) without, and b) with TEM_{00} carrier beam. The presence of the carrier beam is not modifying the quantum properties of the TEM_{10} component of the beam.

agreement [38]. The shot noise is modified between the two cases by the contribution of the TEM_{00} carrier beam, whose power, as stated earlier[39], is not totally negligible relative to the local oscillator power. The absence of cross-talk between the orthogonal modes shows the quality of our experiment. Any drop in a fringe visibility would indeed couple some of the TEM_{00} power into the TEM_{10} component and reduce the amount of squeezing.

These results show the feasibility of the spatial entanglement, and we expect a similar degree of inseparability as obtained in the previous section, since we have shown that the presence of the TEM_{00} carrier beams did not modify the non-classical properties of the

[38] The results obtained without the presence of the carrier even have slightly less squeezing and slightly more anti-squeezing than in the presence of the carrier. This can be explained by the imperfect cancelation of the modulation peak at 4 MHz in the trace without the carrier, testifying that the locking to de-amplification was not perfect during this measurement.

[39] We recall that P_{SQZ}=320 μW, $P_{carrier}$=1.6 mW and P_{LO}=6 mW).

TEM_{10} components of the beam.

The final operation of the experiment is now being done, and has not been finished at the current stage of this thesis yet.

C Conclusion

In this chapter, we have presented two complete quantum imaging experiments involving bi-modal fields, namely a bright TEM_{00} carrier beam and a dim squeezed TEM_{10} mode, which are related to the displacement and tilt of a laser beam. Our experimental results have clearly shown that position and momentum of a TEM_{00} beam were conjugated observables. In order to witness this property, we have proposed a new scheme, which was proven to be optimal in the previous chapters, to detect these variables. The major achievements are the demonstration of displacement measurement below the standard quantum noise limit, and the demonstration of quadrature entanglement in the TEM_{10} mode.

The experimental setup is now being modified in order to produce better non classical states in the TEM_{10} modes. The implementation of periodically poled KTP crystals is investigated. A natural next step to these results could then be to generalize them to the second dimension of the transverse plane similarly to what has been demonstrated in reference [Treps03].

Conclusion and perspectives

In this manuscript, we have proposed a broad study of quantum imaging in the continuous variable regime, and have focused our attention on the possibilities offered by experiments involving a small number of transverse modes. We have demonstrated all the key elements required in image processing experiments and in parallel quantum communication in the Hermite-Gauss mode basis: generation of squeezed and entangled states, modulation, combination, separation and detection of modes. These elements have already allowed us to perform sub-QNL measurements of specific spatial parameters : displacement and tilt.

Although experiments built with such blocks are scalable, we scarcely imagine to implement a setup involving more than a few transverse modes. However, the knowledge developed in the context of this thesis with relatively large components like cavities and interferometers now encourages to develop such elements as integrated components. A promising alternative is offered by periodically poled lithium niobate waveguides devices which are already converting, combining and separating TM_{nm} modes with high efficiency [Kurz03, Kurz04]. Nonlinear effects such as Second Harmonic Generation have been demonstrated [Kurz02], but no quantum correlations have been produced to our knowledge in these systems.

The first part of this thesis has provided an accurate definition of quantum multi-mode light with pure modes - the case of mixed modes remains to be considered. Moreover, for a given type of detection, we have identified a unique transverse mode within an optical image, denominated 'noise-mode of detection', which is contributing to the measured signal and noise. Filling this mode with squeezed light was shown to reduce quantum fluctuations in the measurement below the standard quantum noise limit. As such, we have analyzed in great detail the origin of quantum noise in a multi-pixel measurement. A natural continuation of this work will be to study the optimization of the gain configuration with respect to the signal to noise ratio in such measurement.

The previous result has motivated the proposition of implementing array detectors in optical disc devices in order to distinguish bit sequences at the shot noise level. The model was at this stage limited to a paraxial illumination. Experiments and theoretical developments will be investigated in order to establish a clear relation between diffraction limit and quantum noise limit.

We have then presented the question raised by the definition of the noise-modes of detection regarding the optimal extraction of information from an optical image. This very general theoretical analysis has identified the bound imposed by quantum noise on any intensity or quadrature measurement. We have proposed two practical schemes performing

at this level, which are termed 'optimal'. This analysis was restricted to coherent states and a specific class of non-classical states and we wish to extend the results and allow spatial correlations in transverse plane of the optical image.

In a more experimentally oriented part, we have established a link between Hermite Gauss modes and simple physical parameters of optical beams, displacement and tilt. Moreover, we have detailed their manipulation and presented all the 'building blocks' required to a quantum imaging experiment involving Hermite-Gauss modes. A similar analysis with Laguerre-Gauss modes has been initiated. These developments have necessitated a multi-mode study of SHG and OPA operation in order to produce squeezing in the TEM_{10} and TEM_{20} modes, and which has given interesting results. The multi-mode OPA operation out of the thin crystal approximation remains to be investigated, as it might help understanding the higher losses observed for higher order modes.

Finally, we have generated the first entanglement of higher order Hermite Gauss modes, towards the demonstration of spatial entanglement. Such a scheme could be used as an entanglement source for teleportation or dense coding of displacement and tilt modulations encoded onto a TEM_{00} beam. However, prior to any new experiment, we are currently investigating for the possibility of using periodically poled material in our setup in order to improve its performance. The production of larger noise reductions in the TEM_{10} mode would lead to a degree of EPR paradox smaller than 1, inaccessible at this stage.

What we have demonstrated until now is quadrature entanglement between two single-mode or two bi-mode fields. However the entanglement is until now always generated between modes of identical profiles. We wish now to go one step further and to seek entanglement between quadratures of different modes. This would require a transfer of quantum properties from one spatial mode to another mode. Such a demonstration would increase even more the possibilities offered by optical images.

Similarly to what has been studied with light beams, a multi-mode analysis of low density atom clouds and Bose-Einstein condensates could also be conducted. We wish in the future to consider interaction between optical images with these systems, and study the spatial effects generated by such interaction.

Appendix

A Array detection: two-zone case

A.1 Gain optimization

We have so far limited our analysis to a given configuration of the gains. We will now demonstrate which gains one has to choose to optimize a measurement in the two-zone case, i.e. when we use only two different gains g_1 and g_2 for the whole set of pixels. We will finally prove the efficiency and the experimental advantages of the provided solution, which corresponds to a *difference measurement*, introduced in section 1C.5.2.

Let us consider two detection areas D_1 and D_2 paving the entire transverse plane. The measurement is described by

$$N_{g_1,g_2} = \left[g_1 N(D_1) + g_2 N(D_2)\right] \quad \text{with } \{g_1, g_2\} \in \mathbb{R}^2 \tag{A-1}$$

where g_1 and g_2 are the electronic gains respectively corresponding to D_1 and D_2, and where the mean number of photons detected on both detector are given by

$$N(D_1) = N \int_{D_1} v_0^*(\vec{r}) v_0(\vec{r}) d^2r \tag{A-2}$$

$$N(D_2) = N \int_{D_2} v_0^*(\vec{r}) v_0(\vec{r}) d^2r \tag{A-3}$$

where N is the total mean number of photons detected in the entire beam, and $v_0(\vec{r})$ is the mode carrying the mean field. The signal-to-noise ratio (SNR) of the measurement is given by :

$$SNR = \frac{N_{g_1,g_2}}{\sqrt{\langle \delta \hat{N}^2_{g_1,g_2} \rangle}}. \tag{A-4}$$

The modification of the SNR for a given variation of the image field directly maps the sensitivity of the measurement. In order to find the best possible set of gains corresponding to the maximal sensitivity, we propose to study the influence of a small transverse displacement $d\vec{\rho}$ of the beam on the SNR, according to the choice of the set of gains. We thus compute the values of g_1 and g_2 which optimize the variation of the SNR.

Let us first calculate the variation of the number of detected photons N_{g_1,g_2}, which is proportional to the measured intensity (we assume that the transverse displacement $\mathrm{d}\vec{\rho}$ of the image field is very small compared to the characteristic width of the beam). Using the

conventional vector integral properties, we get

$$\begin{aligned} d\hat{N}_{g_1,g_2} &= N\Big[g_1 \int_{D_1} v_0^*(\vec{r}+d\vec{\rho})v_0(\vec{r}+d\vec{\rho})d^2r + g_2 \int_{D_2} v_0^*(\vec{r}+d\vec{\rho})v_0(\vec{r}+d\vec{\rho})d^2r \quad \text{(A-5)} \\ &- g_1 \int_{D_1} v_0^*(\vec{r})v_0(\vec{r})d^2r - g_2 \int_{D_2} v_0^*(\vec{r})v_0(\vec{r})d^2r\Big] \\ &= N\Big[g_1 \oint_{C_{D_1}} v_0^*(\vec{r})v_0(\vec{r})d\vec{\rho}.\vec{ds} + g_2 \oint_{C_{D_2}} v_0^*(\vec{r})v_0(\vec{r})d\vec{\rho}.\vec{ds}\Big] \end{aligned}$$

where both integrals are calculated on the contour lines of D_1 and D_2, and where $\vec{ds}$ is the circulating unitary vector orthogonal to these contour lines. As D_1 and D_2 are complementary zones of the transverse plane, the first integral is the exact opposite of the second one because of the direction of $\vec{ds}$ during the calculation. Finally, we get

$$d\hat{N}_{g_1,g_2} = N(g_1 - g_2) \oint_{C_{D_1}} v_0^*(\vec{r})v_0(\vec{r})d\vec{\rho}.\vec{ds} \quad \text{(A-6)}$$

We can now evaluate the variation of the SNR when the beam is slightly displaced, assuming that the noise is not modified at first order:

$$dSNR = \frac{d\hat{N}_{g_1,g_2}}{\sqrt{\langle \delta\hat{N}^2_{g_1,g_2}\rangle}} \quad \text{(A-7)}$$

When the incident beam is in a coherent state, it yields :

$$dSNR = \frac{N_0(g_1 - g_2)}{\sqrt{g_1^2 N(D_1) + g_2^2 N(D_2)}} \oint_{C_{D_1}} v_0^* v_0 d\vec{\rho}.\vec{ds} \quad \text{(A-8)}$$

A simple calculation determines the values of g_1 and g_2 that maximize this ratio. They are given by :

$$g_1 = -g_2 \frac{N(D_2)}{N(D_1)} \quad \text{(A-9)}$$

which means that the optimum values of g_1 and g_2 are such as $\hat{M}(\{g_1, g_2\}) = 0$, i.e. a *difference measurement.*

This gain configuration is therefore nonetheless giving the best sensitivity, but is also ideal for classical noise cancelation, as discussed in section 1C.5.2. The general case for n zones will be investigated in further development of this work.

A.2 Non-differential measurement

In section 1C.5, we have exhibited the mode structure of the light in a multi-pixel measurement, using a basis that contain the detection mode. However, when the mean value of the measurement is different from zero, we have shown that this detection mode has a mean electric field value different from zero. In that configuration, it is very difficult experimentally to address the detection mode without modifying the mean field distribution. We have shown that the only basis pertinent for such a task was an eigen-mode basis, we will show here what is the structure of that basis for a two zone measurement of non-zero mean value.

Using the notations of the previous sections, we consider two detectors D_+ and D_- whose gains are respectively $+1$ and -1. We recall here the mode structure defined in the main text of that article. v_0 is the transverse mode carrying the mean field of the beam and w_1 is the detection mode as define in Eq. 1.149 (which, in that case is equivalent to the flipped mode of Eq. 1.140. w_0 is the mode orthogonal to w_1 in the subspace generated by v_0 and w_1. Let us call i_+ and i_- the partial integrals of v_0 on each zone,

$$i_+ = \int_{D_+} v_0^*(\vec{r}) v_0(\vec{r}) d^2r \quad \text{and} \quad i_- = \int_{D_-} v_0^*(\vec{r}) v_0(\vec{r}) d^2r$$

a simple calculation gives

$$\begin{aligned} w_0(\vec{r}) &= \sqrt{\frac{i_-}{i_+}} v_0(\vec{r}) \quad \text{if } r \in D_+ \\ w_0(\vec{r}) &= \sqrt{\frac{i_+}{i_-}} v_0(\vec{r}) \quad \text{if } r \in D_- \end{aligned} \tag{A-10}$$

The first mode of an eigen-basis for the field is v_0. The second one, v_1 is defined as the mode orthogonal to v_0 in the subspace generated by w_0 and w_1, its expression is found to be

$$v_1 \text{ such as } \begin{cases} v_1(\vec{r}) = w_0(\vec{r}) & \text{if } r \in D_+ \\ v_1(\vec{r}) = -w_0(\vec{r}) & \text{if } r \in D_- \end{cases} \tag{A-11}$$

As w_0 is orthogonal to w_1, which is the flipped mode of v_0, one can show that v_0 is orthogonal to v_1, which is the flipped mode of w_0 (see Fig. 6.1).

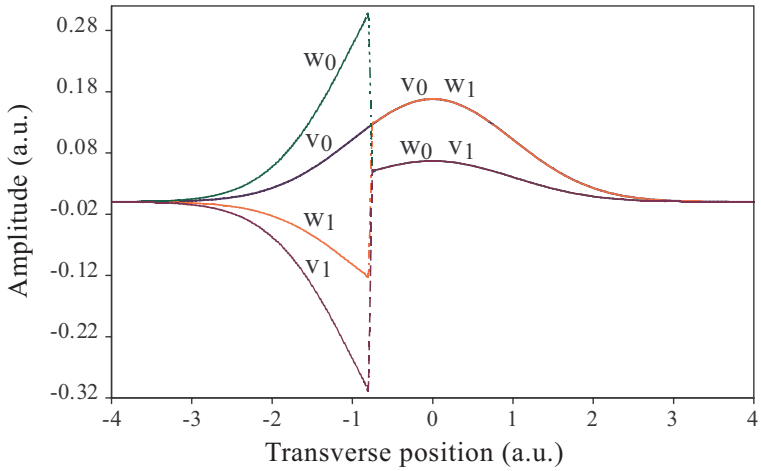

Figure 6.1: Example of a *generalized flipped mode* in the two zone case, when the gains are not equal.

In order to calculate the noise in the measurement using that basis, the flipped mode is expressed as a linear combinaison of the two first modes of the eigenbasis :

$$w_1(\vec{r}) = \alpha v_0(\vec{r}) + \beta v_1(\vec{r}) \tag{A-12}$$

where $\alpha = i_+ - i_-$ and $\beta = 2\sqrt{i_+ i_-}$, which leads to :

$$\langle \delta \hat{X}_{w_1}^{+^2} \rangle = \alpha^2 \langle \delta \hat{X}_{v_0}^{+^2} \rangle + \beta^2 \langle \delta \hat{X}_{v_1}^{+^2} \rangle + 2\alpha\beta \langle \delta \hat{X}_{v_0}^{+} \delta \hat{X}_{v_1}^{+} \rangle \tag{A-13}$$

where $\langle \delta \hat{X}^{+^2}_{w_1} \rangle$, $\langle \delta \hat{X}^{+^2}_{v_0} \rangle$ and $\langle \delta \hat{X}^{+^2}_{v_1} \rangle$ correspond to the noise of the amplitude quadrature of the component w_1 and v_0 and v_1, and where $\langle \delta \hat{X}^{+}_{v_0} \delta \hat{X}^{+}_{v_1} \rangle$ is the correlation term between the amplitude quadratures of components v_0 and v_1. Expressed in an eigenbasis, that do not contain the detection mode, we see that the noise arises from the individual noise of the two first modes and from their correlation function. In that basis, in order to reduce the noise we have several solutions : either the two first modes are perfectly squeezed, either they are perfectly correlated, or any solution in between. Anyway, we can assume that if we want to make a lot of different measurements, it is very difficult to produce correlation between the mean field and the different vacuum modes, hence the easiest solution is to have the mean field squeezed, and the corresponding vacuum squeezed. The same argument as before applies, and we show that we still need an extra mode for each extra information.

B Boyd-Kleinman's derivation of SHG with higher order Hermite Gauss modes

We present here the complete calculation of the SHG of higher order Hermite Gauss modes, using a generalization of the approach adopted by Boyd and Kleinman in reference [Boyd68]. The results have already presented and commented in section 4 B.3.1, and we will therefore only present here the calculations.

We recall that we make three main approximations in all our calculations. First, we consider negligible loss in the crystal for both the fundamental and second harmonic fields. This approximation allows a simplification of the calculations, and does not intrinsically modify the results, as we expect to have similar losses for all transverse modes. Secondly, we consider that the beam propagation axis z corresponds to the optical axis of the Type I nonlinear crystal and therefore omit any walk-off effect of the beams. Finally, we consider that the beam waist of the input beam is centered in the crystal. This corresponds to the optimum case and is generally adopted in the experiments.

We will first detail the case of a TEM_{00} pump mode in a type I crystal [Boyd68]. The results hereby obtained will be taken as a reference for a comparison with the TEM_{10} and TEM_{20} pump cases.

B.1 Calculation for the TEM_{00} pump mode

We start with a TEM_{00} pump mode as the fundamental field at frequency ω incident on the non linear crystal. We use two systems of coordinates (x',y',z') in the crystal, and (x,y,z) in the far field of the crystal. In the crystal, the field is written as

$$E_{\omega,00}(x',y',z') = E_\omega \frac{w_0}{w(z')} e^{-\frac{x'^2+y'^2}{w^2(z')} - ik_\omega z + i\Psi(x',y',z') + i\Phi_G(z')} \tag{B-1}$$

where k_ω[1] is the fundamental wave vector, w_0 is the fundamental waist inside the crystal, Ψ is the phase front curvature, Φ_G is the Gouy phase shift, $E_\omega = A\sqrt{2/\pi w_0^2}$ (where A is the amplitude of the beam), and given that $\tau' = z' = z'/z_R$ where z_R is the Rayleigh range,

$$w(z') = w_0\sqrt{1+\tau'^2} \tag{B-2}$$

$$\Psi(x',y',z') = \frac{k_\omega(x'^2+y'^2)}{2R(z')} = \frac{\tau'(x'^2+y'^2)}{w_0^2(1+\tau'^2)} \tag{B-3}$$

$$e^{i\Phi_G(z')} = e^{i\mathrm{arctan}(\tau')} = \frac{1-i\tau'}{\sqrt{1+\tau'^2}} \tag{B-4}$$

where $R(z')$ refers to the curvature of the phase front. Rearranging the previous field equation yields

$$E_{\omega,00}(x',y',z') = E_\omega \frac{e^{-\frac{x'^2+y'^2}{w_0^2(1+i\tau')}}}{1+i\tau'} e^{-ik_\omega z'} \tag{B-5}$$

[1] Note that in a type I phase matching case with $LiNbO_3$, the fundamental fields are polarized along the extraordinary axis, and $k_\omega = \frac{2\pi n_e(\omega,T)}{\lambda}$, where $n_e(\omega,T)$ is the extraordinary refractive index at frequency ω and temperature T.

The harmonic polarization is proportional to the electric field and can thus be written in the crystal as

$$\mathcal{P}(x',y',z') = \mathcal{P}_\omega \frac{e^{-2\frac{x'^2+y'^2}{w_0^2(1+i\tau')}}}{(1+i\tau')^2} e^{-i2k_\omega z'} \tag{B-6}$$

We now compute the harmonic field outside the crystal and therefore us the other coordinates (x,y,z),

$$E_{2\omega,00}(x,y,z) = A_{2\omega,00}(x,y,z)e^{ik_{2\omega}z} \tag{B-7}$$

The amplitude of this field can be integrated from the field contributions from slabs of thickness dz' inside the crystal

$$\begin{aligned} dA_{2\omega,00}(x',y',z') &= \frac{i4\pi\omega}{cn_o(2\omega,T)}\mathcal{P}(x',y',z')e^{ik_{2\omega}z'}dz' \\ &= \frac{i4\pi\omega}{cn_o(2\omega,T)}\mathcal{P}_\omega \frac{e^{-2\frac{x'^2+y'^2}{w_0^2(1+i\tau')}-i\Delta k z'}}{(1+i\tau')^2}dz' \end{aligned} \tag{B-8}$$

where $n_o(2\omega,T)$ is the refractive index at the second harmonic frequency 2ω, at temperature T, and where we have introduced the phase mismatch Δk defined by

$$\Delta k = 2k_\omega - k_{2\omega} = \frac{4\pi}{\lambda}\left[n_e(\omega,T) - n_o(2\omega,T)\right]. \tag{B-9}$$

If we want to compute the field outside the crystal, we need to know which part can propagate, i.e. the part of the field which is solution of the wave equation, and which can propagate. In order to identify this, we need to decompose $dA_{2\omega,00}(x',y',z')$ in the SH Hermite Gauss basis defined by the TEM_{pq} modes which have a fundamental waist equal to $w_0/\sqrt{2}$. Note that the Rayleigh range of the second harmonic (SH) modes is unchanged as $z_{R_{2\omega}} = \pi(w_0/\sqrt{2})^2/(\lambda/2) = \pi w_0^2/\lambda = z_{R_\omega}$. The expressions of the TEM_{00}, TEM_{10}, TEM_{20} and TEM_{40} modes of this basis are

$$u_{2\omega,00}(x',y',z') = \sqrt{\frac{2}{\pi w_0^2}}\sqrt{2}\frac{e^{-2\frac{x'^2+y'^2}{w_0^2(1+i\tau')}}}{1+i\tau'} \tag{B-10}$$

$$u_{2\omega,10}(x',y',z') = \sqrt{\frac{2}{\pi w_0^2}}\sqrt{2}\frac{2\sqrt{2}x'}{w_0(1+i\tau')}\frac{e^{-2\frac{x'^2+y'^2}{w_0^2(1+i\tau')}}}{1+i\tau'} \tag{B-11}$$

$$u_{2\omega,20}(x',y',z') = \sqrt{\frac{2}{\pi w_0^2}}\left[4\left(\frac{\sqrt{2}x'}{w_0\sqrt{1+\tau'^2}}\right)^2 - 1\right]\frac{(1-i\tau')}{(1+i\tau')}\frac{e^{-2\frac{x'^2+y'^2}{w_0^2(1+i\tau')}}}{1+i\tau'} \tag{B-12}$$

$$u_{2\omega,40}(x',y',z') = \sqrt{\frac{2}{\pi w_0^2}}\frac{1}{\sqrt{12}}\left[\frac{64x'^4}{w_0^4(1+\tau'^2)^2} - \frac{48x'^2}{w_0^2(1+\tau'^2)} + 3\right]\frac{(1-i\tau')^2}{(1+i\tau')^2}\frac{e^{-2\frac{x'^2+y'^2}{w_0^2(1+i\tau')}}}{1+i\tau'}$$

where each mode is normalized such as $\int\int |u_{2\omega,0n}(x',y',z')|^2 dx'dy' = 1$.

The field produced inside the the crystal in the slab of thickness dz', at position (x', y', z') can thus be written using a SH TEM_{00} component as follows

$$dA_{2\omega,00}(x', y', z') = \frac{i4\pi\omega}{cn_o(2\omega, T)}\mathcal{P}_\omega\sqrt{\frac{\pi w_0^2}{2}}\frac{u_{2\omega,00}(x', y', z')}{\sqrt{2}(1+i\tau')}e^{-i\Delta kz'}dz' \quad \text{(B-13)}$$

Only the mode component propagates outside the crystal, and the integrated second harmonic field over the entire length of the crystal l is therefore

$$E_{2\omega,00}(x, y, z) = \frac{i2\pi\omega\mathcal{P}_\omega\sqrt{\pi w_0^2}}{cn_o(2\omega, T)}u_{2\omega,00}(x, y, z)\int_0^l \frac{e^{-i\Delta kz'}}{1+i\tau'}dz'. \quad \text{(B-14)}$$

We introduce dimensionless coordinate parameters $s = x/w_0\tau$ and $s' = y/w_0\tau$. As we detect the SH field in the far field of the crystal, i.e. $\tau -> \infty$ and we can use the following approximations

$$\frac{1}{1+i\tau} \simeq \frac{-i}{\tau}$$
$$\frac{x^2}{w_0^2(1+i\tau)} \simeq s^2$$

Using these approximations in the expression of $u_{2\omega,00}$ given in Eq. B-10, the SH field can thus be written

$$E_{2\omega,00}(x, y, z) = \frac{8\pi^2 z_R\omega\mathcal{P}_\omega}{cn_o(2\omega, T)\tau}H_{0,0}(\xi, \Delta k)e^{-2(s^2+s'^2)} \quad \text{(B-15)}$$

where we have also introduced a dimensionless focusing parameter $\xi = l/2z_R$ and the following real function

$$H_{0,0}(\xi, \Delta k) = \frac{1}{2\pi z_R}\int_0^l \frac{e^{-i\Delta kz'}}{1+i\tau'}dz' = \frac{1}{2\pi}\int_{-\xi}^{\xi}\frac{e^{-i\frac{l\Delta k\tau'}{2\xi}}}{(1+i\tau')}d\tau' \quad \text{(B-16)}$$

Moreover, the effective polarization $\mathcal{P}_\omega$ can be written in terms of the laser fundamental power P_ω

$$\mathcal{P}_\omega = dE_\omega^2 = \frac{16\mathrm{P}_\omega d}{n_e(\omega, T)cw_0^2} \quad \text{(B-17)}$$

where d is an effective non linear coefficient. Using the previous equations, we can write the SHG intensity $I_{2\omega,00}$ as

$$I_{2\omega,00}(s, s') = \frac{n_o(\omega, T)c}{8\pi}|E_{2\omega}|^2$$
$$= 4\pi K\left(\frac{\mathrm{P}_\omega k_\omega}{\tau}\right)^2 e^{-4(s^2+s'^2)}\left[H_{0,0}(\xi, \Delta k)\right]^2 \quad \text{(B-18)}$$

where

$$K = \frac{128\pi^2\omega^2}{c^3n_e^2(\omega, T)^2n_o(2\omega, T)}d^2 \quad \text{(B-19)}$$

The SHG power $P_{2\omega,00}$ can be obtained by integrating the intensity distribution

$$\begin{aligned} P_{2\omega,00} &= w_0^2\tau^2 \int\int I_{2\omega,00}(s,s')dsds' \\ &= 4\pi K \mathrm{P}_\omega^2 k_\omega^2 w_0^2 \frac{\pi}{4} |H_{0,0}(\xi,\Delta k)|^2 \\ &= \pi^2 K \mathrm{P}_\omega^2 k_\omega l \frac{1}{\xi} |H_{0,0}(\xi,\Delta k)|^2 \end{aligned} \tag{B-20}$$

Eq. B-18 and B-20 yield the Eq. 4.17 and 4.21 introduced in section 4 B.3.1, and are analogous to the ones presented in reference [Boyd68].

B.2 Calculation for the TEM$_{10}$ pump mode

We now do the same calculation in the case of a TEM$_{10}$ mode as the fundamental field incident on the non linear crystal.

The incident field is defined by

$$E_{\omega,10}(x',y',z') = E_\omega \frac{w_0}{w(z')} \frac{2x'}{w(z')} e^{-\frac{x'^2+y'^2}{w^2(z')} - ik_\omega z + i\Psi(x',y',z') + i2\Phi_G(z')}$$

Note that the coefficient 2 in front of $\Phi_G(z')$ is due to the Gouy phase shift of the TEM$_{10}$ mode. Rearranging the previous field equation yields

$$E_{\omega,10}(x',y',z') = E_\omega \frac{(1-i\tau')}{\sqrt{1+\tau'^2}} \left(\frac{2x'}{w_0\sqrt{1+\tau'^2}} \right) \frac{e^{-\frac{x'^2+y'^2}{w_0^2(1+i\tau')}}}{1+i\tau'} e^{-ik_\omega z'} \tag{B-21}$$

The use of the TEM$_{10}$ mode leads to an additional factor $2x'/w_0(1+i\tau')$ compared to the previous calculation for the TEM$_{00}$ mode. The harmonic polarization can be written in the crystal

$$\mathcal{P}(x',y',z') = \mathcal{P}_\omega \frac{(1-i\tau')}{(1+i\tau')} \left(\frac{4x'^2}{w_0^2(1+\tau'^2)} \right) \frac{e^{-2\frac{x'^2+y'^2}{w_0^2(1+i\tau')}}}{(1+i\tau')^2} e^{-i2k_\omega z'} \tag{B-22}$$

We now compute the harmonic field outside the crystal

$$E_{2\omega,10}(x,y,z) = A_{2\omega,10}(x,y,z) e^{ik_{2\omega}z} \tag{B-23}$$

The amplitude of this field can be integrated from the contributions of slabs of thickness dz'

$$dA_{2\omega,10}(x',y',z') = \frac{i4\pi\omega}{cn_o(2\omega,T)} \mathcal{P}(x',y',z') e^{ik_{2\omega}z'} dz' \tag{B-24}$$

Again, we need to expand $dA_{2\omega,10}(x',y',z')$ into its propagating components, using Eq. B-10, B-11, and B-12. Its integration over the crystal length yields

$$\begin{aligned} E_{2\omega,10}(x,y,z) = \frac{i\pi\omega\mathcal{P}_\omega\sqrt{2\pi w_0^2}}{cn_o(2\omega,T)} \Bigg[& u_{2\omega,20}(x,y,z) \int_0^l \frac{e^{-i\Delta k z'}}{1+i\tau'} dz' \\ & + \frac{u_{2\omega,00}(x,y,z)}{\sqrt{2}} \int_0^l \frac{(1-i\tau')e^{-i\Delta k z'}}{(1+i\tau')^2} dz' \Bigg] \end{aligned} \tag{B-25}$$

In the crystal far field of the crystal, i.e. for $\tau -> \infty$ the field can be rewritten

$$E_{2\omega,10}(x,y,z) = \frac{4\pi^2\omega\mathcal{P}_\omega z_R}{cn_o(2\omega,T)\tau}e^{-2(s^2+s'^2)}\left[H_{1,0}(\xi,\Delta k)+(8s^2-1)H_{1,2}(\xi,\Delta k)\right] \quad \text{(B-26)}$$

where we have introduced $H_{n,2p}(\xi,\Delta k)$, which integrates the nonlinear effects on the crystal length, and is defined by

$$H_{n,2p}(\xi,\Delta k) = \frac{1}{2\pi}\int_{-\xi}^{\xi}\frac{(1+i\tau)^{n-p}\,e^{-i\frac{l\Delta k\tau}{2\xi}}}{(1+i\tau)^{n-p+1}}d\tau, \quad \text{(B-27)}$$

Similarly to the previous section, using the same notations, we get the SHG intensity $I_{2\omega,10}$ as

$$I_{2\omega,10}(s,s') = \pi K\left(\frac{\mathrm{P}_\omega k_\omega}{\tau}\right)^2 e^{-4(s^2+s'^2)}\left[H_{1,0}(\xi,\Delta k)+(8s^2-1)H_{1,2}(\xi,\Delta k)\right]^2 \quad \text{(B-28)}$$

The SHG power $P_{2,10}$ can be obtained by integrating the intensity distribution

$$P_{2\omega,10} = \frac{\pi^2 K\mathrm{P}_\omega^2 k_\omega l}{\xi}\left[\frac{1}{4}|H_{1,0}(\xi,\Delta k)|^2+\frac{1}{2}|H_{1,2}(\xi,\Delta k)|^2\right] \quad \text{(B-29)}$$

Note that there are no crossed terms, as the SH TEM_{00} and TEM_{20} modes are orthogonal. Eq. B-28 and B-29 yield the Eq. 4.18 and 4.22 introduced in section 4 B.3.1.

B.3 Calculation for the TEM_{20} pump mode

We now do the same calculation again, in the case of a TEM_{20} mode as the fundamental field incident on the non linear crystal, defined by

$$E_{\omega,20}(x',y',z') = \frac{E_\omega}{\sqrt{2}}\frac{w_0}{w(z')}\left[\frac{4x'^2}{w(z')^2}-1\right]e^{-\frac{x'^2+y'^2}{w^2(z')}-ik_\omega z+i\Psi(x',y',z')+i3\Phi_G(z')} \quad \text{(B-30)}$$

The harmonic polarization can be written in the crystal

$$\mathcal{P}(x',y',z') = \frac{\mathcal{P}_\omega}{2}\left[\frac{4x'^2}{w_0^2(1+\tau'^2)}-1\right]^2\frac{(1-i\tau')^2}{(1+i\tau')^2}\frac{e^{-2\frac{x'^2+y'^2}{w_0^2(1+i\tau)}}}{(1+i\tau')^2}e^{-i2k_\omega z} \quad \text{(B-31)}$$

We now compute the harmonic field outside the crystal

$$E_{2\omega,20}(x,y,z) = A_{2\omega,20}(x,y,z)e^{ik_{2\omega}z} \quad \text{(B-32)}$$

The amplitude of this field can be integrated from the contributions of slabs of thickness dz'

$$\begin{aligned} dA_{2\omega,20}(x',y',z') &= \frac{i4\pi\omega}{cn_o(2\omega,T)}\mathcal{P}_\omega(x',y',z')e^{ik_{2\omega}z'}dz' \\ &= \frac{i2\pi\omega}{cn_o(2\omega,T)}\mathcal{P}_\omega\left[\frac{4x'^2}{w_0^2(1+\tau'^2)}-1\right]^2\frac{(1-i\tau')^2}{(1+i\tau')^2}\frac{e^{-2\frac{x'^2+y'^2}{w_0^2(1+i\tau)}-i\Delta kz'}}{(1+i\tau')^2}dz' \end{aligned}$$

Again, we need to expand $dA_{2\omega,20}(x',y',z')$ into its propagating components, using Eq. B-10, B-11, and B-12. Its integration over the crystal length yields

$$\begin{aligned} E_{2\omega,20}(x,y,z) &= \frac{i\pi\omega\mathcal{P}_\omega\sqrt{2\pi w_0^2}}{cn_o(2\omega,T)}\left[\frac{\sqrt{3}}{2}u_{2,40}(x,y,z)\int_0^l\frac{e^{-i\Delta kz'}}{1+i\tau'}dz'\right. \\ &+\frac{1}{2}u_{2,20}(x,y,z)\int_0^l\frac{(1-i\tau')e^{-i\Delta kz'}}{(1+i\tau')^2}dz' \\ &\left.+\frac{3}{4\sqrt{2}}u_{2,00}(x,y,z)\int_0^l\frac{(1-i\tau')^2e^{-i\Delta kz'}}{(1+i\tau')^3}dz'\right] \end{aligned} \tag{B-33}$$

In the crystal far field of the crystal, i.e. for $\tau->\infty$ the field can be rewritten

$$\begin{aligned} E_{2\omega,20}(x,y,z) &= \frac{2\pi\omega_2\mathcal{P}_{0x}}{cn_2\tau}\frac{\pi b}{2}e^{-2(s^2+s'^2)}\left[\frac{3}{4}H_{2,0}(\xi,\Delta k)-\frac{1}{2}(8s^2-1)H_{2,2}(\xi,\Delta k)\right. \\ &\left.+\frac{1}{4}(64s^4-48s^2+3)H_{2,4}(\xi,\Delta k)\right] \end{aligned} \tag{B-34}$$

The SHG intensity $I_{2\omega,20}$ can be written, still using the same notations introduced in section B.1, as

$$\begin{aligned} I_{2\omega,20}(s,s') &= \pi K\left(\frac{\mathrm{P}_\omega k_\omega}{\tau}\right)e^{-4(s^2+s'^2)}\left[\frac{3}{4}H_{2,0}(\xi,\Delta k)-\frac{1}{2}(8s^2-1)H_{2,2}(\xi,\Delta k)\right. \\ &\left.+\frac{1}{4}(64s^4-48s^2+3)H_{2,4}(\xi,\Delta k)\right]^2 \end{aligned} \tag{B-35}$$

The SHG power $P_{2\omega,20}$ can be obtained by integrating the intensity distribution

$$P_{2\omega,20} = \frac{\pi^2K\mathrm{P}_\omega^2k_\omega l}{\xi}\left[\frac{9}{64}|H_{2,0}(\xi,\Delta k)|^2+\frac{1}{8}|H_{2,2}(\xi,\Delta k)|^2+\frac{3}{8}|H_{2,4}(\xi,\Delta k)|^2\right] \tag{B-36}$$

Note that again, there are no crossed terms, as the SH TEM_{00}, TEM_{20} and TEM_{40} modes are orthogonal. Eq. B-35 and B-36 yield the Eq. 4.19 and 4.23 introduced in section 4 B.3.1.

C Knife-edge experiment for single and bi-mode fields

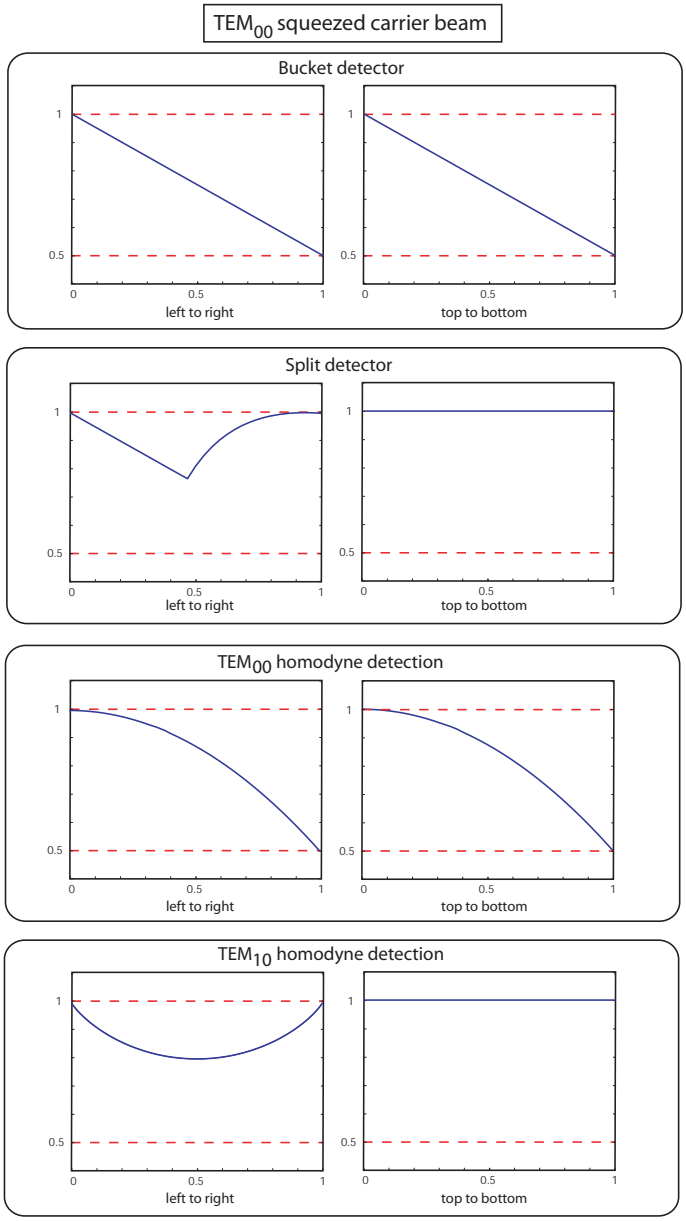

Figure 6.2: Single mode knife edge experiments. Results given for an incident squeezed TEM_{00} mode with $-3\ dB$ of amplitude squeezing.

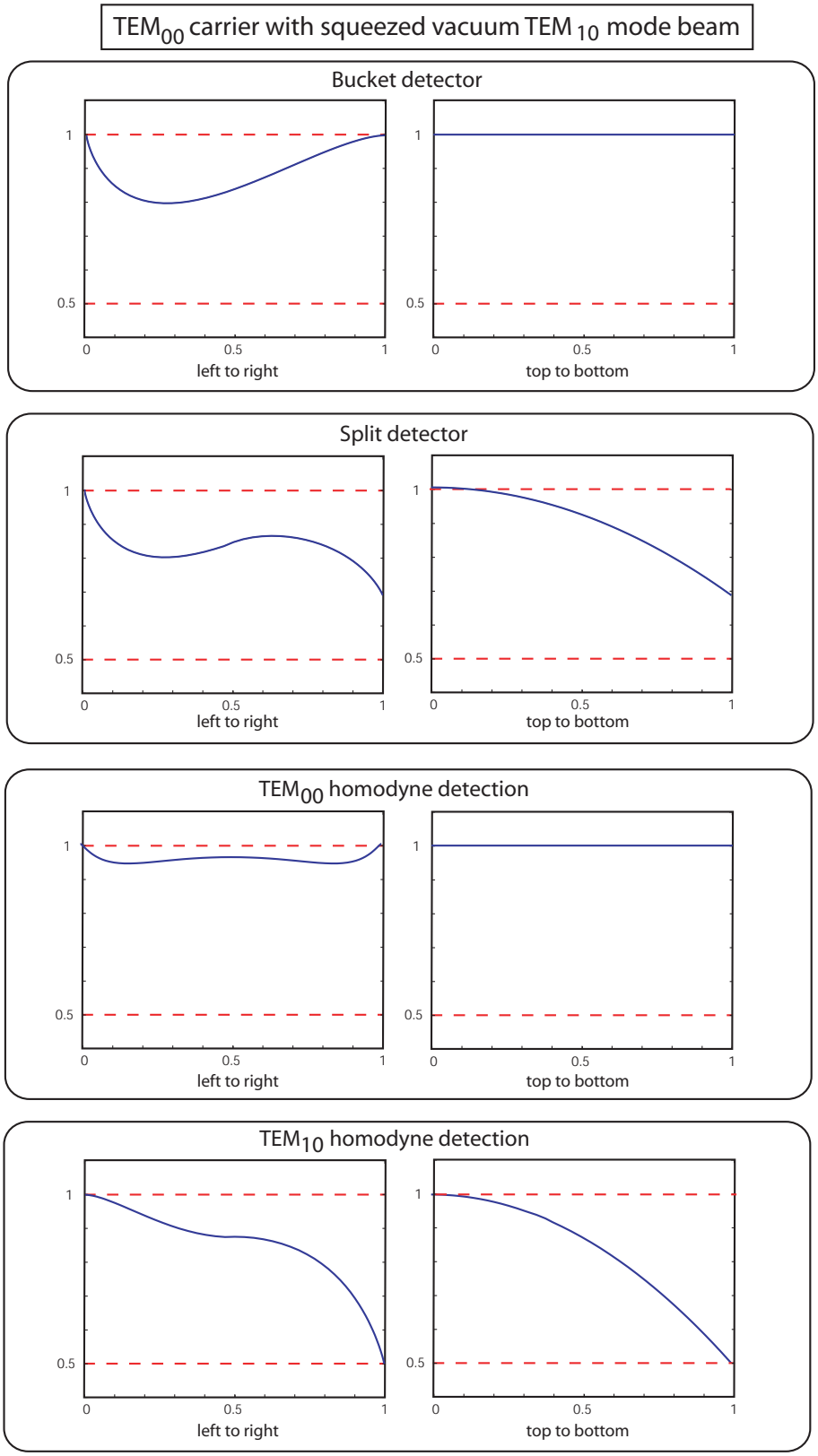

Figure 6.3: Bi-mode knife edge experiments. Results given for an incident coherent bright TEM_{00} mode and a TEM_{10} squeezed vacuum mode with $-3\ dB$ of amplitude squeezing.

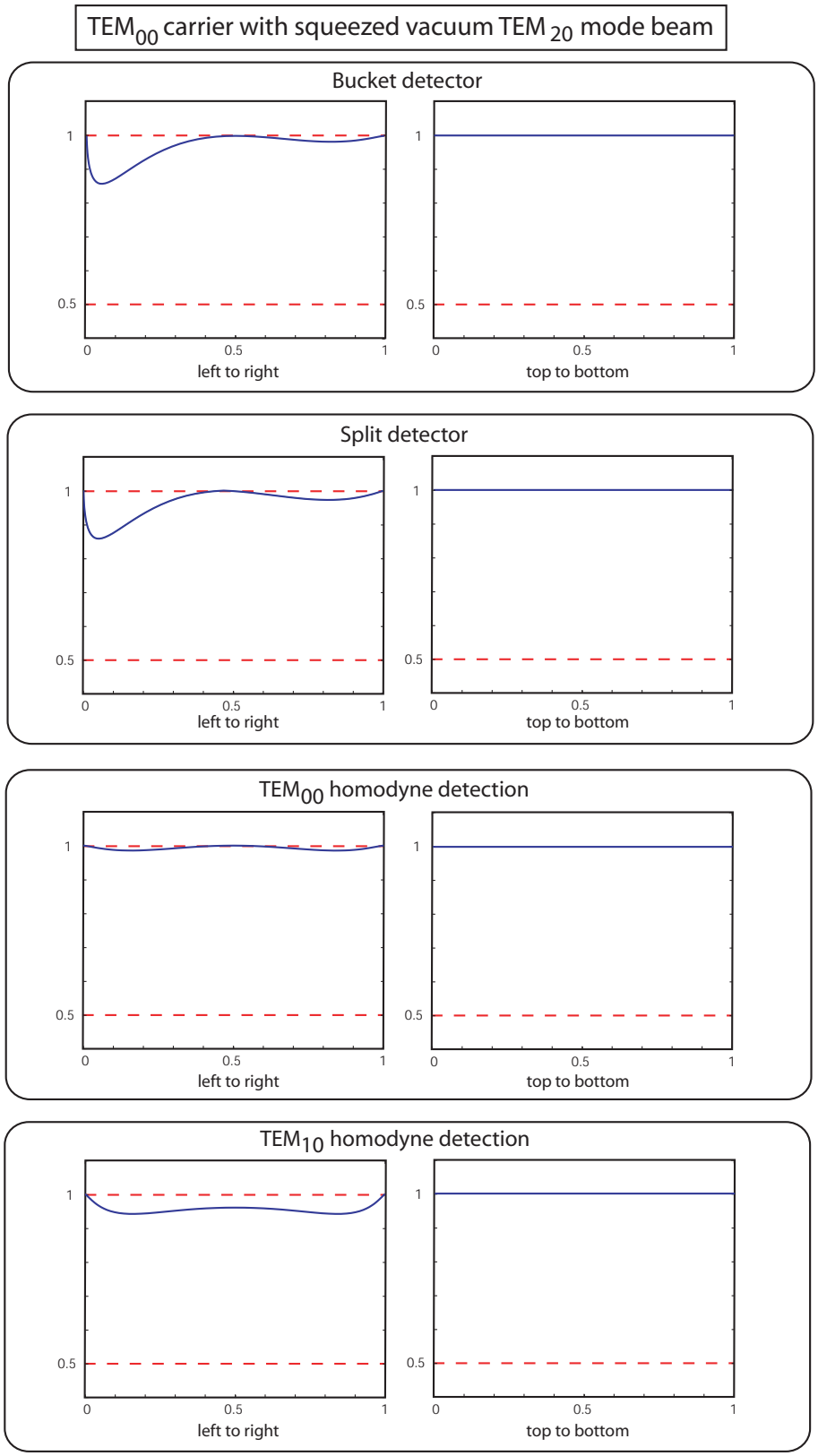

Figure 6.4: Bi-mode knife edge experiments. Results given for an incident coherent bright TEM_{00} mode and a TEM_{20} squeezed vacuum mode with $-3\ dB$ of amplitude squeezing.

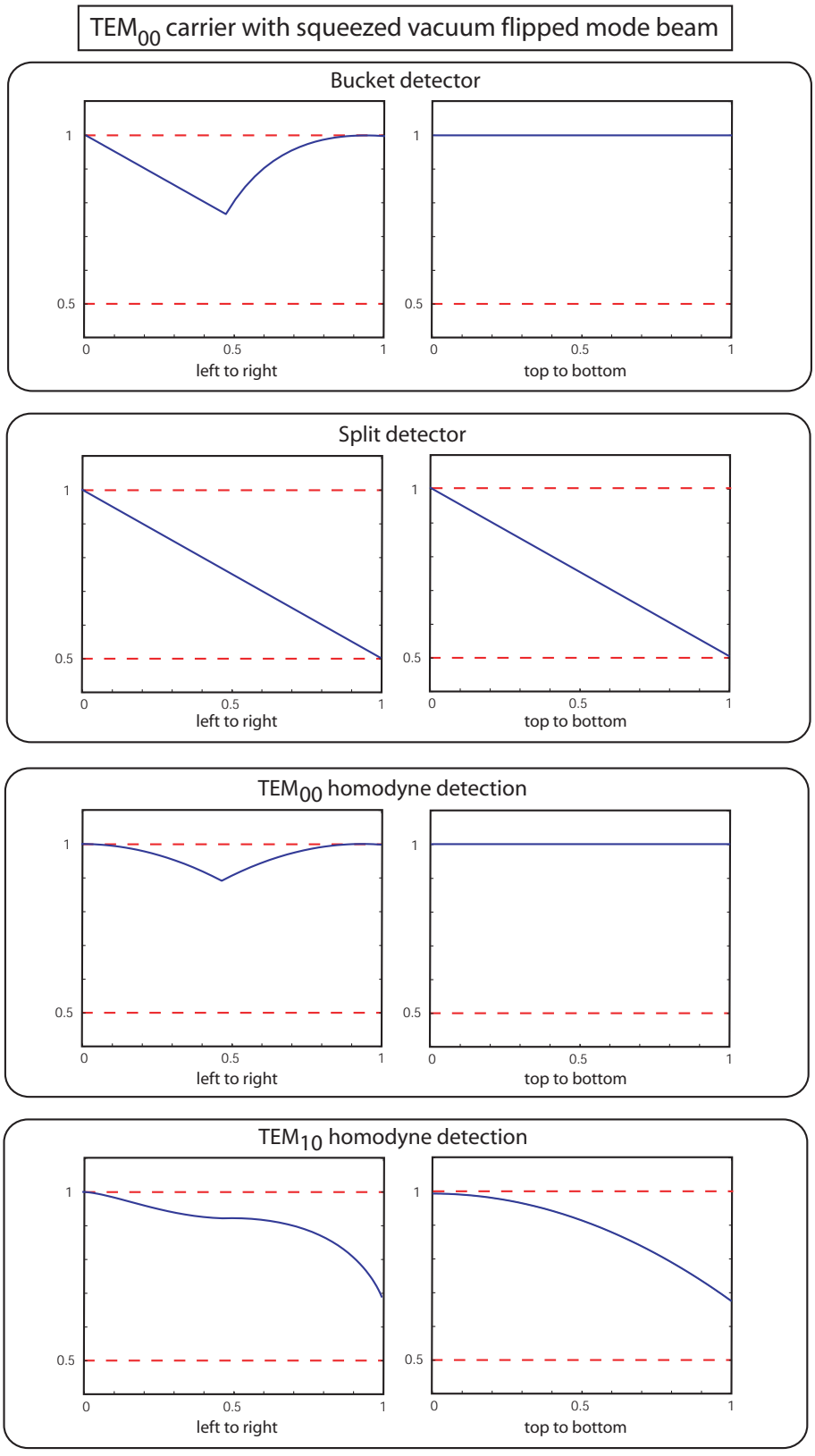

Figure 6.5: Bi-mode knife edge experiments. Results given for an incident coherent bright TEM_{00} mode and a squeezed vacuum flipped mode with $-3\ dB$ of amplitude squeezing.

Bibliography

[Abramowitz72] M. Abramowitz, I.A. Stegun, *Handbook of Mathematical Functions*, U.S. Department of Commerce (1972). Quoted p. 16

[Aizawa04] K. Aizawa, K. Sakaue, Y. Suenaga, *Image Processing Technologies-Algorithms, Sensors, and Applications*, Marcel Dekker (2004). Quoted p. 73

[Anderson84] D. Z. Anderson, *Alignment of resonant optical cavities*, Appl. Opt., **23**, 2944 (1984). Quoted p. 75, 81

[Arlt98] J. Arlt, K. Dholakia, L. Allen and M.J. Padgett, *The production of multiringed Laguerre-Gaussian modes by computer-generated holograms*, J. Mod. Opt. **45**, 1231 (1998). Quoted p. 112

[Basistiy93] I.V. Basistiy, V.Y. Bazhenov, M.S. Soskin, and M.V. Vasnetsov, *Optics of light beams with screw dislocations*, Opt. Commun. **103**, 422 (1993). Quoted p. 84

[Bachor03] H.A. Bachor, T.C. Ralph, *A guide to experiments in quantum optics*, Wiley-VCH (2003). Quoted p. 5, 21, 42, 89, 133, 141, 146, 174

[Bandres04] M.A. Bandres and J.C. Guti}errez-Vega, *Ince-Gaussian modes of the paraxial wave equation and stable resonators*, JOSA A **21**, 873 (2004). Quoted p. 10

[Barnett06] S.M. Barnett, R. Zambrini, *Resolution in rotation measurements*, J. Mod. Opt. **53**, 613 (2006). Quoted p. 83, 105

[Beijersbergen94] M. W. Beijersbergen, R. P. C. Coerwinkel, M. Kristensen and J. P. Woerdman, *Helical-wavefront laser beams produced with a spiral phaseplate*, Opt. Commun. **112**, 321 (1994). Quoted p. 84

[Bertero98] M. Bertero and P. Boccacci. *Introduction to inverse problems in imaging*, IOP Publishing, 1998. Quoted p. 44, 50

[Bertolini06] A. Bertolini, R. DeSalvo, F. Fidecaro, M. Francesconi, *Mechanical design of a single-axis monolithic accelerometer for advanced seismic attenuation systems*, Nuclear Instruments and Methods in Physics Research A, (2006). Quoted p. 5

[Blinov04] B.B. Blinov, D.L. Moehring, L.M. Duan, C. Monroe, *Observation of entanglement between a single trapped atom and a single photon*, Nature **428**, 153 (2004). Quoted p. 22

[Boccara80] C. Boccara, D. Fournier and J. Badoz, *Thermo-optical spectroscopy: Detection by the "mirage effect"*, Appl. Phys. Letters **36**, 130 (1980). Quoted p. 45

[Borah06] D.K. Borah and D.G. Voelz, *Cramer-Rao lower bounds on estimation of laser system pointing parameters by use of the return photon signal*, Opt. Lett. **31**, 1029 (2006). Quoted p. 151

[Born97] M. Born, E. Wolf, *Principles of Optics: Electromagnetic Theory of Propagation, Interference and Diffraction of Light*, Cambridge Univ. Press (1997). Quoted p. 108

[Bowen02] W.P.Bowen, N. Treps, R. Schnabel, P.K. Lam, *Experimental demonstration of continuous variable polarization entanglement*, Phys. Rev. Lett **89**, 253601 (2002). Quoted p. 27, 85, 164, 165

[Bowen03] W. P. Bowen, R. Schnabel, P. K. Lam, and T. C. Ralph. *An experimental investigation of criteria for continuous variable entanglement*, Phys. Rev. Lett. **90**, 043601 (2003). Quoted p. 22, 24, 164, 165

[BowenPhD03] W. P. Bowen, , *Experiments towards a Quantum Information Network with Squeezed Light and Entanglement*, PhD Thesis (Australian National University, Canberra 2003). Quoted p. 21, 22, 25, 134, 136, 169

[Boyd68] G. D. Boyd, D. A. Kleinman, *Parametric interaction of focused Gaussian beams*, J. Appl. Phys., **39**, 3597 (1968). Quoted p. 120, 125, 127, 187, 190

[Buchler99] B.C. Buchler, M.B. Gray, D.A. Shaddock, T.C. Ralph, and D.E. McClelland, *Suppression of classic and quantum radiation pressure noise by electro-optic feedback*, Opt. Lett. **24**, 259 (1999). Quoted p. 19

[BuchlerPhD01] B. C. Buchler, *Electro-optic Control of Quantum Measurements*, PhD Thesis (Australian National University, Canberra 2001). Quoted p. 160

[Caves94] C.M. Caves and P.D. Drummond, *Quantum limits on bosonic communication rates*, Rev. Mod. Phys. **66**, 481 (1994). Quoted p. 2, 73, 105, 120, 150

[Chow04] J. H. Chow, G. de Vine, M. B. Gray, and D. E. McClelland, *Measurement of Gouy phase evolution by use of spatial mode interference*, Opt. Let. **20**, 2339 (2004). Quoted p. 75

[Cohen87] C. Cohen-Tannoudji, J. Dupont-Roc, and G. Grynberg, *Photons et atomes : Introduction à l'optique quantique*, Inter Editions/ Editions du CNRS, Paris (1987). Quoted p. 7

[Coherent] Verdi - DPSS CW Pump Lasers - High-Power (up to 18W), CW, Single-Frequency (532 nm) laser - Coherent Inc. Quoted p. 120

[Curilef05] S. Curilef, F. Pennini, and A. Plastino, *Fisher information, Wehrl entropy, and Landau diamagnetism*, Phys. Rev. B, **71**, 024420 (2005). Quoted p. 89

[Dechoum04] K. Dechoum,P. D. Drummond, S. Chaturvedi, and M. D. Reid, *Critical fluctuations and entanglement in the nondegenerate parametric oscillator*, Phys. Rev. A **70**, 053807 (2004). Quoted p. 40

[Delaubert02] V. Delaubert, D. A. Shaddock, P. K. Lam, B. C. Buchler, H-A. Bachor and D. E. McClelland, *Generation of a phase-flipped Gaussian mode for optical measurements*, J. Opt. A **4**, 393 (2002). Quoted p. 47, 112, 114, 117, 153, 160

[Delaubert06,1] V. Delaubert, N. Treps, C. C. Harb, P. K. Lam and H-A. Bachor, *Quantum measurements of spatial conjugate variables: Displacement and tilt of a Gaussian beam*, Opt. Let. **31**, 1537 (2006). Quoted p. 39, 151

[Delaubert06,2] V. Delaubert, N. Treps, G. Bo, and C. Fabre, *Optical storage of high-density information beyond the diffraction limit: A quantum study* Phys. Rev. A **73**, 013820 (2006). Quoted p. 56

[Delaubert06,3] V. Delaubert, N. Treps, M. Lassen, C. C. Harb, C. Fabre, P. K. Lam, and H-A. Bachor, *TEM_{10} homodyne detection as an optimal small displacement and tilt measurements scheme*, Phys. Rev. A **74**, 053823 (2006). Quoted p. 151

[Delaubert06,4] V. Delaubert, N. Treps, C. Fabre, H.A. Bachor and P. Réfrégier, *Quantum limits in image processing*, quant-ph/0609188 (2006). Quoted p. 89

[Delaubert07] V. Delaubert, M. Lassen, D.R.N. Pulford, H.-A. Bachor and C. C. Harb, *Selective conversion of higher order spatial modes via second harmonic generation*, submitted to Nature Photonics. Quoted p. 120, 131

[Denk90] W. Denk and W. W. Webb, *Optical measurement of picometer displacements of transparent microscopic objects*, Appl. Opt., **29**, 2382 (1990). Quoted p. 151

[Drever83] R.W.P. Drever, J.L. Hall, F.V. Kowalski, J. Hough, G.M. Ford, A.J. Munley, and H. Ward, *Laser phase and frequency stabilization using an optical resonator* Appl. Phys. B **31**, 97 (1983). Quoted p. 113, 118, 139, 173, 174

[Duan00,1] L.-M. Duan, G. Giedke, J. I. Cirac, and P. Zoller, *Inseparability criterion for continuous variable systems*, Phys. Rev. Lett. **84**, 2722 (2000). Quoted p. 23, 24

[Duan00,2] L.-M. Duan, J.I. Cirac, P. Zoller, and E.S. Polzik, *Quantum Communication between Atomic Ensembles Using Coherent Light*, Phys. Rev. Lett. **85**, 5643 (2000). Quoted p. 22

[Einstein35] A. Einstein, B. Podolsky, and N. Rosen, *Can quantum-mechanical description of physical reality be considered complete?*, Phys. Rev. **47**, 777 (1935). Quoted p. 21, 23, 25, 164

[Eisert04] J. Eisert, M. B. Plenio, S. Bose, and J. Hartley, *Towards Quantum Entanglement in Nanoelectromechanical Devices*, Phys. Rev. Lett. **93**, 190402 (2004). Quoted p. 22

[Europe05] *Quantum Information processing and communication in Europe, http://www.cordis.lu/ist/fet/qipc.htm*, Luxembourg (2005). Quoted p. 2

[Fabre85] C. Fabre, *Quantum fluctuations*, Les Houches LXIII (1995). Quoted p. 11

[Fabre00] C. Fabre, J.B. Fouet and A. Maître, *Quantum limits in the measurement of very small displacements in optical images*, Opt. Let. **25**, 76 (2000). Quoted p. 5, 45, 46, 86, 151

[Franken61] P.A. Franken, A.E. Hill, C.W. Peters, and G. Weinreich, *Generation of Optical Harmonics*, Phys. Rev. Lett. **7** 4 (1961). Quoted p. 120

[Furukawa01] Y. Furukawa, A. Alexandrovski, R. Route, M. Fejer, and G. Foulon, *Green-induced infrared absorption in MgO doped $LiNbO_3$*, Appl. Phys. Lett. **78**, 1970 (2001). Quoted p. 146

[Furusawa07] Furusawa's group, 9.5 dB of squeezing in PPKTP, to be published. Quoted p. 19, 131, 133, 147

[Gao98] J. Gao, F. Cui, C. Xue, C. Xie, and P. Kunchi, *Generation and application of twin beams from an optical parametric oscillator including an α-cut KTP crystal*, Opt. Let. **23**, 870 (1998). Quoted p. 89

[Gatti99] A. Gatti, E. Brambilla, L.A. Lugiato and M.I. Kolobov, *Quantum Entangled Images*, Phys. Rev. Lett. **83**, 1763 - 1766 (1999). Quoted p. 164

[Gatti03] A. Gatti, E. Brambilla, and L. A. Lugiato, *Entangled Imaging and Wave-Particle Duality: From the Microscopic to the Macroscopic Realm*, Phys. Rev. Lett. 90, 133603 (2003). Quoted p. 164

[Gatti04] A. Gatti, E. Brambilla, M. Bache, and L. A. Lugiato, *Correlated imaging, quantum and classical*, Phys. Rev. A **70**, 013802 (2004). Quoted p. 1

[GiganPhD04] S. Gigan, *Amplification paramétrique d'images en cavité : Effets classiques et quantiques*, PhD Thesis (Université Pierre et Marie Curie, Paris 2004). Quoted p. 109

[Gigan05] S. Gigan, L. Lopez, N. Treps, A. Maître and C. Fabre, *Image transmission through a stable paraxial cavity*, Phys. Rev. A **72**, 023804 (2005). Quoted p. 109

[Gigan06] S. Gigan, L. Lopez, V. Delaubert, N. Treps, C. Fabre, and A. Maître, *Continuous-wave phase-sensitive parametric image amplification*, J. Mod. Opt. **53** 809 (2006). Quoted p. 105

[Giovannetti03] V. Giovannetti, S. Mancini, D. Vitali, and P. Tombesi, *Characterizing the entanglement of bipartite quantum systems*, Phys. Rev. A **67**, 022320 (2003). Quoted p. 24

[Gittes:98] F. Gittes and C. F. Schmidt, *Interference model for back-focal-plane displacement detection in optical tweezers* , Opt. Lett., **23**, 7 (1998). Quoted p. 151

[Glauber65] R.J. Glauber, *Optical coherence and photon statistics* in *Quantum optics and electronics*, Gordon and Breach (1965). Quoted p. 18, 92

[Grosse06] N. Grosse, W.P. Bowen, K. McKenzie, P.K. Lam, *Harmonic Entanglement with Second-Order Nonlinearity*, Phys. Rev. Lett. **96**, 063601 (2006). Quoted p. 120

[Grote02] H. Grote, G. Heinze, A. Freise, S. Gossler, B. Willke, H. Lück, H. Ward, M. Casey, K.A. Strain, D. Robertson, J. Hough and K. Danzmann, *The automatic alignment system of GEO 600*, Class. Quantum Grav. **19**, 1849 (2002). Quoted p. 75

[Grynberg97] G. Grynberg, A. Aspect et C. Fabre, *Introduction aux lasers et à l'optique quantique*, cours de l'école Polytechnique, Ellipses, 1997. Quoted p. 5, 7, 29, 34, 120

[Guo03] H.-L. Guo, C.-X. Liu, Z.-L. Li, J.-F. Duan, X.-H. Han, B.-Y. Chen and D.-Z. Zhang, *Displacement and Force Measurements with Quadrant Photodetector in Optical Tweezers*, Chinese Phys. Lett., **20**, 950 (2003). Quoted p. 151

[Haine05] S.A. Haine and J.J. Hope, *Outcoupling from a Bose-Einstein condensate with squeezed light to produce entangled-atom laser beams*, Phys. Rev. A **72**, 033601 (2005). Quoted p. 22

[Heaney06] L. Heaney, J. Anders, V. Vedral, *Spatial Entanglement of a Free Bosonic Field*,quant-ph/0607069. Quoted p. 164

[Hermier99] J.-P. Hermier, A. Bramati, A. Z. Khoury, E. Giacobino, J.-P. Poizat, T. J. Chang, Ph. Grangier, *Spatial quantum noise of semiconductor lasers*, J. Opt. Soc. Am. B, **16**, 2140 (1999). Quoted p. 33

[Hetet06] G. Hétet, O. Glöckl, K. A. Pilypas, C.C. Harb, B.C. Buchler, H.-A. Bachor and P.K. Lam , *Squeezed light for bandwidth limited atom optics experiments at the Rubidium D1*, preprint : quant-ph/0611204. Quoted p. 131

[Horodecki97] P. Horodecki, *Separability criterion and inseparable mixed states with positive partial transposition*, Phys. Lett. A **232**, 333 (1997). Quoted p. 24

[Howell04] J. C. Howell, R. S. Bennink, S. J. Bentley, and R. W. Boyd, *Realization of the Einstein-Podolsky-Rosen paradox using momentum-and position-entangled photons from spontaneous parametric down conversion*, Phys. Rev. Lett. **92**, 210403 (2004). Quoted p. 164

[Hsu04] M. T. L. Hsu, V. Delaubert, P. K. Lam and W.P. Bowen, *Optimum Small Optical Beam Displacement Measurement*, J. Opt. B : Qu. Semiclass. Opt.**6**, 495 (2004). Quoted p. 75, 85

[Hsu05] M. T. L. Hsu, W. P. Bowen, N. Treps and P. K. Lam, *Continuous-Variable Spatial Entanglement for Bright Optical Beams*, Phys. Rev. A **72**, 013802 (2005). Quoted p. 79, 108, 164, 168

[Hsu06] M. T. L. Hsu, V. Delaubert, W.P. Bowen, C. Fabre, H-A. Bachor and P. K. Lam, *A quantum study of multi-bit phase coding for optical storage*, IEEE Journal of Quantum Electronics **10**, 1001 (2006). Quoted p. 56

[Innolight] Diabolo laser, InnoLight - Innovative Laser und Systemtechnik GmbH. Quoted p. 137

[Jain89] A.K. Jain, *Fundamentals of digital image processing* information and system sciences series. Prentice Hall, 1989. Quoted p. 44, 50

[Jing06] J. Jing, S. Feng, R. Bloomer, and O. Pfister, *Experimental continuous-variable entanglement from a phase-difference-locked optical parametric oscillator*, quant-ph/0604134. Quoted p. 22, 164, 165

[Josse04] V. Josse, A. Dantan, A. Bramati, M. Pinard, and E. Giacobino, *Continuous Variable Entanglement using Cold Atoms*, Phys. Rev. Lett. **92**, 123601 (2004). Quoted p. 164

[Juwiler99] I. Juwiler, A. Arie, A. Skliar, and G. Rosenman, *Efficient quasi-phase-matched frequency doubling with phase compensation by a wedged crystal in a standing-wave external cavity*, Opt. Let. **24**, 1236 (1999). Quoted p. 143

[Katsaggelos91] A.K. Katsaggelos. *Digital image restoration*, volume 23 of Springer Series in Information Sciences. Springer-Verlag, (1991). Quoted p. 44, 50

[Khokhlov61] V. Khokhlov, *Wave propagation in nonlinear dispersive lines*, Radiotek. Electron **6** 1116 (1961). Quoted p. 120

[Kimble87] M. Xiao, L.-A. Wu, and H. J. Kimble, *Precision measurement beyond the shot-noise limit* , Phys. Rev. Lett. **59**, 278 (1987). Quoted p. 89

[Knobel03] R. G. Knobel, and A. N. Cleland, *Nanometre-scale displacement sensing using a single electron transistor*, Nature **424**, 291 (2003). Quoted p. 151

[Kogelnik64] H. Kogelnik, *Coupling and conversion coefficients for optical modes*, Proceedings of the Symposium on Quasi-Optics (1964). Quoted p. 81

[Kolobov95] M. I. Kolobov and L. A. Lugiato, *Noiseless amplification of optical images*, Phys. Rev. A. **52**, 4930 (1995). Quoted p. 105

[Kolobov 99] M. Kolobov, *The spatial behavior of nonclassical light*, Rev. Mod. Phys. **71** 1539 (1999). Quoted p. 1, 105

[Kolobov06] M. Kolobov, *Quantum imaging*, Springer (2007). Quoted p. 1

[Korolkova02] N. Korolkova, G. Leuchs, R. Loudon, T. C. Ralph, and C. Silberhorn, *Polarization squeezing and continuous-variable polarization entanglement*, Phys. Rev. A **65**, 052306 (2002). Quoted p. 27, 85, 164

[Kuroda99] K Kuroda *et al.*, *Large-scale Cryogenic Gravitational wave Telescope*, Int. J. Mod. Phys. D (1999). Quoted p. 5

[Kurz92] P.Kürz, R. Paschotta, K. Fiedler, A. Sizmann, G. Leuchs and J. Mlynek, *Squeezing by second-harmonic generation in a monolithic resonator*, Appl. Phys. B **55**, 216 (1992). Quoted p. 120

[Kurz02] J.R. Kurz, X. Xie, and M.M. Fejer, *Odd waveguide mode quasi-phase matching with angled and staggered gratings*, Opt. Lett. **27**, 1445 (2002). Quoted p. 181

[Kurz03] J.R. Kurz, X.P. Xie, C. Langrock, D.S. Hum, M.M. Fejer, *Mode converters and sorters for quasiphase matching waveguide devices*, Conference on Lasers and Electro-Optics, (2003). Quoted p. 181

[Kurz04] J.R. Kurz, J. Huang, X. Xie, T. Saida, and M.M. Fejer, *Mode multiplexing in optical frequency mixers*, Opt. Lett. **29**, 551 (2004). Quoted p. 181

[Lam99] P.K. Lam, T. Ralph, B. Buchler, D. McClelland, H.-A. Bachor, and J. Gao, *Optimization and transfer of vacuum squeezing from an optical parametric oscillator*, Journal of Optics B: Quantum and Semiclassical Optics **1**, 469 (1999). Quoted p. 19, 133

[Langford04] N. Langford, R. Dalton, M. Harvey, J. OBrien, G. Pryde, A. Gilchrist, S. Bartlett, and A. White, *Measuring entangled qutrits and their use for quantum bit commitment*, Phys. Rev. Lett. **93**, 05360 (2004). Quoted p. 105

[Lassen05] M. Lassen, P. Tidemand-Lichtenberg, and P. Buchhave, *Simultaneous measurement of patterns in the signal and idler near and far fields from a confocal optical parametrical oscillator*, Phys. Rev. A **72**, 1 (2005). Quoted p. 139

[Lassen06] M.Lassen, V. Delaubert, C.C. Harb, N. Treps, P.K. Lam and H.-A. Bachor, *Generation of Squeezing in Higher Order Hermite-Gaussian Modes with an Optical Parametric Amplifier*, J Eur. Opt. Soc. Rapid. Pub. **1**, 06003 (2006). Quoted p. 120, 133, 137

[Lassen07] M. Lassen, V. Delaubert, J. Janousek, K. Wagner, H.-A. Bachor,P.K. Lam, N. Treps, P. Buchhave, C. Fabre, C. C. Harb, *Tools for spatial multi-mode quantum information: modulation, detection and quantum correlations*, accepted for publication in Phys. Rev. Lett. Quoted p. 106, 133

[Lastzka06] N. Lastzka, R. Schnabel, *The Gouy phase shift in nonlinear interactions of waves*, preprint : physics/0611257. Quoted p. 127

[LauratPhD04] J. Laurat, *Etats non-classiques et intrication en variables continues à l'aide d'un oscillateur paramétrique optique*, PhD Thesis (Université Pierre et Marie Curie, Paris 2004). Quoted p. 17, 23

[Laurat04] J. Laurat, T. Coudreau, G. Keller, N. Treps, and C. Fabre, *Compact source of Einstein-Podolsky-Rosen entanglement and squeezing at very low noise frequencies*, Phys. Rev. A 70, 042315 (2004). Quoted p. 22

[Laurat05] J. Laurat, G. Keller, J-A Oliveira-Huguenin, C. Fabre, T. Coudreau, A. Serafini, G. Adesso, F. Illuminati, *Entanglement of two-mode Gaussian states: characterization and experimental production and manipulation*, J. Opt. B **7**, S577 (2005). Quoted p. 22, 24

[Laurat06] J. Laurat, G. Keller, C. Fabre, and T. Coudreau, *Generation of two-color polarization-entangled optical beams with a self-phase-locked*

two-crystal optical parametric oscillator, Phys. Rev. A 73, 012333 (2006). Quoted p. 22, 164

[Lopez05] L. Lopez, S. Gigan, N. Treps, A. Maître, C. Fabre, and A. Gatti, *Multimode squeezing properties of a confocal optical parametric oscillator: Beyond the thin-crystal approximation* , Phys. Rev. A **72**, 013806 (2005). Quoted p. 120, 137

[Lopez07,1] L. Lopez, N. Treps, A. Chummo, A. Maître and C. Fabre, to be published. Quoted p. 120

[Lopez07,2] L. Lopez, N. Treps, S. Gigan, A. Maître and C. Fabre, to be published. Quoted p. 105, 120

[Loudon00] R. Loudon, *The Quantum Theory of Light*, Oxford University Press (2000). Quoted p. 92

[Lue87] J.T. Lue and C.J. Sun, *Limiting factors for parametric generation with focused high-order transverse- and multilongitudinal-mode lasers*, J. Opt. Soc. Am. B **4** 1958 (1987). Quoted p. 125

[Lugiato02] L. Lugiato, A. Gatti, and E. Brambilla, *Quantum imaging*, J. Opt. B: Quantum and Semiclassical Optics **4** S176 (2002). Quoted p. 1, 105

[Luo00] Z.-P. Luo, Y.-L. Sun, and K.-N. An, *An optical spin micromotor*, Appl. Phys. Lett. **76**, 1779 (2000). Quoted p. 84

[MacDonald02] M. P. MacDonald, L. Paterson, K. Volke-Sepulveda, J. Arlt, W. Sibbett, K. Dholakia, *Creation and Manipulation of Three-Dimensional Optically Trapped Structures*, Science **296**, 1101 (2002). Quoted p. 132

[Mair01] A. Mair, A. Vaziri, G. Weihs and A. Zeilinger, *Entanglement of the orbital angular momentum states of photons*, Nature **412**, 313 (2001). Quoted p. 83

[Mandel95] L. Mandel, E. Wolf, *"Optical Coherence and Quantum Optics"*, Science (1995). Quoted p. 83

[Marrucci06] L. Marrucci, C. Manzo, and D. Paparo, *Optical Spin-to-Orbital Angular Momentum Conversion in Inhomogeneous Anisotropic Media*, Phys. Rev. Lett. **96**, 163905 (2006). Quoted p. 83

[Martinelli03] M. Martinelli, N. Treps, S. Ducci, S. Gigan, A. Maitre and C. Fabre, *Experimental study of the spatial distribution of quantum correlations in a confocal optical parametric oscillator* , Phys. Rev. A **67**, 023808 (2003). Quoted p. 33, 37

[Mattle96] K Mattle, H Weinfurter, PG Kwiat, A Zeilinger *Dense Coding in Experimental Quantum Communication* , Phys. Rev. Lett. **76**, 4656 (1996). Quoted p. 2

[McKenzie02] K. McKenzie, D.A. Shaddock, D.E. McClelland, B.C. Buchler and P.K. Lam, *Experimental Demonstration of a Squeezing-Enhanced Power-Recycled Michelson Interferometer for Gravitational Wave Detection*, Phys. Rev. Lett. **88**, 231102 (2002). Quoted p. 21

[McKenzie04] K. McKenzie, N. Grosse, W. Bowen, S. Whitcomb, M. Gray, D. Mc-Clelland, and P. Lam, *Squeezing in the audio gravitational-wave detection band*, Phys. Rev. Lett. **93**, 161105 (2004). Quoted p. 19, 133

[MISA] MISA, Laboratory for Micro Sensors and Actuators, Seoul National University, http://plaza.snu.ac.kr/∼micro/research_frameset.html. Quoted p. 112

[Morrison94] E. Morrison, B. Meers, D. Robertson, and H. Ward, *Automatic alignment of optical interferometers*, Applied Optics **33**, 5041 (1994). Quoted p. 75, 81

[Navez01] P. Navez, E. Brambilla, A. Gatti, and L.A. Lugiato, *Spatial entanglement of twin quantum images* , Phys. Rev. A **65**, 013813 (2001). Quoted p. 164

[Neergaard-Nielsen06] J. S. Neergaard-Nielsen, B. M. Nielsen, C. Hettich, K. Mølmer, and E.S. Polzik, *Generation of a Superposition of Odd Photon Number States for Quantum Information Networks*, Phys. Rev. Lett. **97**, 083604 (2006). Quoted p. 17

[Nicholson98] D. Nicholson and A. Vecchio, *Bayesian bounds on parameter estimation accuracy for compact coalescing binary gravitational wave signals* , Phys. Rev. D **57**, 4588 (1998). Quoted p. 89

[Nikulin01] V. V. Nikulin, M. Bouzoubaa, V. A. Skormin and T. E. Busch, *Modeling of an acousto-optic laser beam steering system intended for satellite communication* , Opt. Eng., **40**, 2208 (2001). Quoted p. 151

[Oemrawsingh04] S. Oemrawsingh, A. Aiello, E. Eliel, G. Nienhuis, and J. Woerdman, *How to observe high- dimensional two-photon entanglement with only two detectors*, Rev. Rev. Lett. **92** 217901 (2004). Quoted p. 105

[Ou92] Z.Y. Ou, S.F. Pereira, H.J. Kimble, and K.C. Peng, *Realization of the Einstein-Podolsky-Rosen paradox for continuous variables*, Phys. Rev. Lett. **68**, 3663 (1992). Quoted p. 2, 22, 27, 164, 165

[Ourjoumtsev06] A. Ourjoumtsev, R. Tualle-Brouri, J. Laurat and P. Grangier, *Generating Optical Schrodinger Kittens for Quantum Information Processing*, Science **7**, 83 (2006). Quoted p. 17

[Padgett06] M. Padgett, G. Whyte, J. Girkin, A. Wright, L. Allen, P. Öhberg, and S. M. Barnett, *Polarization and image rotation induced by a rotating dielectric rod: an optical angular momentum interpretation*, Opt. Lett. **31**, 2205 (2006). Quoted p. 83

[Parkins00] A. S. Parkins and H. J. Kimble, *Position-momentum Einstein-Podolsky-Rosen state of distantly separated trapped atoms*, Phys. Rev. A **61**, 052104 (2000). Quoted p. 164

[Paschotta94] S. Paschotta, J. Schiller, J. Mlynek, *82% Efficient continuous-wave frequency doubling of 1.06 m with a monolithic MgO: $LiNbO_3$ resonator* , Opt. Let. **19** 1325 (1994). Quoted p. 120, 123

[Patel66] C. K. N. Patel, *Optical Harmonic Generation in the Infrared Using a CO_2 Laser*, Phys.Rev.Lett. **16** 613 (1966). Quoted p. 120

[Paterson01] L. Paterson, M. P. MacDonald, J. Arlt, W. Sibbett, P. E. Bryant and K. Dholakia, *Controlled rotation of optically trapped microscopic particles*, Science **292**, 912 (2001). Quoted p. 83

[Penn91] C. Penn, H.-A. Bachor, D.E. McClelland, *Automatic alignment and mode-matching of a laser beam to an optical resonator*, Gravitational Astronomy: Instrument Design and Astrophysical Prospects, (1991). Quoted p. 81

[Peres96] A. Peres, *Separability criterion for density matrices*, Phys. Rev. Lett. **77**, 1413 (1996). Quoted p. 24

[Pirandola03] S. Pirandola, S. Mancini, D. Vitali, P. Tombesi, *Continuous variable entanglement by radiation pressure*, J. opt. B Quantum semiclass. opt. **5** S523-S529 (2003). Quoted p. 22

[Plenio00] M. B. Plenio and V. Vedral, *Teleportation, entanglement and thermodynamics in the quantum world*, Contemp. Phys. **39**, 431 (1998). Quoted p. 24

[Poizat98] J.P. Poizat, T. Chang, O. Ripoll and P. Grangier, *Spatial quantum noise of laser diodes*, J. Opt. Soc. Am. B, **15**, 1757 (1998). Quoted p. 33

[Pound46] R.V. Pound, *Electronic frequency stabilization of microwave oscillators*, Rev. Sci. Instrum. **17**, 490 (1946). Quoted p. 173

[Putman92] C.A.J. Putman, K.O. van der Werf, B.G. de Grooth, N.F. van Hulst, F.B. Segerink, and J.Greve, *Atomic force microscope with integrated optical microscope for biological applications* , Rev. Sci. Instrum. **63**, 1914 (1992). Quoted p. 2, 151

[Ralph95] T.C. Ralph, M.S. Taubman, A.G. White, D.E. McClelland, and H.-A. Bachor, *Squeezed light from second-harmonic generation: experiment versus theory*, Opt. Lett. **20**, 1316 (1995). Quoted p. 120

[Rayleigh1879] Lord Rayleigh, *Collected Optics Papers of Lord Rayleigh*, Philos. Mag. 261, 403, 477 (1879), Optical Society of America, Washington D.C., part A, p117 (1994). Quoted p. 2

[Raymer93] M.G. Raymer, J. Cooper and M. Beck, *Many-port homodyne detection of an optical phase*, Phys. Rev. A **48**, 4617 (1993). Quoted p. 52

[Refregier02] P. Réfrégier, *"Théorie du bruit et applications en physique"*, Lavoisier (2002). Quoted p. 89, 90

[Reid88] M. D. Reid and P. D. Drummond, *Quantum correlations of phase in nondegenerate parametric oscillation*, Phys. Rev. Lett. **60**, 2731 (1988). Quoted p. 23, 25

[Reynaud92] S. Reynaud, A. Heidmann, E. Giacobino et C. Fabre, *Quantum fluctuations in optical systems*, Progress in Optics Elsevier Science Publishers, E. Wolf, XXX (1992). Quoted p. 8

[Ribeiro97] P.H.S. Ribeiro, C. Schwob, A. Maître, and C. Fabre, *Sub-shot-noise high-sensitivity spectroscopy with optical parametric oscillator twin beams* Opt. Lett. **22**, 1893 (1997). Quoted p.

[Riedmatten06] H. de Riedmatten, J. Laurat, C. W. Chou, E. W. Schomburg, D. Felinto, and H. J. Kimble, *Direct Measurement of Decoherence for Entanglement between a Photon and Stored Atomic Excitation*, Phys. Rev. Lett. **97**, 113603 (2006). Quoted p. 164

[Robertson02] N. A. Robertson *et al.*, *Quadruple suspension design for Advanced LIGO*, Class. Quantum Grav. **19**, 4043 (2002). Quoted p. 5

[Rohrbach04] A. Rohrbach, C. Tischer, D. Neumayer, E.-L. Florin, and E.H.K. Stelzer, *Trapping and tracking a local probe with a photonic force microscope*, Rev. Sci. Instr. **75**, 2197 (2004). Quoted p. 89

[Santhanakrishnan95] T. Santhanakrishnan, N. Krishna Mohan, M.D. Kothiyal and R.S. Sirohi, *A Non-Contact Simultaneous Measurement of Out-Of-Plane Displacement and Tilt of a Cantilever* , J. Opt., **24**, 109 (1995). Quoted p. 151

[Schnabel06] R. Schnabel's group, 6.5 dB of squeezing, to be published. Quoted p. 131

[Schwarz04] U. Schwarz, M. Bandres, and J. Gutierrez-Vega, *Observation of Ince-Gaussian modes in stable resonators*, Opt. Lett. **29**, 1870 (2004). Quoted p. 139

[Schwob98] C. Schwob, P. Cohadon, C. Fabre, M. Marte, H. Ritsch, A. Gatti, and L. Lugiato, *Transverse effects and mode couplings in OPOS*, Applied Physics B Lasers and Optics **66**, 685 (1998). Quoted p. 123

[Scotto03] P. Scotto, P. Colet, and M. San Miguel, *All-optical image processing with cavity type II second-harmonic generation*, Opt. Lett. **28**, 1695 (2003). Quoted p. 122

[Senden01] Tim J. Senden, *Current Opinion In Colloid & Interface Science* **6**, 95 (2001) Quoted p. 45

[Senior07] R. Senior, J. Janousek, K. Wagner, H-A. Bachor and C.C. Harb, to be published. Quoted p. 19, 133

[Serkland97] D. K. Serkland, P. Kumar, M.A. Arbore and M.M. Fejer, *Amplitude squeezing by means of quasi-phase-matched second-harmonic generation in a lithium niobate waveguide*, Opt. Lett. **22**, 1497 (1997). Quoted p. 120

[Siegman86] A.E. Siegman, *Lasers*, University Science, Mill Valley California (1986). Quoted p. 10, 15, 83, 107, 109, 125

[Silberhorn01,1] Ch. Silberhorn, P. K. Lam, O. Weiss, F. Koenig, N. Korolkova, and G. Leuchs, *Generation of continuous variable Einstein-Podolsky-Rosen entanglement via the Kerr nonlinearity in an optical fiber*, Phys. Rev. Lett. **86**, 4267 (2001). Quoted p. 22, 27

[Silberhorn01,2] Ch.Silberhorn, *Quantum Key Distribution with Bright Entangled Beams* , *et al.*, Phys. Rev. Lett. **86**, 4267 (2001). Quoted p. 2

[Simmons96] R. M. Simmons, J. T. Finer, S. Chu and J. A. Spudich, *Quantitative measurements of force and displacement using an optical trap*, Biophys. J., **70**, 1813 (1996). Quoted p. 151

[Simon00] R. Simon, *Peres-Horodecki separability criterion for continuous variable systems*, Phys. Rev. Lett. **84**, 2726 (2000). Quoted p. 24

[Slusher85] R.R. Slusher, L.W. Hollberg, B. Yurke, J.C. Mertz, J.F. Valley, *Observation of squeezed states generated by four-wave mixing in an opitcal cavity*, Phys. Rev. Lett. **55**, 2409 (1985). Quoted p. 19

[Smith76] S.D. Smith, H.D. Riccius, and R.P. Edwin, *Refractive indices of lithium niobate*, Opt.Comm., **17**, 332 (1976) and **20**, 188 (1977). Quoted p. 128

[Sokolov01] I. Sokolov, M. Kolobov, A. Gatti, and L. Lugiato, *Quantum holographic teleportation*, Opt. Comm. **193** 175 (2001). Quoted p. 105

[SoutoRibeiro97] P. H. Souto Ribeiro, C. Schwob, A. Maître, and C. Fabre, *Sub-shot-noise high-sensitivity spectroscopy with optical parametric oscillator twin beams*, Opt. Let. **22**, 1893 (1997). Quoted p. 21, 45, 89

[SQZ87] Special issue on squeezed states in JOSA B **4**, issue 10 (1987). Quoted p. 19

[Suzuki06] S. Suzuki, H. Yonezawa, F. Kannari, M. Sasaki, A. Furusawa, *7 dB quadrature squeezing at 860 nm with periodically poled $KTiOPO_4$*, Appl. Phys. Lett. **89**, 061116 (2006). Quoted p. 19, 133

[Tian06] L. Tian and R. W. Simmonds, *Coupled macroscopic quantum resonators: entanglement and squeezed state*, cond-mat/0606787,(2006). Quoted p. 22

[Tisher01] C. Tischer, S. Altmann, S. Fisinger, J. K. H. Höber, E. H. K. Stelzer, and E.-L. Florin, *Three-dimensional thermal noise imaging* , Appl. Phys. Lett. **79**, 3878 (2001) Quoted p. 45

[TrepsPhD01] N.Treps, *Quantum effects in optical images*, PhD Thesis (Universit}e Pierre et Marie Curie, Paris 2001). Quoted p. 9, 10, 46, 47

[Treps02] N. Treps, U. Andersen, B. Buchler, P.K. Lam, A. Maître, H. Bachor, C. Fabre, *Surpassing the Standard Quantum Limit for Optical Imaging Using Nonclassical Multimode Light* , Phys. Rev. Lett. **88** 203601 (2002). Quoted p. 2, 44, 45, 105, 115, 116, 151, 154

[Treps03] N. Treps, N. Grosse, W. P. Bowen, C. Fabre, H.-A. Bachor and P. K. Lam, *A Quantum Laser Pointer* , Science, **301**, 940 (2003). Quoted p. 2, 44, 45, 119, 151, 180

[Treps04,1] N. Treps, N. Grosse, W. Bowen, M.T.L. Hsu, A. Maître, C. Fabre, H.A. Bachor, P.K. Lam, *Nano-displacement measurements using spatially multimode squeezed light* , J. Opt. B: Quantum Semiclass. Opt. **6**, S664 (2004). Quoted p. 44, 45, 52, 86, 88, 119, 151

[Treps04,2] N. Treps and C. Fabre, *Title: Criteria of quantum correlation in the measurement of continuous variables in optics*, quant-ph/0407214 (2004). Quoted p. 27

[Treps05] N. Treps, V. Delaubert, A. Maître, J. M. Courty and C. Fabre, *Quantum noise in multipixel image processing* , Phys. Rev. A **71**, 013820 (2005). Quoted p. 28, 44

[Vahlbruch05] H. Vahlbruch, S. Chelkowski, B. Hage, A. Franzen, K. Danzmann, and R. Schnabel, *Demonstration of a Squeezed-Light-Enhanced Power- and Signal-Recycled Michelson Interferometer*, Phys. Rev. Lett. **95**, 211102 (2005). Quoted p. 21

[VanDeNes06,1] A.S. Van De Nes, J.J.M. Braat and S.F. Pereira, *High-density optical data storage*, Rep. Prog. Phys. **69**, 2323 (2006). Quoted p. 2, 3, 55, 56

[VanDeNes06,2] A.S. van de Nes, S.F. Pereira and J.J.M. Braat, *On the conservation of fundamental optical quantities in non-paraxial imaging systems*, J. Mod. Opt. **53** 677 (2006). Quoted p. 56

[Vaziri02] A. Vaziri, G. Weihs, and A. Zeilinger, *Superpositions of the orbital angular momentum for applications in quantum experiments*, Journal of Optics B: Quantum and Semiclassical Optics **4**, S47 (2002). Quoted p. 139

[Vedral97] V. Vedral, M. B. Plenio, M. A. Rippin, and P. L. Knight, *Quantifying entanglement*, Phys. Rev. Lett. **78**, 2275 (1997). Quoted p. 24

[Walls95] D. F. Walls and G. J. Milburn, *Quantum optics*, Springer-Verlag, Berlin, 1 edition (1995). Quoted p. 17, 134

[Willke02] B. Willke *et al.*, *The GEO 600 gravitational wave detector*, Class. Quantum Grav. **19** 1377 (2002). Quoted p. 2, 5

[Wiseman99] H.M. Wiseman, *Squashed States of Light: Theory and Applications to Quantum Spectroscopy*, quant-ph/9904033. Quoted p. 19

[Wu86] L. Wu, H. Kimble, J. Hall, and H. Wu, *Generation of squeezed states by parametric down conversion*, Phys. Rev. Lett. **57** 2520 (1986). Quoted p. 19, 133

[Yu03] L. H. Yu, L. DiMauro, A. Doyuran, W. S. Graves, E. D. Johnson, R. Heese, S. Krinsky, H. Loos, J. B. Murphy, G. Rakowsky, J. Rose, T. Shaftan, B. Sheehy, J. Skaritka, X. J. Wang, and Z. Wu, *First Ultraviolet High-Gain Harmonic-Generation Free-Electron Laser* , Phys. Rev. Lett. **91**, 074801 (2003). Quoted p. 120

[Zambrini03] R. Zambrini, A. Gatti, L.A. Lugiato and M. San Miguel, *Polarization quantum properties in a type-II optical parametric oscillator below threshold* , Phys. Rev. A **68**, 063809 (2003). Quoted p. 164

[Zeilinger00] A. Zeilinger, *Quantum entangled bits step closer to IT*, Science **289**, 405 (2000). Quoted p. 105

[Zhang:95] J.Y. Zhang, Jing-Yuan Zhang, Jung Y. Huang,*Optical Parametric Generation and Amplification*, CRC Press (1995). Quoted p. 133

[Zhang00] Y. Zhang, H. Wang, X. Li, J. Jing, C. Xie, and K. Peng, *Experimental generation of bright two-mode quadrature squeezed light from a narrow-band nondegenerate optical parametric amplifier*, Phys. Rev. A. **62**, 023813 (2000). Quoted p. 22, 27